The University Of Sheffield.

Characterisation and Optimisation of the Hole Transport Interface in Organic Solar Cells for Improved Performance and Stability of the Devices

By:

Gabriel Eduardo Pérez García

A thesis submitted in partial fulfilment of the requirements for the degree of Doctor of Philosophy

The University of Sheffield

Faculty of Engineering

Department of Chemical and Biological Engineering

September 2019

To the glory of God almighty, my refuge and strength,

whose power is made strong in our weaknesses

Abstract

The increased atmospheric concentration of greenhouse gases due to the combustion of fossil fuels and its impact on the temperature of the planet has led to the development of alternative energy generation methods. Organic solar cells (OSCs) are a promising technology that is simple to process, flexible, customizable, and potentially low-cost. However, relatively low efficiencies, and short lifetimes compared with other photovoltaic technologies are as the main challenges of organic solar cells. This thesis aims to characterise and optimise the hole transporting interface to improve the efficiency and long-term stability of OSCs. To achieve this, first, the device fabrication process of P3HT:PCBM based devices was optimised to produce devices that perform at a standard commensurate with those reported in literature with a similar architecture and fabricated under similar conditions. In particular, two different evaporation techniques for the deposition of the electron conducting electrode were compared. Electron-beam evaporation significantly decreased the crystallinity of P3HT while thermal evaporation proved to be effective for producing P3HT and PCDTBT based devices with an efficiency comparable to the values reported in literature for a similar device architecture.

In an attempt to improve the efficiency of devices, the electrical conductivity of the PEDOT:PSS hole transporting layer was increased by almost two orders of magnitude using a zwitterionic additive (DYMAP) to dope the PEDOT:PSS dispersion. The liquid and solid phase structural modifications of the conductivity enhanced PEDOT:PSS were studied to understand the effects of conductivity enhancing additives on the morphology of PEDOT:PSS. Small angle neutron scattering revealed that the interchain distance between PSS backbone chains, and the screening length of neutralised PSS segments increase as the concentration of DYMAP increases from 0 to 25 mM. However, at 30 mM doping concentration, DYMAP induces gelation in the PEDOT:PSS dispersion resulting in a decreased interchain distance similar to that of the undoped PEDOT:PSS, and a significantly increased screening length compared to that of the 25 mM doped dispersion. The vertical structure of DYMAP doped PEDOT:PSS films was studied with neutron reflectivity which revealed that at low doping concentration, the film separates into a quasi-bilayer film in which the dopant segregates at the bottom of the film. However, at higher DYMAP doping concentration, DYMAP is evenly distributed throughout the

film which results in a homogeneous single structure. The DYMAP doped PEDOT:PSS films were then incorporated as the hole transporting layer in OSCs which resulted in the decreased photovoltaic performance of devices compared to the control devices. This was found to be mainly due to the poor contact between the doped HTL and the active layer as a result of the increased phobicity of the doped PEDOT:PSS films to the solvent of the active layer.

Another approach to improving the device efficiency and stability was to incorporate three variants of a $P3HT_{50}$-*b*-PSS_x block co-polymer as an interfacial layer between PEDOT:PSS and P3HT:PCBM to improve the hole transport and stability between such layers. The incorporation of a 10 nm $P3HT_{50}$-*b*-PSS_{16} and a 13 nm $P3HT_{50}$-*b*-PSS_{23} interfacial layer resulted in a 9% and 12% increased device efficiency respectively compared to the reference devices. This was mainly due to a 9% increase of the open circuit voltage caused by the more energetically favourable alignment of the HOMO of the block co-polymers with the HOMO of P3HT. The fill factor of the 10 nm $P3HT_{50}$-*b*-PSS_{16} and 13 nm $P3HT_{50}$-*b*-PSS_{23} incorporated devices also increased by 2.8% and 6.2% respectively due to a smoother surface than PEDOT:PSS and the more compatible contact between the P3HT block of the block co-polymer and the P3HT, and the PSS block with the PEDOT:PSS. Moreover, the devices with the interfacial block co-polymer had a higher normalised efficiency than the control devices after 2200 hours of storage, demonstrating that the block co-polymer not only improves device efficiency, but crucially prevents degradation by stabilising the interface between PEDOT:PSS and P3HT.

Acknowledgements

I would like to thank all the people who supported me throughout my PhD for without them, the completion of this thesis would not have been possible. First, I would like to thank my supervisor, Alan Dunbar for giving me the opportunity to work under his guidance and tutelage, but most importantly for his trust in me. I am thankful that my professional practice has been shaped by his work ethics, curiosity, and passion for science. I would also like to thank the National Council of Science and Technology (CONACyT) of Mexico and the Mexico Secretary of Energy (SENER) for the provision of a PhD scholarship.

Furthermore I want to express my gratitude to all my colleagues from different departments who helped me with my research either through assisting me with my experiments or by sharing helpful advice. Those I shared a lab with, Dr Chankyu Kwak, Dr Noura Alhazmi, Francesco Bastianini, Kostas Tsevas and Edwin Pineda. Colleagues from the Department of Physics and Astronomy, Dr Benjamin Freestone, Joel Smith, Dr Michael Stringer, Tarek Alanazi, Rachel Kilbride, Dr Andrew Parnell, and Prof David Lidzey. Colleagues from the Department of Chemistry, Ali Alkorbi, and Prof Ahmed Iraqi. Colleagues from other institutions, Dr Gabriel Bernardo, Dr Joshaniel Cooper, and Dr Stephen King. I would also like to thank the ISIS Neutron and Muon Source for the opportunity to use their top class facilities.

I would also like to thank my family and friends who supported me throughout this stage of my life, in particular my parents, Maria del Carmen García Soto and Antonio Eduardo Peréz Balbuena, who gave everything they could so I could have the opportunities in life that led me to where I am today. My sister, Karla Suleny Peréz García. A huge thank you to my in laws, Ian and Monica Coates who since the very beginning treated me as if I was their son, giving me a feeling of belonging in a country where I felt like a stranger before meeting them. Thanks to my friends and brothers in Christ João Vasco, Errol Legister, and Vino Michael who I met at the start of this journey and whose friendship keeps me strong and steady. A special thanks to my friend José Cervantes Blanca and his family for constantly keeping me in their prayers.

Lastly, and most importantly, I would also like to thank my wonderful wife, Sonia Pérez, whose unconditional support and encouragement got me through difficult times. From driving me to the laboratory late at night and bringing me dinner during long evenings at the office, to proofreading this thesis, you constantly were my driving force and reason to smile at the end of tough days. You truly are a blessing from God.

Publications and conferences

C. Kwak, G.E. Pérez, B.G. Freestone, S.A. Al-Isaee, A. Iraqi, D.G. Lidzey, A.D.F. Dunbar, "Improved efficiency in organic solar cells via conjugated polyelectrolyte additive in the hole transporting layer," *Journal of Materials Chemistry C*, vol. 4, p. 10722-10730, 2016.

G.E. Pérez, G. Bernardo, H. Gaspar, J.F.K. Cooper, F. Bastianini, A.J. Parnell, A.D.F. Dunbar, "Determination of the Thin-Film Structure of Zwitterion-Doped Poly(3,4-ethylenedioxythiophene):Poly(styrenesulfonate): A Neutron Reflectivity Study," *ACS Applied Materials and Interfaces*, vol. 11, no. 14, p. 13803-13811, 2019

F. Bastianini, G.E. Pérez, A.R. Hobson, S.E. Rogers, A.J. Parnell, M. Grell, A. Flores Gutiérrez, A.D.F. Dunbar, "In-situ monitoring Poly(3-hexylthiophene) nanowire formation and shape evolution in solution via small angle neutron scattering," *Solar Energy Materials and Solar Cells*, vol. 202, p. 110128, 2019

G. Bernardo, H. Gaspar, G.E. Pérez, A. Shackleford, A.J. Parnell, M. Bleuel, A. Mendes, S.M. King, S.R. Parnell, "Impact of 1,8-diiodooctane on the morphology of organic photovoltaic devices - A Small Angle Neutron Scattering (SANS) study," *Polym. Test.*, vol. 82, p. 106305, 2020

G.E. Pérez, A. Alkorbi, A. Iraqi, F. Bastianini, E. Pineda, S.M. King, A.D.F. Dunbar, "Interchain Spacing and Screening Length Modification of PSS Backbone Chains in Zwitterion Doped Poly(3,4-Ethylenedioxythiophene):Polystyrene Sulfonate," Accepted, 2020

G.E. Pérez, H. Erothu, P.D. Topham, F. Bastianini, T.I. Alanazi, G. Bernardo, A.J. Parnell, S.M. King, A.D.F. Dunbar, "Improved performance and stability of organic solar cells by the incorporation of a block co-polymer inter-facial layer to enhance the contact quality between the hole transporting and photoactive layers," Submitted 2019

ISIS Student meeting conference 2016. Oxford, UK, September 2019. Oral presentation

European Conference on Neutron Scattering 2019, Saint Petersburg, Russia, July 2019. Poster presentation

Contents

1 Introduction

1.1 Research aim, and structure of the thesis

The aim of this thesis is to characterise and optimise the hole transporting interface of organic solar cells. Specifically, this has been done to improve the efficiency and long-term stability of P3HT:PCBM based devices with a PEDOT:PSS hole transporting layer within its architecture. The specific procedures to achieve these objectives will be detailed in section 3.8.

The thesis is structured in 8 chapters. The first chapter provides a broad background overview that discusses the motivation and need for more environmentally friendly energy generation technologies such as the one investigated in this work. The second chapter describes the basic working principle of photovoltaic technology and discusses the theory used to perform a qualitative and quantitative analysis of the performance of a photovoltaic device. The third chapter discusses the theory of organic photovoltaics and reviews the relevant literature concerning the work in this thesis. At the end of these initial chapters, the specific objectives, and how they will be attempted to be achieved, are presented. Chapters four, five, and six contain the research contributions of this thesis and constitute the core of this document. A format in which each experimental chapter contains its own introduction and/or justification, experimental methods, results and discussion, and conclusions has been chosen for ease of reading and to favour a coherent structure that provides the reader with the relevant information at an appropriate point in the document. The first of two concluding chapters, chapter seven, summarizes the conclusions and results of this research and discusses their contribution to each specific objective described in section 3.8. The last chapter briefly discusses different opportunities for future work based on the findings of this thesis and several routes toward the continuation of the research presented in this document.

1.2 Energy generation and its implications

Energy services are essential to meet human needs, from the most basic to the most complex. Therefore, the provision of energy is a fundamental priority for the development of mankind. Since the discovery of combustion, the burning of carbon has been the predominant method for extracting energy; this has been particularly intense since the industrial revolution broadened the range of uses for such obtained energy. This is evident by the total global energy consumption of 2018; of all energy 84.7% was produced by fossil fuels[1]. This dependency on the burning of carbon to meet the growing energy demand has been a major contributor to the alteration of the intrinsic concentration of some greenhouse gases in the atmosphere, in particular methane (CH_4), nitrous oxide (N_2O), and carbon dioxide (CO_2), the later of which is predominant. This is because such greenhouse gases are released as a byproduct of the combustion reaction. The greenhouse gases alteration in the atmosphere mentioned above can be appreciated in figure 1 produced by Froster et al.[2] inasmuch, as 87% of the total anthropogenic emissions of CO_2 are produced by the burning of fossil fuels[3]. The anthropogenic contributions of CH_4 and N_2O to their total concentration in the atmosphere are considerably lower than those of CO_2 (60% and 40% for CH_4 and N_2O respectively[3;4]), however, as it can be seen in figure 1 the anthropogenic contributions of CH_4 and N_2O are sufficiently significant to surpass the average concentrations within the past 2000 years. This has caused the historical increase in the atmospheric concentrations of CO_2, CH_4, and N_2O by 40%, 20%, and 150% respectively from 1750 to 2011.

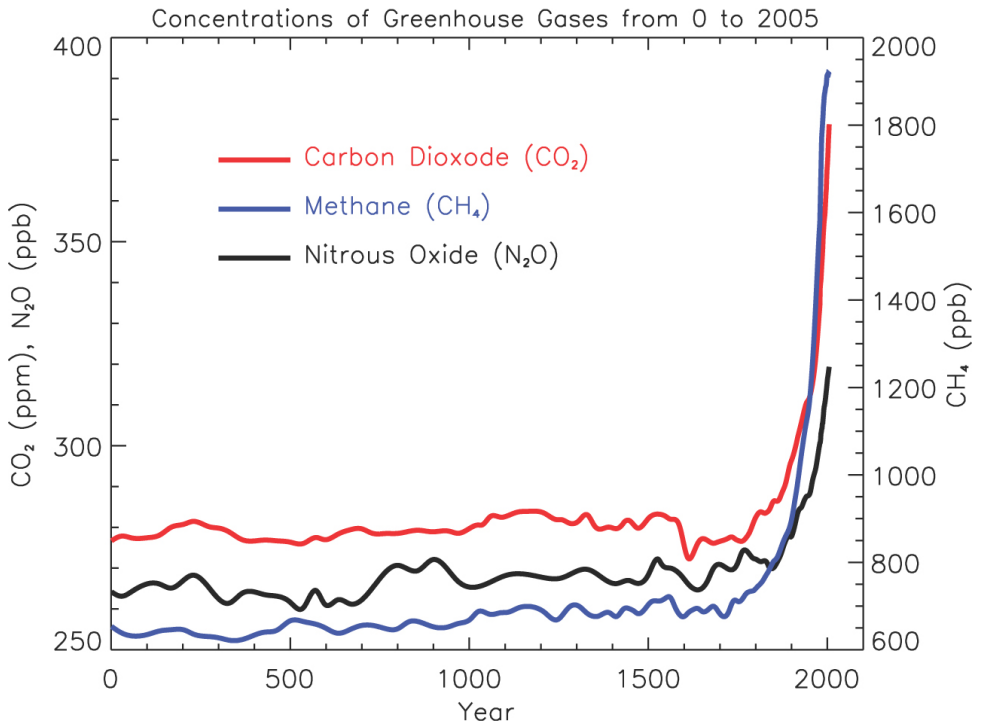

Figure 1: *"Atmospheric concentrations of important long-lived greenhouse gases over the last 2,000 years. Increases since about 1750 are attributed to human activities in the industrial era. Concentration units are parts per million (ppm) or parts per billion (ppb), indicating the number of molecules of the greenhouse gas per million or billion air molecules, respectively, in an atmospheric sample. (Data combined and simplified from Chapters 6 and 2 of the cited report.)". Original image and caption produced by the IPCC and reproduced with permission. Original image (FAQ 2.1 figure 1) is found in the second chapter of the IPCC Fourth Assessment Report: Climate Change 2007 (AR4), Working Group I Report "The Physical Science Basis"*[2].

The increased concentration of greenhouse gases in Earth's antmosphere has a significant impact on the temperature of the planet. However, even though as far back as 1896 Svante Arrhenius calculated that doubling the amount of CO_2 in the atmosphere would melt the ice caps and change the global temperature[5], no major concern about the environmental impacts of burning fossil fuels rose until the mid twentieth century. It was after Guy Callendar first published evidence that suggested that the increase of CO_2 in the atmosphere and the increase in global temperature were related[6], that efforts to reduce the environmental impact of human activities were considered by different nations. This led to the birth of intergovernmental treatises and institutions that, amongst other goals, aimed at monitoring[7] and reducing[8] the anthropogenic greenhouse gas emissions, in particular CO_2 which is the most emitted, thus most influential in the Earth's greenhouse effect. Given the high percentage of anthropogenic CO2 emissions mentioned before, this

requires the significantly partial or total reduction of fossil fuel energy production.

Since the publication of Callendar there has been growing evidence that shows a correlation between the increase in global temperature and the concentration of greenhouse gases in the atmosphere. In figure 2, produced by Jansen et al.[9], a compilation of proxy temperature measurements are compared with the historical concentrations of CO_2, CH_4, and N_2O. These measurements suggest that the behaviour of Earth's temperature is correlated to, and highly likely caused by, the atmospheric greenhouse gas concentrations.

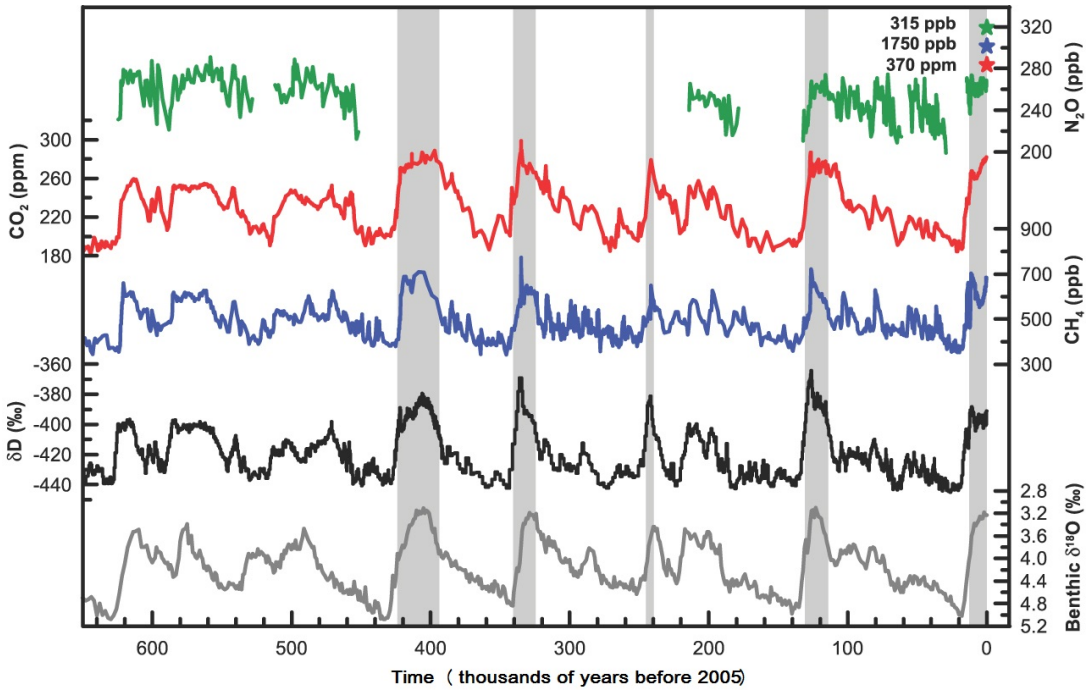

Figure 2: *"Variations of deuterium (δD; black), a proxy for local temperature, and the atmospheric concentrations of the greenhouse gases CO_2 (red), CH_4 (blue), and nitrous oxide (N_2O; green) derived from air trapped within ice cores from Antarctica and from recent atmospheric measurements. The shading indicates the last interglacial warm periods. Interglacial periods also existed prior to 450 kyr, but these were apparently colder than the typical interglacials of the latest Quaternary. The length of the current interglacial is not unusual in the context of the last 650 kyr. The stack of 57 globally distributed benthic $\delta^{18}O$ marine records (dark grey), a proxy for global ice volume fluctuations, is displayed for comparison with the ice core data. Downward trends in the benthic $\delta^{18}O$ curve reflect increasing ice volumes on land. Note that the shaded vertical bars are based on the ice core age model, and that the marine record is plotted on its original time scale based on tuning to the orbital parameters. The stars and labels indicate atmospheric concentrations at year 2000." Original image and caption produced by the IPCC and reproduced with permission. Original image, and detailed description of the elements of the figure such as the explanation of the working principles behind the proxy measurements (figure 6.3 in the referenced document), is found in the sixth chapter of the IPCC Fourth Assessment Report: Climate Change 2007 (AR4), Working Group I Report "The Physical Science Basis"[9].*

Despite efforts to reduce the production of energy from fossil fuels, such still accounted for more than 80% of the world's total primary energy supply from 1971 to 2018 [1;10]. At the present time this represents not only an environmental issue, but an economic one too. Due to their low regeneration rate and relatively uncertain availability, fossil fuel prices have been high and volatile in the last decade[11]. These changes have brought geopolitical consequences that include international conflicts and economical instability for developing countries[12].

In order to maintain both a sustainable global climate system, and a sustainable economy that is capable of providing essential goods and services to the people of all nations, a major shift in how energy is obtained and utilized is required.

1.3 An alternative to fossil fuels

The IPCC[13] defines renewable energy (RE) as "any form of energy from solar, geophysical or biological sources that is replenished by natural processes at a rate that equals or exceeds its rate of use". Additionally, and with the exception of some biofuels, RE is obtained through technologies that emit little to no greenhouse gases once they are operating. This makes RE a suitable alternative to provide energy services in a sustainable manner and, in particular, help mitigate the onset of climate change. However, there are some challenges that RE has to overcome in order for it to become a definitive alternative to fossil fuels. One of the main challenges for RE is its intermittency, and therefore, energy storage is a very active area of research, but, not the one concerning this work. The main challenge for RE is to provide the energy capacity required to satisfy the current and future demand for energy.

According to Nathan Lewis the energy rate demanded by humans was 13 Terawatts (TW) in 2007 and is expected to rise to approximately 30 TW by the year 2050[14]. This means that regardless of the method used to produce and deliver energy, it has to account for a value safely above the required quantity. Lewis also did a detailed analysis of the potential of different renewable energies and considered them in relation to this required quantity of energy. The result is that, individually, all but solar energy fail to

deliver in either capacity, accessibility, or availability. While it is true that a combination of different renewable energy generation methods is advantageous, the possibility of having one technology capable of supplying the present and future energy needs would allow global efforts and investments to be specifically focused. Focusing on a single technology could promote an increased rate in the development of this technology.

The Sun provides Earth with 120,000 TW[14]. This energy comes in photons which have to be converted into a more practically useful form of energy such as electricity. Currently, there are three main methods to harvest solar energy. Producing fuels such as hydrogen and methane using solar radiation can provide a source of energy when the main resource (in this case sunlight) is not available, however this energy generation method is currently very costly and the least efficient method to produce a more practically usable form of energy from sunlight[15]. Moreover, one of the main selling points of solar fuels is the production of some fuels such as diesel that are currently used by the existing infrastructure. This may result in the overall decrease of CO_2 emissions by producing the fuel in a more environmentally friendly way, however, the subsequent conversion of the fuel into energy will still result in the emission of CO_2 nonetheless. Solar thermal converts light into thermal energy that can be subsequently used as it is, or to produce steam and run a turbine to generate electricity. Given that electricity and heat generation currently account for 42% of the total anthropogenic CO_2 emissions[16], substituting the conventional, high CO_2 emitting energy sources such as fossil fuels for technologies that produce electricity without emitting CO_2 when operating would substantially reduce the total CO_2 emissions. Solar thermal holds a huge potential at the industrial or utility scale level in certain areas of the world where the solar resource is abundant and constant throughout the whole year. This is due to its high beam to electricity efficiency of 30 to 40%[17], however, these efficiencies are only achievable at very large scales. Moreover, since this method is not a direct way of producing electricity, the complexity of its deployment and operation substantially limit its implementation. Thus, at the domestic scale for example, solar thermal can only be realistically used to provide intermittent heat. Photovoltaic energy converts a specific range of the electromagnetic spectrum of light into electricity through a device called a solar cell. This last method is the most direct way of converting photons provided by the sun into electricity. In

theory, 0.1% of the Earth's surface covered with 10% efficient devices would be enough to satisfy the total energy needs of humanity[18]. In practice, this scenario would require the transmission of the produced electricity to extremely remote places relative to the generation site, and an enormous energy storage capacity for the times when there is no sunlight. Neither situation is feasible in the short-term with the current available technology. However, the 0.1% surface coverage with 10% efficient devices theoretical analysis demonstrates the tremendous potential of photovoltaic technology. Moreover, since photovoltaic technology provides a simple and direct way of converting sunlight into electricity, the implementation of this technology is not restricted by scale and therefore can be used at the domestic level. The domestic use of photovoltaic technology is thus only limited by location, architecture, and the cost-efficiency of the technology which can be addressed with research and development[19]. In the next chapter, a general overview of photovoltaic technology and the theory used to characterise its performance is presented, followed by a brief, non exhaustive review of the current market dominant photovoltaic technologies.

2 Photovoltaics

2.1 The basic principle

The photovoltaic effect can be explained by quantum theory, which states that light is made up of packets of energy called photons[20]. The photon energy depends upon the frequency of the specific electromagnetic radiation which, if high enough, is capable of exciting electrons that are bound into solids up to higher levels of energy where they are less bound to the solid. Upon photon absorption and electron excitation, a positive quasi-particle called a hole is generated at the ground state where the electron was originally bound before being excited. However, the excited electron quickly relaxes back to its initial or ground state reoccupying the generated hole. In order for a photovoltaic device to work, the excited electron has to be separated from the hole before relaxation, and transported to the electrical contacts that connect the device to an external circuit. To achieve this, the photovoltaic materials need to have a semiconducting behaviour which allows the absorption of some photons and the relatively slow relaxation of electrons which makes possible their separation from holes. The potential difference generated by the extra energy of the excited electron is the force that ultimately drives the electrons through a load in the external circuit to do electrical work.

Since the energy input is limited by the incoming electromagnetic radiation, which for solar cells is the fixed solar spectrum, the efficiency of a photovoltaic device can be considered to be practically dependant, from an engineering perspective, upon the effectiveness of light absorption, and charge separation and transport, which at the same time are dependant upon the intrinsic physical and chemical properties of the chosen materials and on the device structure. Moreover, depending on the type of photovoltaic technology that the device is made from, the specific physics that govern charge separation and transport differ from one another. For instance, conventional inorganic semiconductor solar cells rely on a built in electric field generated as a result of a semiconductor p-n junction built into the device to drive the charges to their respective electrodes. However, an organic conjugated polymer based solar cell relies an energy gradient created by the different electrochemical potential of the materials within the device to separate the

charges and transport them to the relevant electrodes. This is due to the fact that the energy that bounds the electron-hole pair after charge excitation is significantly higher for conjugated, polymer based, solar cells than for inorganic photovoltaics.

Since the efficiency of a photovoltaic device can be mathematically quantified with the power input (P_{in}), short circuit current density (J_{sc}), open circuit voltage (V_{oc}) and fill factor (FF), the remainder of chapter 2 will focus on explaining such terms with sufficient detail to understand the results presented in this research, and a further in-depth analysis of the physics of the specific photovoltaic technology researched in this thesis will be presented in chapter 3.

2.2 The solar resource

As mentioned in the previous section, the energy input of solar cells is determined by the Sun. Therefore, understanding the solar resource is essential for successful device design, especially when selecting the materials and device architecture that can optimally interact with the energy provided by the Sun to produce electricity.

As shown in figure 3, the solar electromagnetic spectrum covers wavelengths from the ultraviolet to the infrared, but most of its irradiance (energy per unit time per unit area as a function of wavelength) is contained within the visible and near infrared part of the spectrum from approximately 300 to 1000 nm[21]. For solar cell design, this means that the light absorbing materials need to absorb in such range of wavelengths to potentially work as solar photoactive materials.

The solar spectrum is very similar to the one of a black body at 5250°C (grey curve) and can be identified in figure 3 as the yellow area. This, however, is for extraterrestial conditions where radiation has travelled through the vacuum of space only. When the solar radiation reaches the Earth's atmosphere, light is absorbed and scattered by the molecules in the air like ozone (O_3), water (H_2O), oxygen (O_2), carbon dioxide (CO_2) among others. This results in less radiation reaching the Earth's surface at specific wavelengths as shown in figure 3 (red area).

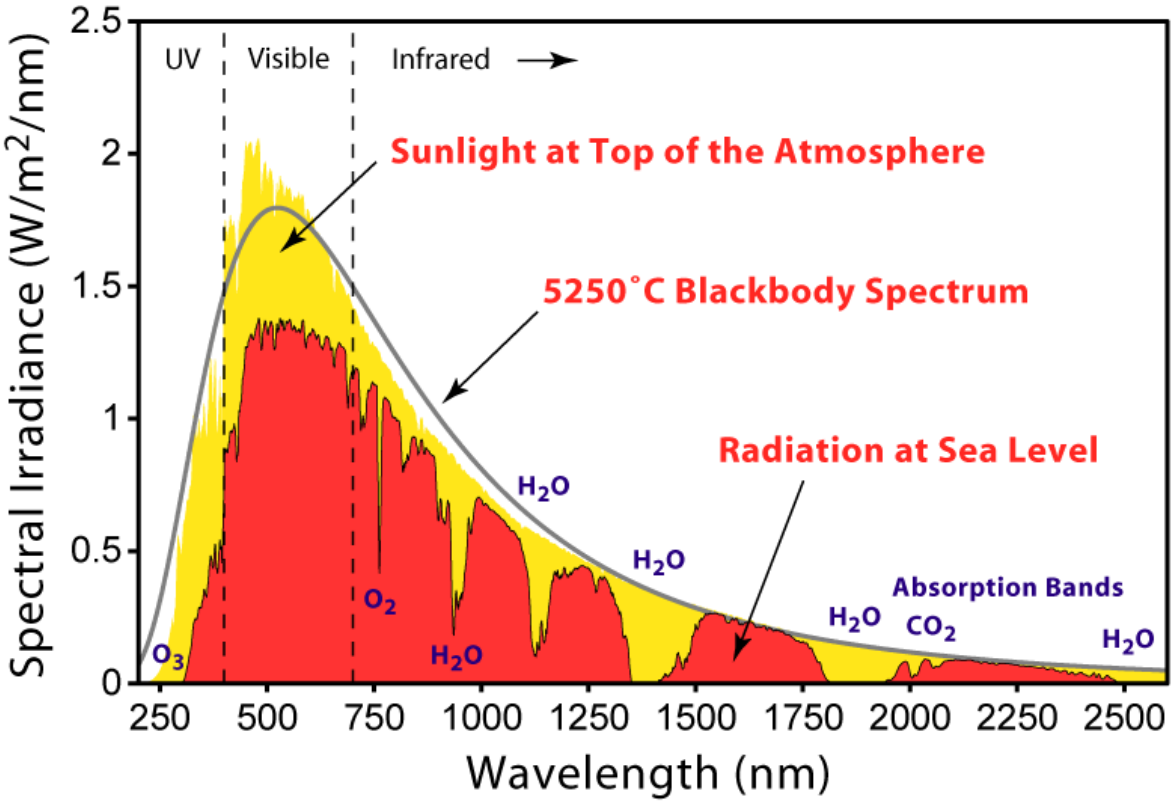

Figure 3: *Radiation emitted by a perfect black body at 5250° C (gray curve), extraterrestrial solar radiation (yellow), and solar radiation reaching the surface of the planet (red). Image originally created by Global Warming Art (https://en.wikipedia.org/w/index.php?title=Image:Solar_Spectrum.png&redirect=no&oldid=137131966) and reproduced under the Creative Commons Attribution-Share Alike 3.0 Unported license (https://creativecommons.org/licenses/by-sa/3.0/deed.en).*

The attenuation of solar radiation by the Earth's atmosphere is quantified by a term called *Air Mass* (AM) which in principle defines the mass of atmosphere that light has to travel before reaching the surface of the planet. This path length is defined by the angle of the Sun's radiation incident on any given surface of the Earth respective to an ideal case where the Sun is positioned perpendicular to the horizontal plane of such surface. Air mass is then defined by

$$AM = \frac{1}{cos\theta} \tag{1}$$

where θ is the mentioned angle. This means that if the Sun was positioned perpendicular to the horizontal plane of the Earth the AM would be 1. This case is only possible at certain locations during a specific time of the year and lasts for a very short

period of time, for example, on the equator of the Earth at noon during the equinoxes. This means that most of the time the sun is at a lower position in the sky and therefore, as the Sun is farther away from that ideal vertical position, θ increases elevating the amount of AM that the light has to travel through. This thus is time and location dependant, but for solar cells testing, the worldwide accepted standard value of power input (P_s) is a simulated solar radiation at AM=1.5 global (G) with a total insolation of 1000 W m^{-2} [22].

2.3 Current and voltage

The detailed current-voltage characteristics of a solar cell are a complex combination of several physical phenomena and it is highly complicated to quantitatively express them with absolute accuracy. However, different theories and approximations allow the simplification of these phenomenons to a level whereby it is possible to have a solid understanding of the principles of a solar cell current-voltage response for the correct design of devices. In this section and in sections 2.4 and 2.5, the current-voltage characteristics and efficiency of a solar cell will be described based on the reasoning found in the textbook by Jenny Nelson[23] and the website pveducation.org by Honsberg and Bowden[24].

A solar cell is the basic building block of a photovoltaic system. This cell can be considered as a two terminal device that conducts like a diode in the dark. When illuminated, a voltage is developed within the cell. This electro-motive force is capable of driving a current both within the device and through a load connected to an external circuit (which ultimately is the objective in order to extract electrical power from the cell). If the terminals of the device are isolated (which is equivalent to them being connected through an infinite resistance load) there is no flow of current allowing the voltage to reach its maximum possible value called the open circuit voltage (V_{oc}). Meanwhile, when the terminals are directly connected together (which is equivalent to them being connected through a zero resistance load) there is no potential difference between the terminals allowing the current to reach its maximum value called the short circuit current I_{sc}. For any other than an infinite or zero resistance load, the cell develops a voltage greater than

0 and lower than V_{oc}, generating a current such that

$$V = IR_L \tag{2}$$

where R_L is the total resistance within the entire circuit. This current-voltage relationship is shown in figure 4. The characterisation of the performance of a solar cell, and therefore its efficiency, is highly based on its current-voltage relationship. This relationship will be explained in detail in section 2.5.

Since a solar cell behaves like a diode, the dark current can be mathematically described by the diode equation[25]:

$$I = I_o[exp(\frac{qV}{nkT}) - 1] \tag{3}$$

where I_o is the dark saturation current (a leakage current that flows in the dark and that is inversely related to the material quality due to its dependence on recombination events[26]), q is the electrical charge, V is the applied voltage, n is the diode ideality factor (how close to an ideal diode the actual diode is), k the Boltzmann's constant, and T the temperature. The current voltage response of this case where the solar cell is not under illumination is shown in figure 4a. However, and as it was mentioned above, when a solar cell is illuminated the developed voltage generates an additional current. Applying the superposition approximation suggested by Lindholm et al.[27] the total current of the solar cell when it is under illumination can be expressed as the sum of the dark current and the illumination current (I_L). Then equation 3 becomes:

$$I = I_o[exp(\frac{qV}{nkT}) - 1] - I_L \tag{4}$$

and its current voltage response can be appreciated in figures 4b and 4c. As it is convention to report and analyse the photovoltaic parameters of a solar cell as positive values, the previous equation is multiplied by -1 to obtain the current in the first quadrant

(figure 4d). Additionally, since current is fairly proportional to the illuminated area it is more useful to report the current density (J) which is the current normalised to the illuminated area (I/A). This is particularly useful for scaling up this technology. However, in the remaining sections of this chapter the theory of current-voltage characteristics will remain described in terms of I for simplicity.

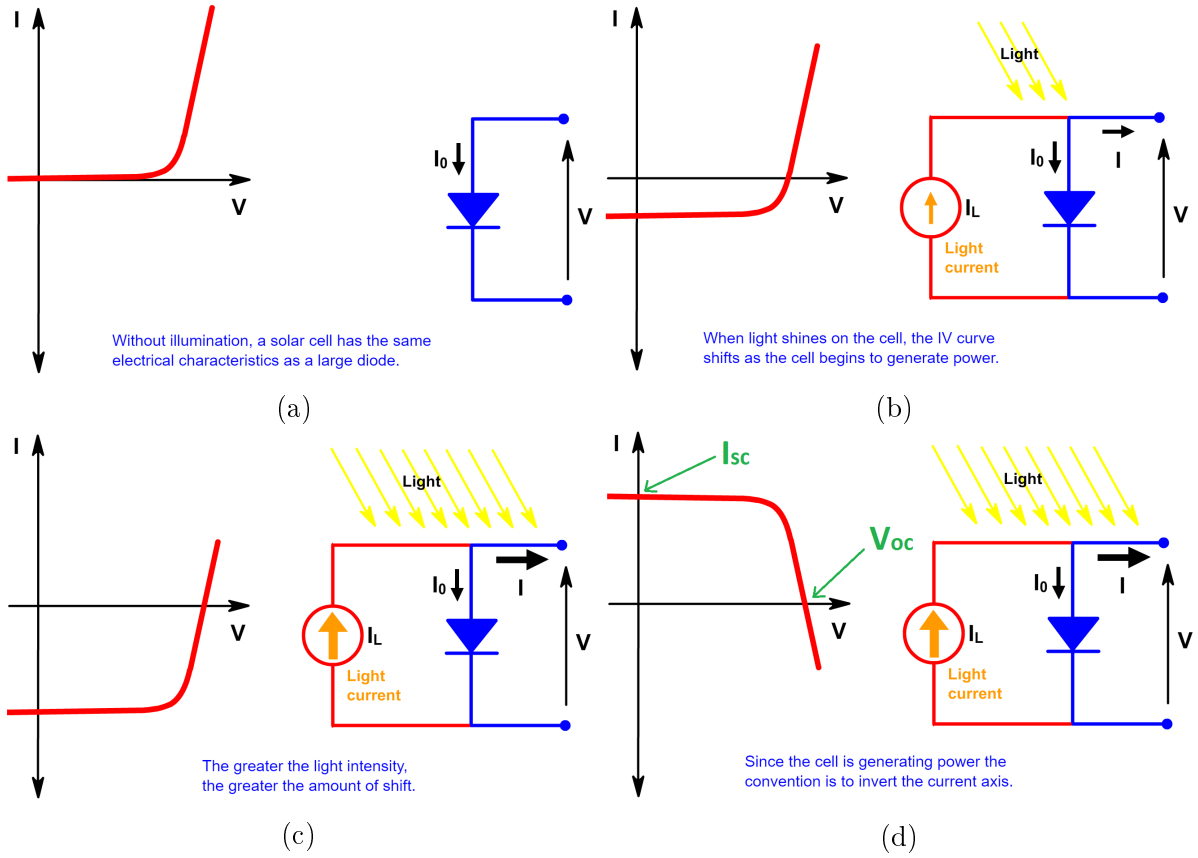

Figure 4: *Curent-voltage characteristics and equivalent circuit diagram of a solar cell in a) the dark, b) under illumination, c) under a higher intensity illumination, and d) in the corrected quadrant for convenient expression of power generation (location of I_{sc} and V_{oc} in the I-V curve is shown). Images produced by Honsberg and Bowden*[28].

It was mentioned before that the efficiency of a solar cell is dependant on the illumination and the effectiveness of light absorption and charge extraction. This can be now seen in the following equation

$$J_{sc} = q \int b_s(E) QE(E) dE \tag{5}$$

which shows that the short circuit current density is dependant on the incident

spectral photon flux $b_s(E)$ (W m^{-2}) and its energy range, the electronic charge q (A S), and the quantum efficiency QE (%)[23]. This last term describes the number of charge carriers generated per incident photon. QE is dependant on the light absorption coefficient, and effectiveness of charge transport and charge extraction of the solar cell's materials and structure, but it is independent of the illumination. This independence that QE has from the incident light makes QE a useful term to understand the performance of a solar cell device.

2.4 Fill factor

The current and voltage of a solar cell allow power (P) to be calculated by the solar cell through the following relationship

$$P = IV \tag{6}$$

which means that a combination of the maximum attainable values for I and V would in theory produce the most power. However, as mentioned above and shown by figure 4, the maximum values of I and V are the I_{sc} and the V_{oc} respectively which means that, when one of those values are reached, the other one at the same time is zero resulting in no power produced. Therefore, power is generated when the current and voltage values are other than I_{sc} and V_{oc}. Moreover, the I-V values should be rather seen as a relationship in which the increase of one of those values will result in the decrease of the other one. This means that the maximum power produced by the device will occur at some combination of I and V. It is worth noting that power generation in solar cells is only true for an I-V combination in the fourth quadrant (or the second one if corrected for positive convention), and that an I-V combination in any other quadrant will result in power consumption rather than power generation. This is because any I-V combination in the first or third quadrant requires the voltage to be negative or reverse biased, and on the second quadrant (when not corrected for positive convention) equation 4 results in a shift in an I value with the opposite sign which means a change in the direction of the flow of current.

At a given specific combination of current and voltage, the power reaches its maximum value which is called the maximum power point (P_{max} or MPP). These values of current and voltage at which P_{max} is obtained are called the maximum power current (I_{mp}) and the maximum power voltage (V_{mp}) respectively. The ratio between the product of I_{mp} and V_{mp} (i.e. the maximum power P_{max} that the solar cell is capable of producing) and the product of the I_{sc} and the V_{oc} is called the fill factor (FF) which is used to indicate the "squareness" of the I-V curve and it essentially describes how well the solar cell behaves as a diode. This is shown in figure 5 where the larger squared area (pale blue) represents the product of I_{sc} and V_{oc}, and the smaller area (dark blue) represents the maximum power attainable from the solar cell. The closer the smaller area is to the larger area the higher the fill factor will be and therefore the more squared the I-V curve will be, which represents a closer behaviour to a good diode. Figure 5a) shows an I-V curve that results in a good fill factor. In contrast, figure 5b shows a worse fill factor is evidenced by the reduced small area and the less squared I-V curve. A plot of voltage against power is also shown in figure 5 (green line) to demonstrate how a reduced fill factor results in a reduced power output from the device.

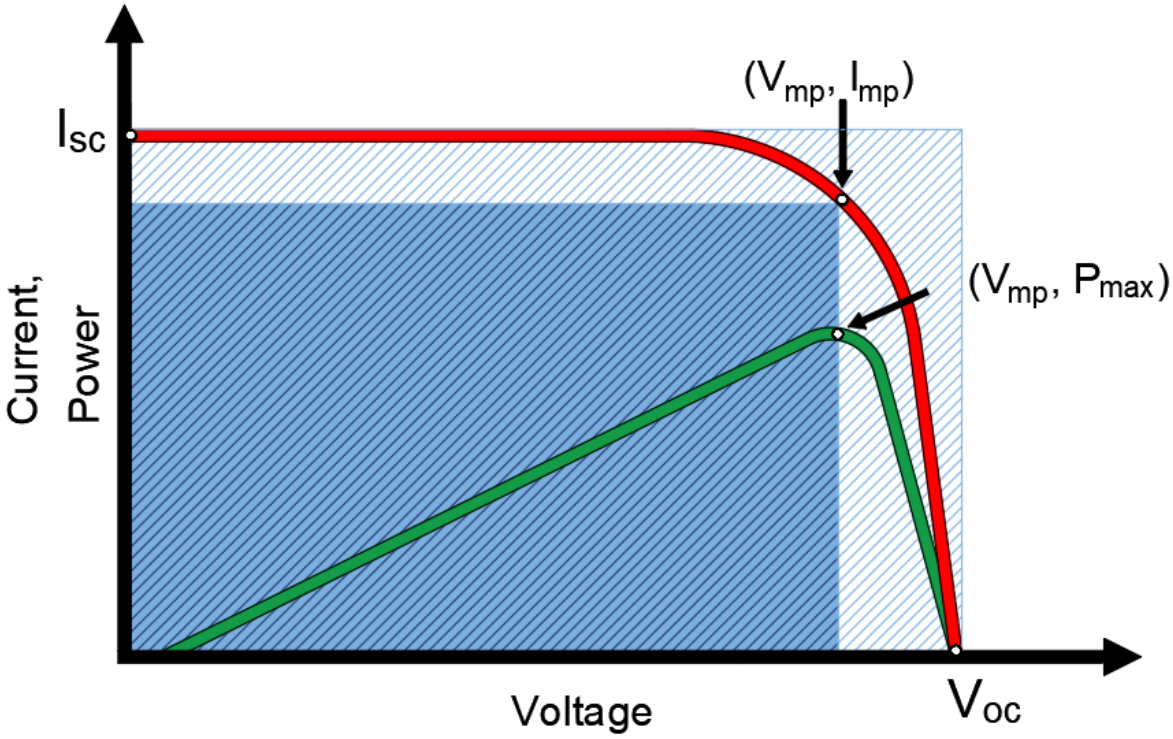

(a) *Large fill factor*

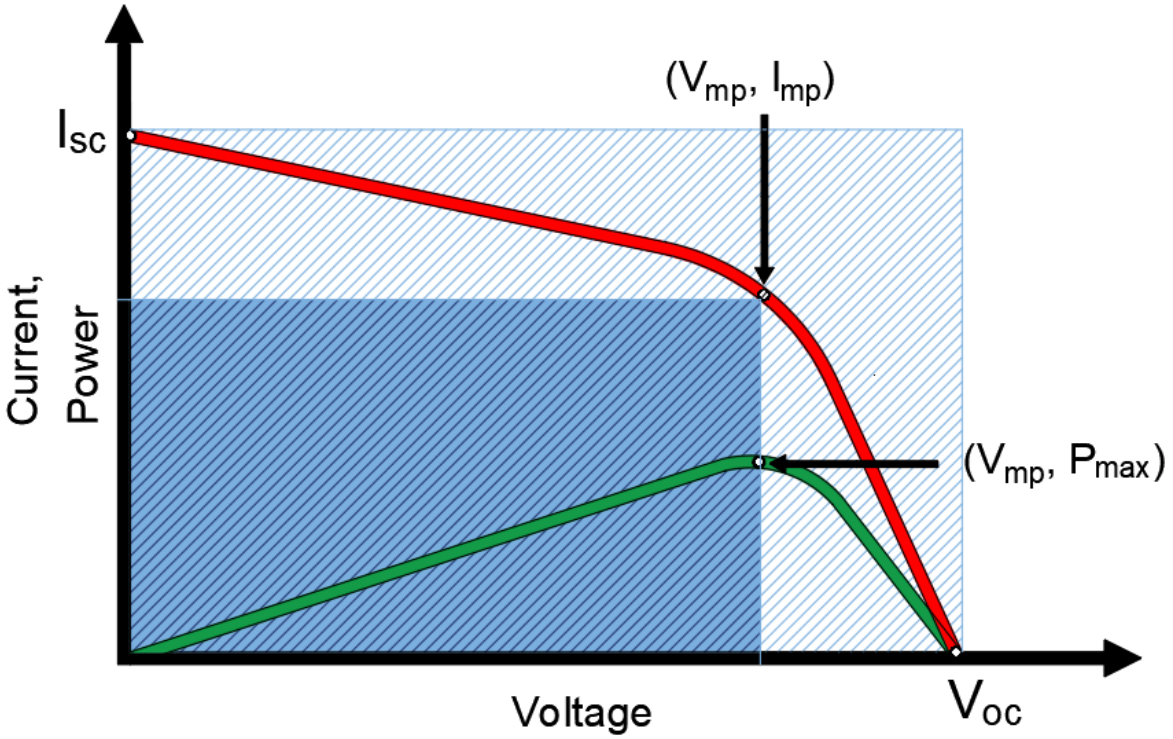

(b) *Small fill factor*

Figure 5: *Comparison of two fill factors (blue box); a) a good (high) fill factor, and b) a poor (low) fill factor. The pale blue coloured box represent the product of the I_{sc} and the V_{oc}. The red curve represents the I-V curve of the solar cell, and the green curve represents the power as a function of the voltage.*

In a solar cell, the current has to flow within the device before being able to

travel through the external circuit, and therefore, the device is subject to current-voltage losses due to the various resistances present within the materials and architecture of the device. The fill factor is strongly affected by such parasitic resistances and thus is a good indicator to diagnose the origin of the loss of photovoltaic performance due to internal resistances. The most common are the series (R_s) and shunt (R_{sh}) resistances.

The R_s exists mainly due to three factors; the resistance of the materials within the device to the flow of current (which is dependant on the carrier mobility and surface contact between each of the comprising layers), the quality of the contact between the electrodes (see section 3.5) and their adjacent layers, and the resistance inherent to the electrodes. The R_s inversely affects the fill factor (see figure 6), but does not affect the V_{oc} (since there is no current flowing at this value). However, the I-V curve is severely affected near the V_{oc} and therefore, determining the slope of the I-V curve at the V_{oc} value can be done to calculate the R_s[29]. Mathematically, the current is affected by the R_s as shown in equation 7.

$$I = I_o[exp(\frac{q(V + IR_s)}{nkT}) - 1] - I_L \tag{7}$$

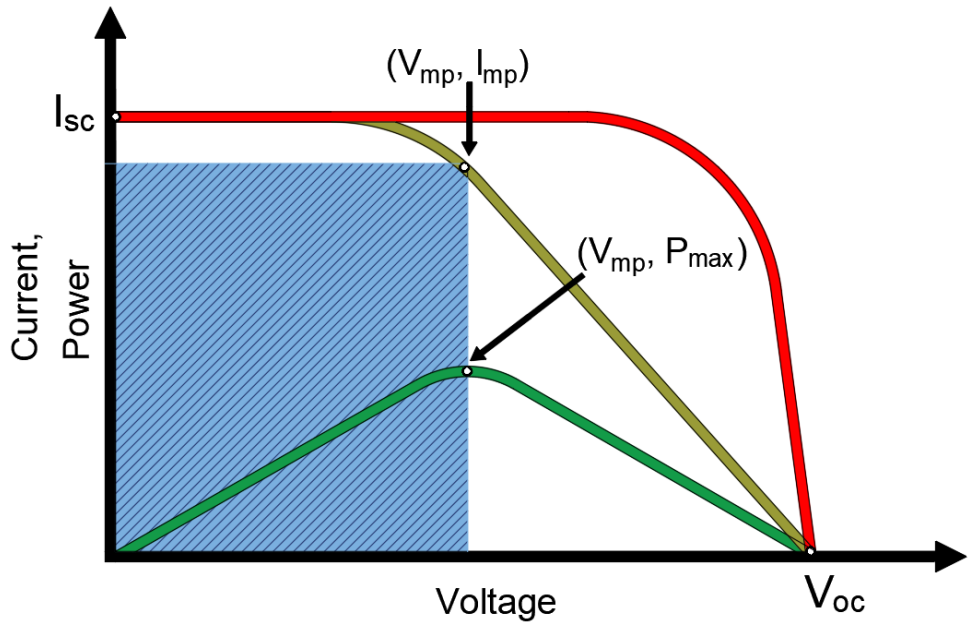

Figure 6: *Effect of R_s on the fill factor and the I-V curve (pale green). The green curve represent the power as a function of the voltage of the I-V curve affected by R_s. The red curve represents an I-V curve without any parasitic resistances.*

The R_{sh} is caused by the leakage of current through the device. This leakage occurs due to an alternate path being provided for the current to flow resulting in the decrease of the V_{oc}. This can be caused by poor quality materials (defects or impurities) or by the edges of the cell. Just as the R_s, the R_{sh} holds a direct relationship with the fill factor (see figure 6). In contrast to an I-V curve with significant R_s, an I-V curve with significant R_{sh} will be mainly affected near the I_{sc}. This means that a low R_{sh} is a sign of a poor rectifying behaviour of the device. Mathematically, the current is affected by the R_{sh} as shown in equation 8.

$$I = I_o[exp(\frac{q(V + IR_s)}{nkT}) - 1] - I_L - \frac{V}{R_{sh}} \tag{8}$$

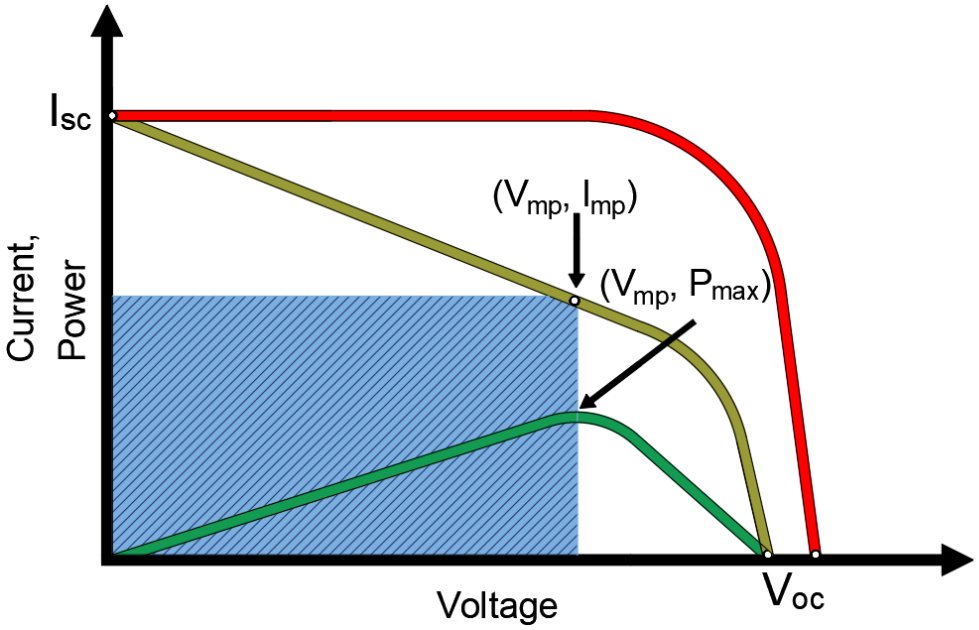

Figure 7: *Effect of R_{sh} on the fill factor and the I-V curve (pale green). The green curve represent the power as a function of the voltage of the I-V curve affected by R_{sh}. The red curve represents an I-V curve without any parasitic resistances.*

A simplified equivalent circuit diagram of the parasitic resistances in the solar cell is shown in figure 8.

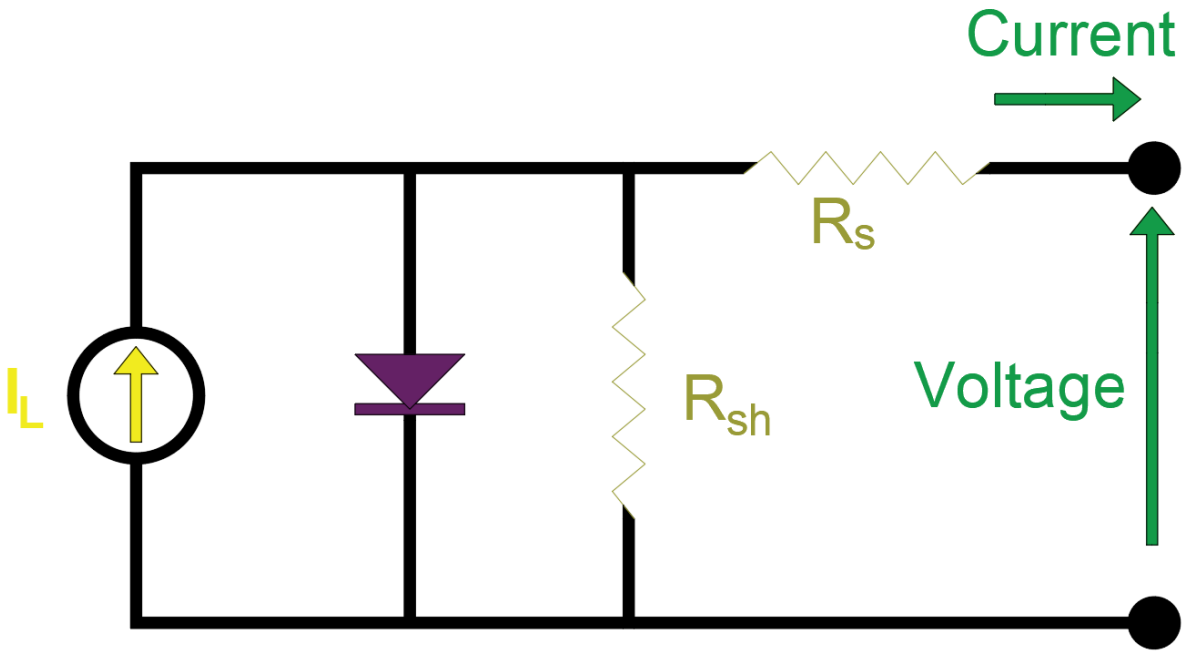

Figure 8: *Simplified equivalent circuit diagram of a solar cell with R_s and R_{sh}.*

2.5 Power conversion efficiency

The efficiency of a solar cell is quantified by the total power conversion efficiency (PCE) of the device and this value can be calculated with the four quantities described in the previous sections of this chapter: P_{in} I_{sc}, V_{oc}, and FF.

The total power conversion efficiency of a device is given by:

$$PCE = \frac{I_{mp}V_{mp}}{P_s} \tag{9}$$

where P_s is the standardized power input from the sun (recall from section 2.2). Since the fill factor can be mathematically described as:

$$FF = \frac{I_{mp}V_{mp}}{I_{sc}V_{oc}} \tag{10}$$

then the power conversion efficiency can be calculated as:

$$PCE = \frac{I_{sc} V_{oc} FF}{P_S} \tag{11}$$

which is the main equation used to quantify the photovoltaic performance of the devices fabricated for this research.

2.6 Inorganic photovoltaics

Since the photovoltaic effect was first observed in 1839 by Edmund Becquerell[30] when exposing a silver electrode to radiation in an electrolyte, different attempts to use it to produce current and voltage were made[31]. However, it was not until knowledge of p-n junctions and transistors were developed and combined that the basis of modern day inorganic solar cell's physics were established[25]. Soon after, the first conventional silicon solar cells were fabricated by Chapin et al.[32] and a deeper understanding of the p-n junction along with the concept of the bandgap and the thermodynamics of solar cells were developed[33]. These particular events, along with the different oil crises around the world during the last five decades, produced a strong impulse for the development of inorganic photovoltaics that led to their commercialisation. Since then, optimising manufacturing processes and improving the technology have been the main focus of this particular technology, mainly to reduce its cost and facilitate its quick implementation as a viable substitute for other conventional energy generation methods[34–36].

At the time of writing this thesis, the whole solar cell market is comprised of inorganic solar cells and more than 92% of it is dominated by crystalline silicon (c-Si) based cells[35]. This first generation of photovoltaic technology consists basically of a bulk semiconductor sliced into a thin sheet or wafer of which the main component is doped crystalline silicon. The overwhelming dominance of c-Si based solar cells in the market is caused by several factors. First, Si is one of the most abundant materials on Earth's crust eliminating any foreseeable limits to its extraction and subsequent use. Solar cells based on s-Si are also some of the most efficient type of photovoltaic technology

(commercial efficiencies range from 17% to 22%[37]) currently available in the market being outperformed only by gallium arsenide (GaAs) based solar cells, however the use of GaAs solar cells is somewhat limited by the toxicity of GaAs. Moreover, c-Si solar cells are capable of performing at their nominal efficiency for more than 20 years. These advantages have kept c-Si solar cells as the dominant photovoltaic technology and have ben continually improved, since. This has resulted in the significant decrease in cost of c-Si solar cells achieving an all-time low record of 0.37 W/$ in 2018 and is expected to decrease to 0.28 W/$ in 2020[37]. There are however some limitations to c-Si solar cells. In the first instance there is a limitation to substantially increase the efficiency of c-Si solar cells since, according to Shockley and Queisser, the maximum theoretical efficiency that can be obtained for single junction (not more than one light absorbing-charge generation material within the device structure) silicon based solar cells is ≈29%[33]. Currently, the record efficiency for c-Si is 26.7%[38] which is close to its technical limit. Additionally, the fabrication process of this specific technology requires high temperatures around 1100 °C for the Si ingot[19]) and thus a high energy consumption and CO_2 emissions[39]. Moreover this fabrication process requires a large amount of silicon to be processed for the wafer, and the wafering process, which according to Schumann et al.[40] accounts for 22% of the entire production cost of this type of cell, wastes approximately 50% of the ingot[35]. C-Si solar cells are also very rigid and fragile which limits their deployment where space is limited or in non-flat surfaces. It is also important to point out that the fabrication of c-Si solar cell is highly complex and therefore, this particular industry requires the support of three different factories for wafer, cell, and module production. This means that in order for this industry to stay competitive in the market, an integration of these three separated manufacturing process into one single factory is preferred which is not simple to achieve. Finally, in a technologically growing world where the demand of silicon is going to continue increasing to satisfy all other type of semi-conductor applications and needs[41], it is uncertain if the availability of silicon will remain constant. The possibility that the silicon solar cells industry may experience volatility in its prices due to a potential temporary shortage of silicon such as the one from 2005 to 2008 should not be discarded.

There is a second generation of photovoltaic technologies currently available in the market that avoid the use of silicon wafers and can be more easily processed as

thin films. The main feature of some of the second generation photvoltaics such as CdTe solar cells is that they can be fabricated with a more simple method than to c-Si since they can be solution processed. This allows its energy payback time (∼0.5 years) to be considerably less than that of c-Si solar cells (1.5-2.5 years)[42]. CdTe solar cells have a lower average commercial module efficiency compared to c-Si (16.1%[19]) however an efficiency of 21% has been reached in the research scale[37]. The main issue with this type of solar cell is that cadmium is toxic and tellurium is not abundant[43]. This makes the disposal of CdTe pannels an issue in the large-scale commercialization since they pollute during decommissioning. Moreover, the toxicity of CdTe is a health hazard to the user. Due to these significant disadvantages CdTe solar cells Cadmium tellurium (CdTe) solar cells occupy only 5% of the market[35]. Copper indium gallium selenide (CIGS) solar cells are another type of thin film second generation solar cells that share most of the advantages of CdTe solar cells. Currently, CIGS solar cells have a 2% share in the market and this is unlikely to increase since the use of indium tin oxide in LCD products have increased the indium demand by several hundred of dollars per kilogram during the last three decades[44]. Moreover the selenization of these solar cells requires a highly toxic (classified as environmental hazard) source of selenium which is hydrogen selenide. This increases the complexity of the production of CIGS solar cells and thus, is reflected on their cost.

Despite the significant advances in photovoltaic technology since it was first developed, and that photovoltaic energy generation has had a fast pace growth in the last decades, it still accounted for less than 2.5% of the world's total electricity production in 2018[45]. In order for this technology to become one of the main energy generation methods, its competitiveness must be increased to challenge the current dominant electricity generation methods. This could be achieved through a fast processing, low cost, more flexible, nontoxic and environmentally friendly alternative to the conventional inorganic solar cells, which would potentially translate into a more simple to produce, and lower cost option.

3 Organic photovoltaics

3.1 Introduction and general overview

In 1977 a new door opened for photovoltaic technology when Shirikawa et al.[46] discovered that polymers can behave as semiconductors. This led to the birth of a third generation of photovoltaics that are commonly referred to as polymer photovoltaics or organic solar cells (OSCs). OSCs work under a similar physical principle of photoexcitation than the conventional inorganic solar cells, but are comprised of relatively more easily accessible (e.g. synthesis in laboratory) and processable materials than second and third generation photovoltaics[47]. These materials are conjugated polymers.

The advantages of OSCs are numerous. The first major selling point of OSCs is their processability. In comparison to first and second generation solar cells that depend on complex processing techniques such as epitaxy or close-space sublimation; polymer based solar cells can be processed by simple coating techniques due to the solubility of the materials. This is also in part enabled by the high absorption coefficients of the light absorbing materials in OSCs which allows their processing as very thin films ($\sim$ 50 to 500 nm) while still absorbing a sufficient part of the solar spectrum[48]. At the present time, most laboratory scale OSCs require additional processing techniques for some of the other layers that comprise the device structure, however, complete solution processed cells have already been demonstrated to be a possibility by Krebs et al.[49]. Another advantageous feature of OSCs is their flexibility. Due to the molecular structure of polymers, OSC based solar panels can take the shape of any surface increasing the width of its applications and installation methods by, for example, being rolled onto a roof. Additionally, due to the synthetic versatility of carbon, it is possible to design a wide range of non-toxic organic materials that comprise the structure of OSCs from a large variety of monomers, functional groups, or side chains for different specific purposes. Such tunability of device materials is not easily achieved with inorganic materials which narrows the choice of materials for solar cells sometimes causing important features such as non-toxicity (e.g. CIGS solar cells) to be sacrificed in order to achieve good performance. The tunability of OSCs materials also avoids to some extent the risk of facing a volatility in production

prices due to material scarcity or high demand in other areas. Another interesting feature of OSCs is their compatibility with inorganic materials. Researchers have proven that organic solar cell materials can be combined with inorganic materials to produce high efficiency solar cells[50;50]. This means that organic solar cells can also be used with reliable solar cell technologies such as silicon to overcome some of their disadvantages. The features mentioned above have encouraged intensive research in this field during the last couple of decades mainly due to the promise of a low cost up-scaled photovoltaic technology capable of being printed or coated by well-known industrial techniques such as roll to roll or inkjet printing processes which are comparable to those used in the printing of newspapers or crisp packets[51;52]. It is also worth mentioning that there is another type of new generation solar cells that has attracted a lot of interest within the last decade and that shares some of the advantages of organic solar cells such as good flexibility and simple solution processability. Perovskite solar cells are a hybrid between organic and inorganic solar cells and they have been intensively researched since the first application of a perovskite structure for solar cells. Their main attractive feature (besides flexibility and solution processability) is their high efficiency; a maximum of 23.7% has been achieved for single junction perovskite so far[53]. Perovskite solar cells can also be combined with silicon solar cells and currently the highest efficiency achieved by a silicon-perovskite solar cell is 28%[53]. However, the main disadvantages of perovksites is the poor stability of the perovskite structure due to different degradation mechanisms[54].

Despite the many enticing advantages of polymer solar cells listed above, there are two main drawbacks to this type of technology that scientists are actively investigating in order to overcome them. First, polymer based devices have a tendency to degrade relatively quickly compared to inorganic silicon-based solar cells[55]. The latter, for example, can perform in real-world conditions operating at more than 80% (Ts80) of their nominal efficiency for at least 20 years as advertised by most manufacturers, while OSCs struggle to perform at Ts80 for more than a year[56]. Even though the stability of organic solar cells is better than other solution processed solar cells such as perovskites, it is paramount to improve the lifetime of organic solar cells for the commercialisation of this technology. In the past few years there has been substantial progress in understanding the degradation mechanisms of some of the most used polymers in OSC's[57;58] along

with the development of some specific fabrication conditions and physical treatments to increase device stability[59;60]. Moreover, efforts to characterize some of those polymers regarding their specific influence on the degradation of OSC's along with the effect of variable environmental conditions have been undertaken with promising results towards increasing device stability[61]. The other main drawback of OSCs is their relative low efficiency compared to that of first and second generation photovoltaics. For a long time, the efficiency of OSCs was limited to less than 10%, however, in the last 10 years, efficiencies between 10% and 16% for single junction OSCs have been achieved[62–67]. Such progress corroborates the potential of OSCs, however, for industry scale, the effiencies reached so far are still significantly below the average 20% efficiency of the commercially available first and second generation solar cells. For this reason, finding methods to improve the efficiency of OSCs remains as the most active area of research within the field of organic photovoltaics. Moreover, if the processing of OSCs is sufficiently low-cost, the efficiency does not need to match or surpass that of the other types solar cell technology to become the most cost-effective option given that the area of deployment is not a restricting factor.

Organic solar cells have good potential and a promising future. It has been estimated that 15% efficient devices with a lifetime of 20 years could produce electricity at a cost of less than 0.07 \$/kWh[68] which is less than the average cost of electricity produced in 2019 in the United States of America (0.11 \$/kWh[69]), the highest energy consuming country. However, given the current state of the performance of OSCs, it is clear that in order for them to become a feasible and reliable technology that can successfully provide major solutions to the problems described in section 1, the two main drawbacks of OSCs need to be overcome. In the remainder of section 3, the physics of OSCs will be explored and described with sufficient detail to provide the basis for understanding the working principles of this technology, and by doing so, providing the reader with the necessary fundamental knowledge to understand the research carried out in this thesis.

3.2 Semiconductor behaviour

It can be stated that the whole process of converting solar radiation into electricity starts at the light absorbing material where photons transfer their energy to the electrons that will eventually be used to produce work. This process will be analysed in detail in section 3.3. However, in order for a polymer to be a suitable material that can be used as the light absorbing layer in a solar cell, it must first have semiconducting properties. This is achieved through orbital hybridisation of carbon-based backbone molecules and conjugation (see figure 9).

Carbon has a ground electronic state of $1s^2 2s^2 2p_x^1 2p_y^1$[70]. In this state, only two electrons are available for bonding. This is in disagreement with the well known four valence electrons that allow the formation of the organic molecular structures in which carbon is involved. This is due to a physical phenomenon called hybridisation in which the p orbitals merge with the s orbital (hence the term hybridisation) allowing carbon to form 4 equivalent bonds. The energy required for this process is accounted for during bond formation, and depending on the energy available during the bonding step, three different types of hybridisation can occur; sp^3, sp^2, or sp. It is the sp^2 hybridisation that is of particular interest to understand semiconducting polymers. In this type of hybridisation, the $2s$ orbital combines with two $2p$ orbitals to form three sp^2 orbitals that have a $\approx$33.3% s and $\approx$66.7% p character. This results in the three sp^2 hybridised orbitals having an energy level higher than the original $2s$, but lower than the original $2p$ orbitals. These hybridised sp^2 orbitals are responsible for the formation of covalent bonds which are also commonly referred as σ bonds. σ bonds are formed by strongly bounded and highly localised electrons, making them unable to be efficiently used as part of a dynamic electronic process other than the convalent bonding unless a significant amount of energy is introduced into the system (e.g. heat, electromagnetic radiation, reactive compounds, etc). Thus, their main function within the polymer is to contribute to the stability of the molecular structure[71]. In sp^2 hybridised systems there is, however, one $2p$ orbital that remains unhybridised and lies perpendicular to the the σ bond plane. This unhybridised orbital allows the formation of a weaker type of bond with another unhybridized $2p$ orbital called a π bond, and when it coexists with a σ bond

it is commonly called a double bond (see figure 10). The electrons of π bonds are less tightly bound and are therefore more delocalised than those of σ bonds due to the lower energy that the π bond is bound by. This allows the π electrons to be easily removed from their original π bond by a minimum amount of energy ($\ll k_B T$) to form an adjacent π bond if the structure of the system has a particularly favourable resonance structure for this type of π electron movement. In semiconducting polymers, this favourable resonance structure occurs when a backbone chain of alternating single and double bonds is present which allows the π electrons to move along a certain length of the continuous, alternating structure in the chain or even in-between neighbouring chains of similar structure. Such alternating structures are called conjugated polymers (examples shown in figure 11).

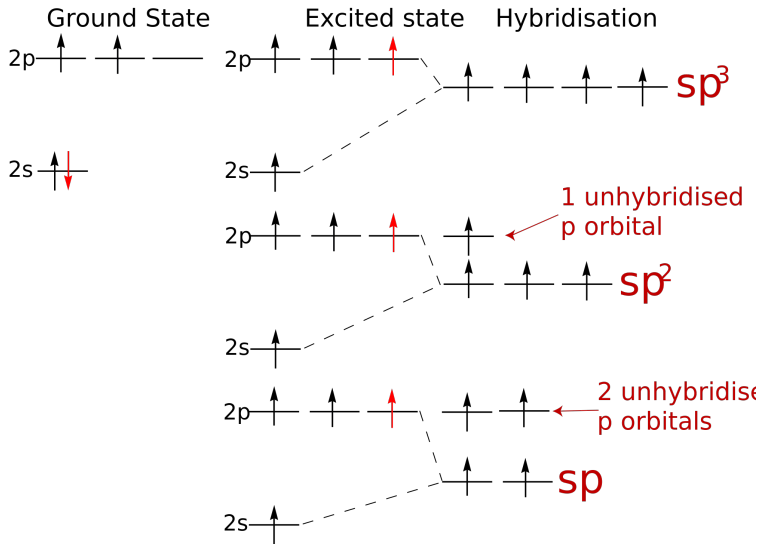

Figure 9: *Electronic ground state of carbon and its different hybridisations. Electron promotion occurs due to bond formation.*

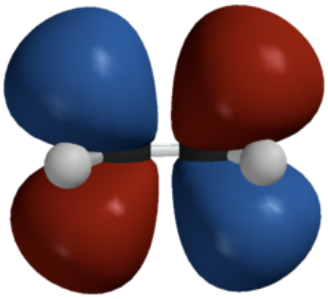

(a)

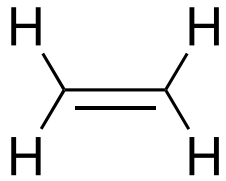

(b)

Figure 10: *A 3D model (a) and 2D structure (b) of an ethene molecule in which sp^2 hybridization happens. The blue and red bulges in the 3D model represent the π orbitals which are perpendicular to the C-C and C-H σ bonds.*

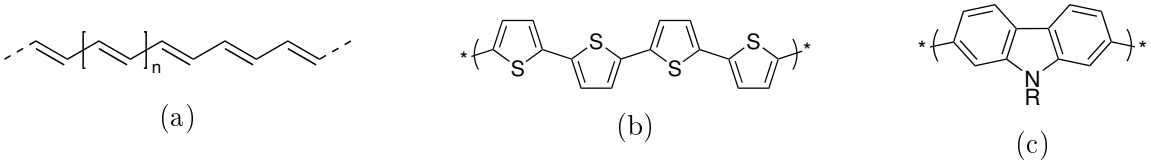

(a) (b) (c)

Figure 11: *Three examples of conjugated polymers; polyethene (a), polythiophene (b), and poly[2,7 carbazole] (d).*

Since electrons are waves, they can constructively or destructively interfere when they superimpose (e.g. come together to form a bond). When two π orbitals are in phase, they interfere constructively and form an energy state called bonding. Bonding is a lower energy state than the original isolated (non-bonding) $2p$ states and therefore it is more energetically beneficial for electrons to occupy the bonding state rather than the non-bonding state. This is the cause of the formation of double bonds; when the two atoms that can form a double bond come together, the bonding state of their π electrons is energetically more favourable than the isolated state of the π of each atom. When the two π orbitals are in opposite phases, they interfere destructively and form an energy state called antibonding. This state is higher in energy compared to the original isolated $2p$ states being less energetically favourable to be occupied than the non-bonding

and bonding states. In semiconducting polymers the π bonding state gets filled by the electrons during bond formation while the $\pi*$ antibonding state remains unfilled. This is why in a polymer semiconductor π molecular orbital diagram, the highest energy π bonding level corresponds to the highest occupied molecular orbit (HOMO) and the lowest energy π anti-bonding level corresponds to the lowest unoccupied molecular orbit (LUMO). The energy separation between the HOMO and the LUMO levels is called the energy band gap (E_g)

$$E_g = E_{LUMO} - E_{HOMO} \tag{12}$$

and it is an intrinsic property of any given material that for any non-metal is >0.

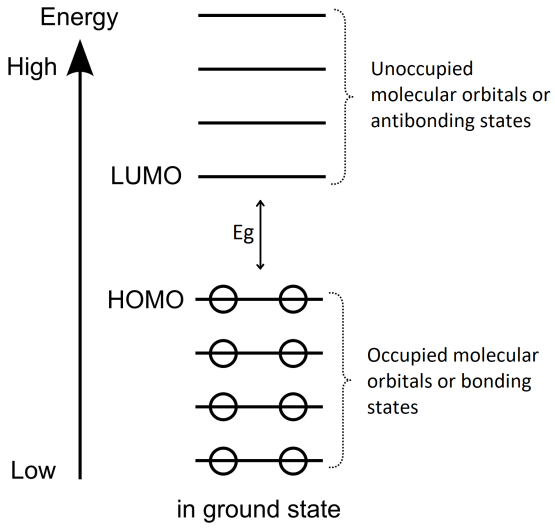

Figure 12: *HOMO and LUMO conceptualization. The difference between these two levels is called the band gap.*

As mentioned above, conjugated polymers are characterised by having a one-dimensional path of alternating single and double bonds along the backbone. According to resonance theory, the alternating single and double bonds would be expected to be equidistant from one another. This would mean that the π electrons are delocalised along the whole polymer chain making it metallic instead of semiconducting due to the equivalence of the π and $\pi*$ states. However, in 1983 Yannoni and Clarke observed that

the single and double bonds in polyacetylene (a conjugated polymer) had different length distances of 1.36 and 1.44Å respectively[72]. This bond length difference is characteristic of conjugated polymers and it is caused by the Peierls distortion[73]. Peierls explains that in an attempt to lower its total energy, the polymer creates an alternating structure of short and long bonds to lower the energy of the system and make it more stable. This limits the delocalization of the π electrons only to a certain number of neighbouring carbon atoms, and it also limits the delocalisation of the electron density to a few repeat units instead of the whole polymer chain.

The HOMO and the LUMO levels of organic semiconductors can be conceptualized as the valence and conduction bands respectively of inorganic semiconductors and therefore, the electrons in the HOMO level can be promoted momentarily to the LUMO by injecting energy to the conjugated polymer system. As will be explained in the following section, the energy needed to excite an electron from the HOMO to the LUMO level depends on the E_g which can be easily tuned by modifying the conjugation length or chemical structure and composition of the organic semiconducting molecules. As mentioned in section 3.1, such tunability is not easily achieved for inorganic semiconductors due to the lower versatility and compatibility of inorganic molecules and therefore, as mentioned in section 3.1, one of the major advantages of semiconducting polymers is their tunability.

3.3 Light absorption

When a photon with an equal or higher amount of energy than the E_g of an organic semiconductor strikes an electron in the $HOMO$ level, it is promoted to the $LUMO$ level or to a higher vibration energy level respectively. This can be expressed mathematically as

$$E_{photon} = \frac{c * h}{\lambda_{photon}} \geq E_g \tag{13}$$

where E_{photon} is the energy of the photon, c is the speed of light, h is the Planck's

constant, and λ_{photon} is the wavelength of the photon. If the photon has the exact same amount of energy as the E_g of the organic semiconductor, the electron will be promoted directly from the HOMO to the LUMO. However more commonly, if the photon has more than one discrete level of energy than the E_g of the organic semiconductor, the electron will be promoted to a higher energy level than the LUMO and it will subsequently undergo vibrational relaxation until it reaches the LUMO level (figure 13a). This vibrational relaxation happens in a timescale of less than one picosecond. Upon excitation the polymer will also change its structure from bonding to antibonding (figure 13b).

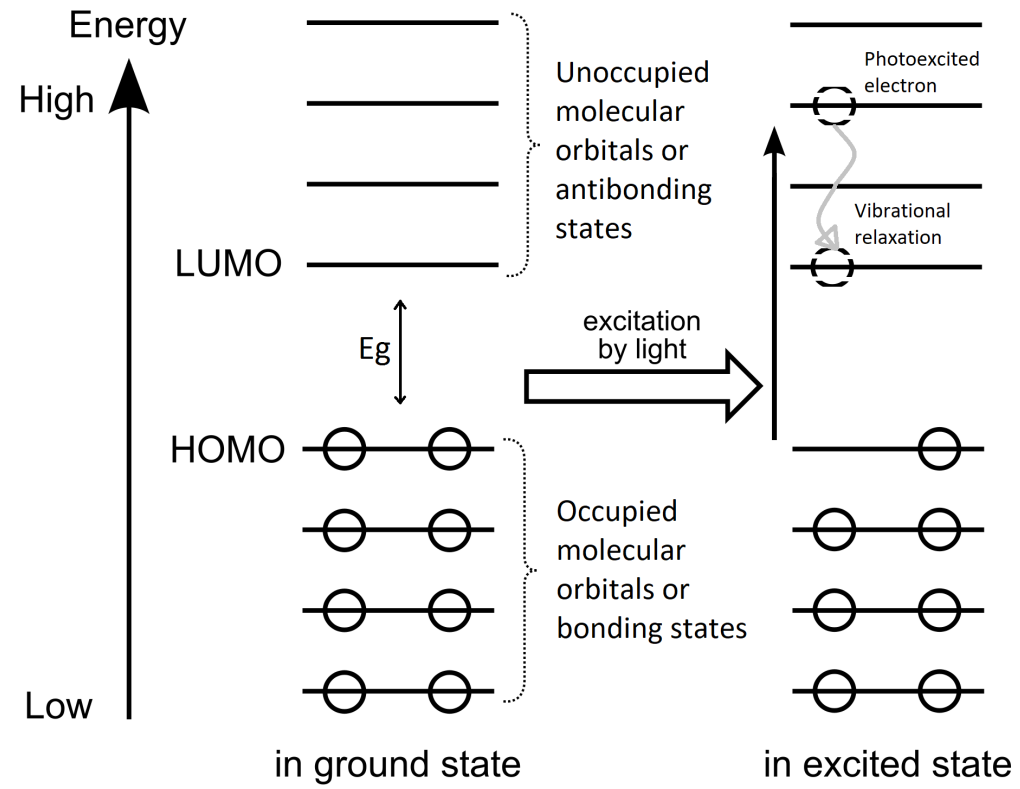

(a)

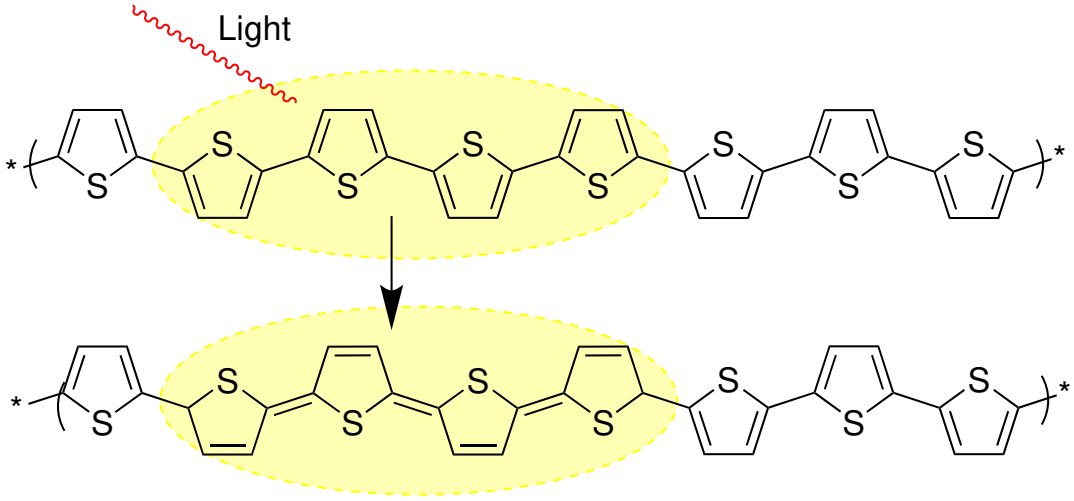

(b)

Figure 13: *(a) schematic representation of the effect of a photon of light which energy is* $> E_g$ *on a HOMO electron and its vibrational relaxation to the LUMO (a). (b) Polythiophene on its bonding structure (top), and antibonding structure when struck by light (bottom).*

When the electron is excited to the $LUMO$ level, a positive quasi particle called a hole is created in the $HOMO$ level. This pair of electron and hole is referred as an exciton and it is bound by coulomb forces. After a statistically determined time (in the

order of 100 picoseconds to 1 nanosecond), there is a high probability that the exciton will go under a process called recombination where the electron collapses to the $HOMO$ level to recombine with the hole left behind destroying the exciton. This recombination may result in the emission of phonons, or given the right conditions, this process can also cause the emission of light through phosphorescence or fluorescence. However for solar cells, recombination is absolutely undesirable as the objective is to use the excited electrons to produce a current to do electrical work. Therefore, exciton dissociation into charge carriers before recombination can occur is necessary.

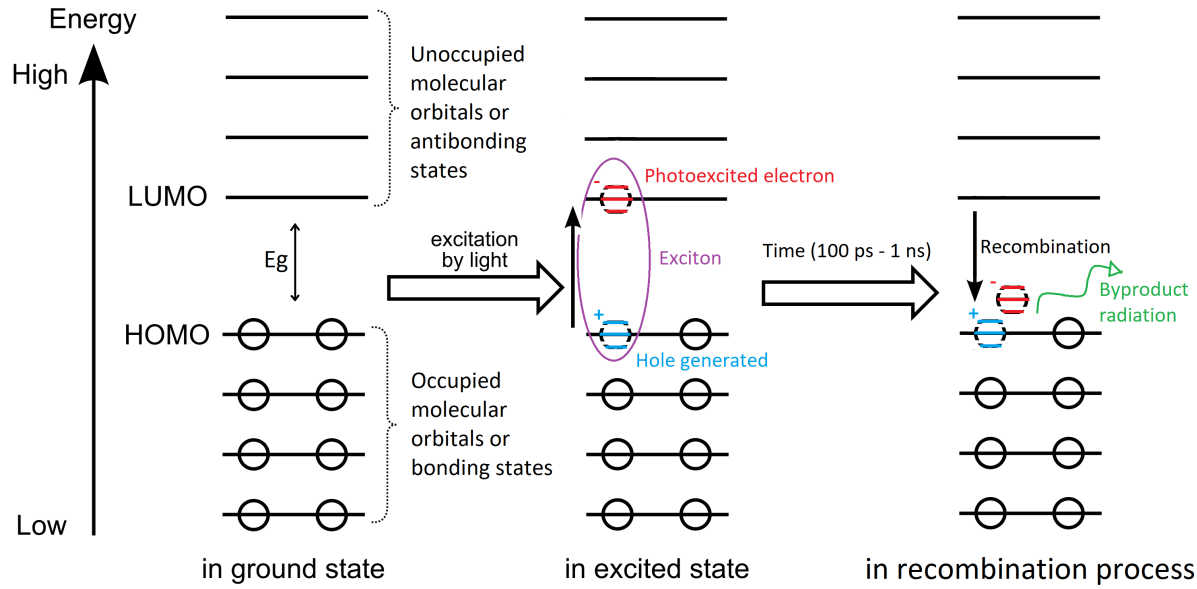

Figure 14: *Schematic representation of the recombination process*

The binding energy of excitons generated by organic semiconductors is significantly higher than the binding energy of excitons generated by inorganic semiconductors and thus, the binding energy of inorganic and organic excitons is one of the main differences between these two types of photovoltaic technology. Inorganic semiconductors have a relatively high dielectric constant ϵ_r. This results in the coulomb force that is binding the electron hole-pair being significanlty lower than the value of k_BT (e.g. silicon has an exciton binding energy of 0.0027 eV[74]), enabling the generation of free charge carriers without any further energy input required than just room temperature. For organic semiconductors the opposite is true. Due to the relatively low ϵ_r, the coulombic attraction of the exciton is much higher than k_BT (typically 0.3-0.5 eV[75]), requiring additional energy to separate both charges and impede exciton recombination. In the following section, the

most commonly used method to separate the exciton into positive and negative charge carriers in organic semiconductors will be explained.

3.4 Charge separation

In order to generate electrical work from the exciton generated by the organic semiconductor, it is necessary to first overcome the binding energy of the exciton and separate it into its free unbound positive and negative charges. To disassociate an organic exciton it is possible to use a heterojunction, which is also referred to as the active layer or photoactive layer (PAL) in solar cell argot, comprised of an electron donor material (i.e. the conjugated polymer where the exciton is formed by light absorption) and an electron acceptor material (i.e. another organic semiconductor with a higher electron affinity that can snatch the electron from the donor material). The acceptor must have an energy level beneficial for the photoexcited electron to move to, and an energy barrier that blocks the holes from transfering from the donnor to the acceptor (see figure 15). This can be achieved by using an acceptor which both $HOMO$ and $LUMO$ levels are sufficiently lower (or further away from the vacuum level) than those of the donor. To dissociate the exciton, the difference between the $LUMO$ levels of the donor and the acceptor has to be greater than the exciton bonding energy for the electron migration to occur:

$$E_{exc-b} \leq E_{LUMO}^{donor} - E_{LUMO}^{acceptor} \tag{14}$$

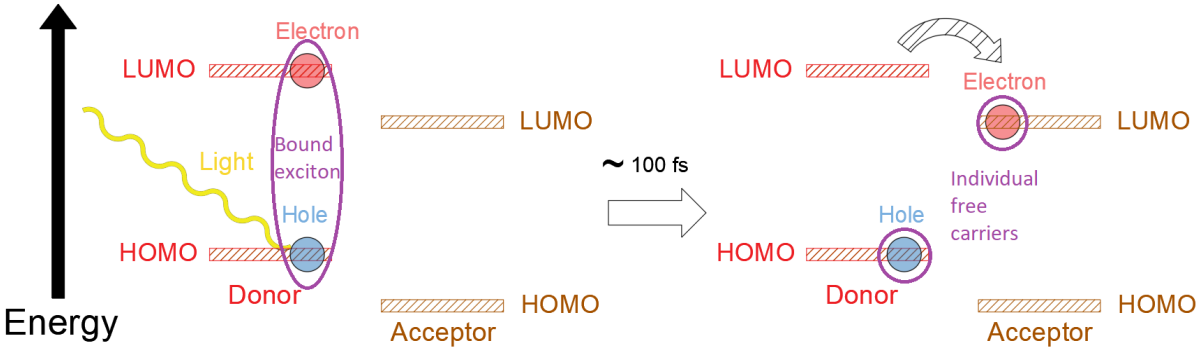

Figure 15: *By using an acceptor material with an energy level beneficial for the electron to relax to before it can recombine, the exciton can be dissociated and charge extraction becomes possible.*

Exciton dissociation can only occur at the donnor-acceptor interface and therefore, it becomes paramount for the excitons to be generated close enough to this interface such that they can diffuse to it. An exciton has a determined lifetime L before it recombines. This means that it can only travel a certain distance before the electron-hole pair can be separated. This distance is called the diffusion length and is given by:

$$L_D = \sqrt{D\pi} \tag{15}$$

where D is the diffusion coefficient. This means that the distance from where the exciton is photo-generated to the donor-acceptor interface must be lower than L_D in order for the exciton to be successfully dissociated. If the distance is larger that L_D the exciton will recombine before reaching the interface resulting in an unsuccessful charge separation. According to literature, a typical acceptable distance between exciton generation site and donor-acceptor interface should be in between 5 to 30 nm[76–79]. At first glance, a logical approach to heterojunction engineering would be to create a 10 nm thick bilayer of donor-acceptor in order to increase the charge generation per photon absorbed (i.e. quantum efficiency) as much as possible. However, Beer-Lambert states that the absorbance A of light has a direct dependence on optical depth τ:

$$A = \frac{\tau}{\ln 10} \tag{16}$$

meaning that a higher thickness would result in more photons being absorbed and more exictons formed. According to Dang et al[80]., a minimum thickness of $100nm$ is required to absorb most of the photons available in the specific electromagnetic spectrum range that conjugated polymers can optically interact with. If a $100nm$ thick simple bilayer heterojunction (figure 16a) was to be used, only the region that is within $10nm$ of the interface would contribute to current generation. The rest of the heterojunction would generate excitons upon light absorption, but they would recombine before reaching the interface. Therefore an ideal heterojunction for optimal efficiency would need a controlled architecture (figure 16b) that has a large amount of thin interfacial areas. This nanoscale structuring has being achieved using imprint lithography[81], however it is

a complex process that at the moment would hinder the price competitiveness of organic solar cells. Therefore, it has been proven that the most successful way of fabricating the most optimal active layer so far is through a self-organised, bulk heterojunction. This architecture is very simple to create as it only requires the donor and the acceptor polymers to be soluble in the same organic solvent. A solution blend can then be produced and coated onto a substrate. Upon drying, the materials distribute effectively through the bulk heterojunction as shown in figure 16c. As can be inferred, controlling the morphology of the bulk heterojunction is crucial to obtain maximum exciton dissociation and charge generation. This is a whole separate area of research within the organic solar cell field that is not the primary focus of this thesis, and therefore, the reader is advised to consult the literature suggested in the following references[82–84]. In the same manner, it is important to note that even after the electron transfers from the donor to the acceptor, the electron and hole pair still exists (bound by weaker forces estimated to be in the order of a few hundred meV[85]) and may recombine due to geminate and non-geminate recombination[86–88]. This is known as charge-transport (CT) recombination and the cited references provide an in-depth review to this topic which is not the focus of this thesis.

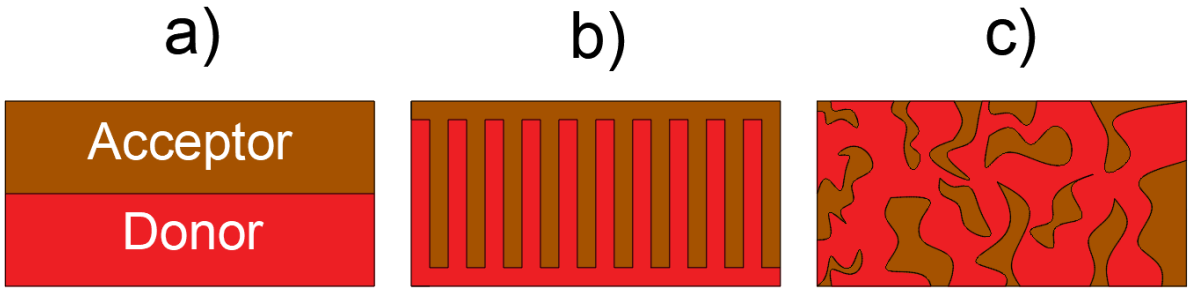

Figure 16: *A bi-layer heterojunction (a), an ideal heterojunction (b), and a bulk heterojunction (c) comprised of a donor-acceptor interface.*

3.5 Charge transport

Once the charges have been generated and separated to the respective donor and acceptor phases, and the exciton successfully dissociated, the charges need to be transported and collected at two different electrodes in order for them to be able travel throughout an external circuit and a load. To avoid recombination events at any of the electrodes, holes and electrons must be collected at separate electrodes. Otherwise any electron

encountering a hole will result in the recombination and loss of those respective charges.

First, the charges have to travel within the bulk heterojunction to its adjacent layers. In disordered organic semiconductors the charges are localised to single molecules (the conjugated segments mentioned in section 3.2). Charge transport then occurs by temperature and electric field assisted hopping[89] which at the same time is dependant on the density of charge carriers and the energetic and spatial distribution of transport states. The organic field effect transistor (OFET) model has been used to relate the molecular structure to charge carrier mobility, however it is still not completely understood how the molecular ordering influences the charge transport properties of polymers. Nevertheless a well accepted parameter to measure the charge transport is carrier mobility μ which is positively related to the efficiency of the device. Therefore, donor and acceptor materials with a high carrier mobility will facilitate charge transport within the bulk heterojunction.

Since the electrodes are placed opposite to each other and adjacent to the bulk heterojunction (figure 17a), the electrons and holes need to travel to their respective electrode and be prevented from reaching the other one where the opposite charge is being collected. In an ideal heterojunction (such as the one shown in figure 16b) the collection of electrons and holes at their respective electrodes would be facilitated by the arrangement of the acceptor and the donor materials (i.e. the donor material would prevent most of the the electrons from going into the hole conducting electrode, and the acceptor material would prevent most of the holes from going into the electron conducting electrode). However in a bulk heterojunction the phase distribution is randomized (16c) and therefore some donor material is in contact or very close ($<L_D$) to the electron conducting electrode (and vice versa with the acceptor and the hole conducting electrode) promoting recombination due to the migration of both electron and hole to the same electrode. To prevent this, electrodes with different work functions ϕ can be employed, such that they provide a favourable energy level for the desired charge carrier and at the same time a non favourable energy level for the non desired charge carrier. Therefore, an electrode with a low ϕ (ideally equal to the LUMO of the acceptor) can be employed to extract electrons and block holes, and an electrode with a high ϕ (ideally equal to the HOMO of the donor) can be employed to extract holes and block electrons. When these ideal conditions are true the materials form an Ohmic contact. In reality, finding

a combination of donor-acceptor and electrode materials that match each other's energy levels to such level of perfect alignment is very difficult to achieve. Moreover, even if a perfect combination of donor-acceptor and electrodes were to be achieved, some recombination events would still occur due to some charges migrating to the wrong electrode as a result of probability. Additionally, the electrodes can have energy levels that promote exciton quenching, and therefore, when the electrode is in direct contact exciton dissociation can be increased when the electrode is in direct contact with the exciton generation sites. To reduce recombination events at the electrodes, buffer layers that sit at the bulk heterojunction-electrode interface are normally incorporated to the device structure. Such buffer layers have energy levels that have two main functions; to provide a more favourable energy level for the transition of the desired charge to its respective electrode (this is, if the work function of the electrodes is not perfectly matched in an Ohmic contact with its respective active layer materials) and to block the opposite charge from reaching that electrode by having an unfavourable energy level for such charge to travel to the electrode (figure 17b). Due to their main function in facilitating the transport of charges, these buffer layers are commonly referred as electron transport layer (ETL), and hole transport layer (HTL).

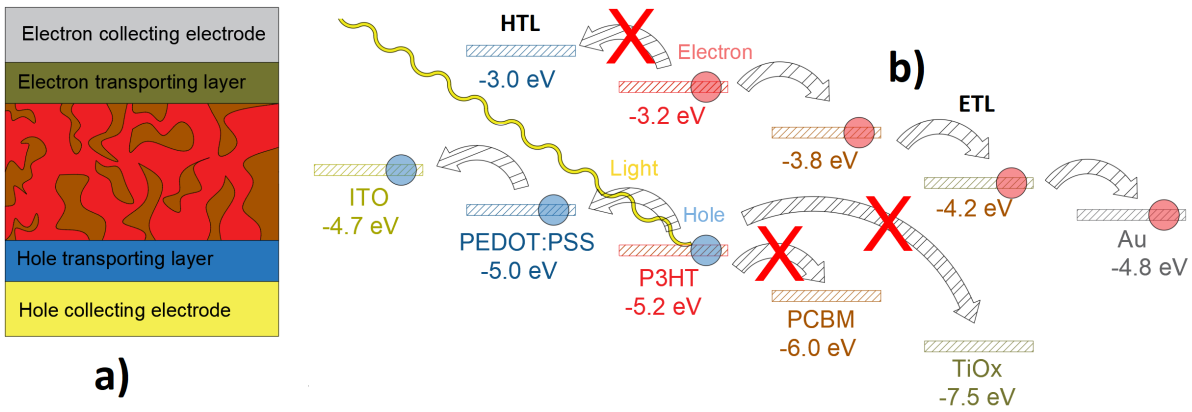

Figure 17: *(a) Cross sectional view of the bulk heterojunction, electrodes, and buffer layers. (b) Schematic example of a favourable energy alignment for charge transport. Energy levels of the hole conducting electrode indium tin oxide (ITO), hole transporting layer (PEDOT:PSS), donor material (P3HT), acceptor material (PCBM), electron transporting layer titanium oxide (TiOx), and electron conducting electrode (gold) are reported by Kettle et. al. and Yoshida et. al.*[90;91].

Since the main focus of this thesis is an investigation on the active layer-hole collecting electrode interface, a separate section on buffer layers is presented later in this

thesis (3.7). This section was just an introduction to the charge transport phenomena in organic solar cells.

3.6 Device architecture and relevance of P3HT:PCBM based devices

The device architecture of organic photovoltaics have evolved substantially in the past three decades. During the very first age of organic photovoltaics, these consisted of only a photo-sensitive layer placed between two electrodes with different ϕ. For example, in 1982, Weinberger et al.[92] achieved a QE of 0.3% through a polyacetylene based solar cell sandwiched between graphite and aluminium. Different polythiophenes were later investigated and devices with an improved V_{oc} were achieved[93]. Efficiencies up to 0.1% were then achieved by using a poly(p-phenylene vinylene) based active layer between indium tin oxide (ITO) and Al[94]. The low efficiency of these devices could be attributed to the strong exciton binding energy generated in the photo active material, and as this became more clear, OSCs research shifted towards the emerging bi-layer donor-acceptor heterojunction solar cells.

Tang et al.[95] were the first OSCs researchers to achieve and even patent a device with a PCE of 1%. It consisted of a bi-layer heterojunction of copper phthalocyanine and a perylene derivative. They were also the first to observe and propose that charge separation is much more effective at a donor-acceptor interface than at an electrode interface. Soon after the first use of the bi-layer heterojunction, different acceptors were investigated along with conjugated polymers to produce higher efficiency devices. During this time, a major breakthrough occurred for the whole field of material's science. The fullerene C_{60} molecule was discovered by Kroto et al.[96], and its properties proved to be highly suitable for organic photovoltaic applications mainly due to its processability, conductivity and transparency. Sariciftci et al.[97] reported the first device based on a poly[2-methoxy-5-(2'-ethylhexyloxy)-p-phenylene vinylene] (MEH-PPV)/C_{60} bi-layer heterojunction that was placed between ITO and gold electrodes. The researchers demonstrated that the photocurrent of the C_{60} incorporated devices was more than 20 times higher than that of the devices whose active layer consisted only of MEH-PPV. C_{60} quickly became one of

the most used acceptors in heterojunction cells, specifically in the form of phenyl-C61-butyric acid methyl ester ($PC_{60}BM$ or PCBM). However, as explained in section 3.4, in a bi-layer heterojunction structure a significant amount of excitons are not succesfully dissociated because they do not reach the interface before recombination and therefore, no major increase in the PCE of organic solar cells occurred until the use of the bulk heterojunction.

Some of the first bulk heterojunction based devices were demonstrated by Yu et al. who reported the use of a blend of MEH-PPV and C_{60}[98]. The same researchers, who had also previously attempted the use of a bulk heterojunction with the same type of polymer-fullerene blend[99], were the first to spin-coat a 20/80 ratio blend of MEH-PPV and C_{60} on ITO evaporating calcium as the top electrode. This resulted in a QE of 29% and a PCE of 2.9%. Soon after, Shaheen et al.[100] reported a QE of 85% and a PCE of 2.5% using a bulk heterojunction based on a PPV-derivative. Due to its success and simplicity, the use of a bulk heterojunction has become the most used and investigated morphology in organic solar cells. This has led to the development and research of different donor materials such as PCDTBT[101], PSiF-DBT[102], PSPTPB[103], PTPT[104], PTB7[105], PffBT4T-2OD[106], PBDB-T-Cl[107] among others, all of which have been combined with a wide range of acceptors[108], including the currently popular non-fullerene acceptors[109]. This diversity of bulk heterojunction materials has allowed OSC technology to reach efficiencies of up to 17.3%[110] so far for single junction architectures. However, the most investigated and understood bulk heterojunction for OSCs by far is poly[3-hexylthiophene](P3HT):PCBM[80].

To date, the highest efficiency achieved for P3HT:PCBM devices has been over 6.5%[111], however the average efficiency for these type of devices is ≈2.5%[80]. The influence of several factors on the efficiency of P3HT:PCBM based devices have been investigated such as solvent selection[112], vapor annealing[113], ink viscosity[114], and annealing temperature[115], among others. One of the most influential and easier to control parameters that strongly impacts the morphology of the bulk heterojunction and thus, the efficiency of the devices, is the P3HT to PCBM solution ratio[116]. It has been proven that a weight ratio of 1:0.8 of P3HT:PCBM is close to optimal for achieving the best morphology for improved device efficiency[80]. The morphology can also be strongly influenced by a ther-

mal annealing treatment. This treatment enables the blend nanodomains to be increased to values corresponding to the exciton diffusion lengths in each material[117]. However, an excess of these nanodomains can actually hinder the PCE of the P3HT:PCBM blend, and therefore, the annealing time and temperature has to be optimized. It is also possible to add dopants to the blend solution in order to optimize the phase separation between P3HT and PCBM[118] resulting in a more beneficial morphology for the dissociation of excitons. The thickness of the BHJ is also a parameter that strongly influences the PCE of the device. A P3HT:PCBM blend can have thicknesses up to 266 nm which allows for a good light absorption, however, high thicknesses have been proven to experience a high amount of recombination events likely caused by the wide domain sizes of the bulk heterojunction[119;120]. Therefore, an optimal thickness for this blend has been determined to be between 50 and 100 nm.

Depending on the regioregularity and molecular weight, P3HT has HOMO and LUMO levels between -5.2 and -4.8 eV, and -3.2 and -3.6 eV respectively which results in an average optical E_g of approximately 2.0 eV. This can arguably be a limitation to the maximum attainable PCE for P3HT:PCBM based solar cells due to the fact that the large E_g of $\approx$ 2 eV results in an absorption of light limited to wavelengths lower than 650 nm. For the solar spectrum this means that under AM=1.5G, less than 23% of the total amount of photons are absorbed. This was one of the motivations for the development of low band gap polymers such as PCDTBT, which through lower HOMO and LUMO levels have a longer wavelength absorption onset (890 nm for PCDTBT) allowing them to absorb more in the visible and infra-red region of the electromagnetic spectrum. However, low band gap polymers usually do not absorb strongly in the lower wavelengths of the solar spectrum being unable to use the full potential of all the solar resource available. This has caused the emergence of a device architecture that combines two or more active layers called tandem solar cells or multi-junction solar cells. Such an architecture is not exclusive to OSCs, and has proven to produce the highest efficiency devices for different type of solar cell technologies[53]. Tandem solar cells however have a much more complex device architecture due to the numerous materials involved in their structure compared to single active layer devices and therefore are more susceptible to degradation mechanisms and thus reduced lifetimes. This has been a major limitation

for the scaling up of full organic tandem solar cells. On the other hand, single junction P3HT:PCBM based devices have already been scaled up and tested in real-environmental conditions showing promising results[121–123]. The readiness of P3HT:PCBM based OSCs for large-scale production has allowed research on P3HT:PCBM to stay relevant and active within the scientific community and to date, P3HT:PCBM devices are still being actively investigated. Moreover, given the extensive study and good understanding of P3HT:PCBM based devices, such blend is highly convenient to use when investigating novel ideas, materials, and methods that impact the other aspects of the device architecture (e.g. other layers, or processing conditions). This is due to the fact that the number of unknowns or not understood phenomenons can be reduced and attributed to the effects produced by any new material or methodology used for the fabrication of the device. The characteristics mentioned above about P3HT:PCBM blends are to some extent true for the PCDTBT:$PC_{70}BM$ blend. Since this research intends to investigate the interface between the active layer and the HTL, a P3HT:PCBM blend was chosen as the main active layer to be investigated due to the reasons mentioned above. Hence, any principle behind the improvement of the interface quality between the P3HT:PCBM active layer and HTL determined in this research can be equally applicable to other higher performing active layer blends. The PCDTBT:$PC_{70}BM$ blend was also used in this research using the same reasoning than for the P3HT:PCBM.

Irrespective of how optimal an active layer can be achieved, the efficient transport and collection of charges at the electrodes plays a crucial role in the efficiency of OSCs. As discussed in the previous section, charge collection is not optimal when the active layer is placed in between two electrodes only. The use of interfacial layers between the electrodes and the active layer was first reported for organic light emitting diodes (OLEDs) which operate with the same basic physics principles that OSCs. The interfacial layers used in OLEDs showed that they can significantly affect the active layer-electrode interface by inducing interfacial charge redistributions, geometry modifications, and chemical reactions[124;125]. Soon after, interfacial layers were used in OSCs significantly improving the photovoltaic performance of the devices. The addition of the two interfacial layers between the electrodes completes the device architecture (figure 17) that is commonly used nowadays for OSCs and that will be used in this thesis.

3.7 Buffer layers

Whereas efficient charge separation relies heavily on the quality of the donor-acceptor interface, charge extraction depends strongly on the quality of the active layer-electrodes interfaces. As mentioned in section 3.5, the role of the electrodes in a solar cell is to collect the respective positive and negative charges. Therefore, the optimization of the interfaces between the active layer and the electrodes to allow a smooth transition of the charges from the active layer critically affects the PCE of the device[126]. A direct contact between the electrodes and the active layer, however, does not necessarily form an optimal interface for charge transport and extraction, due to different charge loss mechanisms that contribute to a decrease in the PCE of the device. For example, XPS studies reveal that an insulating Al/PPV layer of approximately 30 Å is formed between the PPV active layer and the Al ECE. This insulating layer serves as a blocking barrier for electrons and its thickness increases as a function of time which eventually results in the failure of the device[127]. Another disadvantage of the active layer-electrodes interaction is the non-optimal alignment of the ϕ of the electrodes and the active layer energy levels. For example, ITO, a widely used transparent electrode in OSCs, has a ϕ of 4.7 ev which is neither aligned with the $HOMO$ level of the most common donor polymers nor the $LUMO$ of fullerenes[128]. This means that ITO has no selectivity of negative or positive carriers making it a recombination site when both types of charges reach the electrode. Additionally, and particularly for ITO, it has been proven that within time, indium diffuses into the organic layer forming trap sites for recombination[129]. As mentioned above, such reactivity between electrode and active layer also happens for other electrodes such as Al[130], and needs to be avoided in order to extend the functionality of the device over an extended period of time. In order to solve the problems related to the interaction between active layer and electrodes, several materials have been employed as inter-facial layers between the electrodes and the active layer including organic molecules, metal oxides, and composites of organics with inorganic dopants[131;132]. These interfacial materials can serve as exciton blocking layers that have selectivity for charge carriers. This means that they have the capability of allowing one type or charge carrier and block the other type or charge carrier[124]. Interfacial layers also serve as an insulating buffer layer that can prevent chemical reactions between the organic materials in the active layer and the

electrodes as well as the diffusion of metal ions from the electrodes to the BHJ[133].

The interfacial layers placed between the electron conducting electrode and the active layer are called cathode buffer layers or electron transport layers (ETLs) and their function is to improve the transport and collection of electrons generated in the active layer to the external circuit. As mentioned in section 3.6, the most used acceptors in organic solar cells are fullerenes, specifically PCBM, and since its LUMO level ($\sim$ -3.8 eV) is not aligned with the most commonly used electron conducting electrodes like Al (ϕ= -4.3 eV) some V_{oc} losses occur[134] affecting the efficiency of the device. Moreover, as mentioned above, the randomized morphology of the BHJ can provoke hole transport from the active layer to the electron conducting electrode fomenting recombination. Therefore the three main functions of a ETL are to facilitate the transport of electrons generated in the electron donor material to the electron conducting electrode, to form an Ohmic contact with the electron acceptor material, and to block positive carriers (holes) from reaching the electron conducting electrode. Low ϕ metals are commonly used as ETLs in organic solar cells, calcium (Ca) being one of the most popular due to the formation of an ideal Ohmic contact at the interface between PCBM and Al leading to an increase in V_{oc} which results in the improved efficiency of the devices[135]. Heeger et al. obtained a FF of 75.1% in OSCs by using Barium as a ETL which was alleged to prevent Shockley-Read-Hall recombination at the interface and to increase the R_{sn} of the device that also resulted in the decrease of R_s[136]. Metal oxides such as titanium oxide (TiOx) and zinc oxide (ZnO)[137] are also commonly used as ETL due to their ϕ being close to the LUMO of PCBM and Al resulting in the formation of a good Ohmic contact between them. ZnO in particular has attracted significant interest due to several attractive characteristics. First, ZnO has a Fermi level that matches that of PCBM (-4.3 eV) facilitating the electron transfer from PCBM to the electron conducting electrode. Moreover, ZnO has high electron mobility (2.5 cm^2 V^{-1} s^{-1})[138] and very simple solution processability[139].ZnO also can be doped with metals such as Al to improve its electrical conductivity[140]. One of the main disadvantages of metal oxides is that they require a relatively high temperature (>200 °C) to be sol-gel processed, however, alternative processing techniques, such as vapour deposition, can be used to deposit the metal oxides onto the substrates of the devices[141]. Other type of metallic compounds that have been succesfully incorporated

as ETLs in OSCs are alkali metallic compounds, among which the most commonly used is lithium fluoride. For example, Brabec et al. reported enhanced FF and V_{oc} of OSCs when a thin layer of LiF layer was deposited between the active layer and the electron conducting electrode (different devices with Al or Au were fabricated). This resulted in an improved PCE by more than 20% (compared to the reference devices without LiF) which was attributed to the formation of a dipole moment accross the junction due to either a chemical reactions or the orientation of the LiF[142]. Other alkali metals such as KF, CsF, and NaF have also been successfully incorporated as ETLs in OSCs to improve the PCE of the devices by reducing the R_s of the devices. However, it was reported that ultra thin layers of less than 1.2 nm are required for these ETLs to improve the PCE of the devices[143]. Some organic materials such as bathocuproine (BCP)[144], poly(ethylene glycol) (PEG)[145], and PFN[146], and even fullerene C_{60} derivatives[147] have also been successfully employed as ETLs in OSCs to improve the PCE of the devices. Each of the mentioned organic ETLs incorporated in different device structure compositions improved the efficiency of devices through different mechanisms, corroborating the complexity of the interactions between the different layers within the OSCs structure. There are also a few reports of graphene derivatives such as cesium-neutralized graphene oxide (GO-Cs) that have been succesfully incorporated as ETLs to improve the PCE of OSCs[148], however, the other mentioned ETLs have been more extensively used. Since the focus of this thesis is the interface between the active layer and the hole transport and conducting layers, ETLs will not be discussed any further, however, should the reader wish to know more about such interfaces, an in depth review on ETLs can be found in the following cited references[124;125;132].

The interfacial layers placed between the hole conducting electrode and the active layer are called anode buffer layers or hole transport layers (HTLs) and their function is to improve the transport and collection of holes generated in the active layer to the external circuit. In order for HTLs to improve the performance of OSCs they should have certain characteristics. In a similar way to ETLs (but with the opposite charge), HTLs need to improve the transport of holes generated in the electron donor material to the hole conducting electrode (e.g. by having good hole mobility). Moreover, HTLs need to form an Ohmic contact with the electron donor, and to have a good electron

blocking capability to reduce the number of recombination events at the hole conducting electrode. Ideally, HTLs should also be easily processed (e.g. sol-gel) and have a surface energy compatible with the hole conducting electrode for good adhesion with both the hole conducting electrode and the active layer (e.g. by having a smooth surface that enhances the contact with adjacent layers). In addition to these characteristics, in normal OSC architectures such as the one used in this thesis (unless otherwise stated) HTLs need to be as transparent as possible in the solar electromagnetic spectrum to allow light to reach the active layer. This is also true for the electron conducting electrode which is one of the main reasons why ITO is very commonly used in OSCs. Ever since researchers started to use buffer layers, different HTLs have been incorporated into the structure of OSCs. The main HTL material used in this thesis will be discussed in detail in sections 3.7.1 and 3.8, however, other commonly used HTLs in OSCs will be discussed in brief here. Metal oxides such as molybdenum oxide MoO_3[149], vanadium oxide V_2O_5[150], tungsten oxide WO_3/WOx[151], nickel oxide NiOx[152], and copper oxide CuOx[153] have been widely investigated as HTLs in OSCs. Such metal oxides have good optical transparency in the visible and the near infrared part of the electromagnetic spectrum and their conduction band is sufficiently higher than the LUMO of most organic donor materials to block electrons from leaking into the metal oxide and hole conducting electrode. Moreover, the Fermi level of metal oxides is also well aligned with the HOMO of polymer donors leading to the formation of an Ohmic contact with the hole conducting electrode that has little to no resistance. Additionally, metal oxides degrade much slower than some of the organic materials used as HTLs which improves the lifetime of the devices compared to those that use organic HTLs. When metal oxides were first used as HTLs, the predominant method to deposit them was by vapour deposition, however, a sol-gel process has been proven as equally effective and relatively more simple[154;155]. The degree of oxidation of metal oxides plays a crucial role in determining their energy levels and thus the efficiency of the device, and it can be controlled either by changing the annealing temperature or by using an oxygen plasma treatment. However, controlling the degree of oxidation of metal oxides has proven to be difficult and very dependant on slight variations in the surrounding environment where the metal oxide is processed. Despite the advantages of metal oxides, organic HTLs have been much more widely investigated and incorporated to OSCs. This is probably due to their simpler processability (sol-

gel and <150 °C thermal annealing). Among the most popular organic HTLs used in OSCs are poly[aniline] (PANI)[156], and PEDOT:PSS[134], however, as will be discussed in the following section, the latter is by far the most studied HTL in OSCs due to its numerous advantages over other HTLs. It is worth noting that graphene oxides have also been used as HTLs and have shown to improve the stability of devices compared to those using organic HTLs[151], however patterning the graphene oxides is complicated due to its required small thicknesses and high sensitivity to contamination by other organic materials that are either within the structure of the device, or used for the processing of the graphene oxide (e.g. photoresist)[157]. Given that one of the main foci of this thesis is investigating PEDOT:PSS as an HTL for in OSCs, the following two sections are dedicated to the detailed description of PEDOT:PSS.

3.7.1 PEDOT:PSS

The PEDOT polymer was first developed by BAYER AG in the 1980s. To synthesise PEDOT, the EDOT monomer needs to be obtained first. This can be achieved by several methods, however, a four step synthetic strategy that starts from thiodiglycolic acid can be used to obtain 3,4-ethylenedioxythiophene-2-5-dicarboxylic acid which can be subsequently decarboxylated by using a copper salt to obtain the EDOT monomer with a total of five synthesis steps (see figure 18)[158–160]. This monomer is produced on a large scale by Bayer AG and is commonly known as Baytron M. It is worth noting that different EDOT derivatives have also been successfully synthesised using different routes[161], however they have not being applied in OSCs. To polymerise EDOT, there are three different routes that can be used; oxidative chemical polymerisation, electrochemical polymerisation, and a transition metal-mediated coupling of a dihalo derivative of EDOT. Oxidative chemical polymerisation is the most commonly used method used to synthesise PEDOT. An example of this method is shown in figure 19 in which Iron(III) p-toluenesulfonate ($Fe^{III}[OTs]_3$) and imidazole as a base are used at high temperature to polymerise EDOT[162].

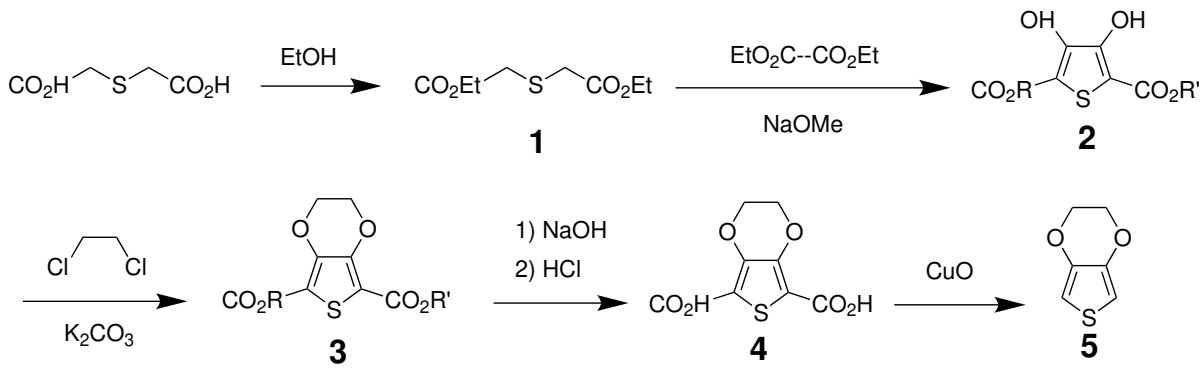

Figure 18: *Five step synthetic procedure for 3,4-Ethylenedioxythiophene.*

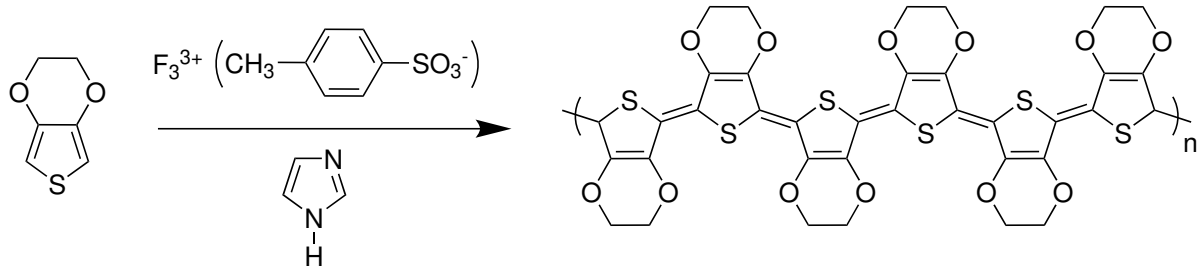

Figure 19: *An example of an oxidative chemical polymerisation of EDOT.*

When PEDOT was first synthesised, it exhibited a decent electrical conductivity of 300 S cm^{-1}, high transparency when coated as a thin film, and good stability in the oxidized state[159;163]. However, due to its strong p-type character, PEDOT proved to be insoluble which hindered its processability and practical use in most applications. To solve the solubility problem, researchers at Bayer AG polymerised the EDOT monomer in an aqueous solution of the negatively charged polyelectrolyte poly(styrerene sulfonic acid) (PSS) using $Na_2S_2O_8$ as the oxidising agent. The water soluble PSS serves as a counter ion for the positively charged PEDOT. The polymerisation process resulted in a PEDOT:PSS dispersion typically called Baytron P that can be easily be processed into a thin film by different methods[134].

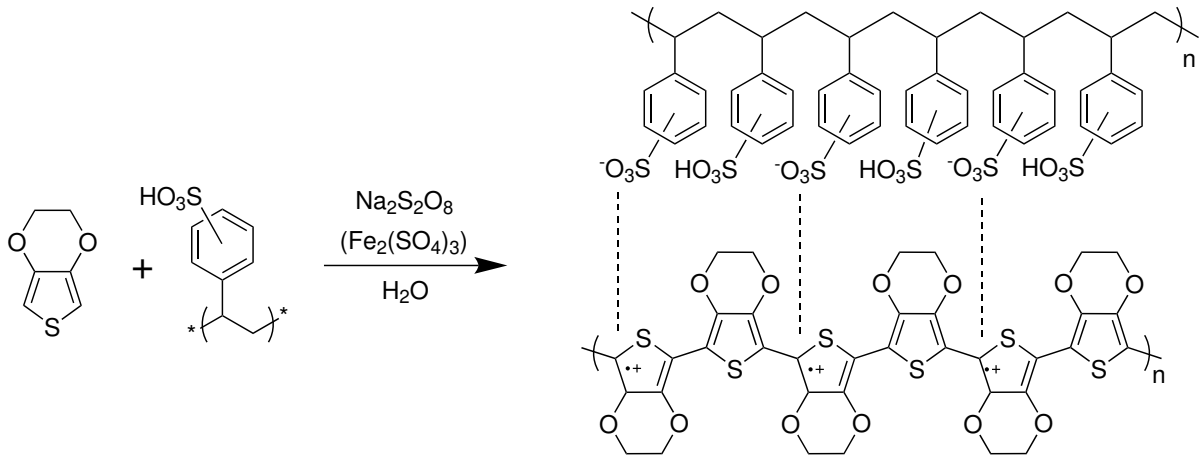

Figure 20: *Synthesis process of the Baytron P PEDOT:PSS.*

Poly(3,4-ethylenedioxythiophene):polystyrene sulfonate (PEDOT:PSS) is one of the most widely used conducting polymers,[134] with applications that range from OLED based displays[164;165] and solar cells[124;166] to bone regeneration[167] and nanobiointerfaces[168;169]. This is due to its numerous advantageous characteristics such as its biocompatibilty[170;171], good thermal and mechanical stability[172–174], excellent water solubility[134], and optical transparency in the visible spectrum when processed as a thin film[163]. In addition to this, it has low toxicity, a high enough LUMO (see figure 17) to block electrons generated by most polymer donors, and a high work function which allows it to make a good Ohmic contact also with most polymer donors[175]. All of the characteristics mentioned above make PEDOT:PSS a good material to be used as an HTL in OSCs[176]. Given that P3HT:PCBM is also the most investigated active layer blend, it is no surprise that PEDOT:PSS is the most used HTL in P3HT:PCBM based OSCs, including the scaled up P3HT:PCBM photovoltaics[177]. Despite the many advantageous properties of PEDOT:PSS, it far from being an optimal HTL material for the fabrication of efficient and stable OSCs. For instance, the conductivity of PEDOT:PSS is relatively low compared to PEDOT or other conductive materials such as metals or metal oxides resulting in a reduced hole transport capability and hence, lower J_{sc} of the device. This is due to the highly insulating nature of PSS which, in order to make PEDOT soluble, needs to be present with at least twice as much PSS as PEDOT in the PEDOT:PSS dispersion. The good water solubility of PSS also makes it highly hygroscopic[178] which is undesirable for device stability since H_2O and O_2 are highly damaging to the device due to their reactiv-

ity with the different materials within the device structure. Moreover, when deposited as a thin film the highly acidic nature of PSS triggers reactions between PEDOT:PSS and the organic active layer that degrades the interface between those materials resulting in the reduced lifetime of devices[179]. In addition to this, the different surface energy levels of PEDOT:PSS and organic active layers (such as P3HT) thin films result in the poor adhesion between them which allows the formation of non-adherence that increase the sheet resistance of the device and serve as degradation seeding points[180–182]. The specific mechanisms of degradation between the PEDOT:PSS and P3HT:PCBM are described in section 6.1 where such issues are addressed as part of the objectives of this thesis. Due to the non-optimal characteristics of PEDOT:PSS mentioned above, it has become common practice to use chemical and physical treatments to modify PEDOT:PSS in order to overcome its disadvantages as an HTL in OSCs. The next section provides a brief summary on such practices.

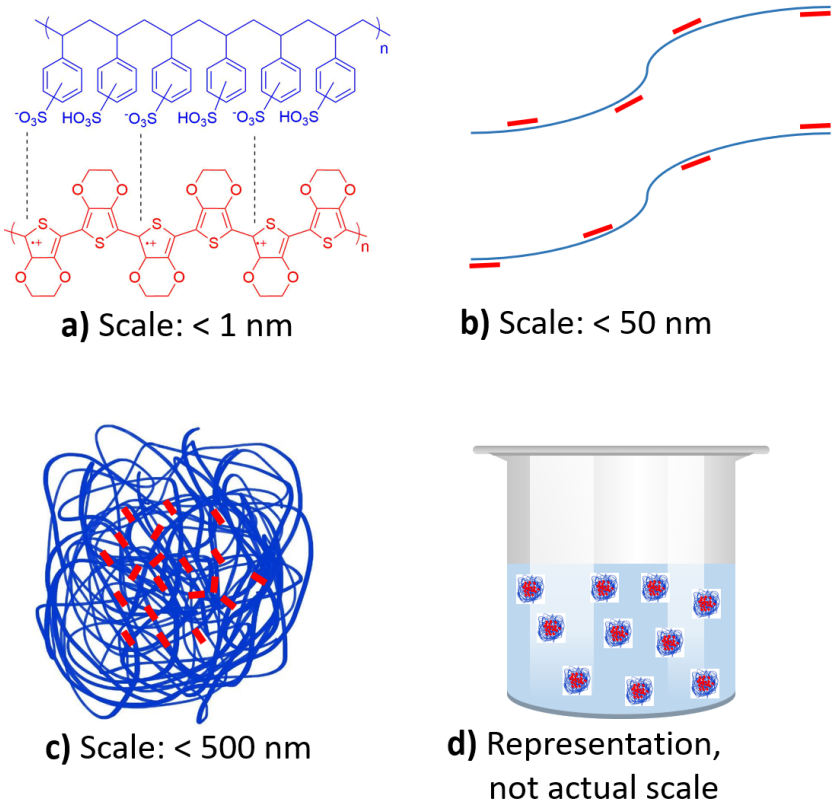

Figure 21: *Schematic representation of PEDOT:PSS at different scales.*

3.7.2 Improving the capabilities of PEDOT:PSS as a hole transport layer

There are two main routes towards improving the properties of PEDOT:PSS as an HTL in OSCs, physical and chemical treatments. A thermal annealing treatment is the most common and widely used physical treatment for PEDOT:PSS thin films. Kim et al. showed that a thermal annealing treatment of 75°C to 230°C applied to the PEDOT:PSS HTL results in a significant improvement of the J_{sc} of P3HT:PCBM based devices[183]. The increase in J_{sc} was probably due to the removal of absorbed ambient water from the PEDOT:PSS film which led to a slight increase in the conductivity of the film, however, other authors suggest that a change in the work function and surface roughness of the PEDOT:PSS film were responsible for the increased J_{sc}[124]. UV treatment has been shown to increase the work function of PEDOT:PSS improving the Ohmic contact with P3HT without damaging the PEDOT:PSS film[184]. Oxygen plasma treatment has also shown to improve the hole collection of PEDOT:PSS films resulting in the improved FF of OSCs[178].

Chemical treatment of PEDOT:PSS is commonly done by adding dopants to the PEDOT:PSS dispersion or diping the PEDOT:PSS film in any given doping solution. The main issue that has been tackled by researchers in the field is the low conductivity of PEDOT:PSS ($<$10 S cm^{-1}). Chemical treatments to the PEDOT:PSS film include immersion on DMF[185], zwitterions[186], and sulfuric acid[187] that resulted in the increase of PEDOT:PSS conductivity by several orders of magnitude. The increased conductivity was attributed to the removal of PSS from the PEDOT:PSS film by the treating agent. In regard to the chemical treatment of the PEDOT:PSS dispersion, several types of additives have been mixed with PEDOT:PSS, in order to improve its hole transporting properties in OSCs, specifically by improving its electrical conductivity[132]. These additives include polar solvents[188;189], alcohols[190;191], ionic liquids[192], polyelectrolytes[166] acids[193;194], surfactants[195], salts[196–199], and zwitterions[200]. The inclusion of these asymmetrically charged additives into PEDOT:PSS causes a variety of complex morphological changes in its molecular structure. For example, the increase in conductivity of PEDOT:PSS by doping it when in aqueous dispersion (solvent doping) has been widely interpreted as a result of the weakening of the Coulombic attractions between the positively charged conducting PEDOT and the negatively charged insulating PSS moieties induced by the

dual-charge dopant[186;196–203]. This is argued to cause a phase separation between the two moieties which causes a conformational change of the originally entangled PEDOT and PSS chains[196;199;203] into a more ordered conducting network that facilitates improved charge transport[204] when deposited as a thin film. While this is a widely accepted theory in the field, this change in morphology has been mostly studied using surface techniques rather than as a thin film due to the fact that most bulk techniques are not very sensitive to disordered polymer blends composed of two materials close in nature (i.e. PEDOT and PSS). The lack of a more precise understanding about how these changes occur has caused ambiguity and inconsistencies in the literature, hindering progress in understanding the effect additives have on the morphology of PEDOT:PSS thin films. Therefore, efforts to understand these morphological changes that the doped PEDOT:PSS goes through after being doped need to be done for optimal PEDOT:PSS engineering.

3.8 Specific objectives

As mentioned in section 1, the general objective of this research is to optimise the hole transporting interface to improve the efficiency and stability of P3HT:PCBM based solar cells with PEDOT:PSS as the hole transporting layer. In order to achieve this, three different specific objectives have been set for this thesis that are addressed in the three experimental chapters of this document.

The first specific objective of this thesis is to optimise the device fabrication process to produce devices that perform at a standard compared to those reported in literature, and thus, proceed with subsequent work to attempt to improve the standard efficiency of such devices. In particular, the effects that two different evaporation techniques (thermal and electron beam) for the ECE deposition have on the P3HT:PCBM active layer will be investigated. This will be done by analysing the UV-Vis absorbance spectrum of the P3HT:PCBM active layer of the device after the electrode deposition. Given that there are currently no reports in literature comparing the effect that different electrode evaporation techniques have on the absorption spectrum of the P3HT:PCBM active layer, it is intended to fill this gap in literature. PCDTBT:$PC_{70}BM$ and PBDB-T-SF:IT-4F based devices will be also fabricated to confirm the effectiveness of the evap-

oration technique that produce the most efficient P3HT:PCBM devices.

The second specific objective of this thesis is to improve the electrical conductivity of PEDOT:PSS films by doping the PEDOT:PSS dispersion with a previously unreported zwitterion as a dopant, and to determine some of the liquid and solid phase structural modifications of the zwitterion doped PEDOT:PSS. The motivation to do this is to provide insight on the morphological changes that PEDOT:PSS goes through after being doped with a conductivity enhancing additive. This is expected to contribute an understanding on doped PEDOT:PSS for its optimal engineering to improve charge transport from the active layer to the hole conducting electrode in organic solar cells. This specific objective is divided into three different sub-objectives. The first sub-objective is to determine which of four previously unreported zwitterionic dopants for the PEDOT:PSS dispersions improve the conductivity of PEDOT:PSS. This will be done by processing the doped dispersions into thin films and measuring their sheet resistance with a four point probe technique. The films with the most significant sheet resistance decrease will be then characterised with ellipsometry to determine their thickness and then their conductivity will be determined. The second sub-objective is to determine the morphological changes that the PSS backbone chain in PEDOT:PSS experiences while in dispersion when doped with the conductivity enhancing additive, and to determine the vertical stratification of the doped PEDOT:PSS when cast as a film as a function of the doping concentration. This will be done by using small angle neutron scattering to study the doped PEDOT:PSS dispersions and neutron reflectivity to study the respective processed films. The third sub-objective is to incorporate the conductivity enhanced PEDOT:PSS films as HTLs in P3HT:PCBM and PCDTBT:$PC_{70}BM$ devices to determine if their photovoltaic performance is improved.

The third specific objective of this thesis is to incorporate three different variants of a newly developed P3HT-*b*-PNSS block co-polymer as an interfacial layer between the PEDOT:PSS HTL and the P3HT:PCBM active layer to improve the hole transport and compatibility between those two layers. The resulting improved hole transport interface is expected to improve the efficiency of the devices and to prevent some degradation mechanisms which occur due to the reaction between the PEDOT:PSS HTL and the P3HT:PCBM active layer. This research will be done by casting different thicknesses

of the block co-polymers and by incorporating them into P3HT:PCBM based devices. The thicknesses will be determined by ellipsometry. If the photovoltaic performance is improved, the successful (in improving the efficiency of devices) block co-polymers will be studied with different characterisation techniques such as small angle neutron scattering, atomic force microscopy, ultraviolet-visible spectroscopy, and ultraviolet photoelectron spectroscopy, to determine the origin of device performance improvement. To determine if the block co-polymers prevent some degradation mechanisms product of the reaction between the PEDOT:PSS HTL and the P3HT:PCBM active layer, a lifetime test under constant illumination, and a lifetime test while stored in the dark will be conducted on the block co-polymer incorporated devices and a control device without a block co-polymer layer.

In summary, at the end of this research it is expected that the performance and stability of standard performing (compared to literature) P3HT:PCBM OSCs will be improved by optimising and characterising the hole transporting materials mentioned above. In the process of doing such, it is expected to provide deep understanding on the mechanisms of morphological modifications of conductivity-enhanced doped PEDOT:PSS, and on the hole transport interface improvement that a P3HT-*b*-PNSS block co-polymer interfacial provides, between the active layer and the PEDOT:PSS HTL of P3HT:PCBM based devices.

4 Optimisation of the organic solar cells fabrication process

4.1 Introduction

In the research field of organic solar cells (OSCs), the first step towards improving their efficiency is the development of a fabrication process that is capable of consistently producing control devices whose performance compares to the standard values reported in literature. This is necessary as the inter-facility reproducibility of results in the OSCs research field is difficult to achieve in a short period of time, complicated by the significant effect that subtle differences in the processing conditions have on the performance of devices. Therefore, the first experimental chapter of this thesis is focused on optimising the device fabrication procedure to make P3HT:PCBM and PCDTBT:$PC_{70}BM$ based devices performing at a standard comparable to those in the literature. This chapter focuses particularly on the deposition of the metal electron conducting electrode (ECE) by comparing two different ECE deposition techniques to determine the most effective.

OSC literature often reports most of the device fabrication methodology with sufficient detail to reproduce the experiment, however, the information on the processing of the ECE is often ambiguous or scarce slowing down the optimisation of device fabrication for scientists starting research in the field of organic photovoltaics. For instance, there are some reports of standard performing OSCs fabricated by depositing the ECE using an electron beam (e-beam) evaporation technique[205–207]. However, for this thesis more than 25 different batches of devices were fabricated using an e-beam evaporation technique to deposit an aluminium (Al) ECE that resulted in very poor photovoltaic performance or no solar cell behaviour at all. It was found that the organic photoactive P3HT:PCBM layer is damaged during the e-beam evaporation possibly due to high energy radiation produced by the highly energetic electron beam striking the evaporation source. Such damage to the active layer was not found in devices in which the Al ECE was deposited using a thermal evaporation technique. The damage to the active layer was investigated by measuring and comparing the UV-Vis absorption spectra of the e-beam

evaporated devices against the thermally evaporated ones. At the end of this chapter, the fabrication of standard performance P3HT:PCBM and PCDTBT:$PC_{70}BM$ based devices was achieved by using the thermal evaporation technique to deposit the Al ECE.

4.2 Experimental

4.2.1 Materials

Glass substrates (20 mm x 15 mm x 1.1 mm) coated with a pre-patterned (6 or 8 pixel) ITO layer (100 nm thickness) were used as the base for the devices and as the hole conducting electrode (HCE) respectively (see figure 22). PEDOT:PSS aqueous dispersions with a PEDOT to PSS ratio of 1:2.5 (M124) was used as the HTL for all types of devices. The electron donors used were P3HT (95.7% regioregularity, 65,200 Mw, and 29,600 Mn), PCDTBT (34,900 Mw, and 16,200 Mn), and PBDB-T-SF (87,845 Mw, 30,282 Mn) while the electron acceptors used were $PC_{60}BM$ (99% purity), $PC_{70}BM$ (95% purity), and IT-4F. Float glass coverslips (12 mm x 15 mm x 0.55 mm) were used to encapsulate the devices with an epoxy (formula undisclosed by the provider) that cures upon exposure to light of wavelengths below 450 nm. All aforementioned materials were purchased from Ossila Ltd. PFNBr (>10,000 Mw) used as the electron transport layer for PBDB-T-SF:IT-4F based devices was purchased from Lumtech. Hellmanex ™III, ethanolamine, 2-methoxyethanol, 1,8-diiodooctane (98.0% purity), and chlorobenzene (99.8% purity) were purchased from Sigma Aldrich. Propan-2-ol, methanol, and zinc acetate dihydrate were purchased from Fischer Scientific International Inc. D.I. water was produced in the lab with an Elga Purelab flex 3 purification system. MoO_3 pellets were purchased from Lesker and aluminum (99.98% pure) used as the ECE was purchased from BDH Chemical Ltd.

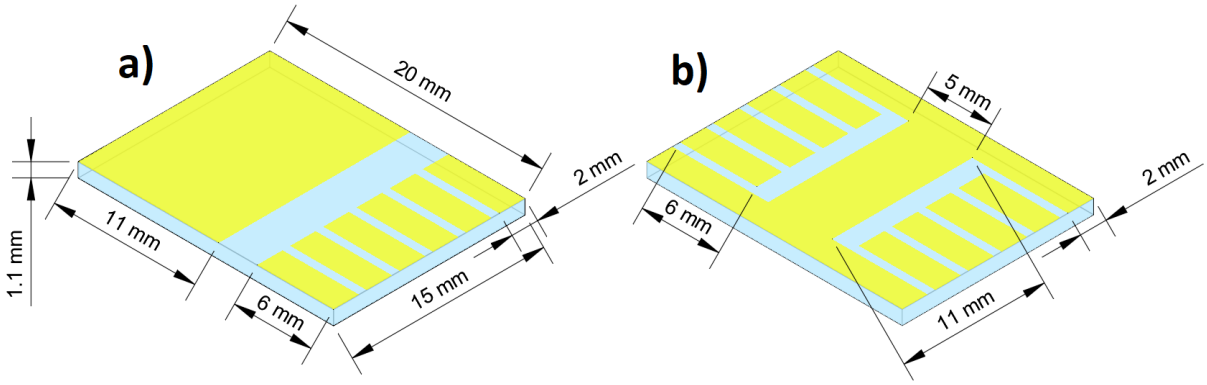

Figure 22: *Sketch of 20 x 15 x 1.1 mm glass substrates coated with a 100 nm thick layer of ITO (yellow) used for the fabrication of organic photovoltaic devices. Two types of substrates, one with Six (a) pixels and another one with eight (b) pixels, which will account for a measurement each once the device is complete.*

4.2.2 Preparation of inks

For P3HT:PCBM based devices, a 1:0.8 (wt.%) P3HT to PCBM ratio blend was used due to its reported optimal performance compared to other ratios[80;208;209]. In order to make a solution with such ratio, 25 mg of P3HT and 25 mg of $PC_{60}BM$ (weighed in a BL 120 S Sartorius micro-balance) were placed in separate 4 mL amber vials (Fisher Scientific) and then 1 mL of Chlorobenzene was added to each. The solutions were left stirring on a hot plate (Bante Instruments MS300 Magnetic Stirrer) at 70°C for 2 hours. Subsequently 0.8 mL of the $PC_{60}BM$ solution were added to the P3HT solution and then the active layer solution was left stirring on the hot plate at 70°C for 30 more minutes. Finally the solution was left for approximately 10 minutes to cool down to ambient temperature and then filtered through a 0.45 μm PTFE filter before use.

For the PCDTBT:$PC_{70}BM$ based devices, a ratio of 1:4 (wt.%) was selected for optimal performance as well[56;210;211]. In order to achieve this ratio, 4 mg of PCDTBT were placed in a 4 mL amber vial and then 1 mL of chlorobenzene was added to it. The solution was left stirring at 80°C overnight and then 16 mg of $PC_{70}BM$ were added to the solution. The active layer solution was then left stirring for 2 additional hours at 80°C, subsequently left to cool down for 10 minutes, and finally filtered through a 0.45μm PTFE filter before use.

For the PBDB-T-SF:IT-4F based devices, a ratio of 1:1 was selected for optimal performance[62;107]. 5 mg of PBDB-T-SF and 5 mg of IT-4F were mixed in a 4 mL amber vial and then 0.5 mL of a 99.5%:0.5% mixture of chlorobenzene:DIO mixture were added. The solution was left stirring overnight at 75°C and left to cool for 10 minutes before use.

Before use, the PEDOT:PSS dispersion was taken out of the fridge where it had been previously stored at 4°C and was left for approximately 10 minutes to warm to room temperature. The dispersion was then filtered through a 0.45 μm polyvinyl difluoride (PVDF) filter before use.

To prepare the ZnO precursor solution, 0.2 g of zinc acetate dihydrate and 0.055 mL of ethanolamine were dissolved in 2 mL of 2-methoxyethanol. The solution was stirred at 20°C for 2 hours.

The PFNBr solution was prepared by putting 0.5 mg of PFNBr in a 4 mL amber vial and then adding 1 mL of methanol. The solution was stirred at 20°C for 2 hours.

All the solutions were used either on the same day of preparation or the following day. No solutions older than two days were used to prevent any ageing effects.

4.2.3 Cleaning of substrates

In order to remove traces of organic contamination attached to the ITO coated glass substrates they were cleaned in an ultrasonic bath (MXBAOHENG PS-60A) at 60° C for 10 minutes with a 0.5% (v/v) solution of a strong alkaline compound patented as Hellmanex ™III in boiling D.I. water. The substrates were then rinsed twice in boiling D.I. water to remove any trace of contaminants attached to the substrates. The substrates were also rinsed once in cold water. The substrates were subsequently sonicated again for the same time at the same temperature with IPA to remove any trace of Hellmanex ™III. The substrates were further rinsed twice in boiling water and once in cold water after the IPA sonication. The substrates were then dried with nitrogen gas and cleaned with oxygen plasma (Zepto system, electronic diener plasma-surface technology) for 5 minutes

to further clear the ITO surface of contaminants and improve the wettability between the HTL and HCE.

4.2.4 Device fabrication

The inks were processed into thin films using a spin-coating technique due to its high reproducibility. During this procedure, the ink is dropped onto the centre of a substrate that is spun at a controlled speed causing the centrifugal forces to spread the solution evenly along the substrate while the solvent evaporates[212]. This results in the formation of a thin film of a determined thickness that is dependant on the viscosity of the material and the shear forces applied during the spinning step which can be controlled by the spin speed and time[213]. To deposit the ECE, a physical vapour deposition technique was used, specifically, electron beam and thermal evaporation. These techniques heat the source material under a high vacuum up to its boiling point, allowing the evaporated material to travel in straight lines away from the source, and coating any surface in its travel pathway. The main difference between thermal and e-beam evaporation is the energy source used to heat the source material. For e-beam evaporation the energy source used is a beam of electrons, while for thermal evaporation it is an electrically heated boat or filament. In both cases the evaporation rate (thickness as a function of time) can be customised by controlling the input current to the heating element or the intensity of the electron beam. A high vacuum is essential for these techniques as it provides a free route for the evaporated particles to avoid colliding with other particles such as O_2 and N_2. In particular Al reacts with O_2 to form Al_2O_3 which is highly undesirable due to its high electrical resistivity compared to pure Al.

In this chapter, the 6 pixel substrates (figure 22a) were used for the P3HT and PCDTBT based devices. PEDOT:PSS was spin-coated (Laurell Technologies Corporation WS-400-6NPP-LITE) onto the cleaned substrates at 4000 RPM for 40 seconds and then $\sim$ 3 mm and $\sim$ 8 mm wide stripes at the top and bottom parts of the samples respectively were formed by removing part of the PEDOT:PSS film with a cotton swab (dampened in D.I. water) to allow the formation of the device circuit as shown in figure 24 (d and e). To remove any ambient moisture absorbed by PEDOT:PSS, the samples

were then thermally annealed at 150°C for 15 minutes on a hot plate and subsequently left for approximately 5 minutes to cool down to room temperature before the deposition of the next layer. The active layer solution was then spin-coated onto the substrates. For the P3HT:PCBM based devices, the active layer solution was spin-coated at 2000 RPM for 30 seconds, while for the PCDTBT:$PC_{70}BM$ base devices, the active layer solution was spin-coated at 800 RPM for 30 seconds. The top and bottom stripes were formed with a cotton swab damped in chlorobenzene. The samples were then loaded into an evaporation mask (Ossila Ltd.) to define the ECE area (2 mm x 6 mm per pixel for the 6 pixel substrates) and the mask was then loaded into an electron beam (Moorfield Nanotechnology custom assembled) or a thermal (Edwards 306 Auto) evaporator to deposit a 150 nm aluminum layer as an ECE. The evaporation rate for the thermally evaporated ECEs was 0.5 nm s^{-1} during the first 50 nm and then increased to 4 nm s^{-1} for the remaining 100 nm, while the evaporation rate for the e-beam evaporated ECEs was 0.6 Å s^{-1}. After the vapour deposition of the ECE, the P3HT and PCDTBT based devices were thermally annealed at 150 °C for 30 min and 80 °C for 15 min respectively to enhance the contact between the PAL and the ECE[59]. Finally, to prevent quick degradation by humidity and oxygen, the devices were encapsulated with float coverslips and epoxy and exposed to a 362 nm light for 15 minutes. In addition to P3HT and PCDTBT based devices, PBDB-T-SF based devices were also fabricated in this chapter, however, their fabrication process was slightly different than the one presented above and therefore it is described in section 4.3.3 where it is more appropriate.

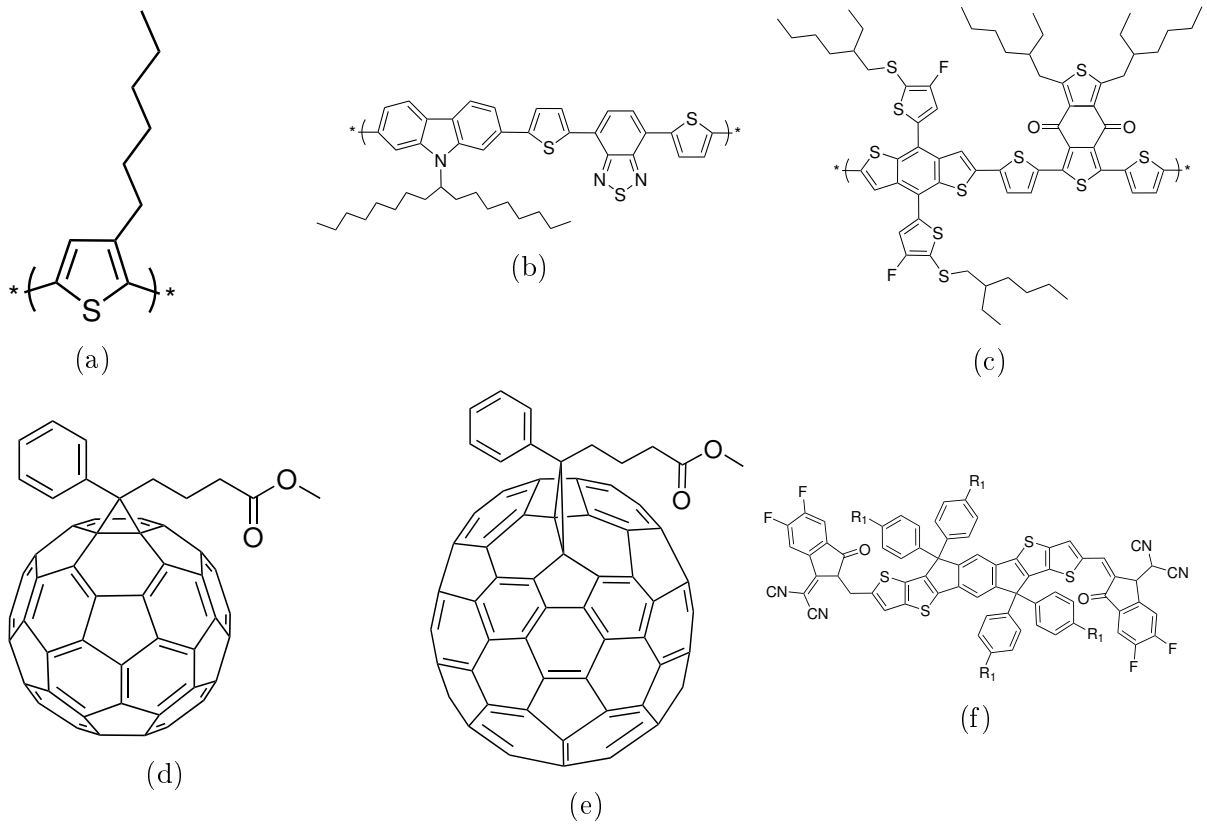

Figure 23: *Chemical structures of the donors (top) P3HT (a), PCDTBT (b), PBDB-T-SF (c), and the acceptors (bottom) PCBM (d), $PC_{70}BM$ (e), and IT-4F (f).*

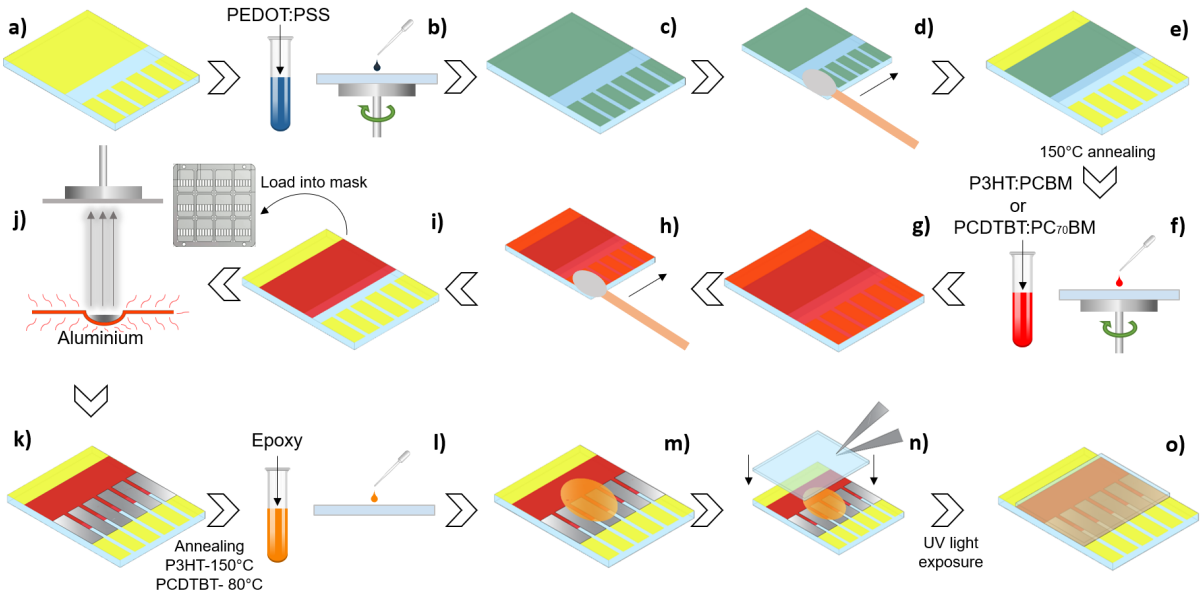

Figure 24: *Sketch showing the device fabrication procedure for the P3HT:PCBM and PCDTBT:$PC_{70}BM$ based devices.*

4.2.5 Device characterisation

To measure the photovoltaic performance of the devices, their J-V curves were obtained while under illumination. A shadow mask was placed between the device and the light source to define an effective illuminated area of 0.0256 cm^2 for each measurement. A Newport 92251A-1000 solar simulator (figure 25) was used to expose the devices to an AM 1.5 sunlight with a 100 mW/cm intensity calibrated against a NREL certified silicon reference cell. Device performance was studied by probing the exposed ITO areas and sweeping a voltage (Keithley 237, -1 V to 1 V, 0.02 V steps) to obtain the J-V curve from each one of the six pixels in every device. The J_{sc} and V_{oc} were obtained from the J-V curve and the FF and PCE were calculated using equations 10 and 11. Each pixel accounted for one solar cell measurement.

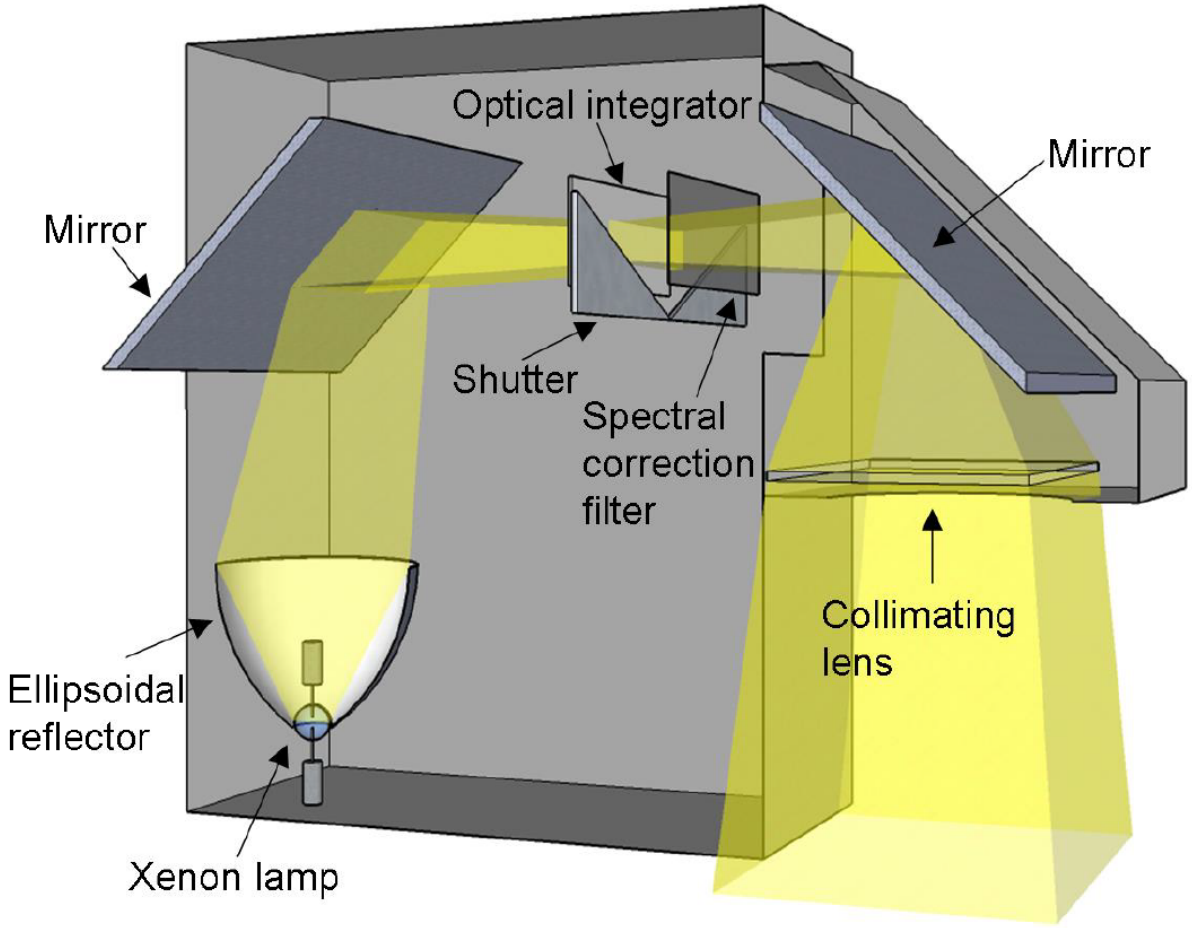

Figure 25: *Schematic representation of the solar simulator used for the characterisation of devices. Image produced by Darren Waters*[214]

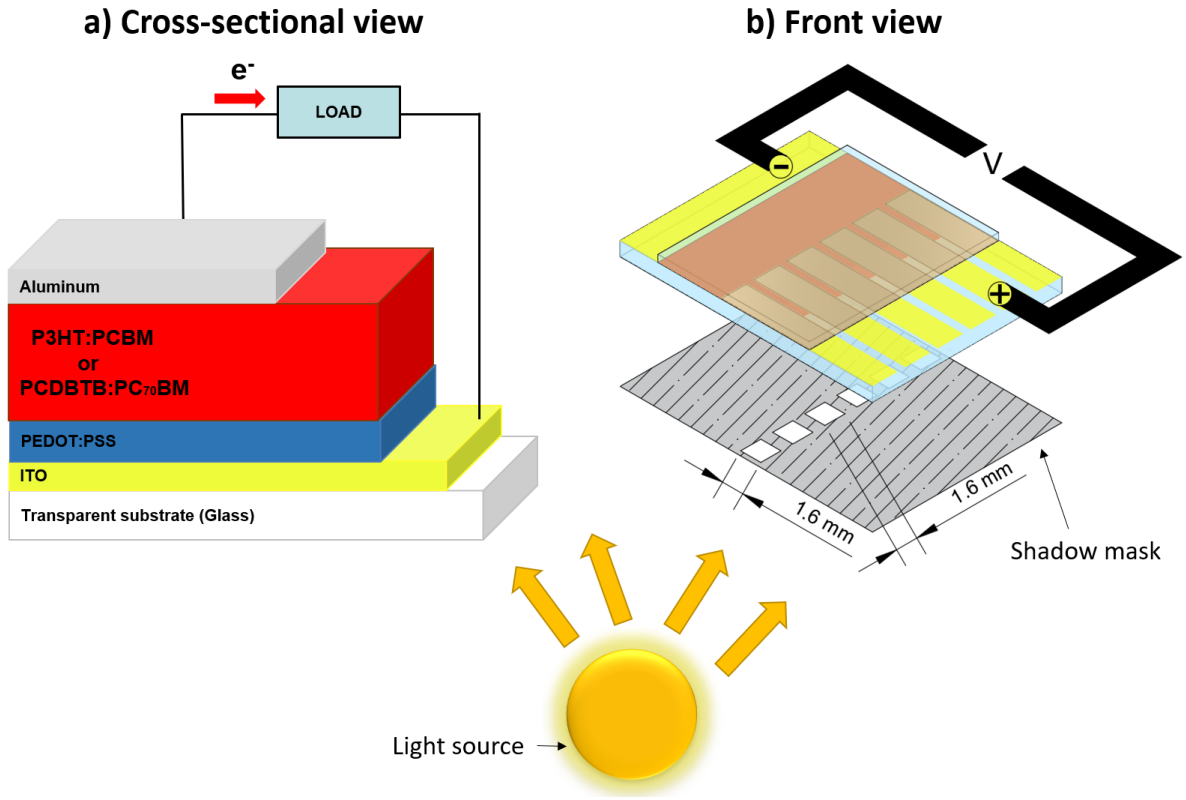

Figure 26: *Schematic representation of the characterisation of devices. The different layers can be observed in the cross-sectional view of the devices (a) while the shadow mask and the placement of the probes are shown in the front view of the device (b)*

4.2.6 Ultraviolet-visible spectroscopy

Ultraviolet-visible absorption spectra was obtained using an Ocean Optics USB2000+ spectrometer and a DT-MINI-2-GS combined with a Deuterium-Halogen light source. To measure the UV-Vis spectra of the fabricated devices, they were oriented with their transparent side facing the optical probe in such way that the UV-Vis light would penetrate through the glass, the ITO, the PEDOT:PSS, and the P3HT:PCBM being reflected by the aluminium layer to return to the emmiting/sensing probe carrying the information of all the penetrated layers. A schematic drawing of this procedure is shown in figure 27. An aluminium coated Menzel-Gläser microscope glass slide was used as the light reference.

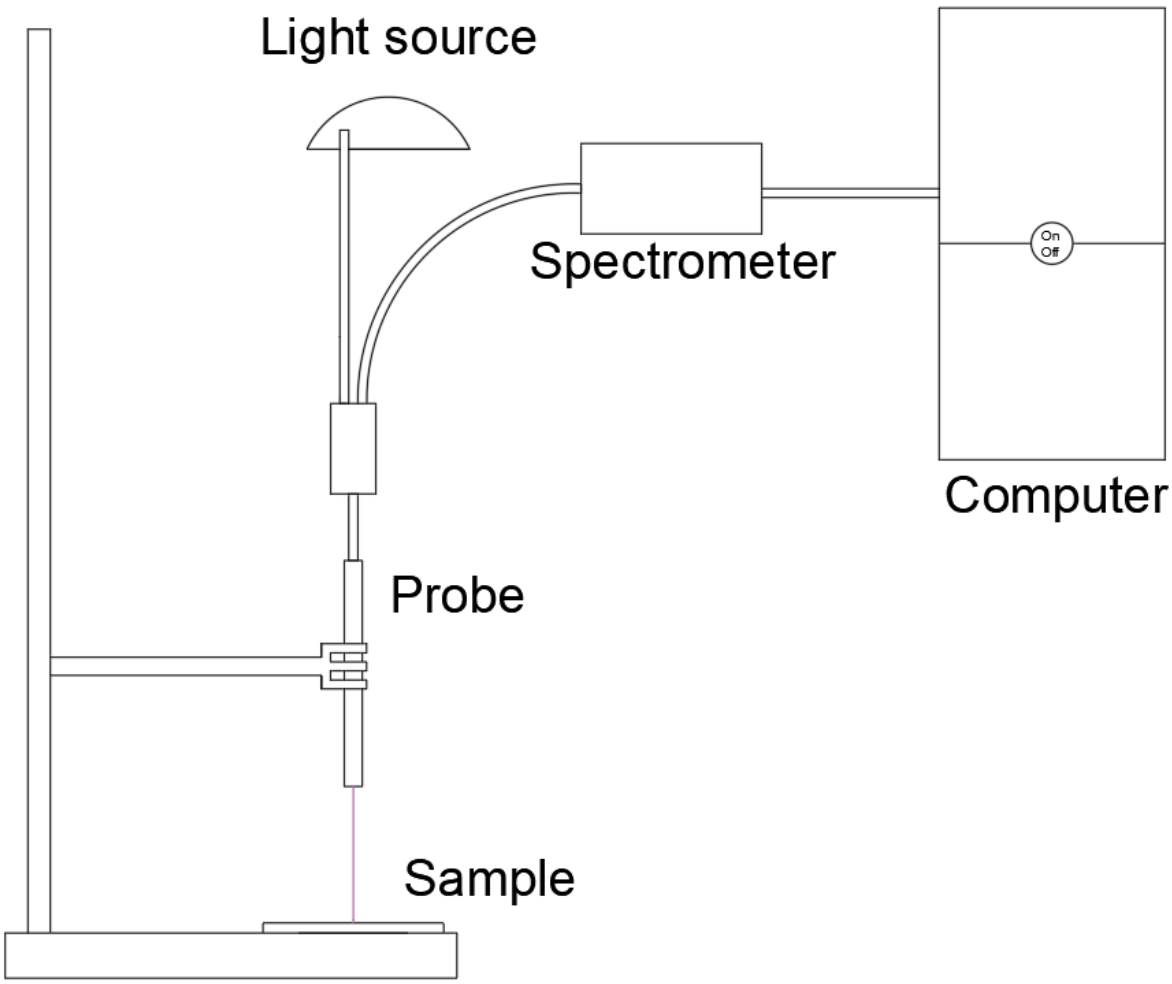

Figure 27: *Schematic representation of the UV-Vis measurements performed on the P3HT:PCBM devies.*

To obtain the UV-Vis absorption spectra of PEDOT:PSS, P3HT (25 mg mL^{-1} in chlorobenzene), PCBM (25 mg mL^{-1} in chlorobenzene), and P3HT:PCBM (prepared as described in section 4.2.2), the PEDOT:PSS solution was spin-coated at 4000 RPM for 30 seconds, and the P3HT, PCBM, and P3HT:PCBM solutions were spin-coated at 2000 RPM for 30 seconds on 25 x 12 mm glass substrates that were cut from Menzel-Gläser microscope glass slides. The UV-Vis measurements were then taken in the more conventional way of placing the samples between a light emitting probe and the detector. A reference microscope glass slide was also used as the light reference for these measurements. This was done for an ITO glass substrate as well to obtain the UV-Vis spectra of ITO. A reference Menzel-Gläser microscope glass slides was used as the light reference for these measurements

4.3 Results and discussion

4.3.1 Photovoltaic performance of P3HT:PCBM devices

Figure 28a and table 1 show the photovoltaic performance of P3HT:PCBM devices with their Al ECE deposited by e-beam and thermal evaporation . The devices with the e-beam evaporated Al exhibited significantly lower average PCE of 0.007±0.005% compared to the 2.06±0.21% of the thermally evaporated Al ones. The low PCE of the e-beam evaporated devices is mainly consequent of the very low average J_{sc} (0.071±0.042 mA cm^2) which results in a poor average FF of 11.61±3.40% as shown by the J-V curve shape of the best e-beam evaporated Al device in figure 28b. In contrast, the average J_{sc} of the thermally evaporated devices is almost two orders of magnitude higher (6.84±0.44 mA cm^2) and the average FF is 56.94±1.70%, almost five time higher. Interestingly, the average V_{oc} of the e-beam evaporated devices was higher (0.749±0.055 V) than that of the thermally evaporated ones (0.529±0.040 V).

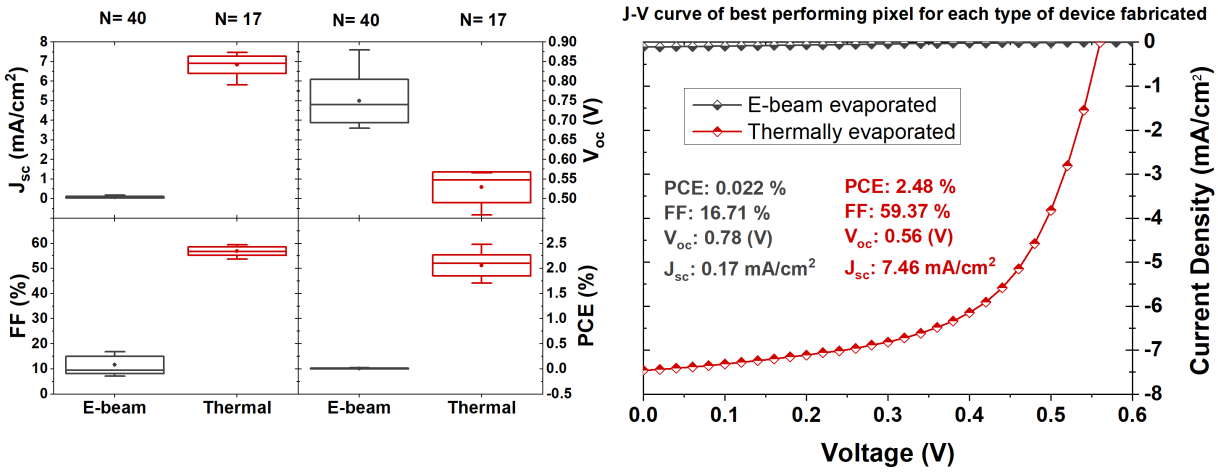

Figure 28: *Box plots (left) showing the Photovoltaic performance (short circuit current, open circuit voltage, fill factor, and power conversion efficiency) of P3HT:PCBM based devices with an e-beam evaporated (black) and a thermally evaporated (red) Al electron conducting electrode. N equals the number of measurements for each type of device, the width of the box represents one standard deviation on each side of the mean average value, the top and bottom ticks are the maximum and minimum values respectively, the horizontal line in the box is the median, and the circle in the middle of the box is the mean average value. The J-V curve (right) of each champion device is also shown for performance comparison.*

Table 1: *Photovoltaic performance metrics of P3HT:PCBM based devices with an e-beam and a thermally deposited Al electron conducting electrode. The errors represent one standard deviation of 40 and 17 different measurements for e-beam evaporated Al, and thermally evaporated Al devices respectively.*

	Average				Maximum value			
	Jsc (mA/cm^2)	Voc (V)	FF (%)	PCE (%)	Jsc (mA/cm^2)	Voc (V)	FF (%)	PCE (%)
E-beam evaporated ECE	0.071±0.042	0.749±0.055	11.61±3.40	0.007±0.005	0.172	0.88	16.88	0.022
Thermally evaporated ECE	6.84±0.44	0.529±0.040	56.94±1.70	2.06±0.21	7.46	0.565	59.37	2.48

The increased V_{oc} of the e-beam evaporated devices can be attributed to the formation of an Al-P3HT complex interfacial layer created by the highly energetic Al e-beam evaporated particles[205]. Given that Al has a strong affinity with organic oxygen, the formation of an Al-O-C complex is highly likely to be triggered by the high energy e-beam evaporated Al particles[215]. This Al-P3HT complex interlayer is believed to have dipoles formed by deep interface positive hole traps in P3HT and the negatively charged Al atoms, which cause an offset on the vacuum level of the interlayer. This results in an effective work function of the Al-P3HT complex interlayer lower than that of Al[206] which has been argued to be favourable for an increased V_{oc} of the devices[216]. However, during the formation of the Al-P3HT layer, the Al atoms can reduce the π conjugation of the polythiophene backbone chains of P3HT by inducing sp^3 hybridisation to the carbon[130]. This results in trap sites that can hinder current collection by delaying the movement of electrons[217]. Moreover, it has been shown before that the highly energetic e-beam Al particles cause damage to the P3HT contributing further to the decrease of J_{sc} and the FF[207]. The magnitude of this damage has been reported to depend on the evaporation rate which depends on the energy of the electron beam. For this work, it is worth noting that 20 additional e-beam evaporated Al device batches were made varying the evaporation rate, however, even the lowest rate resulted either in very poor performing devices, or non working devices (PCE=0%). Since the only variable parameter to control the rate in the Moorfield evaporator used is the current, it is possible that the reason for the poor performing devices was the default set high voltage of 10,000 V which produces high-speed electrons. In addition to the detrimental effects to the active layer by the e-beam evaporated Al particles described above, high-speed electrons can also displace some core electrons of the source material atoms producing high energy radiation such as x-rays that damage the organic active layer.

4.3.2 Investigation of the device damage caused by e-beam evaporation

From the J-V characteristics of figure 28b it is clear that the e-beam evaporated Al devices exhibit significant damage within the device structure. Given that the only significant difference between the e-beam deposited Al and the thermally deposited Al devices is the deposition of Al on the PAL, it is highly likely that most of the damage done by the e-beam evaporation is on the PAL. To corroborate this, the absorption spectra of three different devices was obtained and analysed using UV-Vis spectroscopy. One device was fabricated depositing the Al ECE by thermal evaporation and had a PCE of 2.23 %, and the other two were fabricated depositing the Al ECE by e-beam evaporation which PCEs were 0% and 0.02% respectively. Figure 29 shows the absorption spectra of the three devices, where it is immediately noticeable that the three devices exhibit an absorption peak at λ=383 which corresponds to the characteristic absorption peak of PCBM that is normally at λ=339, but that in this sample is red shifted probably due to the improved crystalisation induced by the 150 °C thermal annealing step after the Al deposition. The appearance of such peak in both the e-beam evaporated Al devices and the thermally evaporated Al device corroborates that the PCBM is unaffected by the highly energetic Al particles and the high energy radiation produced by the electron beam during the deposition of the ECE. This is not the case for P3HT as only the absorption spectrum of the thermal evaporated device exhibits the three characteristic vibronic shoulders of P3HT films at λ=485, λ=551, and λ=605 nm[218]. It is worth noting that the peak at 485 nm is slightly blue shifted (normally at λ=530 before annealing) probably due to the reordering of its chains induced by the 150 °C thermal annealing step. This causes the average $\pi - \pi*$ spacing to increase resulting in the absorption of higher energy photons evidenced by the blue shift in the absorption spectra peak.

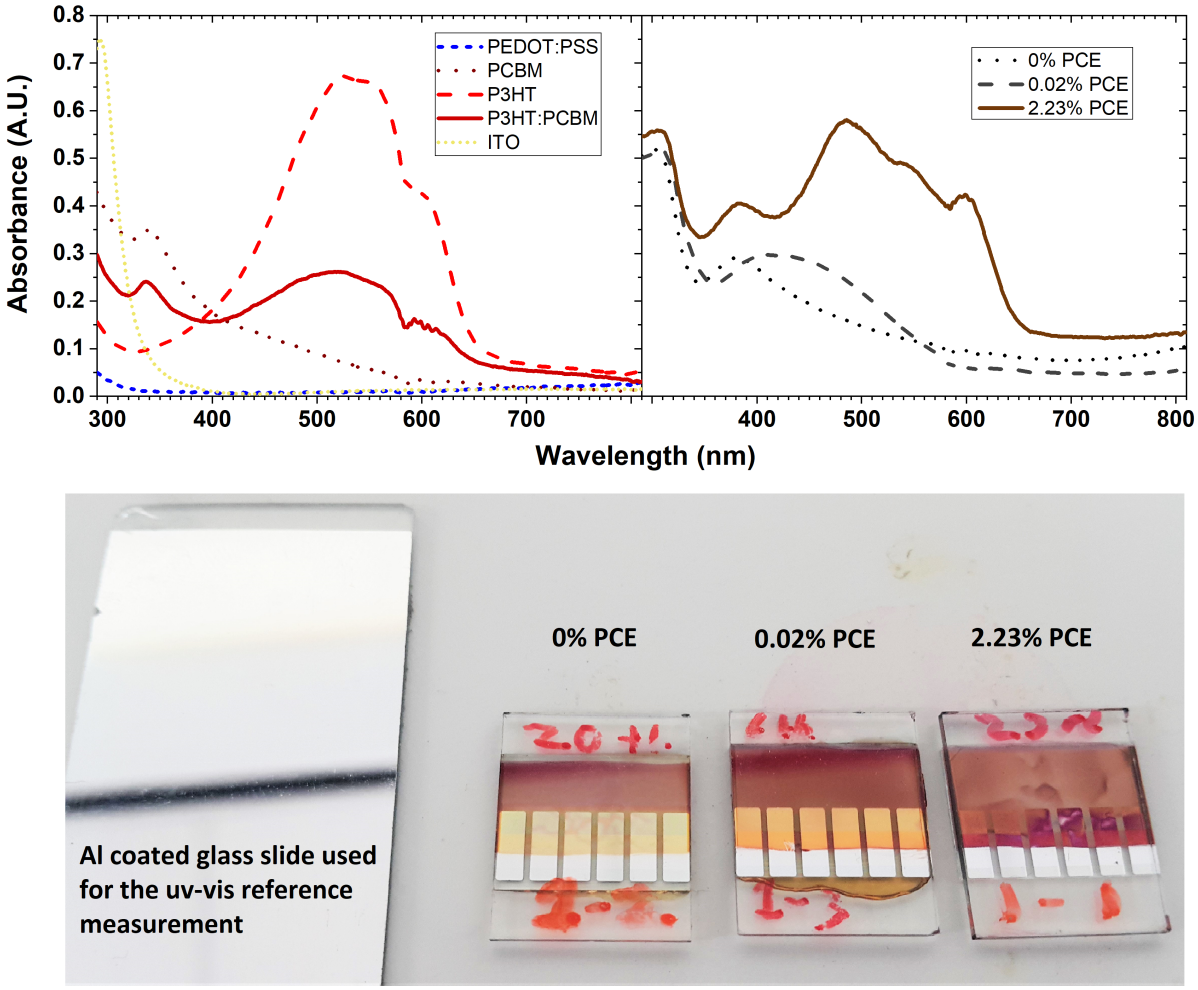

Figure 29: *Absorption spectra of different thin films (top left) and of the three types of devices (top right). The 0% PCE device (black, dotted line) and the 0.02% PCE (grey, dashed line) had their Al ECE deposited by e-beam evaporation, and the 2.23% PCE (brown, straight line) had its Al ECE deposited by thermal evaporation. At the bottom, a picture of the fabricated devices and the Al coated glass slide used as the reference measurement.*

The three P3HT peaks are indicative of crystallinity within the film, and are caused by the $\pi - \pi*$ transitions within the higher degree ordered chains that give regioregular P3HT its photoactive properties[219;220]. The absorbance spectrum of the 0.02% PCE e-beam evaporated device reveals that the λ=551 and λ=605 nm peaks have completely disappeared, and that the λ=485 nm peak has been significantly reduced and experienced a blue shift. This is caused due to significantly reduced $\pi - \pi*$ transitions which is indicative of a severe change in the ordering of the P3HT chains from a crystalline structure in which chains are close enough each other to allow $\pi - \pi*$ interactions by the absorption of light, to a more amorphous material in which the P3HT chains are

more disordered. This effect is even more pronounced in the absorption spectra of the 0% PCE device in which the three peaks have entirely disappeared. The reason behind the blue shift of the absorption peak in the amorphous material is that, in contrast to a crystalline material, it requires a higher energy light for the $\pi - \pi*$ transitions to occur due to the lack of a periodic structure that would otherwise allow such transition to be triggered with less energy. On the other hand, the reason behind the decreased intensity in the absorption peak of the amorphous material is the loss of the specific interchain spacing distance that corresponds to the particular wavelength absorbed. Given that the J_{sc} in devices depends strongly on the light absorption of the photoactive material, it is not surprising that the e-beam evaporated devices exhibit the poor performance shown in figure 28. Moreover, the disordered structure of the P3HT chains not only hinders charge generation due to the loss of optical absorption, but also the increase of recombination events due to the reduced charge transport. The origin of the damage is less clear, however, as mentioned above it is highly likely that the reaction between the Al and P3HT combined with the high-energy radiation produced by the high voltage electron beam are responsible for the degradation of P3HT. The latter is more likely to be the reason for the poor performance of e-beam evaporated Al devices given that good performing P3HT:PCBM solar cells have been reported by carefully controlling the rate of the evaporator which is dependant on its current-voltage settings[205–207]. However, as mentioned in the previous section, the voltage of the evaporator used was fixed to 10,000 V and unable to be modified. Furthermore, the high energy radiation produced as byproduct of core electron displacement can have sufficient energy to alter the molecular structure of conjugated polymers such as P3HT. It may be possible to reduce this damage by optimising the voltage-current settings of the e-beam evaporation to reduce the high energy radiation produced by the electron beam striking the source material. However, given that the e-beam evaporation procedure is significantly more time consuming (>12 additional hours to achieve the desired vacuum, and 1 additional hour to deposit the material) than the thermal evaporation procedure, and unavoidably damaging to the PAL, thermal evaporation was selected as the deposition method for the Al for the rest of the experimental work for this thesis. It is worth noting that the effects that the radiation produced by e-beam evaporation has on the absorption spectra of P3HT:PCBM layers is yet to be reported in literature, and thus, this work serves as an information source on

this phenomena for organic solar cell researchers.

4.3.3 Thermal evaporation on low bandgap donors based devices

As a final step to corroborate the effectiveness of the thermal evaporation procedure for fabricating standard performing organic solar cells, two additional types of devices were fabricated based on the low bandgap polymers PCDTBT and PBDB-T-SF. The fabrication process for the PCDTBT based devices has been described in section 4.2.4, however, the fabrication process for the PBDB-T-SF based devices was slightly different. The 8 Pixel substrates were used for the PBDB-T-SF based devices (figure 22b). After cleaning the substrates as described in section 4.2.3, PEDOT:PSS was spin-coated at 5000 RPM for 40 seconds and then two ∼6.75 mm deep stripes at the top and bottom were formed as shown by figure 30 (d and e) to allow the formation of the device circuit. The samples were then thermally annealed at 150 °C for 15 minutes and then left cooling to room temperature for 5 minutes. The samples were then transferred to a nitrogen filled glovebox where the active layer solution was spin-coated at 2000 RPM for 30 seconds. The top and bottom stripes were formed with a cotton swab damped in chlorobenzene and then the samples were thermally annealed at 120 °C for 10 minutes. A PFNBr solution was then spin-coated at 3000 RPM for 30 seconds to serve as an electron transport layer within the device (the top and bottom stripes were formed with a cotton swab damped in methanol). The samples were then loaded into an evaporation mask to define the ECE area (2 mm x 4.5 mm) and the mask was subsequently loaded into the thermal evaporator to deposit a 150 nm Al layer. Once the evaporation of Al was completed, the devices were encapsulated as described in section 4.2.4 and characterised.

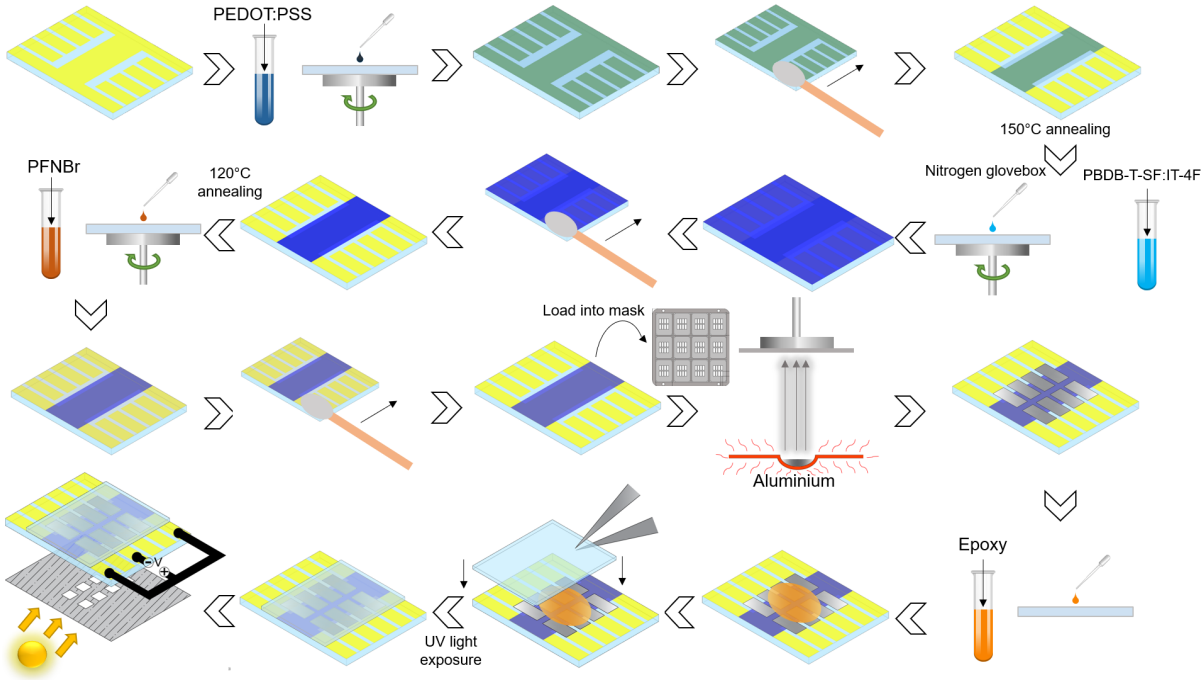

Figure 30: *Sketch showing the device fabrication procedure for the PBDB-T-SF:IT-4F based devices.*

The photovoltaic performances of the three types of devices fabricated in this thesis (P3HT, PCDTBT, and PBDB-T-SF) were compared to typical performances for similar device structures as reported in literature. Figure 31 and table 2 show the photovoltaic metrics for PCDTBT:$PC_{70}BM$ and PBDB-T-SF:IT-4F based devices.

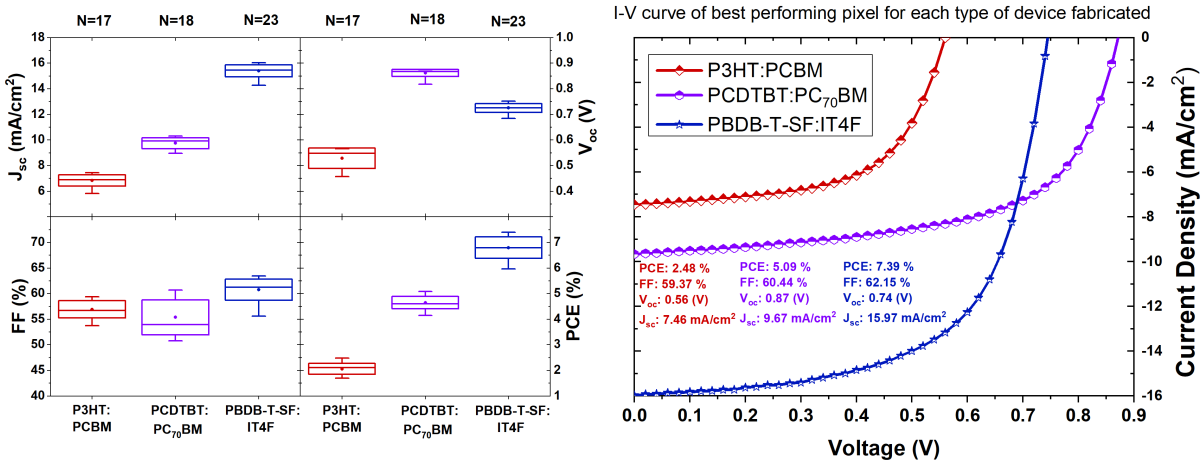

Figure 31: *Box plots (left) showing the Photovoltaic performance (short circuit current, open circuit voltage, fill factor, and power conversion efficiency) of P3HT:PCBM (dark red), PCDTBT:$PC_{70}BM$ (violet), and PBDB-T-SF:IT-4F (dark blue) based devices. N equals the number of measurements for each type of device, the width of the box represents one standard deviation on each side of the mean average value, the top and bottom ticks are the maximum and minimum values respectively, the horizontal line in the box is the median, and the circle in the middle of the box is the mean average value. The J-V curve (right) of each champion device is also shown for performance comparison.*

Table 2: *Photovoltaic performance metrics of P3HT:PCBM, PCDTBT:$PC_{70}BM$, and PBDB-T-SF:IT-4F based devices. The errors represent one standard deviation for 17, 18, and 23 different measurements of P3HT:PCBM, PCDTBT:$PC_{70}BM$, and PBDB-T-SF:IT-4F respectively.*

	Average				Maximum value			
	Jsc (mA/cm^2)	Voc (V)	FF (%)	PCE (%)	Jsc (mA/cm^2)	Voc (V)	FF (%)	PCE (%)
P3HT:PCBM	6.84±0.44	0.529±0.040	56.94±1.70	2.06±0.21	7.46	0.565	59.37	2.48
PCDTBT:$PC_{70}BM$	9.75±0.42	0.862±0.013	55.39± 3.41	4.65±0.24	10.32	0.874	60.71	5.09
PBDB-T-SF:IT-4F	15.41±0.47	0.725±0.017	60.76±2.08	6.80±0.42	16.03	0.751	63.43	7.39

In most literature, the average PCE of P3HT:PCBM devices fabricated with a similar structure and procedure as the one used in this thesis is between 2% and 2.5%[219;221–223]. This means that the average photovoltaic performance metrics reported in section 4.3.1 and table 2 are at the low end of the average performance reported in the literature. This can be attributed to other non-optimised fabrication steps that were eventually optimised for the work reported in subsequent chapters. Nevertheless, the average 2.06±0.21% and maximum 2.48% PCE values obtained for P3HT:PCBM based devices are well within the range of published standards. The PCDBTB:$PC_{70}BM$ based devices had average values of 4.65±0.24%, 55.39±3.41%, 0.862±0.013 V, and 9.75±0.42 mA cm^2 for PCE, FF, V_{oc}, and J_{sc} respectively. These values are in good agreement with those reported in literature for this type of structure which PCE ranges between 3.57% and 5.12%[224–227]. Moreover, the maximum PCE of 5.09% obtained here is near the upper range of 3.14% to 5.45% PCE reported in literature for structures that include an electron transport layer such as calcium[56;228;229] or lithium fluoride[210;227] for improved device performance. Both the P3HT and particularly the PCDTBT device metrics corroborate that the thermal evaporation procedure used in this work is effective for producing standard quality OSCs.

The PBDB-T-SF:IT-4F based devices had average values of 6.80±0.42%, 60.76 ±2.08%, 0.725±0.017 V, 15.41±0.47 mA cm^2 for PCE, FF, V_{oc}, and J_{sc} respectively. These values are significantly lower that the average values reported in the literature for this type of blend and device structure which PCE is above 13%[62;107]. The reason for the low photovoltaic performance obtained for this device structure is unclear, however, two factors are identified as the main possible causes for the poor photovoltaic peformance of

PBDB-T-SF:IT-4F based devices. Fist, the fabrication of this type of devices requires the use of a nitrogen glovebox in which the atmospheric conditions must be optimal for device fabrication (i.e. low O_2 and H_2O levels, and negligible solvent content in the nitrogen atmosphere) which at the time of the fabrication of these devices had not been optimised. Secondly, and most probably, the purity and quality of the donor and acceptor polymers are considerably lower when compared to the ones reported in literature. An impurity in PBDB-T-SF means that the chemical structure (as shown in figure 23) is slightly altered or that the monomers are not entirely linked in the same way or by the same elements. This idea was suggested during consultation by a member of the research group that originally synthesized both the PBDB-T-SF and IT-4F[62] used in these devices.

To discard the possibility that the annealing temperature or thickness of the active layer were responsible for the low performance of the PBDB-T-SF based devices, more devices were fabricated by varying these two parameters. Additionally, inverted structure PBDB-T-SF based devices were fabricated by substituting the two organic electron and hole transporting layers with the transparent metal oxides (TMOs) ZnO and MoO_3. In an inverted structure, the transparent ITO and ZnO function as the ECE and the ETL, and the MoO_3 and Al function as the HTL and the HCE. This was done to determine whether the charge transport materials were responsible for the low efficiency of the devices. In this case, the devices were fabricated as mentioned above, but instead of a PEDOT:PSS layer, a ZnO electron transport layer was deposited by spin-coating the precursor solution at 3000 RPM for 30 seconds (the top and bottom stripes were formed with a swab damped in IPA), and then subsequently annealed at 200°C for 60 minutes in air. Additionally, instead of spin-coating a PFNBr layer, the devices were put into the mask straight after the deposition and annealing of the PBDB-T-SF:IT4F layer, and a 10 nm MoO_3 hole transport layer was thermally evaporated at a rate of 0.2 Å s^{-1} before the deposition of Al, which in this inverted structured, functioned as the hole conducting electrode. The photovoltaic performances of all the PBDB-T-SF based devices mentioned above are shown in figures 32, 33 and 34, and in table 3.

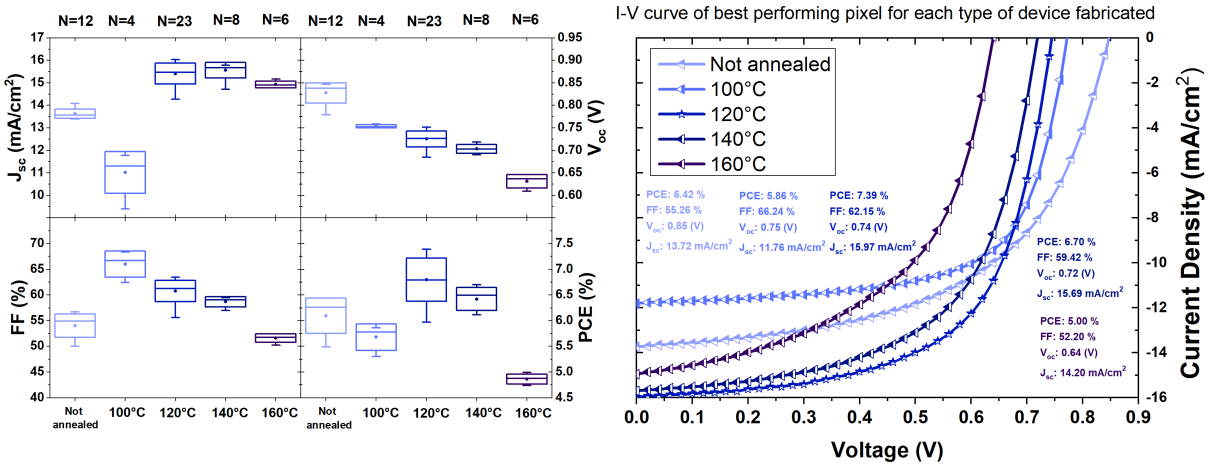

Figure 32: *Box plots (left) showing the Photovoltaic performance (short circuit current, open circuit voltage, fill factor, and power conversion efficiency) of PBDB-T-SF:IT-4F based devices with varying active layer annealing temperature. N equals the number of measurements for each type of device, the width of the box represents one standard deviation on each side of the mean average value, the top and bottom ticks are the maximum and minimum values respectively, the horizontal line in the box is the median, and the circle in the middle of the box is the mean average value. The J-V curve (right) of each champion device is also shown for performance comparison.*

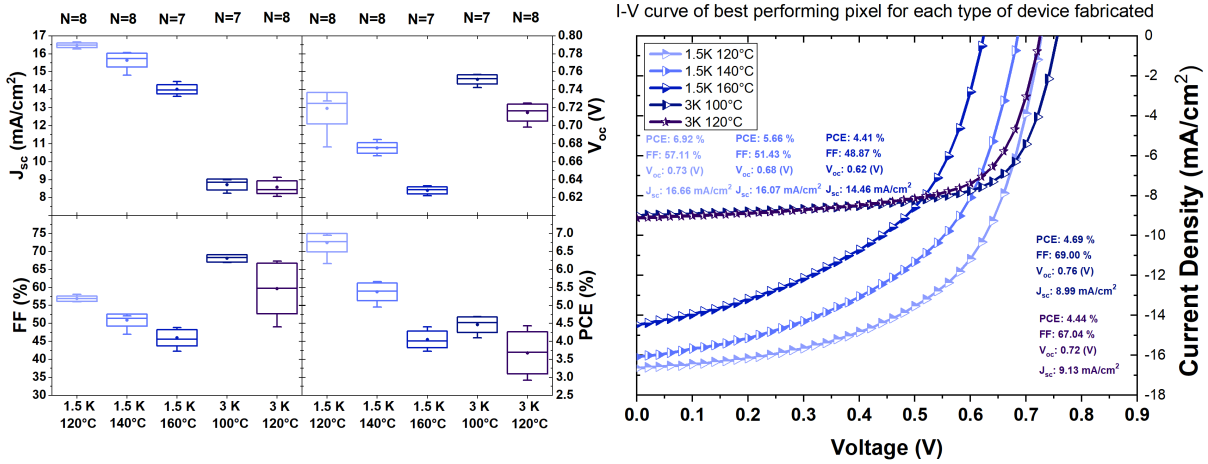

Figure 33: *Box plots (left) showing the Photovoltaic performance (short circuit current, open circuit voltage, fill factor, and power conversion efficiency) of PBDB-T-SF:IT-4F based devices with varying active layer spin speed and annealing temperature. N equals the number of measurements for each type of device, the width of the box represents one standard deviation on each side of the mean average value, the top and bottom ticks are the maximum and minimum values respectively, the horizontal line in the box is the median, and the circle in the middle of the box is the mean average value. The J-V curve (right) of each champion device is also shown for performance comparison.*

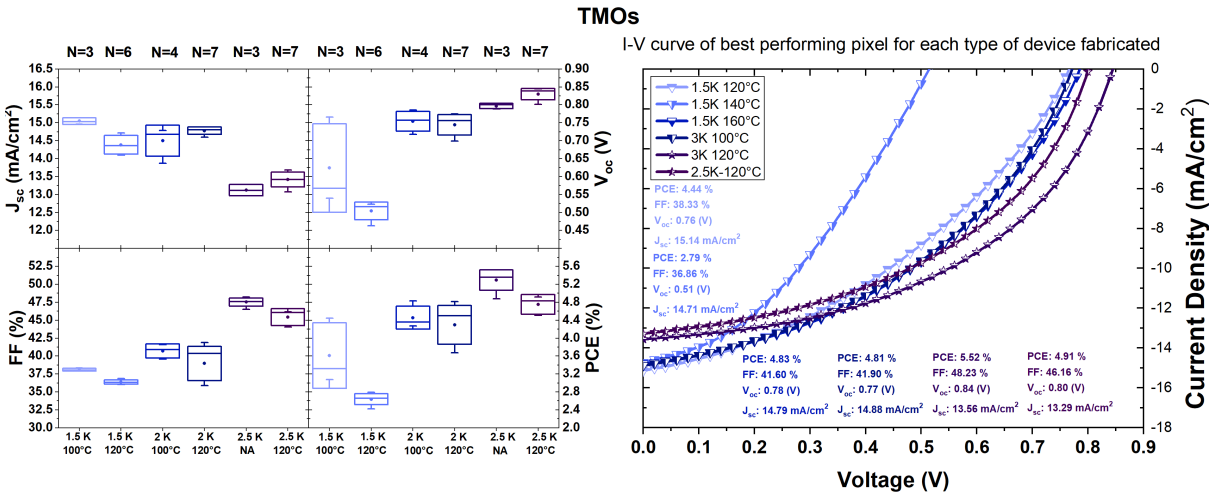

Figure 34: *Box plots (left) showing the Photovoltaic performance (short circuit current, open circuit voltage, fill factor, and power conversion efficiency) of PBDB-T-SF:IT-4F based devices fabricated with ZnO and MoO_3 as the electron and hole transporting layers respectively. N equals the number of measurements for each type of device, the width of the box represents one standard deviation on each side of the mean average value, the top and bottom ticks are the maximum and minimum values respectively, the horizontal line in the box is the median, and the circle in the middle of the box is the mean average value. The J-V curve (right) of each champion device is also shown for performance comparison.*

Table 3: *Photovoltaic performance metrics of PBDB-T-SF:IT-4F based devices fabricated with different spin speeds, annealing temperatures and charge transport layers. The errors represent one standard deviation for 'N' number of measurements.*

	Average				Maximum value				
	Jsc (mA/cm^2)	Voc (V)	FF (%)	PCE (%)	Jsc (mA/cm^2)	Voc (V)	FF (%)	PCE (%)	N
2K RPM, not annealed	13.63±0.20	0.828±0.023	54.04±2.28	6.10±0.34	14.08	0.847	56.70	6.44	12
2K RPM, 100°C	11.01±0.93	0.753±0.004	66.02±2.54	5.68±0.26	11.76	0.758	68.34	5.86	4
2K RPM, 120°C	15.41±0.47	0.725±0.017	60.76±2.08	6.80±0.42	16.03	0.751	63.43	7.39	23
2K RPM, 140°C	15.56±0.35	0.703±0.010	58.67±0.68	6.42±0.22	15.78	0.719	59.46	6.70	8
2K RPM, 160°C	14.93±0.16	0.631±0.015	51.61±0.80	4.86±0.10	15.17	0.646	52.43	5.00	6
1.5K RPM, 120°C	16.47±0.13	0.719±0.017	56.89±0.72	6.74±0.25	16.66	0.728	58.11	6.95	8
1.5K RPM, 140°C	15.64±0.39	0.675±0.006	50.92±1.65	5.38±0.24	16.07	0.685	52.15	5.66	8
1.5K RPM, 160°C	14.02±0.25	0.628±0.004	46.01±2.24	4.05±0.23	14.46	0.633	48.87	4.41	7
3K RPM, 100°C	8.72±0.30	0.751±0.005	68.10±1.01	4.47±0.22	8.99	0.757	69.10	4.69	7
3K RPM, 120°C	8.58±0.35	0.714±0.009	59.71±7.04	3.68±0.58	9.13	0.725	67.31	4.44	8
TMO, 1.5K RPM, 100°C	15.05±0.09	0.624±0.123	38.10±0.21	3.61±0.73	15.14	0.766	38.33	4.44	3
TMO, 1.5K RPM, 120°C	14.38±0.26	0.504±0.025	36.38±0.31	2.64±0.12	14.71	0.523	36.86	2.79	6
TMO, 2K RPM, 100°C	14.50±0.43	0.754±0.028	40.73±0.98	4.46±0.38	14.79	0.786	41.60	4.83	4
TMO, 2K RPM, 120°C	14.78±0.10	0.744±0.029	38.98±2.39	4.30±0.43	14.88	0.774	41.90	4.81	7
TMO, 2.5K RPM, not annealed	13.12±0.16	0.804±0.007	47.52±0.57	5.29±0.23	13.29	0.801	48.23	5.52	3
TMO, 2.5K RPM, 120°C	13.42±0.21	0.830±0.016	45.42±1.20	4.75±0.22	13.68	0.844	46.16	4.91	7

These results show that the best performing type of PBDB-T-SF based device is the one previously reported in figure 31 and table 2 which was thermally annealed at 120°C and spin-coated at 2000 RPM using PEDOT:PSS and PFNBr as the charge transport layers. Any other combination of annealing temperature and spin speed resulted in worse photovoltaic performance including the devices with ZnO and MoO_3 as charge transport layers. This indicates that the reason for the low performance of PBDB-T-SF base devices compared to the one reported in literature is not related to the annealing temperature or thickness of the active layer, or to the charge transport layers used. Moreover, the fact that the P3HT:PCBM and PCDTBT:$PC_{70}BM$ based devies fabricated in this section had performances comparable to those reported in literature for such structures, indicates that the evaporation process can be discarded as the reason behind the poor performance of PBDB-T-SF based devices. This supports the conjecture made before that relates the poor performance of PBDB-T-SF based devices to the nitrogen glovebox atmosphere quality or the purity of PBDB-T-SF and IT-4F. The evident next step to optimise this type of device is to purify both the glovebox and the blend materials, however, given that the focus of this thesis is not on PBDB-T-SF:IT-4F based devices, and that the effectiveness of the thermal evaporation step has been corroborated it was decided not to work on this type of blend any further.

4.4 Conclusions and next steps

Two vapour deposition techniques for the deposition of an Al electrode on organic solar cells were compared; thermal and electron beam evaporation. The e-beam evaporated P3HT:PCBM devices show significantly lower photovoltaic performance due to the loss of crystallinity of P3HT, highly likely to be caused by the high energy radiation byproduct of the high voltage electron beam striking the source material. This is reflected by the complete disappearance of the two vibronic peaks of the e-beam evaporated P3HT film at λ=551 nm and λ=605 nm, and the significantly reduced λ=605 nm peak which was also blueshifted. This results in poor J_{sc} and FF of the devices despite the increased V_{oc} which is believed to be caused by the formation of a P3HT-Al interlayer which work function favours the V_{oc}. The thermal evaporation procedure produced P3HT:PCBM and PCDTBT:$PC_{70}BM$ devices wtih photovoltaic performances within the standard range

repoted in literature confirming the effectiveness of the thermal evaporation process used for this thesis to produce standard quality organic solar cells. PBDB-T-SF:IT-4F devices had a performance lower than the standard reported in literature which is attributed to the quality of nitrogen glovebox atmosphere used, and the purity of the active layer blend materials. Given that standard quality photovoltaic devices were produced consistently it was possible to proceed to investigate methods to improve the photovoltaic performance and stability of OSCs which are discussed in the following chapters 5 and 6.

5 Doping PEDOT:PSS for improved conductivity and performance of devices

5.1 Introduction

Part of the research presented in this chapter has been published in the *ACS Applied Materials and Interfaces* journal[230], and reproduced with permission of the American Chemical Society according to section two, form A of the ACS Journal Publishing Agreement. The other part of this research has been accepted for publication in the *Journal of Surface Investigation: X-ray, Synchrotron and Neutron Techniques*.

The research presented in this chapter aims to improve the conductivity of PEDOT:PSS by doping it with a previously unreported zwitterion (used specifically to dope the PEDOT:PSS dispersion), and to determine some of its liquid and solid phase structural modifications induced by the dopant. It was expected that incorporation of enhaced conductivity PEDOT:PSS in OSCs would result in improved photovoltaic performance due to better charge transport from the active layer to the ECL. Particular focus was given to the determination of the structural changes that zwitterion doped PEDOT:PSS goes after doping to provide insight on the effects of dual-charge additives on PEDOT:PSS.

As mentioned in section 3.7.1 there are several assymetrically charged additives that are known to increase the conductivity of PEDOT:PSS improving its hole transport properties (see section 3.5). When the enhanced conductivity PEDOT:PSS is incorporated as an HTL in OSCs the photovoltaic performance of the device has been reported to improve. The increase in conductivity is normally attributed to the disruption of the coulombic interactions between PEDOT and PSS by the asymmetrically charged dopant[186;196–203] which is believed to promote phase separation of PEDOT and PSS resulting in a more ordered conducting network that facilitates improved charge transport when deposited as a thin film[196;199;203;204]. However, despite the extensive research done on the conductivity enhancement of PEDOT:PSS by the addition of dual-charge dopants, the precise mechanisms by which the conductivity is improved are still not completely

understood and can differ depending on the type of additive used[231;232]. The lack of understanding into the mechanisms of conductivity enhancement poses a major barrier in furthering PEDOT:PSS engineering and achieval of its optimal performance in OSCs and numerous other applications. To fully understand the improvement of the conductivity of doped PEDOT:PSS, it is paramount to determine the structural modifications that the dopant induces within the PEDOT:PSS morphology.

In this chapter, four previously unreported zwitterion dopants, 3-(4-tert-Butyl-1-pyridinio)-1-propanesulfonate (BUPIP), 3-(N,N-Dimethyloctylammonio)propanesulfonate (DOMAP), 3-(Decyldimethylammonio)propanesulfonate (DEMAP), and 3-(N,N-Dimethylmyristylammonio)propanesulfonate (DYMAP) were used to dope the PEDOT:PSS dispersion in different concentrations. The different doped dispersions were then processed as thin films and their sheet resistance measured. The most effective zwitterion (lowest doped PEDOT:PSS sheet resistance) and its effects on PEDOT:PSS were then investigated with small angle neutron scattering and neutron reflectivity. The doped PEDOT:PSS films were then incorporated into P3HT and PCDTBT based devices and their performance was analysed.

5.2 Experimental

5.2.1 Materials

BUPIP (≥98% purity by HPLC), DOMAP (CMC: 330 mM at 20-25 °C), DEMAP (CMC: 25-40 mM at 20-25 °C, 12,600 micellar average molecular weight) DYMAP (≥98% by TLC, CMC: 0.1-0.4 mM at 20-25 °C, 30,200 micellar average molecular weight), iron (III) sulfate hydrate (97%), deuterium oxide (99.9 atom % isotopic purity), ion exchange resins Amberlite IR-120 (hydrogen form, strongly acidic) and Lewatit MP-62 (free base, weakly basic) were all purchased from Sigma Aldrich. Sodium persulfate (≥98%) was purchased from ChemCruz Biochemicals while 3,4-Ethylenedioxythiophene (97%) was purchased from Alfa Aesar. Deuterated poly(styrene sulfonic acid) (d7, 33,800 Mn, 1.04 Mw/Mn) was purchased from Polymer Source and deionized water was obtained from a Purelab Flex 1 dispenser. PEDOT:PSS in aqueous dispersion (HTL Solar), for which the

solid content is between 1.0 and 1.2 wt% and the PEDOT to PSS ratio is 1:2.5, was purchased from Ossila. Menzel-Gläser microscope glass slides were used as substrates for the PEDOT:PSS:DYMAP films that were subject to four point probe (FPP) sheet resistance characterization, contact angle, and profilometry measurements. 425 μm P/Boron doped polished silicon wafers purchased from Si-Mat were used as the substrate for the films that were subject to ellipsometry and atomic force microscopy (AFM) measurements. Polished 4 mm thick circular silicon wafers (50 mm in diameter) were used to support the films that were characterized with NR and were purchased from Prolog Semicor Ltd. The details of all the materials used for device fabrication are described in section 4.2.1.

5.2.2 Films preparation

To prepare the different concentration zwitterion doped PEDOT:PSS dispersions, the required amount of zwitterion was weighed in a 4 mL amber vial and then 0.5 mL of filtered PEDOT:PSS (see section 4.2.3) was added to the vial. The doped PEDOT:PSS dispersions were then sonicated in an ultrasonic bath for 5 minutes before use.

For the sheet resistance, profilometry, and contact angle measurements, the dispersions were spin-coated (see section 4.2.4) at 4000 RPM for 40 seconds onto 25x12 mm cleaned (see section 4.2.3) glass substrates. The samples were then thermally annealed on a hot plate at 150°C for 15 minutes. For the sheet resistance and contact angle measurements, the samples were cooled down to room temperature for $\sim$ 20 minutes before measurement. For the profilometry measurements the samples were measured more than 24 hours after their preparation to allow them to reach equilibrium ambient water absorption. This was done in order to minimize ambient water absorption from the films during the measurements which could compromise the accuracy of the data.

For the ellipsometry and AFM measurements, the dispersions were spin-coated at 4000 RPM for 40 seconds onto 25x12 Si-Mat silicon wafers. The samples were then thermally annealed for 150°C for 15 minutes and subsequently cooled down to room temperature for $\sim$ 20 minutes before the measurement was taken.

For the neutron reflectivity measurements the dispersions were spin-coated at

4000 RPM for 40 seconds onto the 4 mm thick circular silicon wafers. The samples were then thermally annealed for 150°C for 15 minutes. The samples were measured more than 24 hours after their preparation to allow them to reach equilibrium ambient water absorption. This was done in order to minimize ambient water absorption from the films during the measurements which could compromise the accuracy of the data.

5.2.3 Sheet resistance and conductivity

The sheet resistance of films was measured using a four point probe (FPP) technique and a Keithley 2602 source measurement unit. In this technique, four linearly aligned tungsten probes of equal size and separated equidistantly are put into contact with the film. A current is then sourced between the two outer probes and the drop in voltage between the two inner probes is measured (see figure 35). The advantage of the FPP technique over the more conventional two probe resistivity measurements is that the FPP technique is significantly more accurate when measuring the resistance of a thin sheet. This is because the decreased voltage measured in the inner probes is caused exclusively by the resistance of the part of the sample that is located between the two inner probes, and not by the resistance of the wires or other components within the circuit of the measurement setup. This is due to the current entering through one of the outer probes, going through the sample, and exiting through the other outer probe without going into any of the inner probes. Therefore, the voltage drop at the two inner probes corresponds only to the current flowing within those probes where the only existing resistance in the current path is the sample. The sheet resistance can then be calculated with the following formula

$$\rho_{\square}(\frac{\Omega}{\square}) = \frac{\pi}{ln(2)} \cdot \frac{V}{I} \tag{17}$$

where I is the current, V is the voltage, and $\pi\ ln(2)^{-1}$ is 4.53. The result is given in Ohms $\square^{-1}$, a unit that represents the sheet resistance of a square of any dimension. If the thickness of the film t is less than half the space between probes s (condition which is met for the experiments in this research given that s= 2 mm and the

thickness of the film is in the order of tens of nanometers), the thickness of the film can be used to obtain the resistivity of the material by multiplying it by $\rho_{\square}$ 17

$$\rho = \rho_{\square} \cdot t \tag{18}$$

and finally the reciprocal of equation 18 can be obtained to calculate the conductivity described as

$$\sigma = \frac{1}{\rho} \tag{19}$$

.

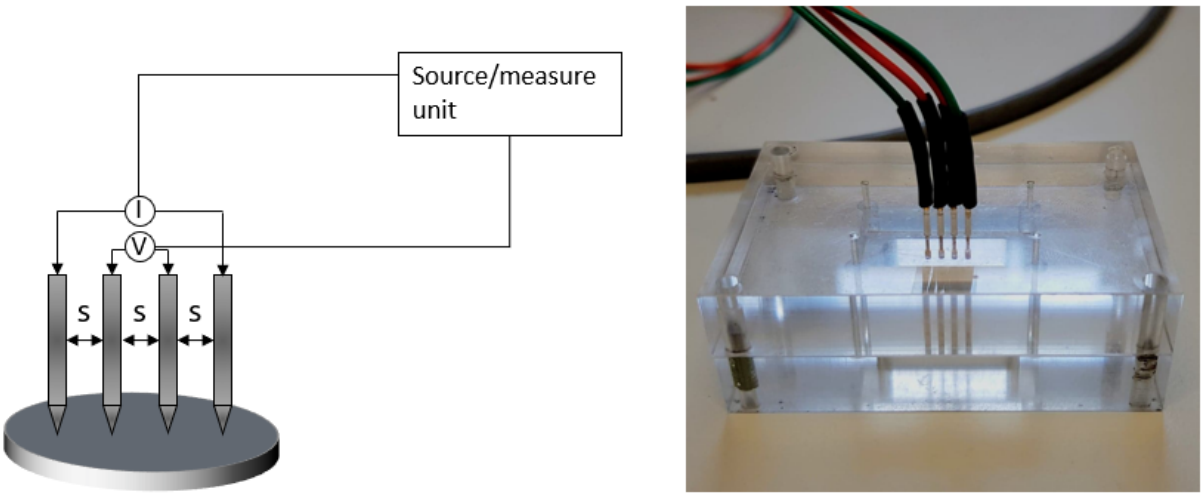

Figure 35: *Schematic representation of the four point probe measurement (left) and a picture of the four point probe kit used (right)*

To obtain the current and voltage characteristics of the films, a current from 1×10^{-7} to 1×10^{-6} A was swept between the outer probes in 10 intervals, measuring the voltage between the two inner probes for each step. This was done four times for each sample resulting in a total of 40 I-V combinations per sample.

5.2.4 Synthesis of PEDOT:deuterated-PSS

The motivation to synthetise PEDOT:d-PSS is presented in section 5.3.2. PEDOT:d-PSS was synthesised following the BAYTRON P synthesis method developed by Bayer AG as reported several times in literature[134;233;234]. The PEDOT:d-PSS dispersion was synthesised in a ∼34%-D_2O ∼66%-H_2O solvent which is SLD matched to the calculated PEDOT SLD of 1.80×10^{-6} Å^{-2}. First, 4.606 mL of D_2O and 9.884 mL of H_2O were mixed in a round bottomed flask and then 0.2 g of d-PSS, 61.7 mg of EDOT, 124.2 mg of $Na_2S_2O_8$, and 1.1 mg of $Fe(SO_4)_3$ were added to the flask. The specific EDOT and d-PSS amounts were chosen to obtain a PEDOT to d-PSS ratio of ∼1:2.5. The dispersion was stirred vigorously at 30 °C in an oil bath and under a condensing column for 7 hours. Then, 20.8 mg of $Na_2S_2O_8$ were added to the dispersion and stirred for a further 14 hours. When the synthesis was complete, 1 gram of each ion exchange resin was added to the flask and the dispersion was left stirring for 2 additional hours at room temperature. The dispersion was then filtered through a 0.5 mm mesh and an additional gram of each ion exchange resin was added to the filtered dispersion which was then stirred for 2 more hours. Finally, the PEDOT:d-PSS dispersion was filtered through the mesh again and a total of 5 mL of dispersion was collected and stored at 4 °C. The total solids content of the dispersion was ∼ 1.75 wt.% determined by gravimetric analysis.

5.2.5 Small angle neutron scattering

Small angle neutron scattering can provide information on the bulk properties at the nano-scale of materials such as size, inter-particle space and interactions, polydispersity, and structure amongst others. In this technique, a beam of neutrons is directed at the sample. The neutrons engage in elastic and inelastic interactions with the nuclei of the sample and are then scattered forming a specific scattering pattern on a detector, which is dependent on the above mentioned properties of the sample. The incident beam k_i and the scattered beam k_f vectors can be added to obtain the momentum transfer q of the neutron scattered. Small angle neutron scattering theory is based on one main assumption and one main approximation. The main assumption is that only elastic scattering occurs. This allows the momentum transfer to be related to wavelength (λ) of

the incident neutron beam, and the scattering angle (θ) as follows:

$$q = \frac{4\pi sin\theta}{\lambda} \tag{20}$$

which consequently makes it possible to control the momentum transfer by controlling the scattering angle and the wavelength through the experimental set up.

The main approximation is the small angle approximation ($\sin\theta \approx 0$). This makes it possible to relate inversely the momentum transfer to real space by the approximation:

$$q \approx \frac{2\pi}{d} \tag{21}$$

and thus the units of q are inverse distance.

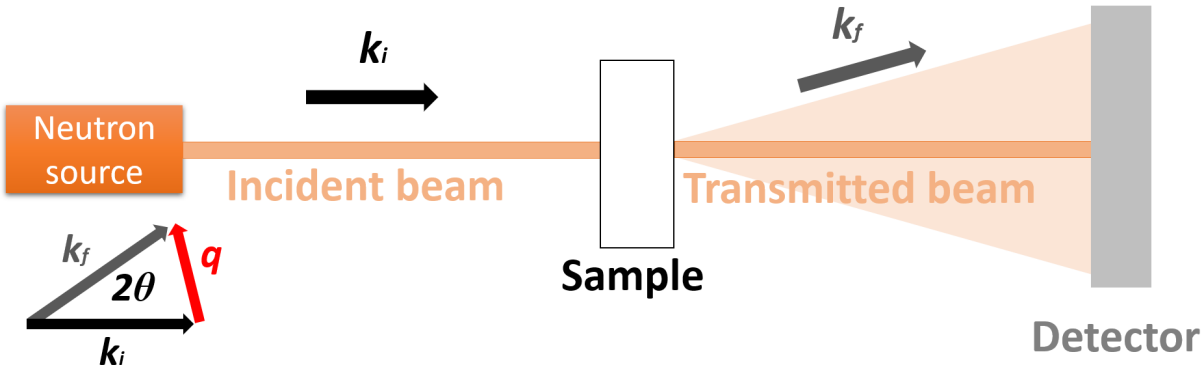

Figure 36: *Schematic representation of the small angle neutron scattering technique.*

The scattering intensity $I(q)$ is the key parameter that contains the information on the size, shape, and interactions between the scattering objects in the sample studied. $I(q)$ can, therefore, be modeled and the desired parameters extracted from the fitted model. For example, as will be explained in section 5.3.2, the function used to model the scattering intensity included a variable that describes the magnitude of the spacing between scattering objects. The function chosen to describe the $I(q)$ is then fitted to the scattering data using a fitting software to obtain the values of the variables

that describe the scattering intensity. One of the main advantages of using neutrons over other electromagnetic probe (such as X-rays) is the way that neutrons interact with the scattering object. Since the scattering of neutrons is dependant on the nuclear composition rather than the electron cloud of atoms, it is possible to use contrast matching to study molecules that are very similar in chemical composition to their surroundings. This can be achieved by deuterating part of the object of study or its environment so that significantly different scattering is obtained from the deuterated scatterers and the non-deuterated scattereres. This is due to the significant difference in coherent scattering lengths densities of hydrogen (-3.74×10^{-13} cm^{-1}) and deuterium (6.67×10^{-13} cm^{-1})[235].

For this chapter, the Small Angle Neutron Scattering (SANS) data was obtained using the LOQ small-angle diffractometer[236] at the ISIS Pulsed Neutron Source (STFC Rutherford Appleton Laboratory, Didcot, UK). A 10 mm diameter pulsed neutron beam modulated at 25 Hz with an incident wavelength range of 2.2 - 10.0 Å was directed through the samples to obtain scattering data within a q range of 0.008 - 0.254 Å^{-1}. The collected data were corrected for detector response and transmission of the sample using the Mantid data reduction software[237] to obtain absolute intensity vs momentum transfer 1D scattering plots. Scattering intensity data that had poor accuracy (evidenced by the wide error bars of each data point) was discarded. The reduced data was fitted with the Broad Peak model[238] using the SasView software[239]. The dispersions for the experiment were prepared by pouring 1 mL of PEDOT:d-PSS in a vial and then adding DYMAP powder in different amounts to obtain the desired concentration in millimolar units. The dispersions were stirred for 5 minutes and then loaded into cells (Hellma Macro-cuvette 404.000-QX 1mm thickness 404-2-46, Lab Unlimited) for neutron scattering measurements. The scattering length densities of PEDOT (1.80×10^{-6} Å^{-2}), d-PSS (4.18×10^{-6} Å^{-2}), DYMAP (4.67×10^{-8}) Å^{-2}, H_2O (-5.61×10^{-7} Å^{-2}), and D_2O (6.39×10^{-6} Å^{-2}) were calculated using the NIST Center for Neutron Research online database[240].

5.2.6 Thickness of the films

The thickness of the films for the calculation of conductivity was determined with ellipsometry. In this technique a beam of linearly polarised light at 45° is directed towards the

sample which reflects the light and changes its linear polarisation to an ellipsometric one. The reflected light, which contains information about the sample such as thickness and the refractive index, is then detected and analysed. The incident light, with its electric field oscillating parallel to the plane of incidence, is called p-polarised light, and the incident light with its electric field oscillating perpendicular to the place of incidence is called s-polarised light. These two beams are reflected differently and the complex reflectivity ratio between them can be defined as

$$\frac{R_p}{R_s} = tan(\Psi)e^{i\Delta} \tag{22}$$

where R_p is the reflected p-polarised light, R_s is the reflected s-polarised light, and $tan(\Psi)$ and Δ are the change in amplitude and phase shift upon reflection respectively. A graph of Ψ and Δ is then plotted as a function of wavelength and a model that includes the thickness of the film as a variable can then be fitted to determine the thickness. An J.A. Woollam Co. M-2000 ellipsometer with detector (charge-coupled devices, CCD camera) and a Cauchy model fitted in the CompleateEase software by J.A. Woolam were used for the thickness measurements.

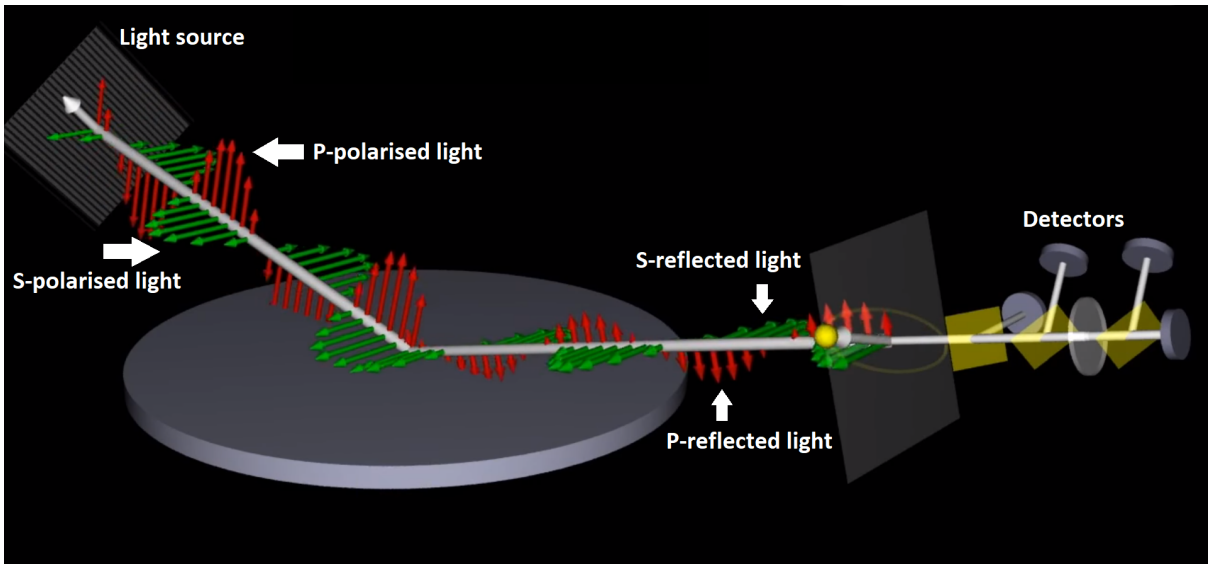

Figure 37: *Schematic representation of the ellipsometry technique. Image originally created by Film Sense (https://www.youtube.com/watch?v=BycPkRIutqg&t=180s).*

Film thickness, for comparison with the neutron reflectivity, data was measured

across a scratch in the film with a Bruker DektakXT stylus profilometer (12.5μm stylus radius) and the Vision64 software (0.33μm/pt scan resolution). For this technique a diamond stylus tip is placed on the the surface of the film and then swept along the surface to obtain information through the force feedback of the tip caused by the topography of the surface.

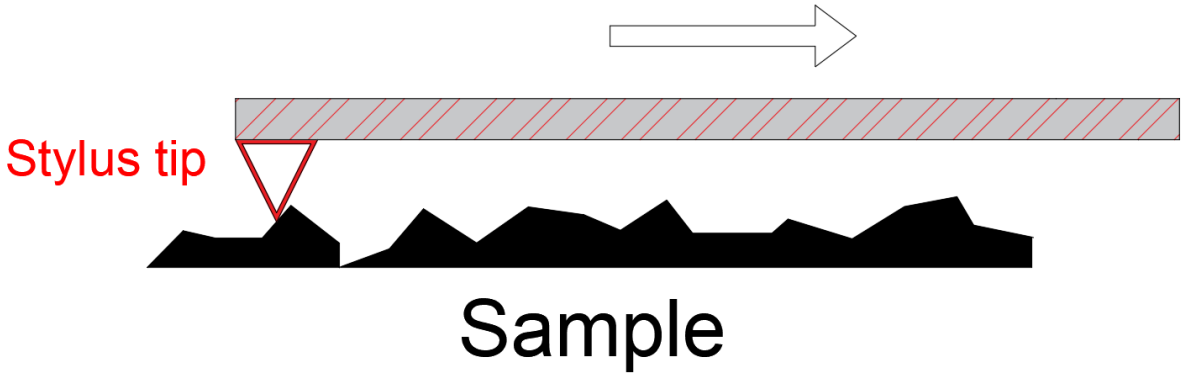

Figure 38: *Schematic representation of the profilometry technique.*

5.2.7 Neutron reflectivity

Neutron reflectivity is a technique that provides information normal to an extremely flat surface and therefore, it is ideal to determine the layered structure within a thin film. This is possible since each different stacked layer has a different scattering length density. In this technique a beam of neutrons is directed onto the sample and the intensity of the specular reflected beam R is measured as a function of the momentum transfer q which is defined in equation 20. Using the Born approximation[241], the specular reflection can be written as:

$$R(q) = \frac{16\pi}{q^2}|\rho(q)|^2 \tag{23}$$

where $\rho(q)$ is the one dimensional Fourier transform of the average scattering length density profile in the direction normal to the interface. Since the same reflection and refraction laws that apply to an electromagnetic wave apply to neutrons, $\rho(q)$ is related to other classical optic parameters such as the refractive index, and the thickness and roughness of the sample[242]. This makes it possible generate a scattering length

density profile of the sample as a function of height (which can be comprised of 1 or more distinct layers) by fitting the reflectivity profile to model that uses equation 23 and other classical optics mathematics. Consequentially, the roughness and thickness of the film can be set as fixed values (if known) of the model used to fit the data, and the scattering length density obtained.

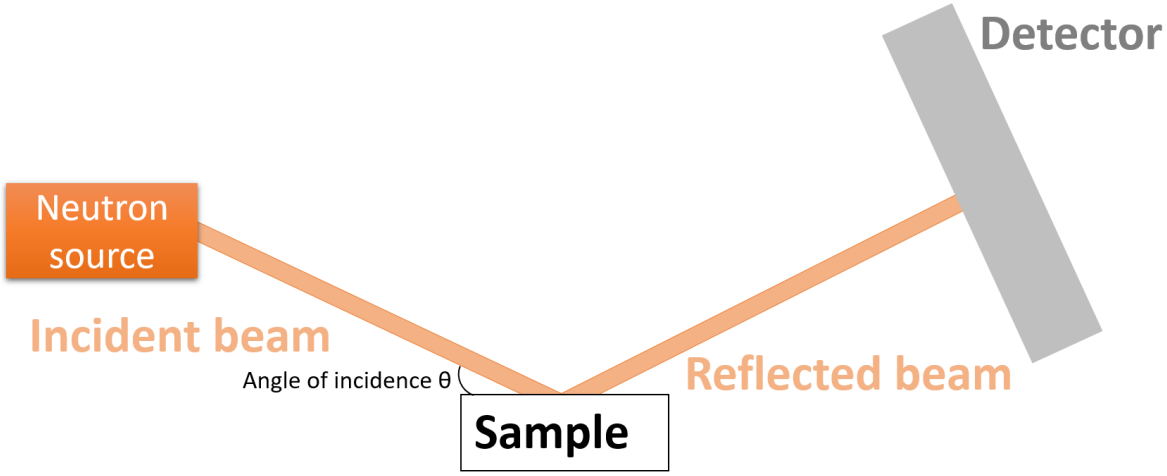

Figure 39: *Schematic representation of the neutron reflectivity technique.*

The neutron reflectivity data were obtained at the ISIS neutron and muon source (Oxfordshire, UK) using the OFFSPEC reflectometer, which has an incident neutron wavelength range from 1.5 Å to 14 Å. Reflectivity data were collected at three different angles (0.4° , 0.9°, and 2.3°) to cover the required momentum transfer range (0.08 to 0.25 $Å^{-1}$). The data were then analyzed with the software GenX using the soft nx model[243]

5.2.8 Atomic force microscopy

AFM images and roughness measurements were obtained with a Veeco Dimension 3100 AFM with a NanoScope IV controller and a TESPA-V2 cantilever (37N/m nominal stiffness and 320 kHz nominal resonance frequency) in 'tapping' mode. As profilometry, this technique provides surface information. However, the main difference is that the AFM tip interacts electrostatically rather than physically with the surface. The data capturing methodology is also slightly different. A laser is pointed towards the tip and is reflected

into a photodiode which feeds information to the detector. The tip is set to vibrate at a given frequency and the interaction of the tip with the surface of the sample causes the vibration frequency of the tip to change. Using specific calibration parameters, these changes in frequency allow the mapping of the surface probed by the tip. Compared to profilometry, this technique allows higher resolution at smaller scales up to the atomic scale, making it an ideal methodology to study nano-scopic surface characteristics such as roughness or phase differences.

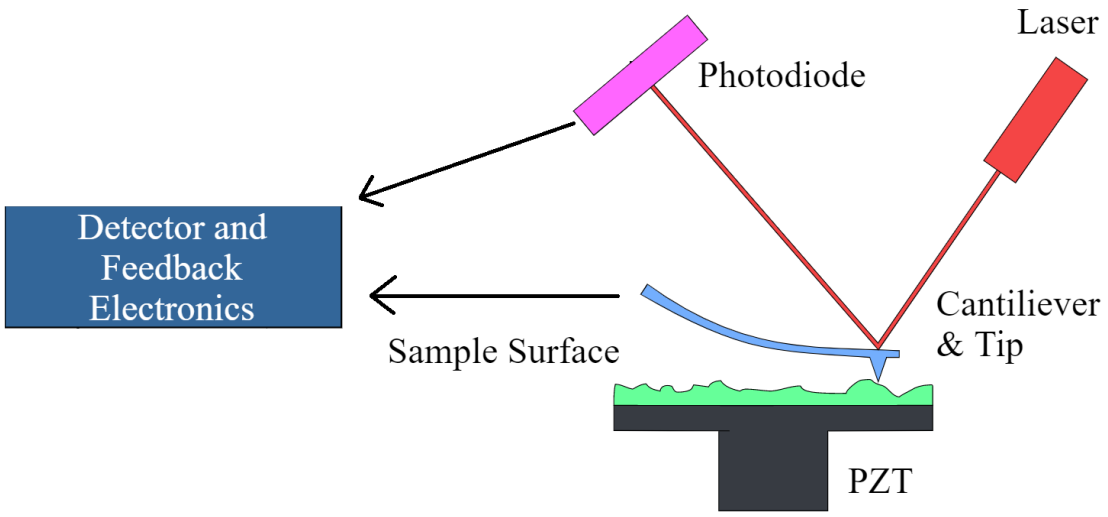

Figure 40: *Schematic representation of the atomic force microscopy technique. Image on originally created by OverlordQ (https://commons.wikimedia.org/wiki/File:Atomic_force_microscope_block_diagram.svg) andreproducedwithpermission.*

5.2.9 Contact angle

Contact angle values were obtained with a Theta Lite Basic kit and integrated software (accuracy of $\pm 0.1°$) from Nima (now Biolin Scientific). During this technique, a liquid drop of a known volume is placed on top of the sample and the angle between the edges of the droplet and the horizontal surface of the sample is measured to determine the wetting properties of the material respective to the liquid used. A high resolution camera is placed in front of the sample for accurate determination of the contact angles.

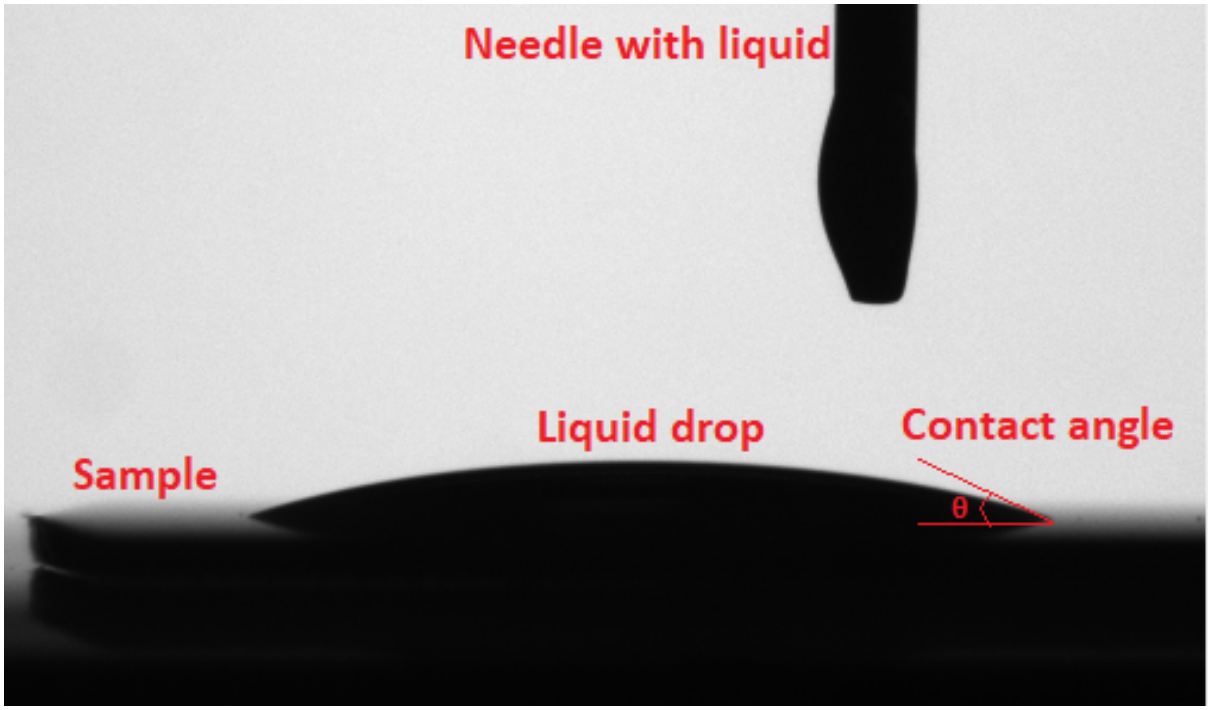

Figure 41: *Contact angle example picture.*

5.2.10 Device fabrication and characterisation

The P3HT:PCBM and PCDTBT:$PC_{70}BM$ based devices fabricated in this section followed the same process described in section 4.2.4. In this chapter, both the 6 pixel and the 8 pixel substrates were used for both types of devices. The photovoltaic performance of the devices was obtained as described in section 4.2.5.

5.3 Results and discussion

5.3.1 Zwitterion selection (S.R.)

To determine which zwitterion had the best potential to improve the conductivity of PEDOT:PSS, the sheet resistance of doped PEDOT:PSS films at different doping concentration of the four zwitterions was measured. The different zwitterions where chosen based on theif differing chemical structures. BUPIP is the only zwitterion selected with a pyridine in its structure, and DOMAP, DEMAP, and DYMAP have a non-polar carbon

chains of different length. However, all four zwitterions have their negative charge in a propanesulfonate group, and DOMAP, DEMAP, and DYMAP have their positive charge in a quaternary ammonium ion. These similarities ensure that electrostatic interactions between all the zwitterions and the PEDOT:PSS are as similar as possible, while the differences between them, could allow to determine if the differences in the non-polar tails of the surfactant molecules have influence on the effectiveness of the zwitterion to reduce the sheet resistance of the doped PEDOT:PSS films.

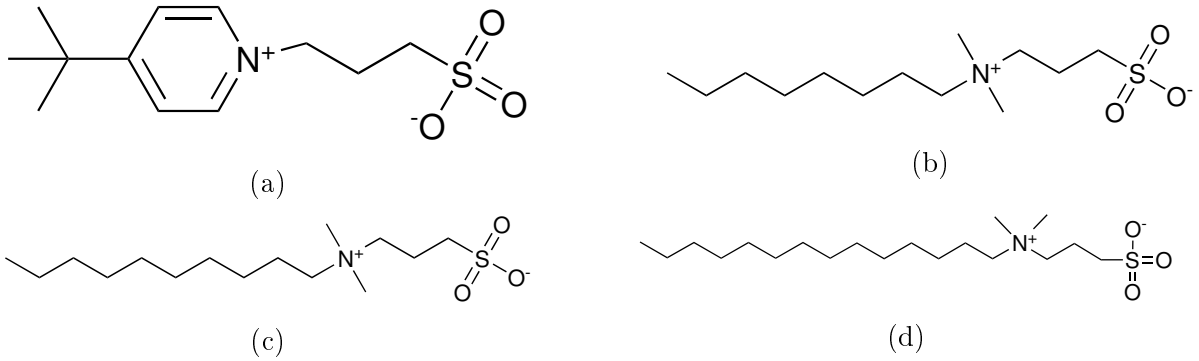

Figure 42: *Chemical structures of BUPIP (a), DOMAP (b), DEMAP (c), and DYMAP (d)*

A wide range of doping concentrations were explored by preparing 5, 10, 15, 20, 25, 30, 50, 70, and 100 mM doped PEDOT:PSS dispersions with each zwitterion. The dispersions were processed into thin films and their sheet resistance was measured and compared to the sheet resistance of a pristine PEDOT:PSS film. The results are shown by figure 43 (errors shown in the Appendices section in figure 77) and table 4. The pristine PEDOT:PSS film had a sheet resistance of 1.59±1.44 x 10^7 Ω □$^{-}$1 which was lower than any of the BUPIP doped PEDOT:PSS films (lowest sheet resistance was that of the 100 mM doped sample at 1.70±1.45 x 10^8 Ω □$^{-}$1). Moreover, the BUPIP doped dispersions showed gelation at 70 and 100 mM concentration which resulted in low quality thin films. Due to these results, BUPIP was discarded as an option to reduce the conductivity of PEDOT:PSS and was not investigated further. The sheet resistance of DOMAP and DEMAP doped films followed a similar trend in which their sheet resistance decreased significantly compared to the pristine film by three orders of magnitude at 50 (2.95±0.019 x 10^4 Ω □$^{-}$1) and 30 (9.67±0.041 x 10^4 Ω □$^{-}$1) mM respectively, and then continued to decrease less abruptly at further doping concentrations. The 50 mM DOMAP doped and 30 mM DEMAP doped dispersions however, exhibited gelation at those and higher

concentrations resulting in low quality thin films making them unsuitable to be used in devices. The 15 mM DYMAP doped PEDOT:PSS film had a sheet resistance of 2.37±0.933 x 10^6 Ω □$^{-}$1 which is one order of magnitude lower than that of the pristine film. Moreover, the sheet resistance of the DYMAP doped films continued to decrease to 3.14±2.74 x 10^5, 2.28±0.005 x 10^4, and 1.66±0.010 x 10^4 Ω □$^{-}$1 at 20, 25, and 30 mM doping concentration respectively. At 30 mM DYMAP doping concentration however, the dispersion exhibited slight gelation and resulted in a low quality thin film and therefore further doping concentrations were not investigated. Out of the four zwitterions tested, only DYMAP decreased the sheet resistance of PEDOT:PSS at doping concentrations that didn't result in the gelation of the dispersion.

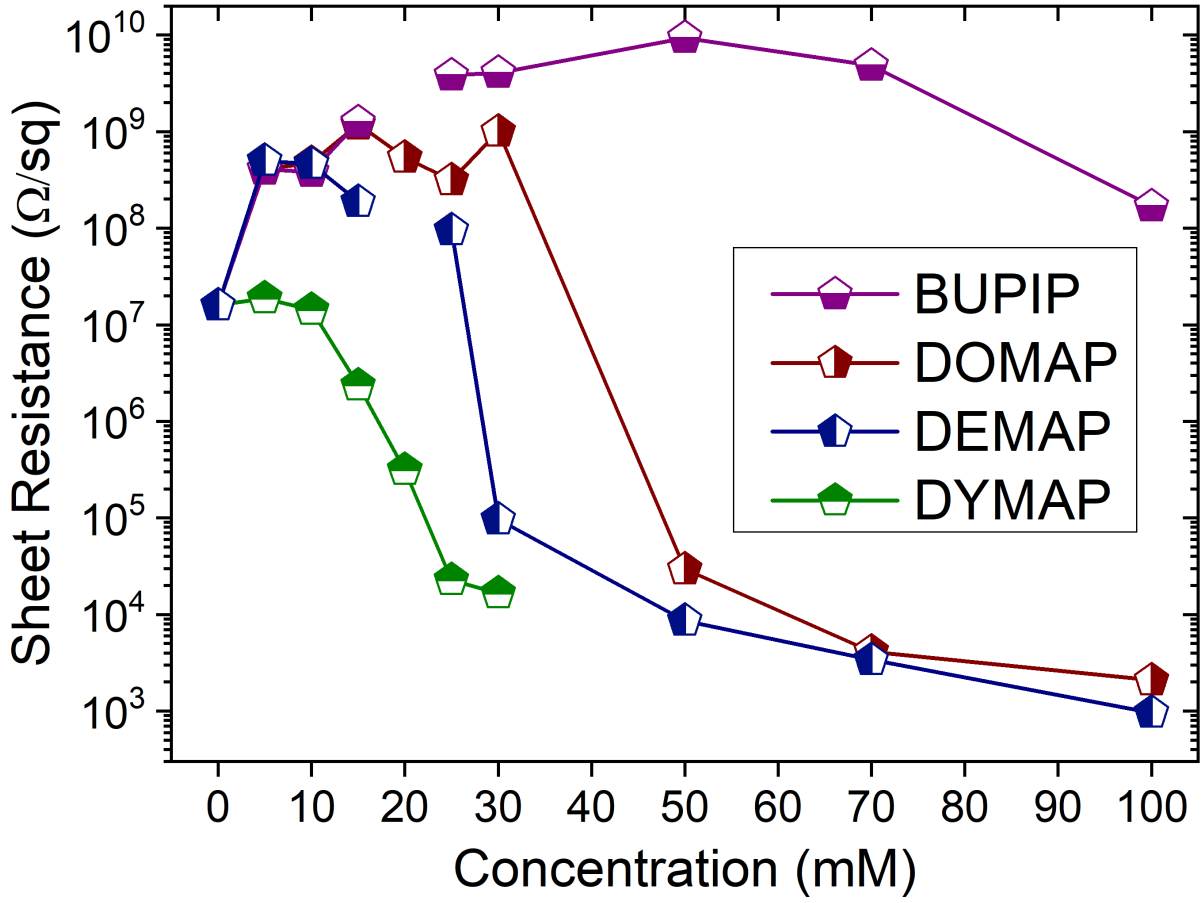

Figure 43: *Sheet resistance measurements of zwitterion doped PEDOT:PSS films as a function of the doping concentration.*

Figure 44: *PEDOT:PSS exhibiting high gelation.*

Table 4: *Sheet resistance values of the zwitterion doped PEDOT:PSS films at different concentrations. The error value represents one standard deviation. For the pristine PEDOT:PSS a total of 320 sheet resistance measurements were obtained. For all DOMAP, BUPIP, and DEMAP concentrations, a total of 40 sheet resistance values were obtained. For the 5, 10, 15, 20, 25, and 30 mM DYMAP doped samples a total of 40, 160, 80, 160, and 40 sheet resistance values respectively were obtained.*

Concentration (mM)	Sheet resistance (Ω $\square^{-1}$)			
	DYMAP	DOMAP	BUPIP	DEMAP
0	1.59±1.44 x 10^7	1.59±1.44 x 10^7	1.59±1.44 x 10^7	1.59±1.44 x 10^7
5	1.88±0.380 x 10^7	4.06±1.64 x 10^8	4.08±2.18 x 10^8	4.99±1.30 x 10^8
10	1.43±0.245 x 10^7	4.75±0.535 x 10^8	3.84±1.42 x 10^8	4.63±1.48 x 10^8
15	2.37±0.933 x 10^6	1.19±0.092 x 10^9	1.26±0.079 x 10^9	1.88±0.793 x 10^8
20	3.14±2.74 x 10^5	5.41±0.696 x 10^8	- - - - - - - - - - - -	- - - - - - - - - - - -
25	2.28±0.005 x 10^4	3.15±0.746 x 10^8	3.85±0.309 x 10^9	9.58±8.26 x 10^7
30	1.66±0.010 x 10^4	1.01±0.402 x 10^9	4.07±0.362 x 10^9	9.67±0.041 x 10^4
50	- - - - - - - - - - - -	2.95±0.019 x 10^4	9.36±0.834 x 10^9	8.60±0.052 x 10^3
70	- - - - - - - - - - - -	4.12±0.041 x 10^3	4.84±0.408 x 10^9	3.39±0.052 x 10^3
100	- - - - - - - - - - - -	2.09±0.056 x 10^3	1.70±1.45 x 10^8	9.60±0.167 x 10^2

Interestingly, all the 5 mM doped films exhibited an increase of sheet resistance relative to that of the pristine PEDOT:PSS sample. This effect was more significant for the 5 mM BUPIP (4.08±2.18 x 10^8 Ω $\square^{-}1$), DOMAP (4.06±1.64 x 10^8 Ω $\square^{-}1$), and DEMAP (4.99±1.30 x 10^8 Ω $\square^{-}1$) doped films than for the 5 mM DYMAP doped film (1.88±0.380 x 10^7 Ω $\square^{-}1$). This indicates that the addition of the dopants in small concentrations increase the resistivity of PEDOT:PSS. A possible explanation for this will be discussed in section 5.3.4, however, it is clear that the effectiveness of these zwitterionic dopants in improving the conductivity of PEDOT:PSS is dependant on the doping concentration used. The sheet resistance of the BUPIP doped films continued to increase as the concentration increased up to 70 mM, at which the sheet resistance

starts to decrease. This trend was shown only by BUPIP, and given that the main difference between BUPIP and the other three zwitterions is the pyridine in the BUPIP structure, it could be possible that the pyridine is responsible for this trend. A possbile explanation for the increased sheet resistance of the BUPIP doped films up to 50 mM dopinc concentration is that the pyridine ring makes the electrostatic interactions between BUPIP and PEDOT:PSS more difficult due to the bulkier and less flexible structure of BUPIP compared to the other zwitterions. The poor packing of BUPIP, caused by its bulk and in-flexible chemical structure, may disrupt the continuous PEDOT:PSS network resulting in trap sites when processed as a thin film, and thus increase the resistivity of the film.

Since the 70 and 100 mM BUPIP doped PEDOT:PSS dispersions exhibit gelation, it is highly likely that the dopant induces an increase of the viscosity of the solutions. Therefore, the decrease of sheet resistance of the respective films is likely to be due to a significant increase in the thickness of the film caused by the highly viscous and slightly gelated dispersion rather than a decrease of the resistivity of the material. This could also be the case for the 50 and 30 mM DOMAP and DEMAP doped films respectively, however, in such cases the decrease in sheet resistance is by 6 and 5 orders of magnitude respectively compared to the previous doping concentrations in each case. This could indicate that the films experience a decrease in resistivity as well as an increase in thickness due to the increased viscosity and gelation of the film. However, as mentioned before the poor quality of the films makes them unsuitable to be incorporated into devices and therefore were not investigated any further.

Since the sheet resistance of the 15, 20, and 25 mm DYMAP doped films was orders of magnitude lower than the sheet resistance of PEDOT:PSS, and such concentrations did not exhibit any gelation resulting in good quality films, it is highly likely the reduced sheet resistance is due to an improvement of the conductivity of DYMAP doped PEDOT:PSS. An interesting observation is that the effectiveness of the zwitterion in decreasing the sheet resistance of PEDOT:PSS appears to be dependant on the length of the non-polar tail of the molecule. As can be observed in figure 43, DOMAP, whose non-polar tail is of 8 carbons, needs to be incorporated at a higher concentration than DEMAP, whose non-polar tail is of 10 carbons, to significantly reduce the sheet

resistance of PEDOT:PSS. Furthermore, DYMAP, which non-polar tail is of 14 carbons, decreases the sheet resistance of PEDOT:PSS at a lower concentration than DEMAP and DOMAP. Due to the potential of DYMAP for improving the conductivity of PEDOT:PSS, DYMAP doped PEDOT:PSS was chosen to be thoroughly investigated and incorporated into devices.

5.3.2 Determining the structural modifications of the DYMAP doped PEDOT:PSS dispersion

Since DYMAP doped PEDOT:PSS showed promising results by exhibiting significantly lower sheet resistance compared to pristine PEDOT:PSS (figure 43) , the nano-scale structure of different concentration DYMAP doped PEDOT:PSS dispersions was studied. Small angle X-ray scattering has been used before to provide more insight on the nanoscopic behaviour of the widely studied dimethyl sulfoxide (DMSO)[244] and ethylene glycol (EG)[245] doped PEDOT:PSS while in dispersion. Following the specific changes that PEDOT and PSS go through separately has hitherto proven to be challenging due to their similar scattering length densities (SLDs). Tracking the morphological changes of PSS and PEDOT separately after doping is crucial to fully understand the origin of conductivity enhancement. Specifically, PSS is of particular interest since it is the major component of the PEDOT:PSS polymer mixture, enabling its solubility in water by countering the hydrophobicity of PEDOT[124;132]. Using neutrons instead of x-rays as the small angle scattering probe allows the labelling of a specific component within the studied system through deuteration. Therefore, by deuterating PSS (d-PSS) it is possible to obtain its individual scattering profile and thus track its changes in isolation from the rest of the system. Using this technique, Etampawala et al. successfully determined that the addition of DMSO to a PEDOT:d-PSS dispersion results in the re-organisation of excess d-PSS, significantly reducing the amount of d-PSS rich domains which contribute to the improved conductivity of PEDOT:d-PSS when spray coated into a thin film[232]. Murphy et al. also studied a PEDOT:d-PSS dispersion using small angle neutron scattering (SANS) to determine the effects of 1-ethyl-3-methylimidazolium tetracyanoborate (EMIM:TCB) on the d-PSS chains arrangement[246]. They found that the negatively charged d-PSS backbone segments are neutralised by the EMIM cation which appears to

improve the packing of the chains due to the screening of charge repulsion. Despite the insight provided by these reports, there is still a significant gap in the understanding of how other additives affect the PEDOT:PSS structural conformation. The different dopants used to improve the conductivity of PEDOT:PSS affect it differently according to the nature of the dopants requiring separate studies to achieve a complete understanding on the mechanisms of conductivity enhancement of PEDOT:PSS. For instance, zwitterions are surfactants that have proven to improve the conductivity of PEDOT:PSS and offer the advantage that their charges are fixed within the molecule so they do not migrate out of the doped PEDOT:PSS layer to other components of the device where PEDOT:PSS is used which can happen with ionic dopants[186;200;247]. However, surfactants behave quite differently to ionic liquids such as EMIM:TCB or polar solvents such as DMSO when dissolved in an aqueous solution which suggests that the structural modifications that they induce in PEDOT:PSS are also different. In this section, the changes that occur to the PSS moiety as DYMAP is added in different concentrations to the PEDOT:PSS dispersion was tracked using SANS and deuteration.

PEDOT and PSS have similar neutron SLDs of 1.80×10^{-6} Å^{-2} and 1.58×10^{-6} Å^{-2} respectively which makes it difficult to distinguish their scattering spectra from each other. Thus, if the solvent's SLD is contrast matched to PEDOT, the scattering signal from PSS would be lost in the background. However, d-PSS has an SLD of 4.18×10^{-6} Å^{-2} providing the necessary contrast with PEDOT to obtain a scattering signal from d-PSS when the solvent is contrast matched to PEDOT. Therefore, in order to study the change in structural conformations due to electrostatic interactions that PSS goes through after DYMAP doping, a PEDOT:d-PSS dispersion in a D_2O/H_2O solvent which SLD was matched to that of PEDOT was synthesised.

To study the effect that DYMAP has on d-PSS in a PEDOT:d-PSS dispersion, the small angle neutron scattering spectra of seven different DYMAP doped PEDOT:d-PSS dispersions were analysed . The seven different samples were pristine PEDOT:d-PSS, and 5 mM, 10 mM, 15 mM, 20 mM, 25 mM and 30 mM DYMAP doped PEDOT:d-PSS. Figure 45 shows the 1D SANS plot of all the samples where it can be immediately observed that the scattering intensity decreases as the DYMAP doping concentration increases. Given that the SLD of DYMAP is 4.67×10^{-8} Å^{-2}, the decreased intensity of

the doped dispersions can be attributed to the decreased scattering contrast caused by DYMAP which, by interacting with d-PSS, reduces its SLD corroborating that the two interact at a molecular level. It is worth noting that the SLD of DYMAP is closer to the SLD of the subtracted background (solvent matched to PEDOT) than to the SLD of d-PSS and hence, most of the scattering from DYMAP gets subtracted with the background during the data reduction process.

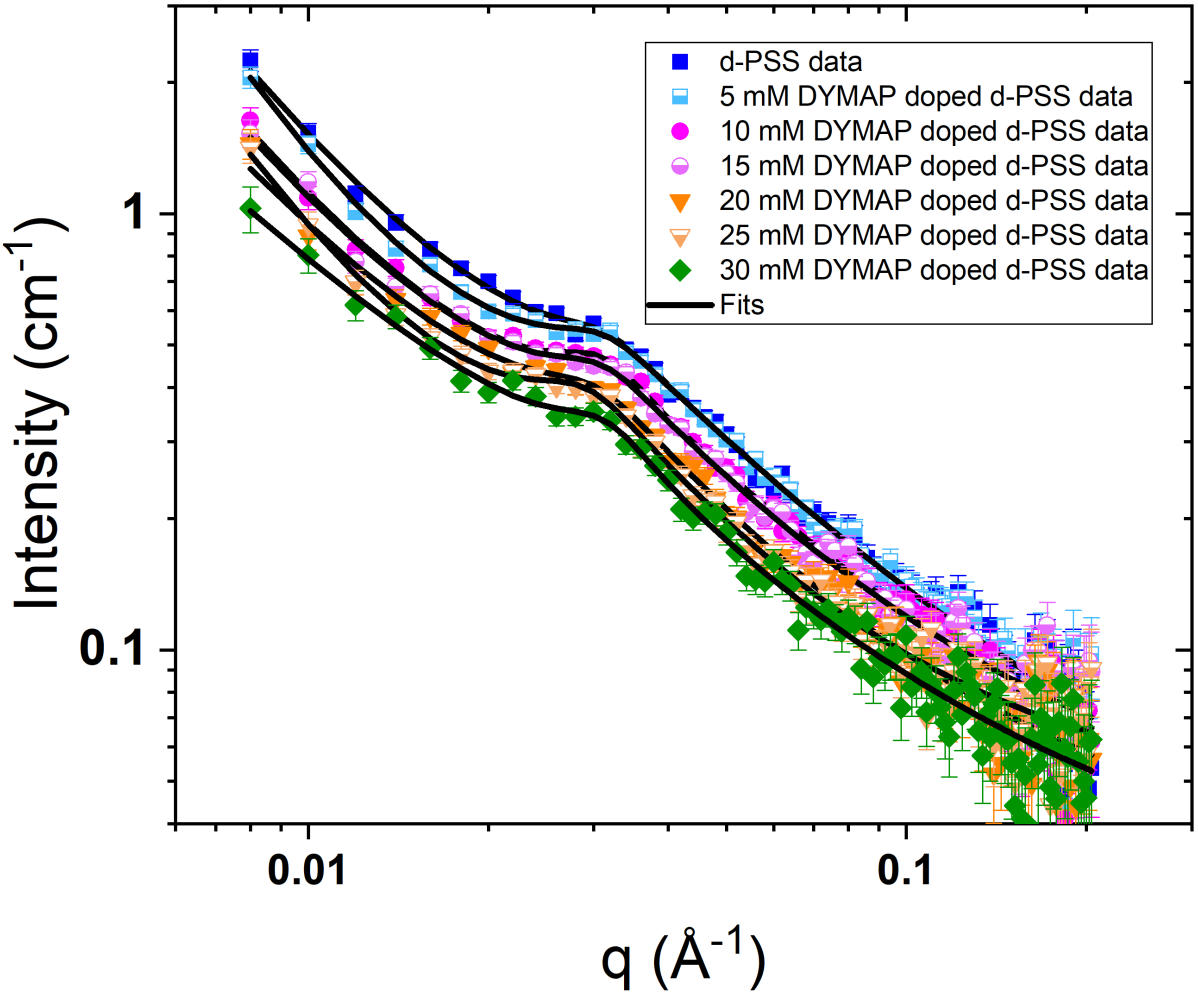

Figure 45: *1D SANS plots and corresponding fits (broad peak model) of pristine and different concentration DYMAP doped PEDOT:d-PSS. Samples were synthesised (and hence dispersed) in a solvent which SLD matches that of PEDOT to obtain information on d-PSS.*

In order to analyse the 1D scattering plots further, an empirical Broad Peak Model was fitted to the data. The model has been used before to fit neutral and charged polymer systems that exhibit electrostatic interactions, including PEDOT:PSS[246;248].

The model is described as

$$I_{(q)} = \frac{A}{q^n} + \frac{C}{1 + (\mid q - q_0 \mid \xi)^m} + B \tag{24}$$

where A/q^n is the low-q clustering term and $C/[1+(\mid q-q_0 \mid \xi)^m+B]$ is the high-q solvation term. More specifically, A is the Porod law scale factor, n the low-q scaling exponent, C the Lorentzian scale factor, m the high-q exponent, ξ the screening length, q_0 is the peak position, and B the q-independent background. Table 5 shows the resulting fitting parameters for each sample. The analysis focused on two particular parameters from the model, the peak position (q_0), and the screening length (ξ). Both parameters are in the high-q solvation term of the model function that describes the interactions between the scatterer and its surrounding environment at the nano scale. First, the peak position is analysed which has a finite value for charged systems and a negligible value for neutral systems[248]. Specifically, in polyelectrolyte systems this peak is characteristic, and is caused by the interchain[249–252] spacing between the charged segments that exist along the polymer chain[253]. This was corroborated for PEDOT:PSS by Murphy et al. who, by conducting a serial dilution SANS study of PEDOT:PSS, confirmed that the q_0 value is representative of the interchain distance between negatively charged rod-like PSS segments that are located along the PEDOT:PSS chain[246]. Therefore, for this experiment it can be safely assumed that q_0 corresponds to an average interchain distance of $2\pi/q_0$ Å between the negatively charged d-PSS segments along the chain backbones that are not attached to the PEDOT oligomers. As shown in table 5, the pristine d-PSS sample had a q_0 of 0.0310 Å^{-1} which corresponds to an average interchain distance between charged d-PSS segments of ≈202.7 Å. This value is similar to that reported by Murphy et al. of ≈196.4 Å [246].

Table 5: *Parameters resulting from the Broad Peak model fits of pristine and different concentration DYMAP doped PEDOT:d-PSS. Samples were synthesised (and hence dispersed) in a solvent which SLD matches that of PEDOT to obtain information on d-PSS.*

Doping concentration (mM)	ξ, Screening length (Å)	q_0, Peak position (Å^{-1})	A, Porod law scale factor	n, Low-q scaling exponent	C, Lorentzian scale factor	m, High-q scaling exponent	χ^2, quality of fit
Pristine	41.16±4.62	3.10±0.10 x 10^{-2}	8.56±4.98 x 10^{-4}	1.58±0.12	-0.35±0.04	-1.01±0.16	0.7603
5	41.40±2.98	3.08±0.08 x 10^{-2}	1.99±1.13 x 10^{-4}	1.86±0.12	-0.41±0.03	-1.05±0.12	0.7308
10	53.35±10.04	3.07±0.07 x 10^{-2}	6.30±4.26 x 10^{-4}	1.57±0.14	-0.37±0.05	-0.80±0.16	0.6080
15	53.84±8.77	3.06±0.09 x 10^{-2}	7.18±5.32 x 10^{-4}	1.53±0.16	-0.30±0.03	-1.04±0.16	0.9555
20	62.90±14.44	2.96±0.12 x 10^{-2}	1.26±1.19 x 10^{-3}	1.39±0.20	-0.22±0.05	-1.16±0.18	0.9005
25	64.81±10.88	2.85±0.09 x 10^{-2}	1.73±1.61 x 10^{-4}	1.80±0.20	-0.28±0.03	-1.11±0.17	0.7589
30	110.07±63.04	3.08±0.12 x 10^{-2}	3.12±3.26 x 10^{-3}	1.17±0.22	- 0.15±0.06	- 1.10±0.42	0.6465

As the DYMAP doping concentration increased, a negligible change in q_0 is initially observed. The q_0 of the 5 mM, 10 mM, and 15 mM doped samples were 0.0308 Å^{-1}, 0.0307 Å^{-1}, and 0.0306 Å^{-1} respectively. Figure 46 illustrates this change where it can be clearly seen that the peak position does not significantly change when DYMAP is added up to a 15 mM concentration indicating that the average interchain distance between the charged d-PSS segments is barely perturbed by the addition of DYMAP up to this doping concentration. However, at 20 mM and 25 mM doping concentration q_0 decreases more abruptly to 0.0296 Å^{-1} and 0.0285 Å^{-1} respectively resulting in the interchain distance between d-PSS charged segments being increased by ~ 7 Å with each of these increased concentration steps. Interestingly, at 30 mM doping concentration the q_0 shifts back to 0.0308 Å^{-1} which means that the average interchain distance between d-PSS charged segments decreases to 203.8 Å reverting back to the approximate same value of pristine PEDOT:d-PSS.

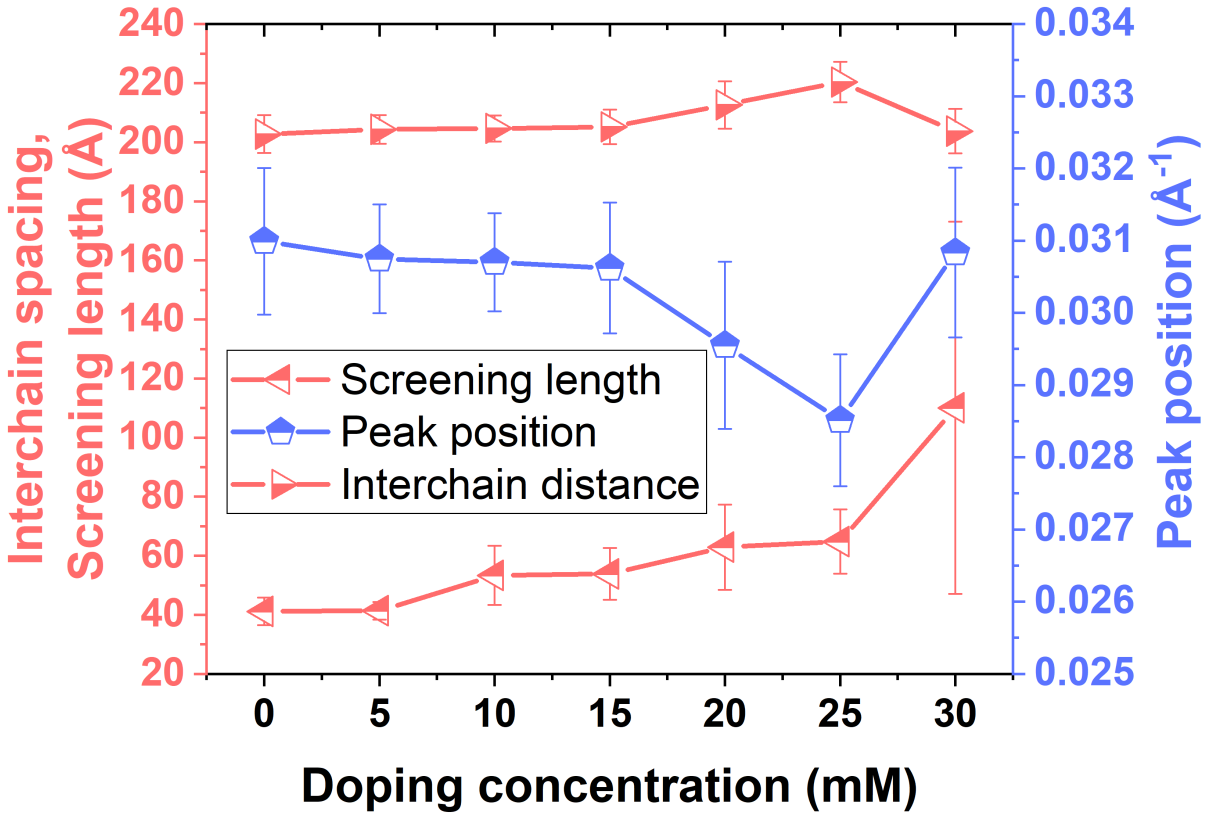

Figure 46: *Screening length, peak position, and interchain distance as a function of DYMAP doping concentration on PEDOT:d-PSS resulting from the Broad Peak model fits. Samples were synthesised (and hence dispersed) in a solvent which SLD matches that of PEDOT to obtain information on d-PSS.*

To understand the interchain distance change between the charged d-PSS segments induced by DYMAP, the behaviour of DYMAP alone in the same aqueous solvent that the PEDOT:d-PSS is dispersed in was separately studied. The 1D scattering plot of two 30 mM DYMAP aqueous solutions was obtained, one was in D_2O/H_2O SLD matched to d-PSS, and the other was in D_2O/H_2O SLD matched to PEDOT. Given that DYMAP is a surfactant it is highly likely that DYMAP forms micelles in polar solvents such as the one used in this study. To confirm this, the scattering data was analysed by fitting it to a spherical form factor[254;255]. The scattering intensity is then described by equation 25

$$I_{(q)} = \frac{scale}{V} \cdot \left[3V(\Delta\rho) \cdot \frac{sin(qr) - qrcos(qr)}{qr^3}\right]^2 + B \tag{25}$$

where *scale* is a volume fraction, V is the volume of the scatterer, r is the radius

of the sphere, $\Delta\rho$ is the difference between the SLDs of the scatterer and the solvent, and B is the background scattering. As shown in figure 47, the scattering profile of both solutions is very similar with the only clear difference being the intensity. As discussed before, this is due to the difference in contrast between DYMAP and each subtracted solvent. Since the SLD of DYMAP is 4.67×10^{-8} Å^{-2}, the solution with a D_2O/H_2O solvent matched to d-PSS (SLD is 4.18×10^{-6} Å^{-2}) has a higher contrast than the one in which DYMAP is dissolved in a D_2O/H_2O solvent matched to PEDOT (SLD 1.80×10^{-6} Å^{-2}). This results in a higher intensity scattering signal from DYMAP when it is in the d-PSS matched D_2O/H_2O solvent. More importantly, the sphere model fitted the data very well and resulted in a radius that was virtually the same for both samples. This was expected given that the scattering object, DYMAP, is the same in both solutions. As shown in table 6, the radius of the d-PSS matched sample was 25.7 Å and the radius of the PEDOT matched sample was 25.4 Å . The radii are in reasonable agreement with the theoretically estimated length of DYMAP (by adding up the standard values for every bond length in the backbone of DYMAP) which is $\sim$ 28 Å . This is strong evidence that DYMAP forms micelles in aqueous solvents. It is worth noting that the technical data sheet of DYMAP provided by the supplier states that the critical micelle concentration of DYMAP is 0.1-0.4 mM at 25°. This is further evidence that even the lowest DYMAP doping concentration used in this work results in the formation of micelles. Moreover, the molecular weight and the average micellar molecular weight of DYMAP are 363.6 and 30,200 respectively which means that, on average, there are ≈80 molecules of DYMAP per micelle.

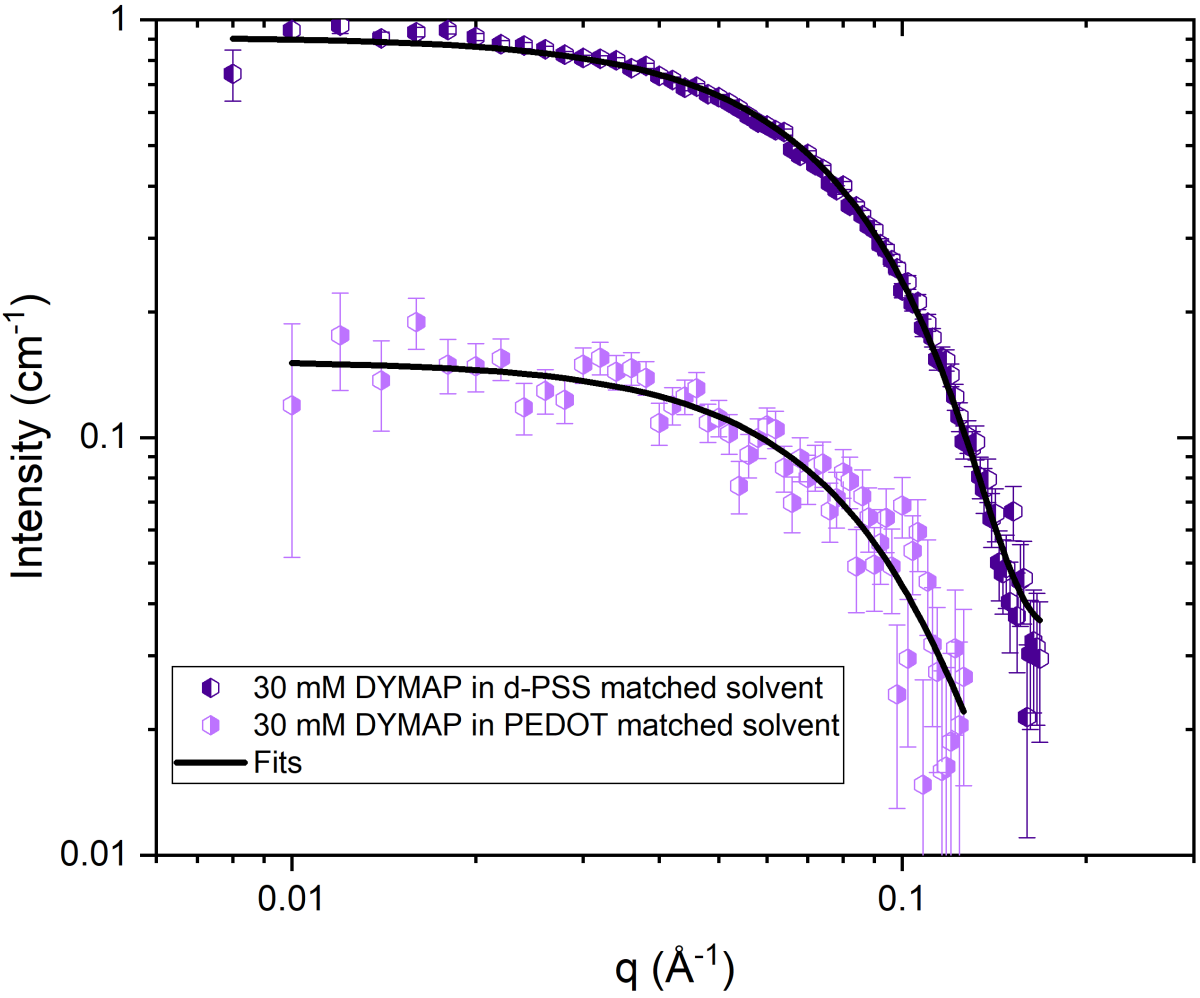

Figure 47: *1D SANS plots and corresponding fits (Sphere model) of 30 mM DYMAP aqueous solutions*

Table 6: *Parameters resulting from fitting the Sphere model to the 1D scattering plots of 30 mM DYMAP aqueous solutions.*

	DYMAP in solvent matched to d-PSS	DYMAP in solvent matched to PEDOT
Scale	7.20±0.10 x 10^{-3}	6.71±2.06 x 10^{-3}
Background (cm^{-1})	3.54±0.12 x 10^{-2}	1.03±0.21 x 10^{-2}
SLD DYMAP (1E-6 $Å^{-2}$)*	0.0467	0.0467
SLD Solvent (1E-6 $Å^{-2}$)*	4.18	1.80
Radius (Å)	25.68	25.43

* Calculated using the NIST Center for Neutron Research online database[240]

While, according to the evidence presented above, DYMAP forms spherical micelles in water, it is known that in the presence of additives with asymmetrically distributed charges such as salts, surfactant micelles in solutions can grow from spherical

objects to long worm-like micelles[256]. This phenomena is driven by thermodynamics and the length and number of worm-like micelles are dependant on the concentration of the additive which at very high concentrations results in gelation. Due to the polyelectrolyte nature of PEDOT:d-PSS it is proposed that a similar effect occurs to DYMAP in the presence of PEDOT:d-PSS. Such an effect could then also be responsible for the change in the interchain distance between charged d-PSS segments induced by the addition of DYMAP.

It is proposed that at low DYMAP doping concentrations from 5 mM to 15 mM, DYMAP starts to form short worm-like micelles in the presence of PEDOT:d-PSS. These worm-like micelles grow as more DYMAP is added, however, up to 15 mM they are significantly smaller than the interchain distance between the negatively charged d-PSS segments. Above 15 mM concentration, the DYMAP worm-like micelles grow long enough to start pushing the charged d-PSS chains apart due to steric hindrance. This effect is corroborated by the linear decrease of q_0 as a function of the dopant concentration above 15 mM which indicates that as the worm-like micelles grow longer with the addition of DYMAP, the charged d-PSS chains are proportionally pushed apart.

At 30 mM doping concentration the DYMAP worm-like micelles have grown long enough to overcome steric hindrance and attach to the negatively charged d-PSS segments. This can be attributed to the quaternary ammonium cation in DYMAP which gets coulombically attached to the negatively charged d-PSS segments. This effect, in which an asymmetrically charged dopant is attached by its positive charge to the negatively charged backbone PSS segments of PEDOT:PSS, has been widely reported in literature[186;196–203]. The coulombic interaction between the positive cation of DYMAP and the negatively charged d-PSS segment results in the relaxation of the backbone segments previously stressed by the steric hindrance caused by the growing DYMAP wormlike micelles.

The existence and growth of DYMAP worm-like micelles are further supported by the observed gelation of the PEDOT:PSS dispersion at 30 mM doping concentration which indicates that at this concentration the DYMAP worm-like micelles have grown long enough to bridge separate strands of d-PSS resulting in the cross-linking of the d-

PSS chains, and thus, the formation of a gel network. Figure 48 illustrates a schematic representation of the effects described above.

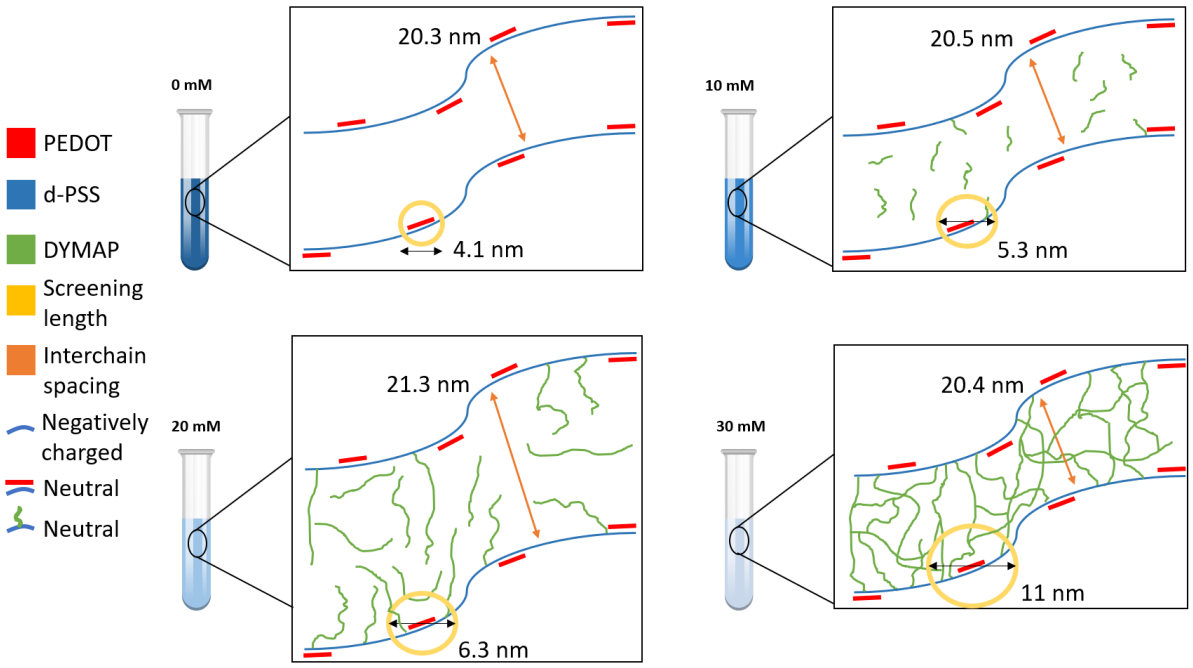

Figure 48: *Schematic representation of the behaviour of DYMAP and its effects on the PEDOT:d-PSS dispersion.*

Now, the screening length (ξ) is analysed. In semi-dilute solutions whereby a chain has been labelled with deuteration, the correlation length can be defined as the size of a blob where the chain does not interact with other chains[257]. For polyelectrolytes this can be interpreted as the average size of screening diameter caused by neutralised objects, which for PEDOT:d-PSS are the d-PSS neutralised chain segments that have the PEDOT oligomers attached along their length. The ξ of pristine d-PSS was 41.16 Å. Upon adding 5 mM DYMAP doping the screening length of the neutralised d-PSS chains stays virtually the same at 41.40 Å which indicates that this amount of DYMAP is insufficient to induce any alterations to the original ξ of neutralised d-PSS. At 10 mM and 15 mM doping concentration the ξ increases by $\sim$ 12 Å relative to pristine d-PSS, and further addition of DYMAP at 20 mM and 25 mM concentration the ξ increases to 62.90 Å and 64.81 Å respectively. Lastly, at the maximum doping concentration of 30 mM, the ξ increases considerably more to 110.07 Å , however the wide uncertainty ($\pm$63.04 Å) in this value makes it difficult to determine the magnitude of this increase. In order to explain the change in ξ as a function of DYMAP concentration, the focus is turned again

to the formation of worm-like micelles by DYMAP due to its surfactant characteristic. As mentioned above, this is an effect driven by thermodynamics since, in the presence of the charged PEDOT:d-PSS, forming worm-like micelles in between the d-PSS chains is probably the more energetically favourable action for DYMAP. However, when the micelles are in very close proximity to the negatively charged d-PSS backbone segments, the quaternary ammonium cation in DYMAP can be attracted to the negative charge in d-PSS, which results in the coulombic binding of DYMAP and the negatively charged d-PSS segments. Therefore, a possible explanation for the increased ξ as a function of the concentration then, is the slow gradual attachment of DYMAP micelles to the negatively attached d-PSS backbone as the concentration of DYMAP increases. While the formation of worm-like micelles is probably the primary and most energetically favourable action for DYMAP when introduced into the PEDOT:d-PSS dispersion, a lesser amount of DYMAP ends attaching to the negatively charged d-PSS backbone segments. This results in a low amount of DYMAP worm-like micelles growing from the d-PSS backbone some of which will grow long enough as more DYMAP is added to connect with other worm-like micelles formed either in other d-PSS backbones or in self-assembled worm-like micelles. More importantly, the slow attachment of DYMAP to the negatively charged d-PSS backbone segments results in the slight neutralisation of those segments which consequently results in the extension of the screening reach of d-PSS. It can be seen in figure 46, by the gradual increase in ξ, the slow and gradual attachment of a small amount of DYMAP particles as the concentration is increased. At 30 mM, however, this effect is increased significantly since the DYMAP fibril network is formed and the crosslinking induced by DYMAP produces a significantly increased ξ of the d-PSS segments.

5.3.3 Conductivity

Now that the nano-scale structure of the DYMAP doped PEDOT:PSS dispersions had been investigated, the thin film characteristics of the DYMAP doped PEDOT:PSS were studied. Since the 0 (pristine) and 5 mM, 10 and 15, and 20 and 25 mM, doped dispersions showed very similar liquid state structures (figure 46), only the 0, 10, and 20 mM DYMAP doped PEDOT:PSS films were selected to be investigated due to the limited experimental time available on the Offspec instrument. First, the conductivity of the

films was calculated using equations 18 and 19 with the sheet resistance values obtained in section 5.3.1 and the thickness values obtained with ellipsometry. The results shown in table 7 corroborate that DYMAP induces an increase of electrical conductivity of almost two orders of magnitude on PEDOT:PSS relative to the pristine sample. This, however, is only true when DYMAP is added at a 20 mM concentration.

Table 7: *Conductivities of pristine, 10, and 20 mM doped PEDOT:PSS as a function of doping concentration.*

Doping concentration	Conductivity (S cm^{-1})	Thickness (nm)
Pristine PEDOT:PSS	(2.2 ± 0.8) x 10^{-2}	38.43 ± 0.17
10 mM DYMAP doped PEDOT:PSS	(1.5 ± 0.3) x 10^{-2}	47.42 ± 0.28
20 mM DYMAP doped PEDOT:PSS	0.84 ± 0.40	62.68 ± 0.71

The results are interesting since it was expected that the conductivity would improve as the concentration of DYMAP in PEDOT:PSS increased, in line with other cases in literature in which PEDOT:PSS is doped with an asymmetrically charged dopant[188;196;201]. The conductivity of pristine PEDOT:PSS was (2.2 ± 0.8) x 10^{-2} S cm^{-1}, slightly higher than the 10 mM doped sample which had a conductivity of (1.5 ± 0.3) x 10^{-2} S cm^{-1}. However, when the doping concentration was further increased to 20 mM, the conductivity increased to 0.84 ± 0.40 S cm^{-1}, more than one order of magnitude higher compared to the pristine sample. As discussed in section 5.3.2, the screening length of the PSS backbone segments increases as more DYMAP is added (see figure 48) due to DYMAP neutralising the negatively charged PSS backbone segments. Such increased screening produced by the dopant has been argued in literature to enhance the hopping rate of charge carriers within the doped PEDOT:PSS when processed as a thin film[258;259] resulting in improved electrical conductivity. Additionally, the dramatic increase in conductivity from the 10 mM doped film to the 20 mM doped one could be indicative of a percolation threshold being crossed. Such effect is worth investigating in follow up studies.

The conductivity results imply that a significant conformational change in the morphology of PEDOT:PSS[132;186;204] is likely to be ocurring as the DYMAP doping concentration is increased from 10 mM to 20 mM. It could be possible that, as the worm-like DYMAP micelles start to from an interconnected network, the charge transport is facilitated through this network due to the dual charge of DYMAP resulting in the improved

conductivity of the highly doped films. Regardless, it is clear that the 20 mM thin film experiences a significant morphological change compared to the 10 mM thin film. Therefore, in the next section the vertical structure of the DYMAP doped PEDOT:PSS films will be investigated.

5.3.4 DYMAP distribution throughout the film

As discussed in section 5.3.3, DYMAP hinders the conductivity of PEDOT:PSS if it is added in low concentrations (i.e. 10 mM), but it is significantly increased when the DYMAP is added in higher concentrations (i.e. 20 mM). A similar effect was shown by two of the other three zwitterions tested in section 5.3.1 in which low concentrated DEMAP and DOMAP doped PEDOT:PSS films had an increased sheet resistance relative to the undoped PEDOT:PSS film, but higher doped films had a significant decreased sheet resistance. Such results indicate that the dopant affects the structure of the PEDOT:PSS films differently at different concentrations. To explain this phenomena, it is proposed that the distribution of DYMAP is not even throughout the film at low concentrations resulting in a more obstructive path for the flow of charges. However, at higher concentrations DYMAP is evenly distributed throughout the whole film providing a homogeneous pathway for charge carriers to flow with the beneficial characteristics discussed in sections 3.7.2 and 5.3.3 that result in the improved conductivity of the doped PEDOT:PSS film. Moreover, the possibility of a non uniform distribution of the additive within the deposited thin film has not been considered in literature, even though the separation of organic compounds within the bulk of a mixture is a common phenomenon during the preparation or the treatment of the film or the device that the film is part of[260;261]. In this section, neutron reflectivity was used to study the vertical structure of 0, 10, and 20 mM DYMAP doped PEDOT:PSS films to determine the distribution of DYMAP throughout the film at different doping concentrations.

Figure 49a shows the NR data for a pristine PEDOT:PSS sample and the model used to fit it. A stack consisting of three layers was required for the model (see figure 49b). From bottom to top these layers were silicon (Si) substrate, a silicon oxide (SiO_2) layer, and the PEDOT(1):PSS(2.5) film. For each layer three parameters were

considered in the model. These were thickness (D), root mean square roughness (σ_{RMS}), and scattering length density (SLD).

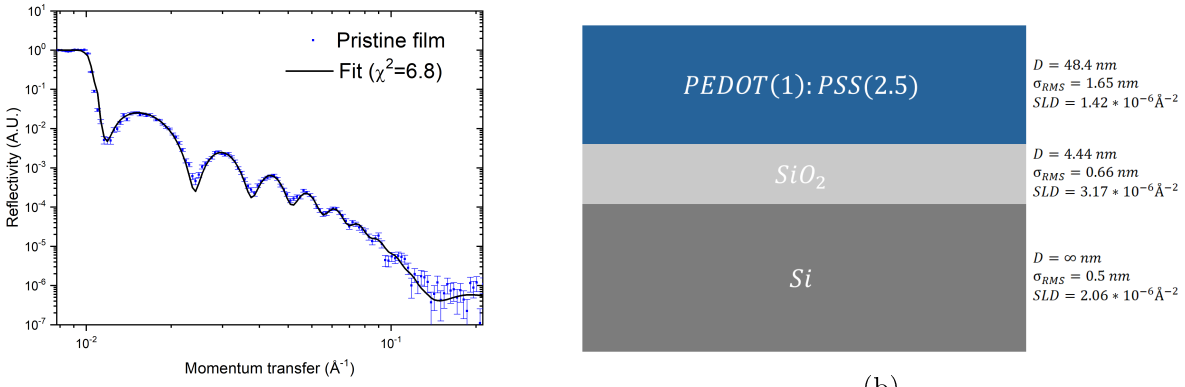

(a) (b)

Figure 49: *(a) Neutron reflectivity data for the pristine PEDOT:PSS film and its corresponding fit. (b) Sketch of the stack proposed for the model (not to scale) along with their respective fit values for thickness (D), root mean square roughness (σ_{RMS}), and scattering length density (SLD).*

The three parameters of the Si layer were fixed to 2.07×10^{-6} Å^{-2}, 5 Å, and ∞ for SLD, roughness, and thickness respectively. The parameters for the SiO_2 layer were all fitted. The thickness of the fitted layer was 4.44 nm. This is slightly high for a native oxide which typically has a thickness between 1 and 3 nm. In order to corroborate that the first modeled layer (one above the Si substrate) was a SiO_2, ellipsometry was conducted on the same sample that was measured with NR. This was done by removing the PEDOT:PSS from half the surface of the substrate with D.I. water and a cotton swab. Figure 50a shows the Psi and Delta values from the ellipsometry measurement along with their respective fits obtained by modelling a 5 nm thick oxidized layer on top of a Si layer. The relative similarity between the fits and the measured data suggests that the native oxide layer is $\approx$ 5 nm. To further corroborate that the 4.44 nm layer determined by NR is a native oxide of the silicon wafer, atomic force microscopy (AFM) was conducted on the same cleaned substrate to obtain the roughness of the surface. The measured σ_{RMS} by AFM was 0.92 ± 0.05 nm which is comparable to the 0.66 nm given by NR. In addition to this, the SLD of the NR fitted layer was 3.17×10^{-6} Å^{-2} which is in between the standard values for SiO (2.90×10^{-6} Å^{-2}) and SiO_2 (4.19×10^{-6} Å^{-2}). Given these results, it is proposed that the layer on top of the silicon substrate is a slightly thicker than expected oxide layer. The reason why this layer was thicker than would normally be expected is unclear, however a possible cause for this is that this particular

substrate came from a different batch of Si substrates that were cleaned with a different process (using a H_2O_2 solution) than the one described in section 5.2.2. To determine the reason for the abnormally high thickness of the SiO_2 more experimentation is needed, however, since such study deviates from the main purpose of this thesis, and it has been corroborated that the layer was a SiO_2 layer, it was decided not to investigate this matter any further.

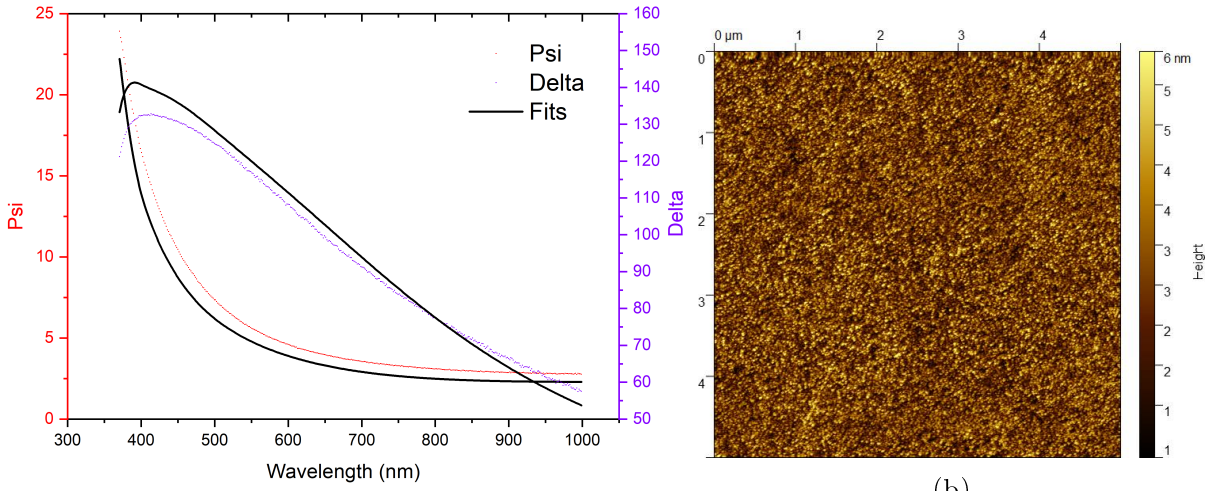

(a) (b)

Figure 50: Ellipsometry data and fits (a) and AFM height image (b) for the SiO_2 layer.

The NR simulation of the PEDOT:PSS layer resulted in a 48.4 nm thick PEDOT:PSS film which was as expected for the spin coating conditions used to deposit the polymer (4000 RPM, 40 s)[262], and is very similar to the 48 nm measured by the profilometer (see table 10). The root mean square roughness (σ_{RMS}) of the film according to the NR data was 1.65 nm which is similar to the 1.19 nm resulting σ_{RMS} from the AFM measurement conducted on the same film. The *SLD* for this particular PEDOT:PSS composition (1:2.5 ratio) was unknown so it was also fitted and the resulting value was 1.42×10^{-6} Å^{-2} which is very similar to the 1.68×10^{-6} Å^{-2} of the more conventional PEDOT:PSS formula (1:6 ratio) reported in the literature[263]. To further confirm the validity of this SLD value, the theoretical SLD values for the EDOT and PSS monomers were calculated using the NIST Center for Neutron Research online database[240]. The SLD values for the EDOT and the PSS monomers were 1.80×10^{-6} Å^{-2} and 1.57×10^{-6} Å^{-2} respectively. These values are slightly higher than the SLD value obtained from the fit. The decreased SLD of the PEDOT:PSS film can be attributed to the absorption

of ambient water by the samples. Since PEDOT:PSS is highly hygrocopic, the samples were measured more than 24 hours after their preparation to allow water absorption to equilibrium, and hence, stability of the film thickness. Therefore, given that the SLD of H_2O is -5.61×10^{-7} Å^{-2}, the presence of water molecules in the film results in the decreased overall SLD of the thin film.

In order to determine if there is a bi-layer structure within PEDOT:PSS:DYMAP after spin-coating, two different models were applied to the NR data of the 10 mM sample. Then, the probabilistic evidence of the two models was compared using χ^2 as the normal constant for both models to determine the most probable structure of films. As suggested by Sivia and Webster[264] a significant change in the probabilistic evidence is strong evidence that the model with the lowest normalistaion constant is the most accurate description for the structure that is being analyzed. Both models consisted of a 10 mM doped PEDOT:PSS film on top of a silicon substrate and a native oxide, however for one model the polymer film was split into two layers, and for the other model the polymer film was simulated as one homogeneous layer. Figure 51 shows the NR data of the 10 mM doped sample along the fits of the two models all plotted as reflectivity multiplied by the Fresnel decay of Q^4 (RQ^4) to emphasize the differences between models, as this representation allows for better appreciation of the quality of the fit[260]. When fitting with the first model, where the PEDOT:PSS was split into two layers, all three parameters (D, SLD, and σ_{RMS}) of the SiO_2 and the layer on top of the SiO_2 (bottom polymer layer) were allowed to be fitted. For the top polymer layer, only D and SLD were fitted and σ_{RMS} was constrained between the minimum and maximum values obtained by AFM (see table 10, and section 5.3.5). According to the best fit achieved, the SiO_2 layer was 2.15 nm thick and had an σ_{RMS} of 1.01 nm, both within the common known ranges of a native oxide layer. The SLD was 3.15×10^{-6} Å^{-2} which is similar to the well known value of 3.47×10^{-6} Å^{-2} reported in literature[265–267], confirming that this layer is a native oxide. Out of the two models used, the bi-layer model had the best fit with a χ^2 of 2.95. The second model considered only one homogeneous PEDOT:PSS layer (similar to the one used to model the pristine sample) and fitted the SLD and D for this homogeneous layer along with the three parameters of the SiO_2 layer. The σ_{RMS} fitting of the PEDOT:PSS layer was again constrained to the AFM minimum and maximum

values just as for the two layer model. The SiO_2 layer obtained with this model had an SLD of 3.6×10^{-6} Å^{-2}, was 2.3 nm thick, and had a σ_{RMS} of 1.7 nm. This model had a χ^2 of 3.6 which is 22% larger (worse) than the χ^2 of the 2 layer model. This improvement in the quality of the fit strongly suggests that the NR data of the 10 mM doped sample are best interpreted by assuming a separation of layers within the polymer film which would confirm the hypothesis described at the begining of this section.

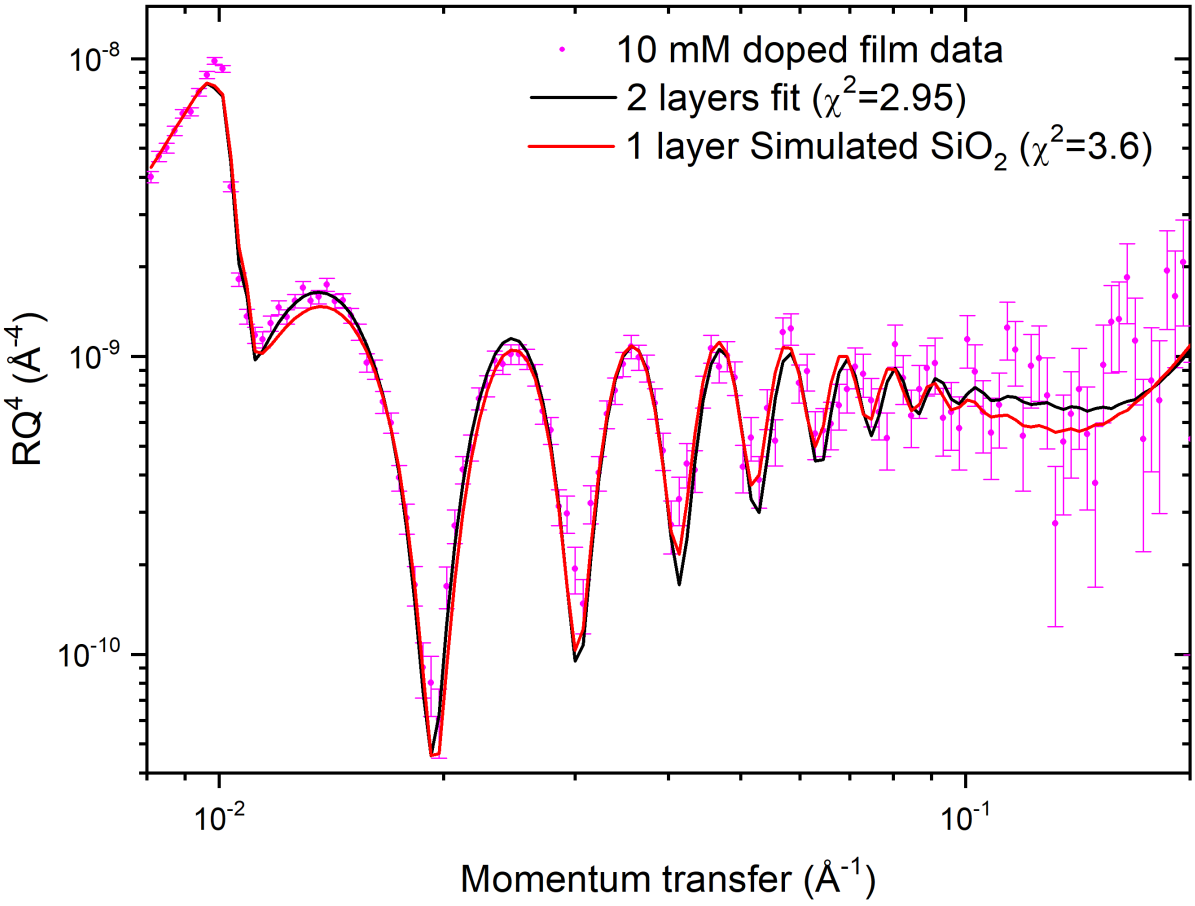

Figure 51: *Neutron reflectivity plotted as RQ^4 data for the 10 mM film and its corresponding fits using the two layer model (black) and the one layer model (red) both under same simulation conditions. The χ^2 values of each fit are shown for comparison evidencing a 22% improvement from the 1 layer model to the 2 layer model.*

The 20 mM doped sample was analyzed in the same way to investigate if this separation continues to occur as the doping concentration increases. The same types of models were applied to the 20 mM doped sample NR data, however, the results were different for this sample showing negligible improvement in the quality of the fit from the one layer model to the two layer model (see figure 52) with their χ^2 being almost identical (1.93 and 1.92 respectively). This suggests that for a doping level of 20 mM, the resulting

film is a homogeneous mixed layer. The comparisons between the χ^2 of both models for the 10 mM and 20 mM are interesting as they suggest that at a lower level of DYMAP doping (10 mM), the PEDOT:PSS:DYMAP deposited film separates into two layers, but forms a homogeneous layer when the amount of zwitterion is increased (20 mM).

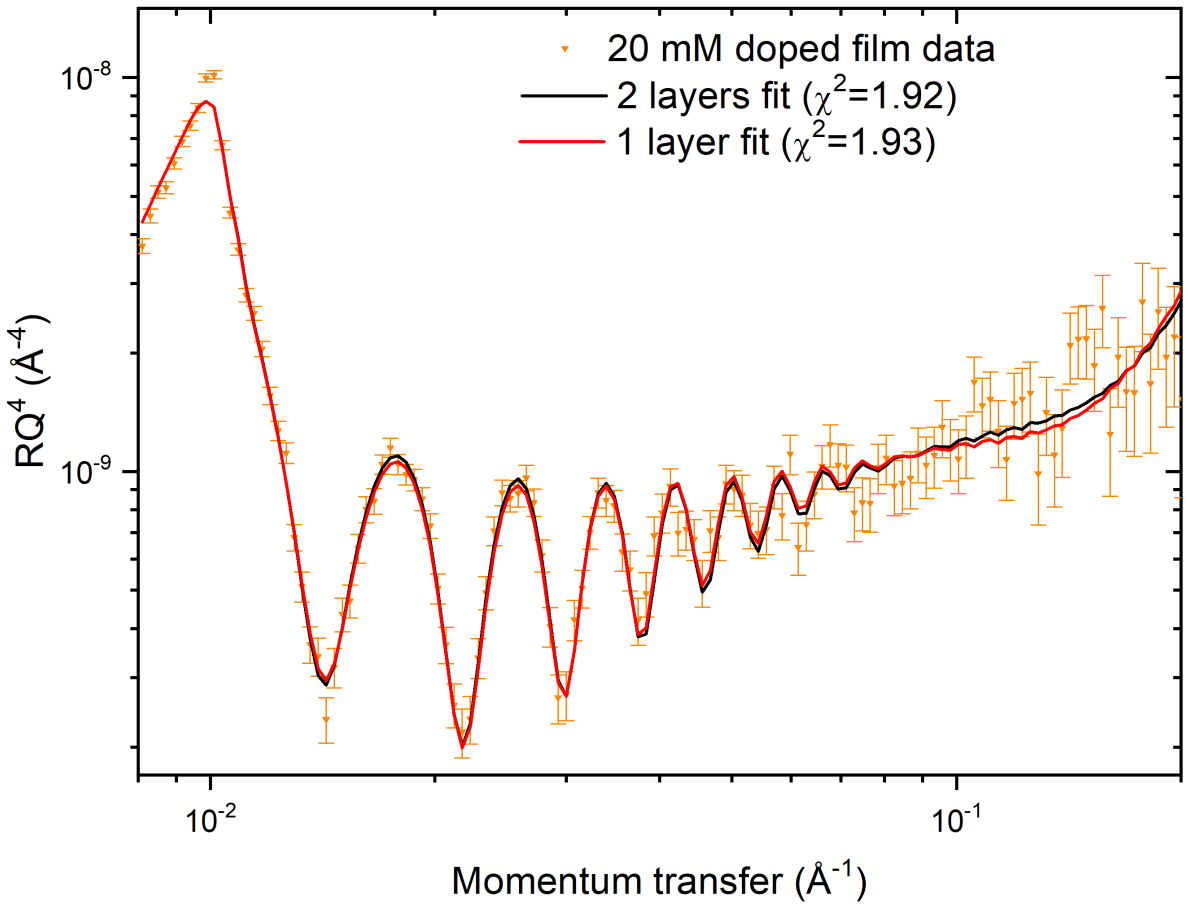

Figure 52: *Neutron reflectivity plotted as RQ^4 data for the 20 mM film and its corresponding fits using a two layer model (black), a one layer model (red) both under the same simulation conditions. The χ^2 values of each fit are shown for comparison of quality of fit evidencing that there is no significant improvement from using a two layer model over a one layer model (1% increase in quality of the fit).*

In order to corroborate the argument discussed above, the validity of the models was tested by applying a two polymer layer model to the pristine sample, and a three polymers layer model to the 10 mM sample. If the one layer model for the pristine sample had a χ^2 very similar to the one of the two layer model then it could be confirmed that the one layer model describes correctly the pristine film structure. Moreover, if the three layer model for the 10 mM sample had a χ^2 very similar to the two layer model then it can be corroborated that the two layer model correctly describes the film structure as well. The results can be seen in figure 53 and table 8.

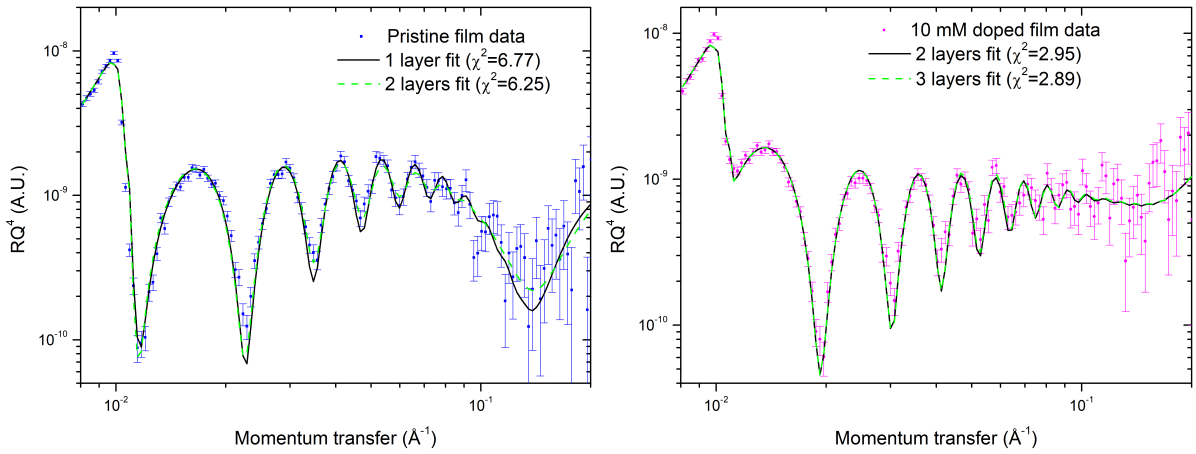

(a) (b)

Figure 53: *Neutron reflectivity plotted as RQ^4 data for (a) the pristine film and its corresponding fits using a one layer model (black line), a two layer model (green spaced line), and for (b) the 10 mM film and its corresponding fits using a two layer model (black line) and a three layer model (green spaced line) both under the same simulation conditions . The χ^2 values of each fit are shown for comparison of quality of the fits.*

Table 8: *Thickness (D), root mean square roughness (σ_{RMS}), and scattering length density (SLD) resulting from modelling a 2 layer and 3 layer model for the pristine and 10 mM sample respectively.*

Pristine (2 layer model)

	D (nm)	σ_{RMS} (nm)	SLD (10^{-6}Å^{-2})
Top Layer	39.78	2.43	1.5
Bottom Layer	8.51	4.94	1.28

10 mM (3 layer model)

	D (nm)	σ_{RMS} (nm)	SLD (10^{-6}Å^{-2})
Top Layer	43.6	1.16	1.37
Middle Layer	2.13	1.91	1.47
Bottom Layer	10.1	6.48	1.07

As it can be observed in figure 53a, the χ^2 values for the one layer and two layer models for the pristine sample are 6.77 and 6.25 respectively, which are very similar (7.7% improvement of the quality of the fit from the one layer model to the two layer model). This implies that the one layer model is the best interpretation for this film structure. Figure 53b shows as well two similar χ^2 values from the three layers (2.95) and two layers (2.89) model for the 10 mM sample (2.1% increase from the two layer model to the three layer model) indicating that, based on the principle of Occam's Razor[268], the two layer model is the best interpretation for this film structure. To further confirm these findings a second analysis for every model was conducted based on the Nevot-Croce scheme[269] and a

different metric for the probabilistic evidence. This analysis can be found in section 9.2 in the Appendices. In summary the secondary analysis agrees with the findings reported in this section, confirming that, the one layer model for the pristine and the 20 mM samples, and a two layer model for the 10 mM sample are the most plausible interpretations for their respective polymer films.

Now, the polymer layers of the 10 and 20 mM samples are analysed. According to the two layer model for the 10 mM sample, there is a 10.1 nm thick layer on top of the SiO_2 with a σ_{RMS} of 8.1 nm. This is an unusually high σ_{RMS} to thickness ratio which indicates that this layer is not completely separated from the top layer, but rather going through a gradual separation. The SLD of the bottom layer was 1.1×10^{-6} Å^{-2} which is slightly lower than that of the undoped PEDOT:PSS film (see table 9). Given that the theoretical SLD value of DYMAP is 4.7×10^{-8} Å^{-2}, the decreased SLD of this bottom layer compared to that obtained for the pristine PEDOT:PSS suggests that the bottom polymer layer likely contains most of the DYMAP precipitated within the polymer film. The top polymer layer had a thickness of 45.86 nm, a σ_{RMS} of 1.15 nm, and an SLD of 1.37×10^{-6} Å^{-2} which is very similar to the one of the pristine sample. This implies that the top polymer layer is mostly comprised of undoped PEDOT:PSS with very small traces of DYMAP as indicated by a minimal decrease in SLD (from 1.42×10^{-6} Å^{-2} to 1.37×10^{-6} Å^{-2}). The total polymer film thickness of the 10 mM sample (bottom and top polymer layers combined) increased by 18% compared to the pristine sample, which hints at a swelling effect induced by DYMAP. As for the 20 mM sample two layer model, the bottom polymer layer had a thickness of 12.1 nm and a σ_{RMS} of 4.1 nm while the top polymer layer had a thickness of 65.7 nm and a σ_{RMS} of 0.96 nm. However, the scattering length densities of both layers were very similar being 0.76 x 10^{-6} Å^{-2} for the bottom polymer and 0.82 x 10^{-6} Å^{-2} for the top polymer. This is a strong indication that the layers are not different from each other, supporting the argument that there is no separation of layers at this high concentration. On the other hand, the one layer model, the polymer layer was 78.02 nm thick and the σ_{RMS} was 0.96 nm. The SLD of the polymer layer was 8.0×10^{-7} Å^{-2} which if compared to the pristine PEDOT:PSS layer and the top layer of the 10 mM sample, is notably lower. This decrease in the SLD could be due to the modified density of the film caused by the dopant since it is 60% thicker compared

to the pristine sample (see table 9). It is worth noting that the 20 mM DYMAP doped PEDOT:PSS dispersion exhibited slightly increased viscosity compared to the pristine PEDOT:PSS dispersion. Therefore, since the same spin-coating conditions were used for both dispersions, the 20 mM film is expected to be thicker. Extracting quantitative results from two effects which have similar outcomes is therefore quite difficult. The increase in thickness of the PEDOT:PSS film caused by an asymmetrically charged dopant is an effect that is rarely considered in literature and has important implications on the interpretation of the morphology modifications of PEDOT:PSS. Moreover, it directly affects the measurement of its parameters such as efficiency in devices which is dependent on the thickness of the film[270–272], and conductivity which is commonly obtained by measuring the sheet resistance and assuming a constant thickness for the pristine and the doped samples.

Figure 54 compares the scattering length density profiles of pristine (1 layer model), 10 mM (2 layer model) and 20 mM (1 layer model) DYMAP doped PEDOT:PSS.

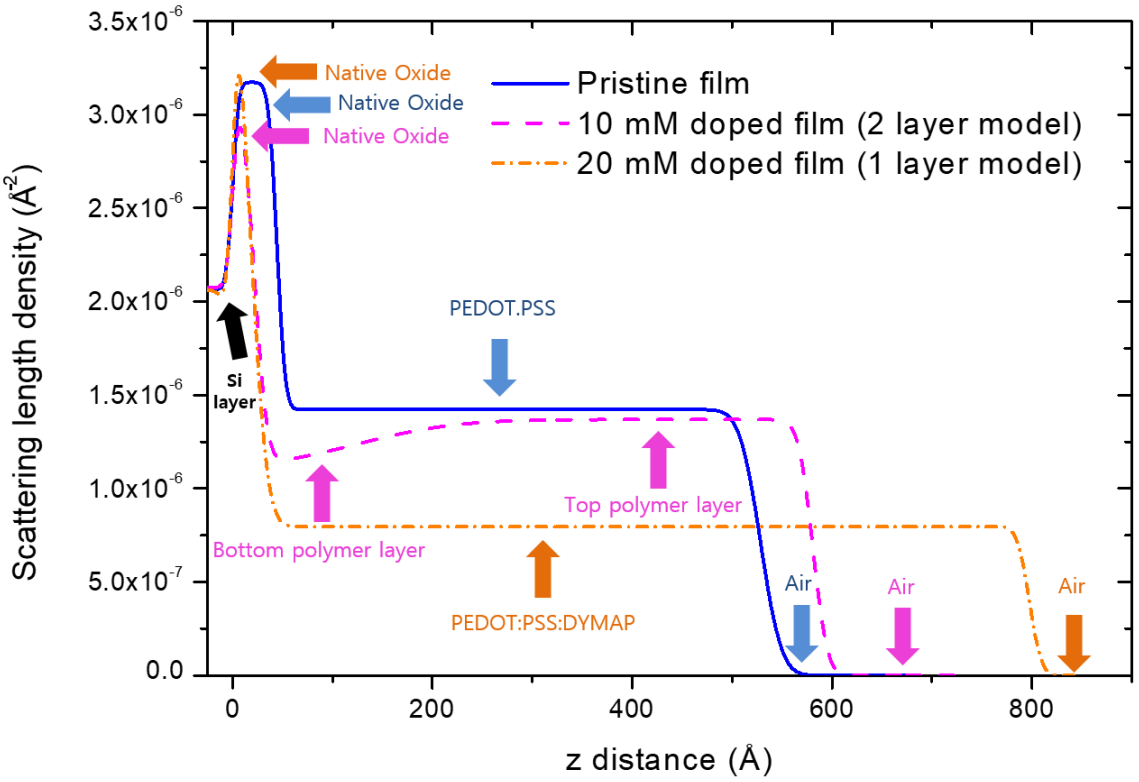

Figure 54: *Neutron scattering length density profiles of pristine, 10 mM(2 layer model), and 20 mM(1 layer model) DYMAP doped PEDOT(1):PSS(2.5).*

Given the results presented in this section, it is proposed that at lower doping concentration (e.g. 10 mM for DYMAP in PEDOT:PSS) the dopant preferentially accumulates close to the substrate surface resulting in a bi-layer structure with the lower layer rich in the dopant (in this case DYMAP), and the top layer comprised of mostly undoped PEDOT:PSS. An explanation for this phenomenon could be that at 10 mM the amount of DYMAP is insufficient to dope all of the PEDOT:PSS molecules. Subsequently, when this mix is processed into a thin film, separated layers form with the heavily doped layer near the Si interface. Moreover, the large effective roughness (relative to film thickness) of the bottom polymer suggests that this separation of layers is not into two distinct types of materials, in which one of them ceases to be at a specific point within the film's height. Instead, the film has a graded structure in which most of the dopant is found near the bottom of the film and its presence gradually decreases as a function of the film's height leaving the top of the film comprised of mostly PEDOT:PSS (see figures 55a and 55b). It is also proposed that when the dopant concentration increases (e.g. the 20 mM DYMAP doped PEDOT:PSS), the more evenly balanced PEDOT:PSS to dopant ratio allows the formation of a homogeneous film (see figures 55c and 55d). It is worth noting that this is a possible explanation suggested by the author and that determining the precise cause for this phenomenon requires a separate study that is out of the scope and objectives of this thesis.

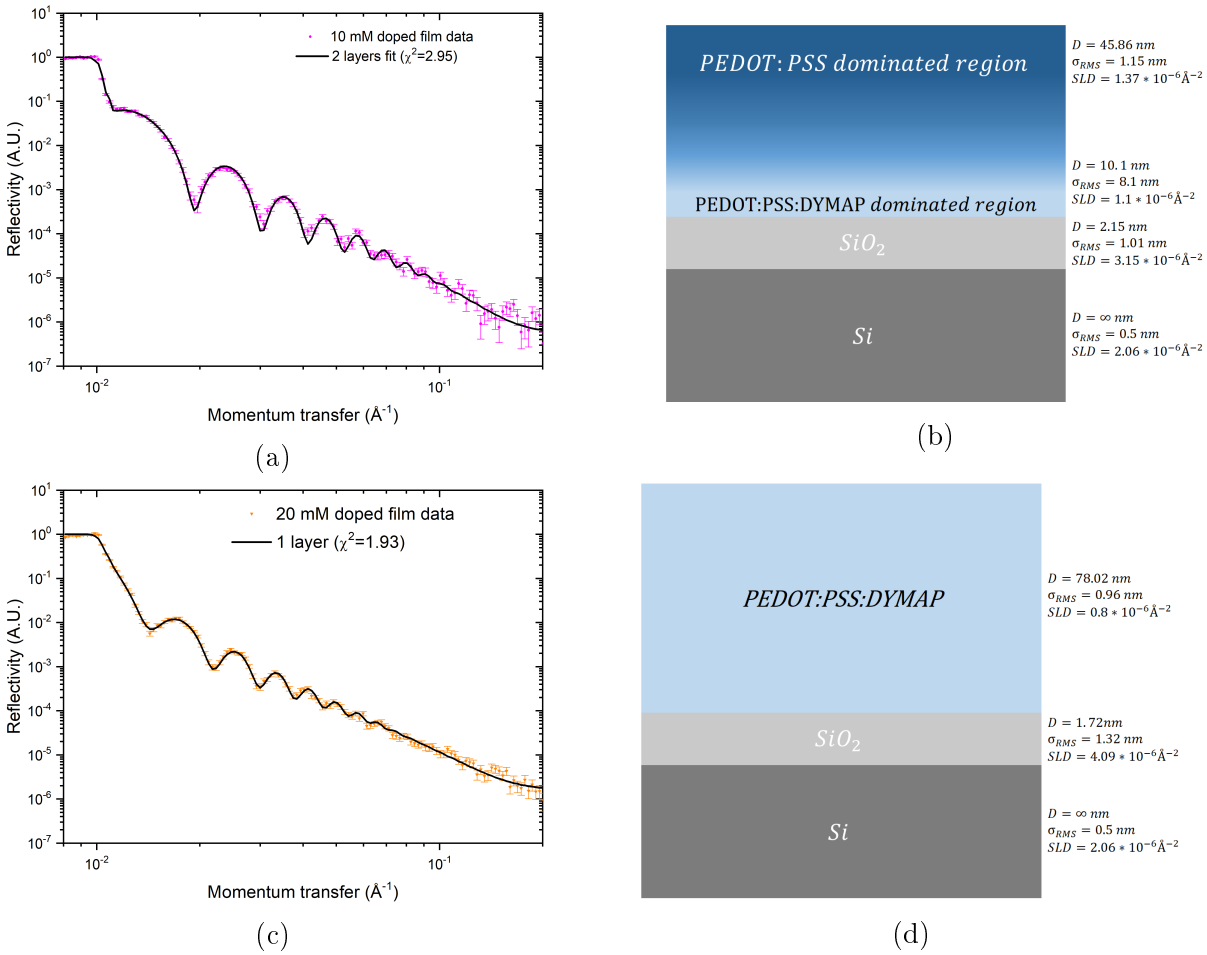

Figure 55: *Neutron reflectivity data for the 10 mM (a) and 20 mM (c) DYMAP doped PEDOT:PSS films and their corresponding chosen fits. The sketches of the 10 mM (b) and the 20 mM (d) samples (not to scale) are also shown along with their respective resulting values for thickness (D), root mean square roughness (σ_{RMS}), and scattering length density. (SLD)*

Table 9: *Thickness (D), root mean square roughness (σ_{RMS}), and scattering length density (SLD) of each sample by layer. The numbers shown for the 10 and 20 mM sample correspond to the 2 and 1 layer model respectively.*

Pristine

	D (nm)	σ_{RMS} (nm)	SLD (10^{-6}Å^{-2})
PEDOT:PSS	48.40	1.65	1.42
SiO_2	4.44	0.66	3.17

10 mM

	D (nm)	σ_{RMS} (nm)	SLD (10^{-6}Å^{-2})
Top Layer	45.86	1.15	1.37
Bottom Layer	10.1	8.10	1.10
SiO_2	2.15	1.01	3.15

20 mM

	D (nm)	σ_{RMS} (nm)	SLD (10^{-6}Å^{-2})
PEDOT:PSS:DYMAP	78.02	0.96	0.80
SiO_2	1.72	1.32	4.09

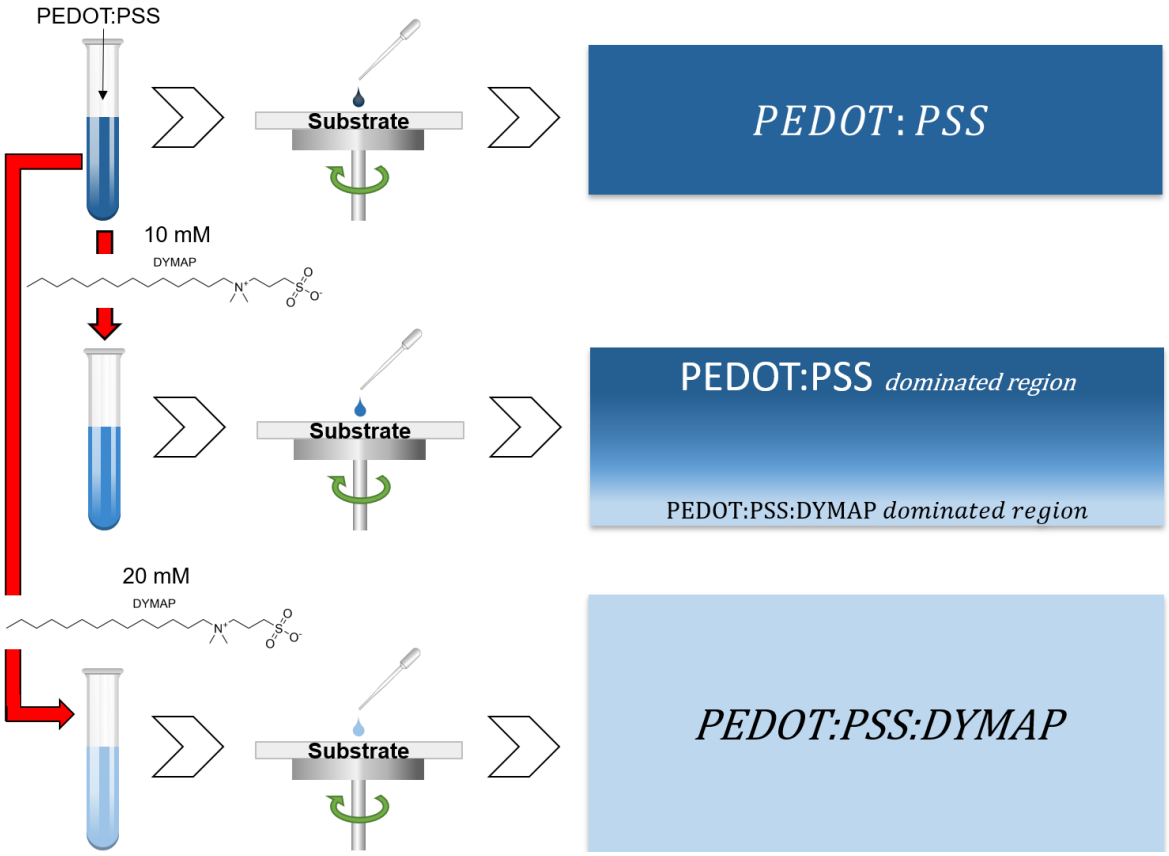

Figure 56: *Schematic representation of the vertical structure modification of DYMAP doped PEDOT:PSS.*

5.3.5 Surface characteristics of the DYMAP doped PEDOT:PSS films

In order to study the surface morphology of the films and to aid the NR data analysis by determining the σ_{RMS}, AFM was conducted. The results can be compared in table 10

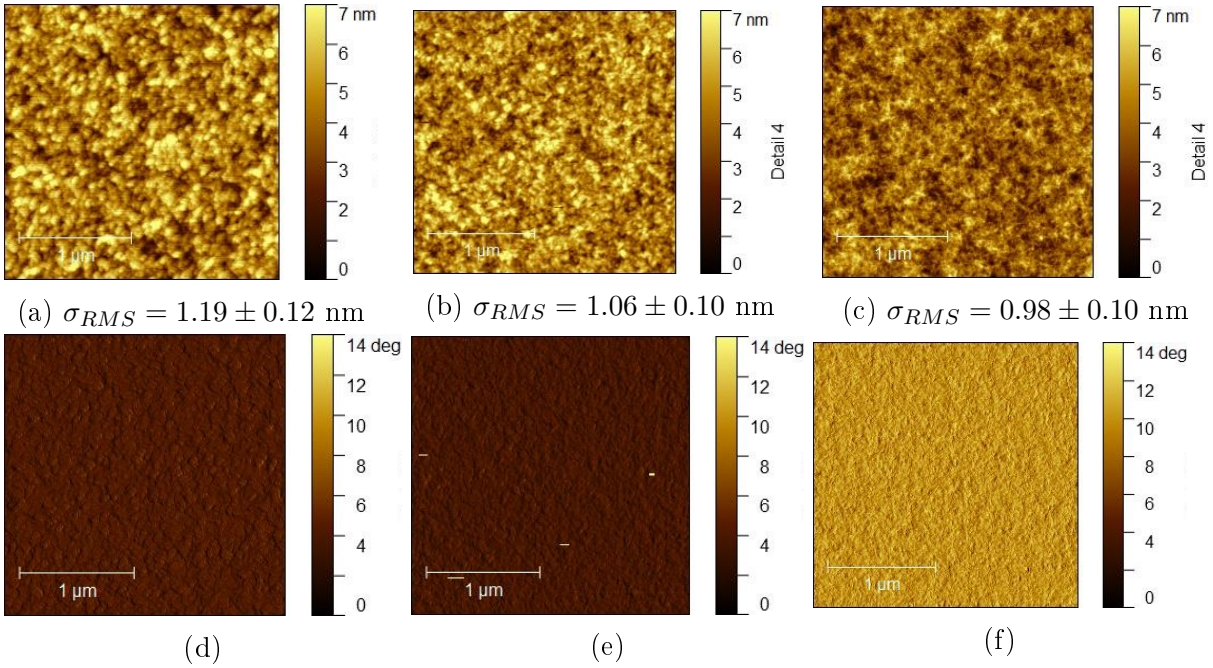

(a) $\sigma_{RMS} = 1.19 \pm 0.12$ nm (b) $\sigma_{RMS} = 1.06 \pm 0.10$ nm (c) $\sigma_{RMS} = 0.98 \pm 0.10$ nm

(d) (e) (f)

Figure 57: *AFM height (top) and phase (bottom) images of pristine PEDOT:PSS (a and d), and 10 mM (b and e) and 20 mM (c and f) DYAMP doped PEDOT:PSS. Images show decreasing root mean squared roughness as the dopant concentration increases.*

Height and phase images are presented in figure 57. The pristine sample (57a and 57d) had an average σ_{RMS} of 1.19 nm, the highest of all samples. Figure 57 also shows that there are clear nodules (spherical features) in the height image which have been identified before as PEDOT aggregates[200]. As the concentration increases, it can be seen how those nodules tend to disappear or dissipate, and instead a more interconnected film network is formed. This observation is also supported by the subtle decrease in the average roughness of the 10 and 20 mM samples which are 1.07 nm and 0.96 nm respectively, as it is known that PEDOT is a rough polymer when deposited as a thin film[201]. To confirm this trend, a 2D fast Fourier transform (FFT) was applied to the height images and then a horizontal cut from the middle of the FFT images was extracted. As shown in figure 58 the peak intensity of the FFT horizontal cut of the images decreases from 6.59 nm (pristine) to 4.44 nm (10 mM) and 3.70 (20 mM) which corroborates a change

in the surface of the films as the doping concentration increases. This trend supports the argument presented in the NR analysis section where it is observed that at a low concentration of DYMAP the surface layer is mostly PEDOT:PSS with minor traces of DYMAP. However as the doping concentration increases, the DYMAP becomes better mixed through all PEDOT:PSS and the resulting surface morphology is considerably different in comparison to the pristine sample being smoother and less aggregated. This change in surface morphology can also be seen in the phase images (figures 57d, 57e, and 57f) where the 20 mM sample looks more homogeneous than the 10 mM and pristine samples supporting the idea described in the NR section of the surface of the film transitioning from PEDOT:PSS to PEDOT:PSS:DYMAP as the dopant concentration increases.

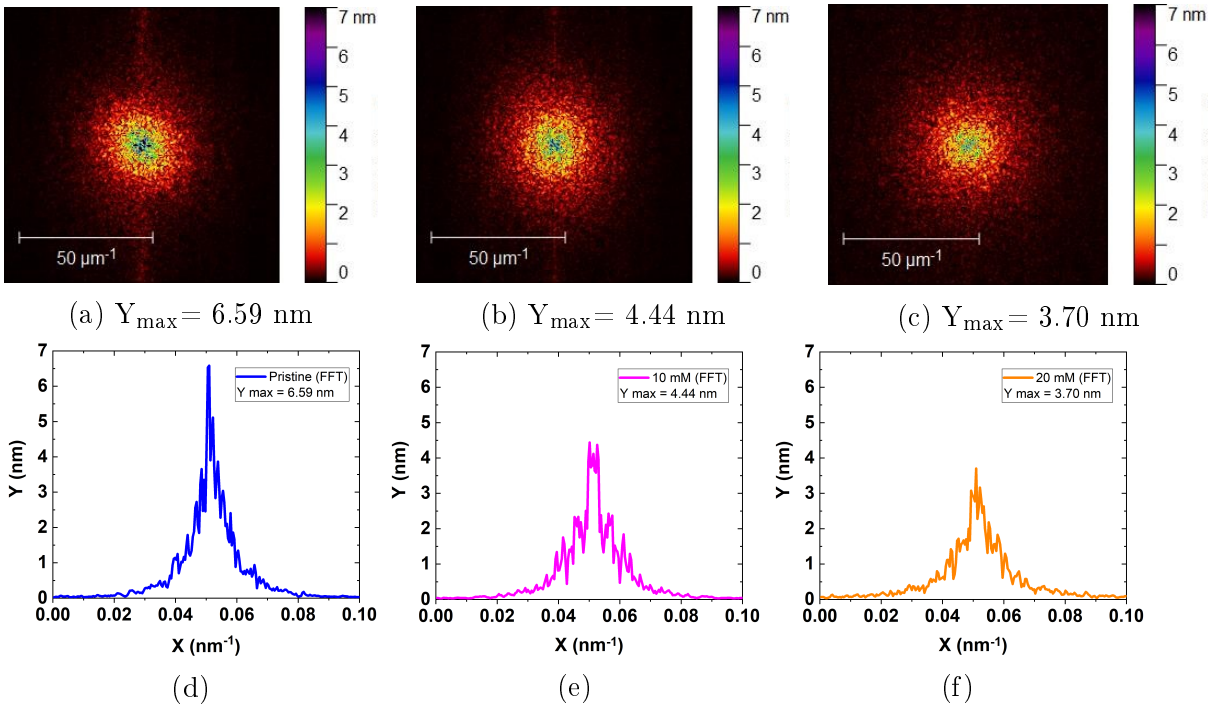

Figure 58: *2D Fast Fourier transforms (FFT) of the AFM height images (top), and their horizontal cut taken from the middle of the images (bottom). Images of pristine PEDOT:PSS (a and d), and 10 mM (b and e) and 20 mM (c and f) DYAMP doped PEDOT:PSS show a decreasing peak intensity as the dopant concentration increases.*

Table 10 shows root mean square roughness and thickness values obtained with neutron reflectivity, AFM, and profilometry. The discrepancy between the NR and profilometry thickness measurements can be attributed by the low accuracy of the profilometry technique at such low scales, and to the different exposure time to ambient

humidity of the samples for each different technique (see section 5.2.2). The ambient water absorption causes the PEDOT:PSS films to swell reaching maximum swelling at maximum absorption at about 24 hours of exposure to constant ambient humidity. Figure 86 in the appendixes corroborates this trend.

Table 10: *Root mean square roughness (σ_{RMS} and thickness (D) values of the pristine, 10 mM, and 20 mM DYMAP doped PEDOT:PSS samples obtained by surface measurement techniques (AFM and profilometer) and neutron reflectivity modeling.*

	$\sigma_{RMS}(nm)$		$D(nm)$	
	NR	AFM	NR	Profilometer
Pristine	1.65	1.19±0.12	48.40	48.0±0.8
10 mM	1.15	1.06±0.10	55.96	58.3±4.5
20 mM	0.96	0.98±0.10	78.02	90.3±5.7

5.3.6 Incorporation of DYMAP doped PEDOT:PSS films into P3HT and PCDTBT based devices

Now that the nano-scopic structure of the different concentration DYMAP doped PEDOT:PSS dispersions and the vertical structure of the respective processed films had been determined, the 0, 10, and 20 mM DYMAP doped PEDOT:PSS films were incorporated into P3HT:PCBM and PCDTBT:$PC_{70}BM$ based devices. As discussed in sections 3.7.2 and 5.1 it was expected that the incorporation of improved conductivity DYMAP doped PEDOT:PSS films into OSCs would result in the enhanced photovoltaic performance of devices. Specifically, an increase in the power conversion efficiency (PCE) of the 20 mM sample as expected since its conductivity is significantly increased by more than one order of magnitude compared to the pristine and the 10 mM sample. The results are shown in figure 59 and table 11.

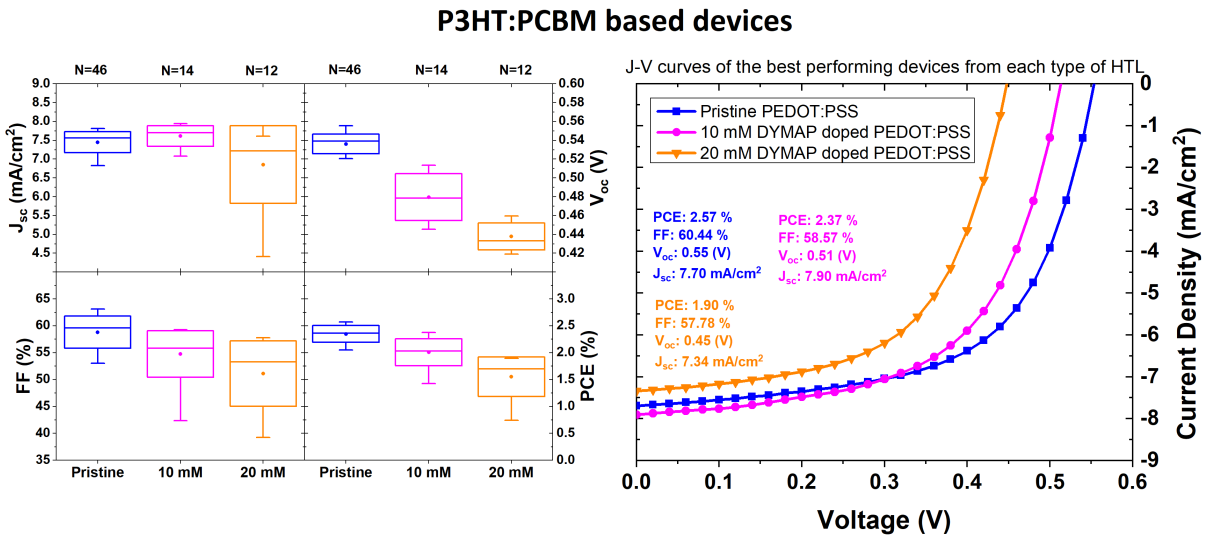

(a)

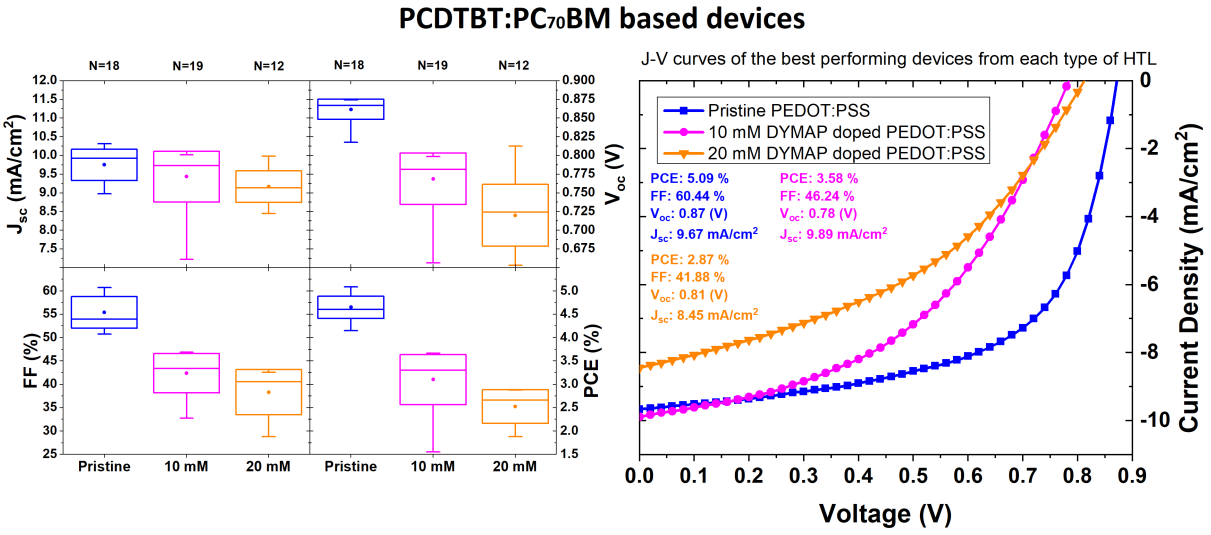

(b)

Figure 59: *Box plots (left) showing the Photovoltaic performance (short circuit current, open circuit voltage, fill factor, and power conversion efficiency) of P3HT:PCBM (a) and PCDTBT:PC$_{70}$BM (b) based devices with pristine (blue), 10 mM DYMAP doped (magenta), and 20 mM DYMAP doped (orange) PEDOT:PSS. N equals the number of measurements for each type of device, the width of the box represents one standard deviation on each side of the mean average value, the top and bottom ticks are the maximum and minimum values respectively, the horizontal line in the box is the median, and the circle in the middle of the box is the mean average value. The J-V curve (right) of each champion device is also shown for performance comparison.*

Table 11: *Photovoltaic performance metrics of P3HT:PCBM and PCDTBT:$PC_{70}BM$ based devices fabricated with DYMAP doped PEDOT:PSS as hole transporting layer in 0, 10, and 20 mM doping concentration. The errors represent one standard deviation for 'N' number of measurements.*

	Average				Maximum value				
	Jsc (mA/cm^2)	Voc (V)	FF (%)	PCE (%)	Jsc (mA/cm^2)	Voc (V)	FF (%)	PCE (%)	N
P3HT:PCBM, pristine	7.45±0.28	0.536±0.010	58.82±3.00	2.35±0.16	7.82	0.555	63.14	2.57	46
P3HT:PCBM, 10 mM	7.61±0.28	0.480±0.025	54.78±4.33	2.01±0.25	7.94	0.514	59.27	2.38	14
P3HT:PCBM, 20 mM	6.85±1.03	0.438±0.014	51.11±6.09	1.56±0.37	7.60	0.460	57.78	1.90	12
PCDTBT:$PC_{70}BM$, pristine	9.75±0.42	0.862±0.013	55.39± 3.41	4.65±0.24	10.32	0.874	60.71	5.09	18
PCDTBT:$PC_{70}BM$, 10 mM	9.43±0.68	0.769±0.034	42.39±4.19	3.10±0.54	10.01	0.799	46.90	3.66	19
PCDTBT:$PC_{70}BM$, 20 mM	9.14±0.46	0.720±0.041	38.30±4.83	2.53±0.36	9.98	0.812	42.54	2.87	12

The results were unexpected since the average PCE of the devices went down from 2.35±0.16% to 2.01±0.25% and 1.56±0.37% for P3HT based devices, and from 4.65±0.24 to 3.10±0.54, and 2.53±0.36 for PCDTBT based devices respectively as the concentration of DYMAP increased. All the other three photovoltaic parameters of PCDTBT base devices also decreased as the concentration of DYMAP increased. Similarly, the V_{oc} and FF of the P3HT based devices with a 10 mM and 20 mM DYMAP doped PEDOT:PSS HTL were lower compared to the reference device, however the 10 mM doped HTL devices had a slightly increased J_{sc}.

To understand the reason behind the lower performance of the doped HTL incorporated devices, the J-V curves of the devices were analysed. As can be seen in figure 59, the J-V curves of the best performing pixels of the doped HTL incorporated P3HT and PCDTBT devices are worse than the reference device. This can be quantified by the FF of the devices which was 58.82±3.00, 54.78±4.33, and 51.11±6.09% for the 0, 10, and 20 mM DYMAP doped PEDOT:PSS incorporated P3HT devices respectively, and 55.39±3.41, 42.39±4.19, and 38.30±4.83% for the 0, 10, and 20 mM DYMAP doped PEDOT:PSS incorporated PCDTBT devices respectively. The fact that the FF of the 10 mM doped HTL P3HT devices is lower than that of the control devices despite the slight increase of J_{sc} (from 7.45±0.28 to 7.61±0.28 mA cm^{-2}), indicates that the lower FFs are not caused exclusively by the decreased V_{oc} of the devices. This is further supported by the less ideal shape of the J-V curve (see section 2.4) of the doped HTL incorporated devices which indicates that the decreased FF of the doped HTL incorporated devices

could be attributed to a lower quality of the contact between the doped HTLs and the active layer. During the spin coating step of the fabrication process, the doped films exhibited an increased phobic behaviour towards the solvent (chlorobenzene)in which the active layer was diluted. This resulted in difficulties spin-coating the active layer onto the doped PEDOT:PSS films evidenced by areas on the HTL layer that were not coated due to the surface repelling the active layer solution. This effect was considerably more intense in the 20 mM doped sample compared to the 10 mM doped one which explains the lower PCE of the 20 mM doped HTL incorporated devices. A phobic behaviour of the doped HTLs towards the PAL solvent can result in the poor adhesion between the HTL and the PAL hindering the photovoltaic performance of the device. In order to corroborate that the doped samples exhibit a phobic behaviour towards chlorobenzene, contact angle measurements were conducted on the pristine, 10 mM, and 20 mM DYMAP doped PEDOT:PSS films by dropping 5 μL of chlorobenzene on the surface of each film. As shown in figure 60, the contact angle increases from 10.58° to 16.15° from the pristine to the 10 mM doped film respectively confirming and increased phobic behaviour of the doped sample towards chlorobenzene. This phobic behaviour was found to have a correlation with the doping concentration since the contact angle of the 20 mM doped film was 20.48° which is higher than the pristine and the 10 mM doped film. These results confirmed that the doped films develop a phobic behaviour towards the active layer solvent. The increased phobic behaviour of the DYMAP doped PEDOT:PSS film hinders the quality of the contact between the HTL and the active layer due to the increased dewetting. This slightly increases the series resistance of the devices and most prominently decreases their shunt resistance (as shown by the shape of the J-V curves in figure 59) allowing for a leakage current to hinder the photovoltaic parameters and performance of the solar cells using DYMAP doped PEDOT:PSS. It is worth noting that the reduced V_{oc} of the 10 and 20 mM HTL incorcporated devices relative to the control devices could indicate that the HOMO and LUMO levels of the doped HTL films may be shifted by the inclusion of DYMAP in PEDOT:PSS hindering its electron blocking capabilities. This could lead to electrons migrating to the doped PEDOT:PSS HTL and the HCE increasing the number of recombination events within the device and hence result in its poor performance.

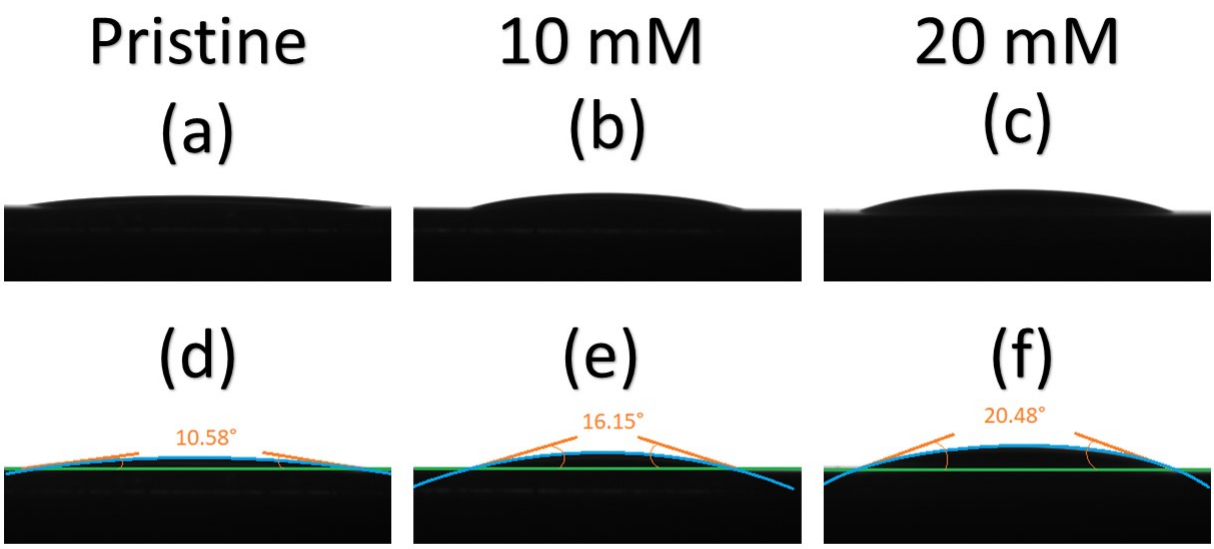

Figure 60: *Contact angle images of the pristine (a and d), 10 mM (b and d), and 20 mM (c and f) DYMAP doped samples. 5 µL of chlorobenzene were dropped on top of the films for these measurements.*

The reason behind the slight increase of J_{sc} of the 10 mM doped HTL incorporated P3HT devices is unclear. A possible explanation for this could be that the bottom DYMAP doped layer in the quasi-bilayer structure of the 10 mM doped film provides a slightly more favourable conductive pathway for the charges to travel through the film (see section 5.1). However, in the case of the 10 mM doped HTL PCDTBT device, the drop in V_{oc} is significant enough to overcome any slight benefit from such favourable conductive pathway resulting in a reduced J_{sc} compared to the reference device. Since the 20 mM doped film is entirely homogeneous, the more favourable conductive pathway throughout the whole film should, on its own, result in the improved efficiency of both the P3HT and PCDTBT devices. However, in such a case the phobic behaviour towards the active layer results in a contact quality that is sufficiently poor to exceed any charge transport benefit. This results in the overall decrease of all the photovoltaic parameters of the devices. Given that the DYMAP doped HTLs decreased the efficiency of OSCs, and that the reason for such an effect was determined, it was decided to not investigate them further. However, it is clear that the increased conductivity of an HTL alone does not necessarily result in the improved efficiency of the device if the interlayer contact

quality is poor.

In chapter 8, different possibilities for future work are suggested to specifically address the contact between DYMAP doped PEDOT:PSS and P3HT:PCBM or PCDTBT:$PC_{70}BM$. From the results of this chapter it is clear that the contact quality between the HTL and the PAL plays an important role in the efficiency of the devices, therefore, the next step in this thesis was to investigate a method to improve the contact quality between the HTL and PAL of OSCs.

5.4 Conclusions and next steps

Four zwitterions were used to dope the PEDOT:PSS dispersion, seeking to improve the conductivity of the films to subsequently incorporate them as HTL in OSCs for improved photovoltaic performance. The sheet resistance of the four zwitterion doped PEDOT:PSS films at different concentrations was determined. Out of the four zwitterions, only DYMAP showed no simultaneous gelation and significantly decreased sheet resistance relative to a pristine PEDOT:PSS film. Different concentration DYMAP dispersions were then investigated with small angle neutron scattering to determine the nano-scale modifications of the PEDOT:PSS structure caused by DYMAP. It was found that DYMAP forms micelles in water, and it was proposed that when in the presence of PEDOT:d-PSS, DYMAP grows into worm-like micelles as the concentration of DYMAP is increased up to the point of gelation of the dispersion. The interchain distance between negatively charged d-PSS backbone segments remains virtually unaffected by the DYMAP worm-like micelles up to 15 mM DYMAP concentration, however, as more dopant is added the worm-like micelles grow long enough to increase the interchain distance between negatively charged d-PSS segments due to steric hindrance. At 30 mM however, the DYMAP worm-like micelles grow long enough to form an interconnected network with the d-PSS chains by coulombically interacting with them which results in the relaxation of d-PSS chains and a decrease in the interchain distance between them. The screening length of the neutralised d-PSS segments that are attached to the PEDOT oligomers increases as DYMAP concentration is increased as a result of the slow and partial neutralisation of some negatively charged d-PSS. This effect is greatly improved

at 30 mM when the gelation of the dispersion occurs due to the interconnected DYMAP network significantly screening the negatively d-PSS backbone segments.

The DYMAP doped dispersions were then processed as thin films and their vertical structure was investigated with neutron reflectivity. It was found that upon doping, the film thickness increases and at low concentration the DYMAP preferentially segregates towards the substrate resulting in two layers with a graded interface after film deposition. The bottom polymer layer is comprised of DYMAP doped PEDOT:PSS and the top polymer layer is mostly comprised of PEDOT:PSS with negligible traces of the zwitterion. The large roughness of the interface between these two layers suggests that across the interface, the zwitterion content decreases as a function of height within the film. This separation into two layers only occurs at the low zwitterion to PEDOT:PSS ratio, however, when the concentration of DYMAP is further increased the NR data shows complete intermixing of the PEDOT:PSS with the zwitterion resulting in a homogeneously mixed film. The AFM results indicate a change in surface morphology from rough to smooth, with fewer PEDOT aggregates on the top surface as it changes from PEDOT:PSS to PEDOT:PSS:DYMAP. The homogeneous 20 mM PEDOT:PSS:DYMAP films have a significantly higher conductivity, by over an order of magnitude ($\sim$20-50 times) compared to the intermediate 10 mM films and the pristine PEDOT:PSS. The latter two had similar conductivities with the 10 mM films showing a similar surface texture and only a slight reduction in conductivity compared to the pristine PEDOT:PSS.

When incorporated as HTLs into P3HT and PCDTBT based devices, it was found that the DYMAP doped PEDOT:PSS films decrease the photovoltaic performance of the devices as the concentration of DYMAP increases. This is attributed to an increased phobicity towards the solvent in which the PAL is diluted of the films caused by DYMAP. This increased phobicity of the films results in the lower quality of the contact between the DYMAP doped PEDOT:PSS films and the active layer which lead to a decrease in the fill factor and open circuit voltage of the DYMAP doped HTL incorporated devices. It is also possible that the energy levels of DYMAP doped PEDOT:PSS are unfavourable to block electrons allowing them to travel from the active layer to the HTL and HCE which would result in an increase of recombination events. It is clear that in order to

improve the quality of the interface between PEDOT:PSS and P3HT:PCBM for improved device performance, the increased electrical conductivity of PEDOT:PSS on its own is not sufficient and that the contact quality between both layers and the beneficial alignment of their energy levels plays an important role in the device performance. Therefore, the next chapter of this thesis focuses on investigating a method to improve the contact quality and the energy level alignment between the HTL and the active layer films. However, the findings on this chapter are expected to contribute with understanding on doped PEDOT:PSS for its future optimisation to improve charge transport in OSCs.

6 Improving the contact quality between the HTL and PAL of P3HT based devices

6.1 Introduction

The research presented in this chapter has been submitted to the *Small* journal.

In the previous chapter it was found that poor compatibility between the HTL and the PAL in OSCs can overcome other improved characteristics within the device such as the conductivity of the HTL resulting in the decreased photovoltaic performance of the device. Therefore, this chapter focuses on investigating a method to improve the contact quality between the HTL and the PAL to improve the efficiency and stability of OSCs. Specifically, the improvement of the quality of the contact between PEDOT:PSS and P3HT:PCBM in ITO/PEDOT:PSS/P3HT:PCBM/Al structured devices will be investigated due to the simplicity, scalability, and potential uses of such structure.

During the last decade, the low power conversion efficiency (PCE) of OSCs has been continually improved by synthesising specifically tuned donor materials[109] such as PTB7[273], PffBT4T-2OD[106], PBDTTT-EFT[274], PBDB-T-Cl[107] , and light absorbing non-fullerene acceptors[64] such as TPB[65], ITIC[66], and IT-4F,[62] achieving PCEs between 10% and 14%. Recently, a 17.3% PCE tandem device was reported demonstrating the promising future for OSCs[110]. Despite this progress, scalability and stability of such highly efficient materials remains a considerable challenge for their commercialization[275–278]. Poly(3-hexylthiophene) (P3HT) based OSCs however, are among the few organic photovoltaic systems that have been successfully scaled-up[121–123] despite their low efficiency, and thus, remain as arguably the most investigated type of OSCs[279]. Due to their proven readiness for commercialization, finding new methods to improve the efficiency of P3HT based OSCs remains an active area in research[280–284].

As mentioned in section 3.7.1, poly(3,4-ethylenedioxythiophene):poly(styrene sulfonate) (PEDOT:PSS) is by far the most used hole transporting layer (HTL) in scaled up P3HT based OSCs due to its simple processability, high transparency to most of

the solar spectrum when processed as a thin film[163], good mechanical and thermal stability[172–174], and excellent water solubility[134]. However, the interface between the PEDOT:PSS and the P3HT:acceptor bulk heterojunction layer is far from optimal as it exhibits poor adhesion and an unfavourable energy difference between adjacent layers[180–182]. Moreover, it has been shown before that PEDOT:PSS coated films have a surface rich in PSS with the sulphate group oriented towards the surface[179;285]. This allows a reaction to occur between PSS and P3HT that results in the p-doping of P3HT and its degradation due to the highly acidic nature of PSS[286]. Additionally, if a >150 °C thermal annealing step is used during device fabrication (like the one used in this thesis 4.2.4) after the P3HT based layer has been deposited on the PEDOT:PSS for improved performance, it has been demonstrated that PSS intermixes with P3HT[179]. Several efforts to improve the contact quality between PEDOT:PSS and P3HT have been made, mainly through doping PEDOT:PSS with different substances in order to change its physical and chemical properties such as selective carrier blocking and mobility, PSS content, and morphology resulting in improved device performance and stability[132;166;200;287]. However, and as demonstrated in chapter 5, since the morphological changes that PEDOT:PSS goes through after doping are complex[230], this route towards improving of the contact quality of PEDOT:PSS and P3HT:acceptor can be unreliable and is risky to scale up. On the other hand, the incorporation of a well understood, organic inter-facial that improves the contact quality between PEDOT:PSS and P3HT:acceptor, and which interactions with each adjacent layer are well known, could have a good scalable potential.

Block co-polymers have been extensively used as compatibilizers[288;289], templating agents[290;291], active materials[292;293], and electrode-active layer inter-facial materials[294;295] to improve the efficiency and stability of organic solar cells. This is due to the advantageous thermodynamic incompatibility between the different blocks in the block co-polymer[296;297]. This incompatibility allows the block co-polymer to separate into different domains of the polymer constituents on the nanoscale, while remaining linked in the macroscale due to the covalent binding of the blocks. These features have allowed the control of the microphase separation of donor-acceptor blends, and the prevention of macrophase degradation, features that are paramount to improve the efficiency and stability of devices[298–300]. Moreover, each block can have different interactions with different

components of the block co-polymer surrounding environment depending on the composition and properties of the blocks. In a previous study, Erothu et al. demonstrated the synthesis and characterisation of a poly(3-hexylthiophene)-*block*-poly(neopentyl p-styrenesulfonate) (P3HT-*b*-PNSS) block co-polymer that upon deposition goes through a thermal treatment of 150°C to remove the neopentyl group in the PSS blocks and convert into P3HT-*b*-PSS (figure 61). The motivation to synthetise this block co-polymer was to use it as an inter-facial layer between the hole transporting layer (HTL) PEDOT:PSS and the photoactive layer (PAL) P3HT:PCBM to enhance the transport of holes between them. The design of this block co-polymer is intended to allow the P3HT block to interact and enhance adhesion with the P3HT based PAL, and the PSS block to engage in electrostatic interactions with the PEDOT:PSS HTL. Due to the polar nature of PSS, the neopentyl group was added to the pre-annealed block co-polymer to enable its solubility in a common organic solvent[301].

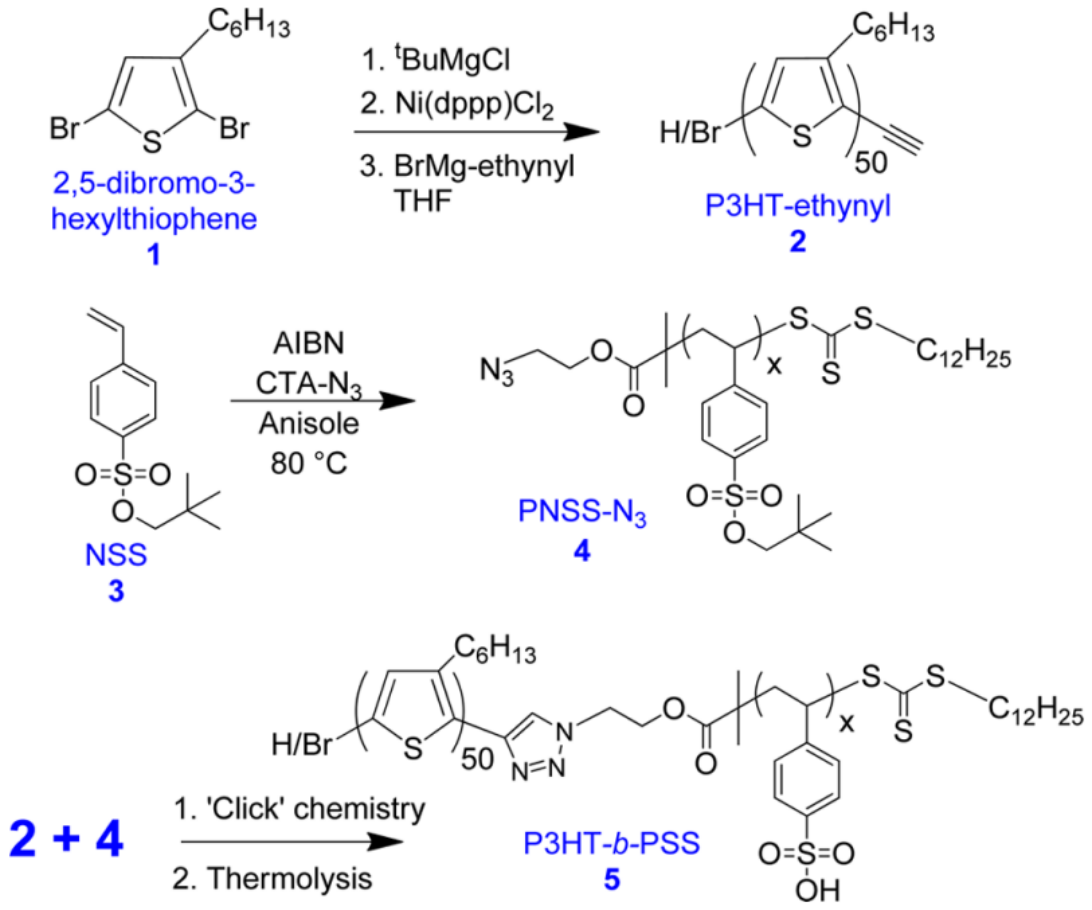

Figure 61: *Synthetic strategy for the preparation pf P3HT-b-PSS. Reprinted with permission from*[301]. *Copyright 2015 American Chemical Society.*

In this chapter, it is demonstrated that specifically designed block co-polymers can be incorporated as inter-facial layers between the HTL and PAL of OSCs to enhance the contact quality between them, improving the photovoltaic performance and stability of the devices. This is done by succesfully incorporating three variants of P3HT-*b*-PNSS with different PSS block lengths (9, 16, and 23 units per 50 units of P3HT) as inter-facial layers between PEDOT:PSS and P3HT:PCBM in ITO/PEDOT:PSS/P3HT:PCBM/Al structured OSCs. The origin of the improved performance and stability of the block co-polymer incorporated devices is investigated by characterising the block co-polymers with ellipsometry, small angle neutron scattering, UV-Vis spectroscopy, atomic force microscopy, ultraviolet and x-ray photon spectroscopy, and testing the device performance under constant and non-constant illumination.

6.2 Experimental

6.2.1 Materials

The $P3HT_{50}$-*b*-$PNSS_9$, $P3HT_{50}$-*b*-$PNSS_{16}$, and $P3HT_{50}$-*b*-$PNSS_{23}$ block co-polymers were synthesised by Erothu et al. Table 12 shows the number average molecular weight (M_n), weight average molecular weight (M_w), and polydispersity values of the three block co-polymers. Other properties of the block co-polymers can be found in the synthesis report[301]. The details of all the other materials used in this chapter are described in sections 4.2.1 and 5.2.1.

Table 12: *Number average molecular weight (M_n), weight average molecular weight (M_w), and polydispersity values of the three block co-polymers.*

	M_n	M_w	Polydispersity
$P3HT_{50}$-*b*-$PNSS_9$	15,000	18,300	1.22
$P3HT_{50}$-*b*-$PNSS_{16}$	18800	23,876	1.27
$P3HT_{50}$-*b*-$PNSS_{23}$	19600	28,420	1.45

6.2.2 Device fabrication and measurement of photovoltaic performance

The 1, 2.5, 5, and 10 mg mL^{-1} block co-polyemer solutions were prepared by putting 0.5, 1.25, 2.5, and 5 mg respectively of each block co-polymer in a 4 mL amber vial each and adding 0.5 mL of chlorobenzene to them. The solutions were then stirred at 75 °C for two hours and subsequently stirred at 30°C overnight. All the other inks used were prepared as described in section 4.2.4.

The 8 pixel type ITO coated substrate (figure 22) was used for the fabrication of devices in this chapter. The substrates were cleaned as described in section 4.2.3. The PEDOT:PSS dispersion was spin-coated (section 4.2.4) at 5000 RPM for 40 seconds and the top and bottom stripes of the film were removed as required for the formation of the circuit, using a cotton swab dampened in D.I. water. The sample was then thermally annealed on a hot plate at 150 °C for 15 minutes. The block co-polymers were then spin-coated onto the samples (the top and bottom stripes of the film were formed with a cotton swab dampened in chlorobenzene) and then transferred to a nitrogen filled glovebox to be thermally deprotected on a hot plate at 150 °C for three hours. The samples were then taken out of the glovebox and the P3HT:PCBM solution was spin-coated at 2000 RPM for 30 seconds onto the substrates forming the top and bottom stripes of the film with a cotton swab damp in chlorobenzene. The active layer solution was filtered through a 0.45 μm polytetrafluoroethylene filter before use. The samples were then placed in a thermal evaporator under a $<2.0 \times 10^{-6}$ Pa vacuum to deposit a 100 nm Al electrode. The devices were then thermally annealed at 150°C for 30 minutes and subsequently encapsulated by using expoxy and glass coverslips and a 15 minutes ultraviolet light curing step. A schematic representation of the fabrication process is shown in figure 62.

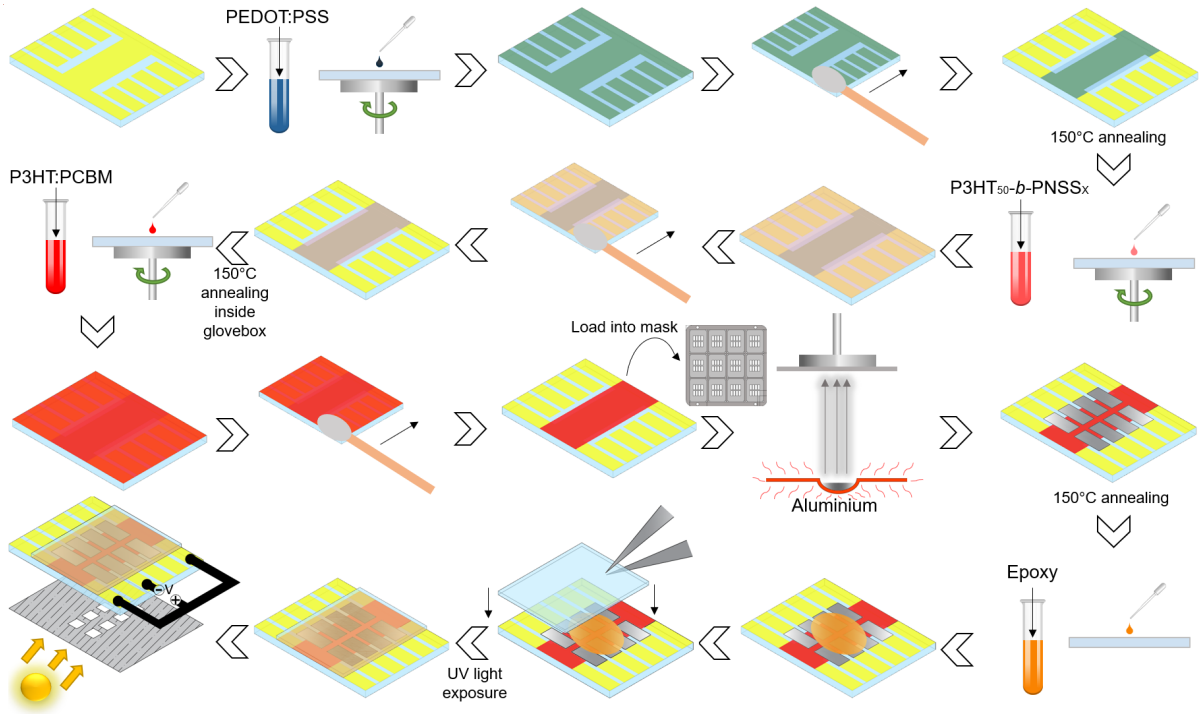

Figure 62: *Sketch showing the device fabrication procedure for the block co-polymer incorporated devices.*

The photovoltaic performance of the devices was obtained as described in section 4.2.5.

6.2.3 Characterisation

The UV-Vis spectroscopy (section 4.2.6), ellipsometry (section 5.2.6), atomic force microscopy (section 5.2.8), and small angle neutron scattering (section 5.2.5) techniques and specifications used in this chapter have been described in previous chapters.

To determine the highest occupied molecular orbital (HOMO) of the thin films, ultraviolet photoelectron spectroscopy was used. In this technique the sample is placed in an ultra high vacuum environment and is then bombarded with ultraviolet photons that remove the valence electrons from the sample. The removed electrons are detected and their kinetic energy KE is measured. An intensity vs KE photoelectron spectrum can then be produced, and using equation 26, where h is Planck's constant, and ν is the

frequency of the ultraviolet photons, the KE can be converted into binding energy BE.

$$h\nu = BE + KE \tag{26}$$

For the type of samples used in this chapter, the kinetic energy at which the left hand cut off occurs in the photoelectron spectrum is equal to the energy gap between the vacuum level and the Fermi level. To determine the HOMO level, the energy gap between the Fermi and the HOMO levels must be added to the KE (see figure 63). The energy gap between the Fermi and the HOMO levels can be determined by superimposing a line through the edge of the photoelectron spectrum at low binding energies and intersect it with a similar line drawn through the background beyond the Fermi edge. The HOMO level can then be determined with the following equation

$$HOMO = KE + E_{\text{HOMO-Fermi}} \tag{27}$$

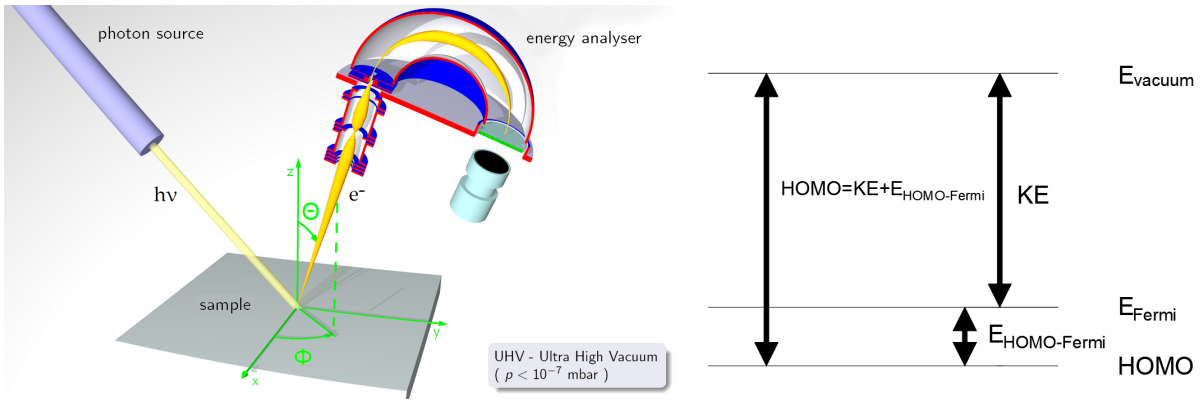

Figure 63: *Simplified schematic representation of the UPS technique (left) and energy level diagram (right) of the different parameters used to calculate the HOMO level of samples. Image on the right originally created by Sahit (`https://commons.wikimedia.org/wiki/File:ARPESgeneral.png`) and reproduced from the Wikimedia Commons free media repository*

To obtain the ultraviolet photoelectron spectra the samples, a Kratos Axis Supra X-ray photoelectron spectrometer with a HeI plasma line with of 21.2 eV was used. The area of analysis was 110 μm diameter spot and the spectra was collected from approximately 20 eV to -5 eV binding energy, at 0.025 eV intervals, 10 eV pass energy for

one 300 second sweep.

6.2.4 Lifetime

For the lifetime test under constant illumination, an Atlas Suntest CPS+ with A 1500 W xenon bulb, quartz IR reducing filters, and internal reflectors was used[302] . The lamp spectrum approximately matches AM1.5G[303]. The combined bulb and internal reflectors irradiance was ≈100 mW cm^{-1}. PCE values reported here are normalised to seven silicon photodiodes that take into account fluctuations in the illumination intensity. The applied bias was swept from 0 to 1 V in 0.01 V intervals with a Keithley 2400 source measurement unit. Devices were held at open circuit between measurements with every device being scanned every ≈15 minutes and were not masked during the measurements. A total of 6 measurements per device, per time unit were obtained to calculate the average values shown in figure 75. Metrics are normalised to their initial values. The temperature of the devices inside the Suntest was 42±3 °C during operation. For the lifetime test not under constant illumination the devices were measured as described in section 4.2.5 immediately after fabrication and then were stored in the dark at 20 °C and 30-40% relative humidity until the next measurement, and then stored again under the same conditions. A total of 8 measurements per sample were taken and averaged to obtain the values shown in figure 76.

6.3 Results and discussion

6.3.1 Thickness of the block co-polymers

An important issue to consider when using an inter-facial layer based on P3HT in the transparent part of the conventional device structure (e.g. between the HTL and the PAL) is the absorption of light by the P3HT chains of such inter-facial layer. This results in less light reaching the active layer and hence less current generated by the device. One way to address this issue is by controlling the thickness of the film. The thinnest inter-facial film allows for maximum transparency. However, if the film is too

thin the quality of the contact between the PEDOT:PSS and the P3HT:PCBM films is hindered, decreasing the fill factor of the devices. First, different thicknesses of the block co-polymers films resulting from different processing conditions were determined. Four different concentration solutions (1 mg mL^{-1}, 2.5 mg mL^{-1}, 5 mg mL^{-1}, and 10 mg mL^{-1}) were prepared and spun-cast at three different speeds (2000 RPM, 4000 RPM, and 6000 RPM) to obtain 12 different thicknesses for each block co-polymer measured with ellipsometry. As shown in figure 64d and table 13, the thickness of the three block co-polymers films decreases as the concentration of the solution decreases, and as the spin speed increases. Such trend is expected, however, the results also show that the thickness of the block co-polymers films have an additional dependence on the length of the PNSS chain. The longer the PNSS chain, the thinner the resulting film is under the same processing conditions, particularly for the higher thicknesses.

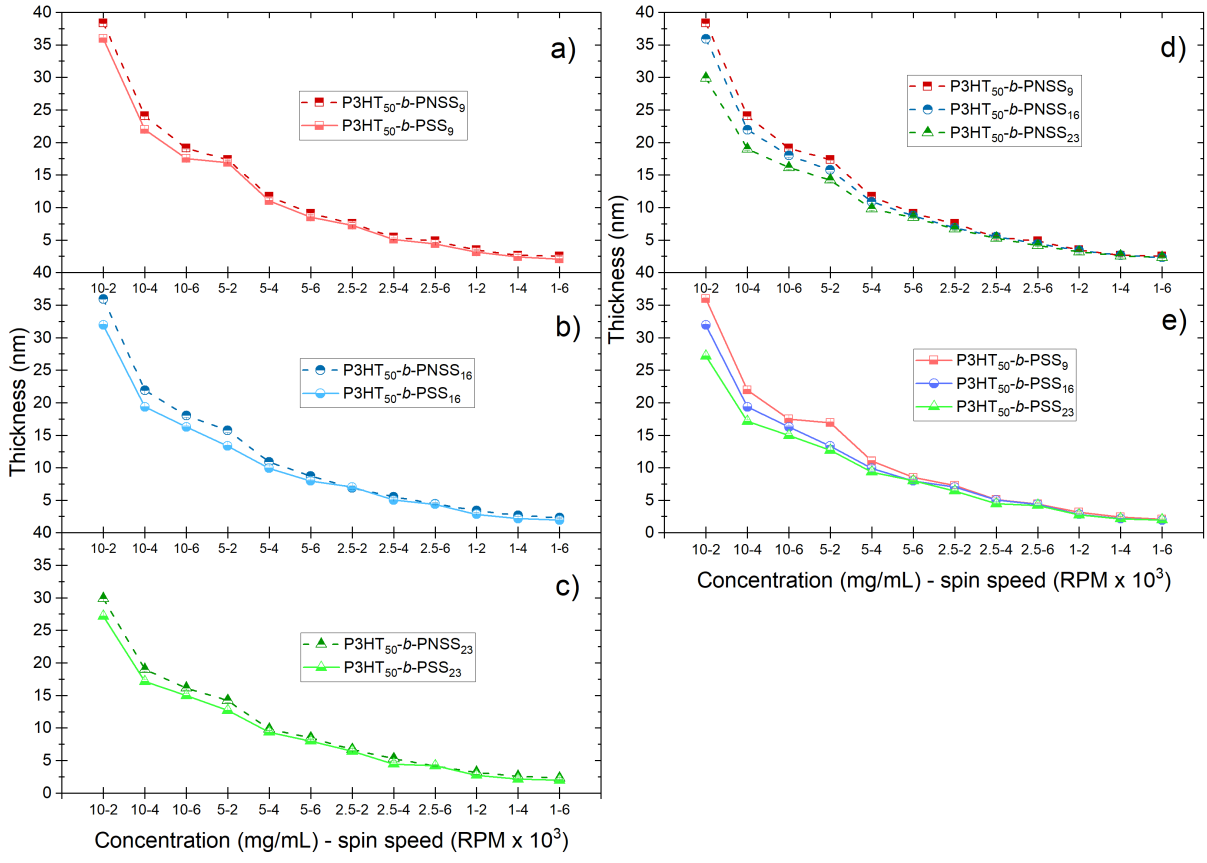

Figure 64: *Thickness of the block co-polymers films as a function of concentration and spin speed. The error bars represent the one standard deviation on each side of the average value. Figures a), b), and c) show the thickness of each block co-polymer separately before and after deprotection, while figures d) and c) show a comparison of the three block co-polymers simultaneously before and after deprotection respectively*

Table 13: *Thickness of the block co-polymer films as a function of the precursor solution concentration and spin speed before and after deprotection. The error bars represent the standard deviation*

	Thickness (nm)					
	Before deprotection			After deprotection		
	$P3HT_{50}$-*b*-$PNSS_9$	$P3HT_{50}$-*b*-$PNSS_{16}$	$P3HT_{50}$-*b*-$PNSS_{23}$	$P3HT_{50}$-*b*-PSS_9	$P3HT_{50}$-*b*-PSS_{16}	$P3HT_{50}$-*b*-PSS_{23}
10 mg mL^{-1} - 2000 RPM	38.38±0.10	35.91±0.05	29.89±0.01	35.96±0.25	31.94±0.16	27.18±0.07
10 mg mL^{-1} - 4000 RPM	24.05±0.07	21.92±0.03	19±0.24	21.95±0.16	19.37±0.3	17.13±0.32
10 mg mL^{-1} - 6000 RPM	19.1±0.08	18.01±0.24	16.13±0.29	17.5±0.17	16.27±0.20	14.96±0.38
5 mg mL^{-1} - 2000 RPM	17.35±0.13	15.78±0.33	14.24±0.33	16.91±0.18	13.34±0.14	12.69±0.07
5 mg mL^{-1} - 4000 RPM	11.71±0.24	10.9±0.28	9.8±0.23	11.03±0.56	9.92±0.41	9.34±0.35
5 mg mL^{-1} - 6000 RPM	9.09±0.12	8.76±0.22	8.48±0.23	8.5±0.27	7.95±0.20	7.97±0.38
2.5 mg mL^{-1} - 2000 RPM	7.54±0.18	6.91±0.29	6.7±0.19	7.23±0.43	7.00±0.16	6.41±0.18
2.5 mg mL^{-1} - 4000 RPM	5.44±0.27	5.52±0.13	5.28±0.31	5.09±0.26	5.01±0.22	4.45±0.21
2.5 mg mL^{-1} - 6000 RPM	4.85±0.24	4.46±0.15	4.17±0.13	4.42±0.26	4.35±0.17	4.19±0.20
1 mg mL^{-1} - 2000 RPM	3.49±0.11	3.39±0.29	3.2±0.33	3.15±0.14	2.82±0.09	2.75±0.07
1 mg mL^{-1} - 4000 RPM	2.64±0.10	2.64±0.18	2.56±0.24	2.43±0.07	2.17±0.05	2.15±0.33
1 mg mL^{-1} - 6000 RPM	2.54±0.08	2.3±0.10	2.3±0.14	2.06±0.05	1.93±0.04	1.98±0.04

In order to investigate the origin of the film thickness dependence on length of PNSS chains of the block co-polymers, the radius of gyration (R_g) of the block co-polymers in solution was determined using small angle neutron scattering (SANS). A 10 mg mL^{-1} solution was prepared for each block co-polymer. Since the theoretically calculated scattering length densities (SLD) of P3HT (6.7×10^{-7} $Å^{-2}$), PNSS (1.02×10^{-6} $Å^{-2}$) , and chlorobenzene (1.82×10^{-6} $Å^{-2}$) are very similar, deuterated chlorobenzene (SLD=4.709×10^{-6} $Å^{-2}$) was used as the solvent to produce a higher contrast between the solvent and the block co-polymers. The R_g of the block co-polymers was then obtained by fitting a Poly Gauss Coil model to the obtained 1D scattering plots. This empirical model describes the scattering from polydisperse polymer chains in theta solvents or polymer melts, assuming a Schulz-Zimm type molecular weight distribution[304–307]:

$$I_{(q)} = scale \cdot I_0 \cdot P_{(q)} + background \tag{28}$$

where

$$I_0 = \phi_{poly} \cdot V \cdot (\rho_{poly} - \rho_{solv})^2 \tag{29}$$

$$P_{(q)} = \frac{2[(1+UZ)^{\frac{-1}{U}} + z - 1]}{(1-U)Z^2} \tag{30}$$

$$Z = \frac{(qR_g)^2}{1+2U} \tag{31}$$

$$U = \frac{M_w}{M_n} - 1 \tag{32}$$

$$V = \frac{M}{(N_A \delta)} \tag{33}$$

and ϕ_{poly} is the volume fraction of the polymer, V is the volume of a polymer coil, M is the molecular weight of the polymer, N_A is Avogadro's Number, δ is the bulk density of the polymer, ρ_{solv} and ρ_{poly} are the SLDs of the solvent and the polymer, respectively, and R_g is the radius of gyration of the polymer coil. As shown in figure 65 and table 14, the R_g of P3HT$_{50}$-*b*-PNSS$_{16}$ is 59.24±0.89 Å which is slightly lower than that of P3HT$_{50}$-*b*-PNSS$_9$ (60.60±0.99 Å). Given that these R_g values are within the statistical uncertainty of each other it is assumed that the difference is minimal. Nevertheless, the lower R_g average value of P3HT$_{50}$-*b*-PNSS$_{16}$ suggests a downward trend that is related to the increased length of the PSS block. This trend is corroborated by the R_g of P3HT$_{50}$-*b*-PNSS$_{23}$ (54.00±0.80 Å), which is considerably smaller than that of P3HT$_{50}$-*b*-PNSS$_{16}$ confirming a trend that reveals an inverse relationship between the R_g and the PNSS chain length. We attribute the decrease in R_g to the inferior solubility of the PNSS block compared to the P3HT block. As mentioned in section 6.1, PSS is not soluble in organic solvents and therefore a neopentyl group was added to it to allow dissolution of the block co-polymers in a single organic solvent. This proved successful, however, the PNSS block remains a low soluble moiety. Therefore, the longer the PNSS block is, the less soluble the block co-polymer becomes. This lower solubility of the block co-polymers with the longer PNSS blocks is not significant enough to have an effect on the macroscopic quality of the solution, however, as a consequence of the phobicity of the PNSS block towards the solvent, the block co-polymer packs into tighter coil as the length of the PNSS block get larger, resulting in a reduced Rg. Morgan & Dadmun[308] also reported a correlation between the decreased Rg of P3HT in solution and its decreased solubility, which leads to the increased P3HT-P3HT interactions that drive the polymer to a more contracted formation. This could explain the reduced film thickness of P3HT$_{50}$-*b*-PNSS$_{23}$

compared to P3HT$_{50}$-*b*-PNSS$_{16}$ and of P3HT$_{50}$-*b*-PNSS$_{16}$ compared to P3HT$_{50}$-*b*-PNSS$_{9}$ when processed under the same conditions. Since the block co-polymers with the longer PNSS blocks pack tighter in solution, they also occupy a lower volume, and when the solution is spin-cast, a lower volume film is formed, resulting in a reduced thickness. This is also supported by the difference in thickness (see figure 64d) between P3HT$_{50}$-*b*-PNSS$_{9}$ and P3HT$_{50}$-*b*-PNSS$_{16}$ which is lower than that of P3HT$_{50}$-*b*-PNSS$_{16}$ and P3HT$_{50}$-*b*-PNSS$_{23}$. This trend seems to emulate that of the Rg and be more significant for the higher thicknesses which confirms that the impact of PNSS block length is subtle, but nonetheless genunine.

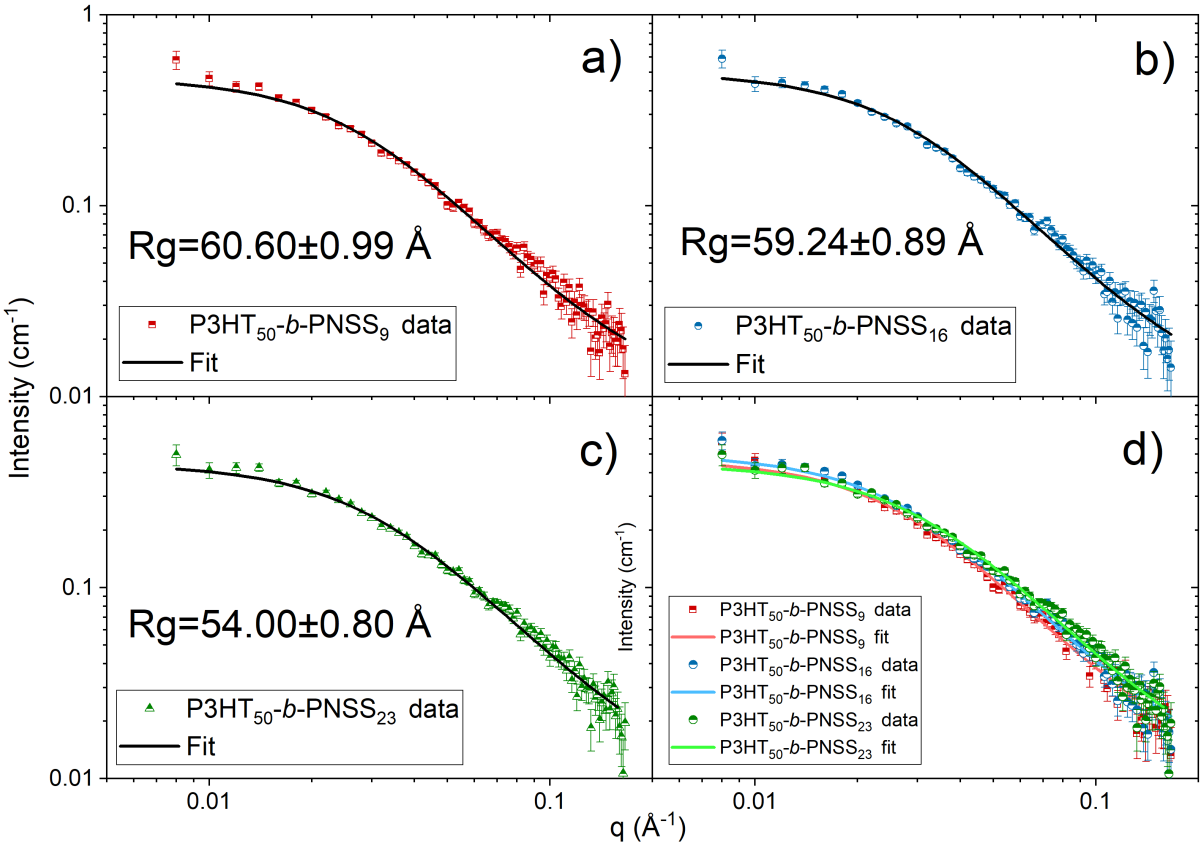

Figure 65: *SANS data and corresponding fits (black) of a) P3HT$_{50}$-b-PNSS$_{9}$, b) P3HT$_{50}$-b-PNSS$_{16}$, and c) P3HT$_{50}$-b-PNSS$_{23}$ dissolved in deuterated chlorobenezene. All data and fits are also shown together (d) for comparison.*

Table 14: *Parameters resulting form fitting the Poly Gauss Coil model to the 1D SANS scattering plots of the three block co-polymers*

	$P3HT_{50}$-*b*-$PNSS_9$	$P3HT_{50}$-*b*-$PNSS_{16}$	$P3HT_{50}$-*b*-$PNSS_{23}$
Rg (Å)	60.60±0.99	59.24±0.89	54.00±0.79
I_0 (cm^{-1})	0.461±0.010	0.490±0.001	0.435±0.008
Polydispersity*	1.22	1.27	1.45
Background (cm^{-1})	0.0094±0.0008	0.0091±0.0008	0.0084±0.0009
Scale	1	1	1
χ^2 (goodness of fit)	1.1824	1.196	1.2329

* Previously obtained in the synthesis report of Erothu et al.[301]

As previously mentioned, in order for the block co-polymers films to function as originally intended in OSCs the polar properties of the PNSS block must be restored by removing the neopentyl group. This is achieved by a thermal deprotection process in which the block co-polymers films are annealed at 150°C for 3 hours. A thermal annealing process is also known to affect the thickness of P3HT based polymers[309] due to the reordering of its polymer chains and increased crystallinity[310;311], and since the block co-polymers are comprised mostly of P3HT, a similar effect can be expected on them. In order to obtain the accurate thickness values of the block co-polymer films that will be incorporated in the devices, their thickness after the deprotection process were measured and found to be slightly reduced by the thermal deprotection process particularly at the higher thicknesses (see figures 64a-d). In addition to the increased crystallinity mentioned above, this decreased thickness is also likely to be caused by the evaporation of the remaining chlorobenzene solvent in the films, which has a boiling point of 132°C. The effects of the thermal deprotection process on the block co-polymers were further investigated with UV-Vis spectrocoscopy and atomic force microscopy in section 6.3.3 of this chapter.

6.3.2 Photovoltaic performance of block co-polymer incorporated devices

The block co-polymers were incorporated as inter-facial films into OSCs in seven different thicknesses, and the photovoltaic performance of the devices was determined and analysed. Devices with the structure ITO/PEDOT:PSS/P3HT-*b*-PSS/P3HT:PCBM/Al

were fabricated in air (except for the deprotection process) and without an electron transport layer for simplicity and industry scalable feasibility. The photovoltaic performance of the devices is shown in figure 66 and table 15. The average PCE, FF, Voc and Jsc of the reference device were 2.35±0.16%, 58.82±3.00%, 0.536±0.010 V, and 7.45±0.28 mA cm^{-2} respectively which are comparable to the values obtained in section 4.3.1 and in the literature for this type of device structure[219;221–223]. The incorporation of P3HT$_{50}$-*b*-PSS$_9$ resulted in a decreased performance of the devices irrespective of the thickness, however, P3HT$_{50}$-*b*-PSS$_{16}$ and P3HT$_{50}$-*b*-PSS$_{23}$ improved the efficiency of the devices optimally by 9%, and 12% respectively when deposited as a 10 nm and a 13 nm film. The devices with a 10 nm thick P3HT$_{50}$-*b*-PSS$_{16}$ inter-facial layer had a PCE of 2.56±0.12%, while the PCE of the devices with a 13 nm thick P3HT$_{50}$-*b*-PSS$_{23}$ inter-facial layer had a PCE of 2.63±0.08%. The enhanced efficiency in both type of devices is mainly caused by a 9% increase in the V_{oc} which was 0.586±0.007 V for the P3HT$_{50}$-*b*-PSS$_{16}$ incorporated device and 0.585±0.008 V for P3HT$_{50}$-*b*-PSS$_{23}$ incorporated device. It is worth noting that even though P3HT$_{50}$-*b*-PSS$_9$ incorporated devices had a significantly lower photovotlaic performance than the reference device, their V_{oc} increased by the same amount that the V_{oc} of the P3HT$_{50}$-*b*-PSS$_{16}$ and P3HT$_{50}$-*b*-PSS$_{23}$ incorporated devices. A slight increase of 2.8% and 6.2% in fill factor of the the P3HT$_{50}$-*b*-PSS$_{16}$ (60.46±2.14%) and P3HT$_{50}$-*b*-PSS$_{23}$ (62.49±1.14%) incorporated devices respectively also contributed to the improved PCE. The increased V_{oc} and FF of the devices with the 10 nm and 13 nm block co-polymer incorporated films compensate for an expected decrease in J_{sc} of 3.2% and 4.0% respectively due to the light absorbance of the block co-polymer layer. The J_{sc} of the P3HT$_{50}$-*b*-PSS$_{16}$ incorporated device was 7.22±0.19 mA cm^{-2} while the J_{sc} of the P3HT$_{50}$-*b*-PSS$_{23}$ incorporated device had a J_{sc} of 7.16±0.17 mA cm^{-2}.

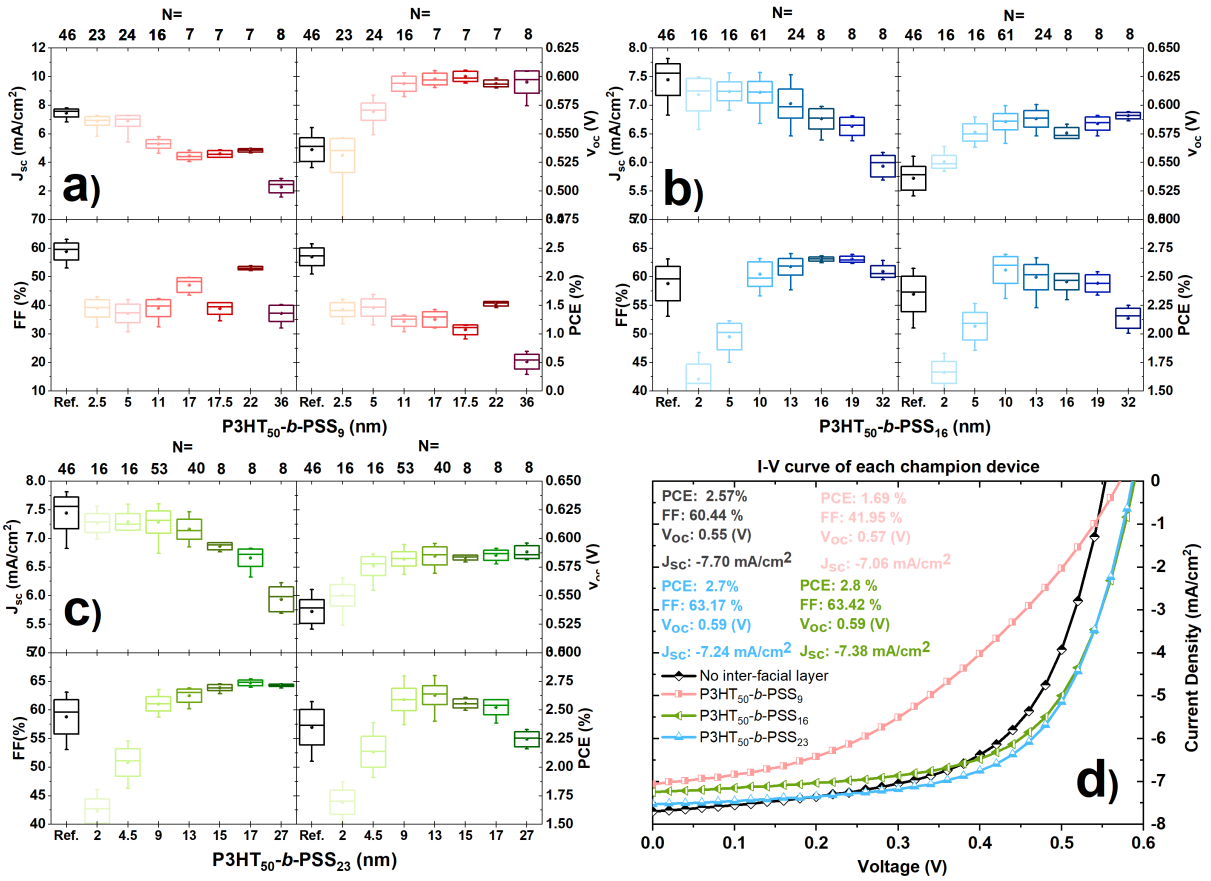

Figure 66: *Box plots showing the Photovoltaic performance (short circuit current, open circuit voltage, fill factor, and power conversion efficiency) of P3HT based OSC devices with $P3HT_{50}$-b-PSS_9(a), $P3HT_{50}$-b-PSS_{16}(b), and $P3HT_{50}$-b-PSS_{23}(c) incorporated as inter-facial layers between the PEDOT:PSS and P3HT:PCBM layers. N equals the number of measurements for each type of device, the width of the box represents one standard deviation on each side of the mean average value, the top and bottom ticks are the maximum and minimum values respectively, the horizontal line in the box is the median, and the circle in the middle of the box is the mean average value. The J-V curve (d) of each champion device is also shown for performance comparison*

Table 15: *Photovoltaic performance metrics of OSC devices with the different block co-polymers incorporated in varying thickness as inter-facial between PEDOT:PSS and P3HT:PCBM. The error bars represent the standard deviation*

	Average				Maximum value				
	Jsc (mA/cm^2)	Voc (V)	FF (%)	PCE (%)	Jsc (mA/cm^2)	Voc (V)	FF (%)	PCE (%)	N
Reference	**7.45±0.28**	**0.536±0.010**	**58.82±3.00**	**2.35±0.16**	**7.82**	**0.555**	**63.14**	**2.57**	**46**
P3HT$_{50}$-*b*-PSS$_9$ (nm)									
2.5	6.89±0.30	0.531±0.015	38.95±3.01	1.42±0.12	7.27	0.546	43.02	1.61	23
5	6.90±0.38	0.569±0.008	37.16±3.18	1.46±0.15	7.24	0.584	41.95	1.69	24
11	5.58±0.31	0.594±0.006	38.98±2.97	1.22±0.08	5.79	0.603	42.34	1.33	16
17	4.44±0.26	0.598±0.005	47.07±2.54	1.25±0.14	4.84	0.605	49.83	1.43	7
17.5	4.59±0.23	0.600±0.004	38.90±2.02	1.07±0.08	4.88	0.606	40.98	1.15	7
22	4.84±0.12	0.594±0.003	53.02±0.55	1.52±0.04	4.99	0.599	53.80	1.56	7
36	2.29±0.42	0.595±0.010	37.12±2.83	0.51±0.13	2.86	0.605	40.22	0.70	8
P3HT$_{50}$-*b*-PSS$_{16}$ (nm)									
2	7.18±0.28	0.550±0.006	42.09±2.59	1.66±0.09	7.50	0.564	46.73	1.83	16
5	7.24±0.16	0.576±0.001	49.51±2.28	2.07±0.12	7.56	0.590	52.32	2.26	16
10	**7.22±0.19**	**0.586±0.007**	**60.46±2.14**	**2.56±0.12**	**7.57**	**0.600**	**63.17**	**2.70**	**61**
13	7.03±0.26	0.588±0.007	61.74±1.44	2.50±0.11	7.53	0.601	64.06	2.67	24
16	6.76±0.18	0.576±0.005	63.10±0.38	2.46±0.07	6.98	0.58	63.65	2.52	8
19	6.63±0.16	0.584±0.006	63.06±0.55	2.44±0.08	6.81	0.591	63.94	2.54	8
32	5.93±0.17	0.591±0.003	60.91±0.01	2.14±0.09	6.18	0.594	62.83	2.25	8
P3HT$_{50}$-*b*-PSS$_{23}$ (nm)									
2	7.27±0.16	0.550±0.009	42.28±2.15	1.69±0.11	7.56	0.566	46.08	1.87	16
4.5	7.29±0.14	0.576±0.008	50.80±2.42	2.13±0.14	7.60	0.586	54.53	2.40	16
9	7.25±0.20	0.582±0.006	61.06±1.26	2.59±0.10	7.60	0.595	63.56	2.80	53
13	**7.16±0.17**	**0.585±0.008**	**62.49±1.14**	**2.63±0.08**	**7.47**	**0.596**	**63.85**	**2.80**	**40**
15	6.86±0.06	0.583±0.002	63.89±0.53	2.55±0.04	6.93	0.585	64.54	2.61	8
17	6.66±0.15	0.585±0.005	64.72±0.50	2.52±0.07	6.82	0.591	65.44	2.60	8
27	5.94±0.22	0.588±0.006	64.31±0.22	2.24±0.06	6.22	0.596	64.54	2.33	8

To determine the origin of the improved V_{oc} of the 10 nm P3HT$_{50}$-*b*-PSS$_{16}$, and 13 nm P3HT$_{50}$-*b*-PSS$_{23}$ incorporated devices, the HOMO energy levels of PEDOT:PSS and the block co-polymers films were studied. As discussed in section 3.5, efficient exciton charge transport is highly dependant on the beneficial alignment between the energy levels of the buffer layers and the active layer. Moreover, it is well known that the V_{oc} of OSCs has a strong dependance on the alignment of the energy levels of the different materials within its structure[216;312;313]. The HOMO level of a P3HT thin film ($\sim$ 100 nm) with a Mw of more than 30,000 measured with UPS has been reported to be in the range of -4.8 to -4.7 eV[314;315]. For holes to efficiently move to the HTL avoiding significant V_{oc} losses, the HTL must have a HOMO higher than the P3HT. To determine if this is the case for the structure of the reference device, the HOMO of a PEDOT:PSS film equal to the one used in the devices was determined with UPS. It was found that the HOMO level of the PEDOT:PSS film was -4.98 eV (agreeing with the value advertised by the provider[316]) which is lower than the HOMO level of P3HT. This is non-ideal for holes to move to since they have to overcome a barrier of $\sim$0.2 eV to move from the P3HT to

the PEDOT:PSS. This results in V_{oc} losses due to the recombination events caused by the holes that are not able to move to the PEDOT:PSS HTL[216] and the excitons that are not successfully dissociated at the PEDOT:PSS-P3HT:PCBM interface. It is possible that the HOMO levels of the block co-polymers provide a a more favourable energy level than PEDOT:PSS for the holes generated in P3HT to travel to. To investigate this, the HOMO levels of 11 nm $P3HT_{50}$-*b*-PSS_9, 10 nm $P3HT_{50}$-*b*-PSS_{16}, and 13 nm $P3HT_{50}$-*b*-PSS_{23} thin films were determined to be -4.50, -4.55, and -4.68 ev respectively. The 11 nm thickness for the $P3HT_{50}$-*b*-PSS_9 was selected for comparison to the similar thicknesses of 10 and 13 nm of the other two block co-polymers. The UPS measurements of the block co-polymers confirmed that they have a higher HOMO than the P3HT which facilitates the transfer of holes from the P3HT to the block co-polymers compared to the transfer from P3HT to PEDOT:PSS (see figure 67). This also implies that it is highly likely that the excitons generated within travel distance of the interface between the block co-polymers and the active layer can dissociate more favourably than the excitons at the interface between PEDOT:PSS and P3HT in the reference device. The more energetically favourable level provided by the block co-polymers results in less V_{oc} losses and thus, a higher V_{oc} of the block co-polymer incorporated devices. This is also confirmed by the fact that the improved V_{oc} of the block co-polymer incorporated devices was increased by approximately the same amount relative to the reference device (see figure 66 and table 15) irrespective of the processing conditions of the block co-polymer (i.e. resluting thickness, and hence UV-Vis transmittance). While it is true that the holes in the block co-polymer layer would still have to overcome an unfavourable energy alignment to travel to the PEDOT:PSS, it is proposed that the electrostatic interactions between the PEDOT:PSS layer and the PSS block in the block co-polymer result in the formation of an intermixed interface that can be considered as homogeneous. This can also be interpreted as the band-bending of the HOMO of PEDOT:PSS to a higher energy level more similar to the one of the block co-polymer enabling the good transition of holes from the block co-polymer to the PEDOT:PSS. It is also possible that the block co-polymer film prevents the contact of PCBM with the PEDOT:PSS ensuring that electrons don't leak to the PEDOT:PSS and eventually to the ITO electrode. The block co-polymer can then be conceptualised as an additional filter for electrons to not reach the hole conducting electrode, and thus avoiding more recombination events that decrease V_{oc} of

the device. The photoelectron spectra of each film is shown in the annex 9.5.

To confirm that the reason behind the improved V_{oc} of the block co-polymer incorporated P3HT devices is the beneficial HOMO levels provided by the block co-polymers for the holes to move from the P3HT, the 4.5, 9, 13, and 17 nm $P3HT_{50}$-*b*-PSS_{23} films were also incorporated in PCDTBT devices. Since PCDTBT has a HOMO level (-5.4 to -5.5[166]) lower than both PEDOT:PSS and the block co-polymer, the holes in PCDTBT would relax more favourable to PEDOT:PSS than to the block co-polymer. This is due to the fact that the HOMO level of PEDOT:PSS (-4.98 eV) is closer to the HOMO of PCDTBT than the HOMO of $P3HT_{50}$-*b*-PSS_{23} (-4.68 eV) is to the HOMO of PCDTBT (see figure 68). Therefore, it would be expected that incorporating $P3HT_{50}$-*b*-PSS_{23} in PCDTBT devices would result detrimental to the V_{oc} of the devices. Moreover, since the PCDTBT donor is not as compatible with the P3HT block in the block co-polymers as the P3HT donor, it is also expected that the fill factor and the overall photovoltaic performance of the device will be lower than the PCDTBT reference device without the interfacial $P3HT_{50}$-*b*-PSS_{23} layer. The photovoltaic performance of the PCDTBT based devices are shown in figure 67 and table 16.

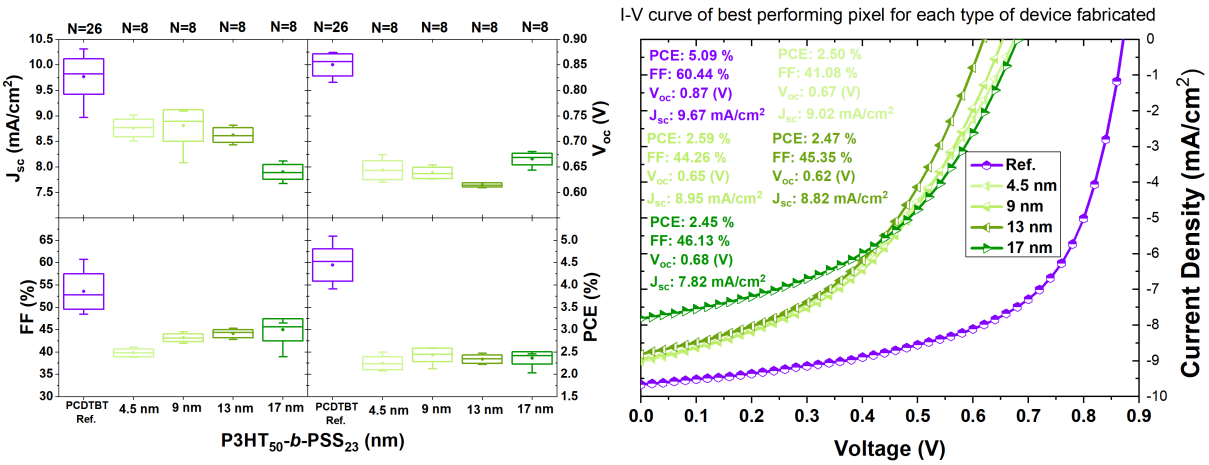

Figure 67: *(Left) Box plots showing the photovoltaic performance (short circuit current, open circuit voltage, fill factor, and power conversion efficiency) of the OSC devices with $P3HT_{50}$-b-PSS_{23} incorporated as interfacial layers between the PEDOT:PSS and PCDTBT:$PC_{70}BM$ layers in different thicknesses. N equals the number of measurements for each type of device, the height of the box represents one standard deviation on each side of the mean average value, the top and bottom ticks are the maximum and minimum values respectively, the horizontal line within the box is the median, and the circle in the middle of the box is the mean average value. (Right) The J-V curve of each champion device is also shown for performance comparison.*

Table 16: *Photovoltaic performance metrics of OSC devices with a P3HT$_{50}$-b-PSS$_{23}$ incorporated as an interfacial between PEDOT:PSS and PCDTBT:PC$_{70}$BM in different thicknesses. The error values represent the standard deviation for 'N' number of measurements.*

	Average				Maximum value				
	Jsc (mA/cm^2)	Voc (V)	FF (%)	PCE (%)	Jsc (mA/cm^2)	Voc (V)	FF (%)	PCE (%)	N
PCDTBT reference	9.77±0.35	0.850±0.021	53.56±3.98	4.45±0.36	10.32	0.874	60.71	5.09	26
4.5 nm	8.76±0.17	0.644±0.018	39.82±0.87	2.25±0.14	9.02	0.674	41.08	2.50	8
9 nm	8.81±0.31	0.638±0.011	43.19±0.87	2.43±0.15	9.09	0.654	44.50	2.59	8
13 nm	8.62±0.14	0.615±0.004	44.12± 0.91	2.34±0.09	8.82	0.619	45.35	2.47	8
17 nm	7.90±0.14	0.666±0.011	44.98±2.48	2.37±0.14	8.12	0.680	46.49	2.45	8

As predicted, the average V_{oc} of the PCDTBT devices with an P3HT$_{50}$-*b*-PSS$_{23}$ interfacial layer was lower (0.644±0.018, 0.638±0.011, 0.615±0.004, and 0.666±0.011 V for the 4.5, 9, 13, and 17 nm thick films respectively) than the average V_{oc} of the reference device (0.850±0.021 V) regardless of the thickness of the block co-polymer used. It is highly likely that the reason behind the reduced V_{oc} in the P3HT$_{50}$-*b*-PSS$_{23}$ incorporated PCDTBT devices compared to the reference devices is the increased V_{oc} losses due to the bigger difference in energy between the HOMO of PCDTBT and the HOMO of P3HT$_{50}$-*b*-PSS$_{23}$ than the HOMO of PCDTBT and the HOMO of PEDOT:PSS. The FF of the P3HT$_{50}$-*b*-PSS$_{23}$ incorporated devices (39.82±0.87, 43.19±0.87, 44.12±0.91, and 44.98±2.48% for the 4.5, 9, 13, and 17 nm thick films respectively) was also lower than the FF of the reference device (53.56±3.98%) regardless of the thickness of the block co-polymer. This could indicate that the contact between the P3HT$_{50}$-*b*-PSS$_{23}$ interfacial layer and PCDTBT is poor resulting in an increased series resistance of the devices.

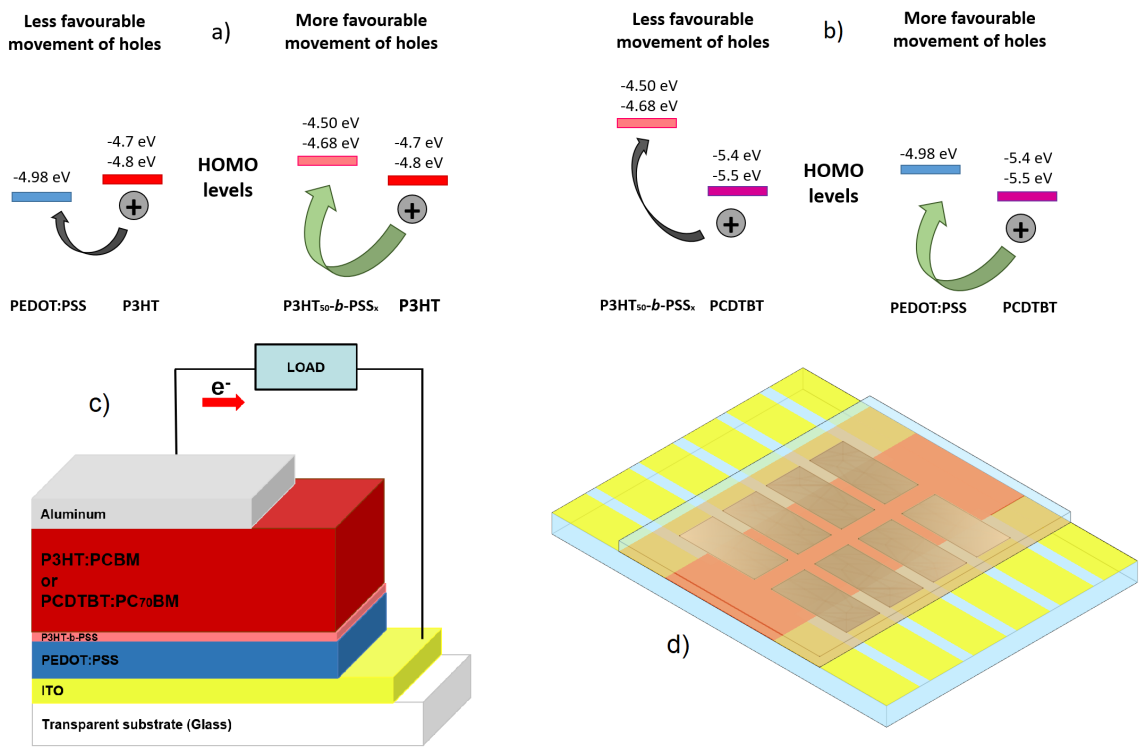

Figure 68: *a) HOMO levels of P3HT, PEDOT:PSS and the block co-polymers and (b) cross sectional view of the structure of the devices.*

In order to corroborate that the decrease in J_{sc} of the block co-polymer incorporated P3HT devices is caused by the light absorption of the block co-polymers, the UV-Vis transmittance of the seven film thicknesses of each block co-polymer used for device fabrication (after deprotection) was measured. Figure 69a, 69b, and 69c show the transmission spectra of the block co-polymers where the three characteristic vibronic shoulders of P3HT films at λ=520 nm, λ=554 nm, and at λ=610 nm can be immediately identified[218]. This is expected since more than 50% of the block co-polymers chains are comprised of P3HT. It is worth noting that PSS absorbs the ultraviolet part (λ<300 nm) of the electromagnetic spectrum[317] and therefore, does not show in these spectra. Moreover, the transmittance of the three block co-polymer films decreases as their thicknesses increase which indicates an increased absorption of light by the thicker films. This is consistent with the decrease in J_{sc} of the devices shown in figure 66 which is also correlated to the increase in thickness of the block co-polymers films. This is further confirmed by figure 69d which shows that the transmittance minima of the 13 nm $P3HT_{50}$-*b*-PSS_{23} film is slightly lower (83.9% at λ=520 nm) than that of the 10 nm $P3HT_{50}$-*b*-PSS_{16} film (85.0% at λ=520 nm) which explains the reduced J_{sc} of the $P3HT_{50}$-*b*-PSS_{23} block co-polymer

incorporated device compared to that of the P3HT$_{50}$-*b*-PSS$_{16}$ incorporated one.

The Uv-vis data also shows that the block co-polymer films with the longer PSS blocks have lower transmittance than the block co-polymer films with the shorter PSS blocks even if the different films have the same thickness. Figure 70 compares the Uv-vis spectra of the 7 nm P3HT$_{50}$-*b*-PSS$_9$ and the 7 nm P3HT$_{50}$-*b*-PSS$_{16}$ deprotected films. Despite having the same thickness, the P3HT$_{50}$-*b*-PSS$_{16}$ film has a higher transmittance than the P3HT$_{50}$-*b*-PSS$_9$ film. Since both films were cast from solutions with the same concentration of block co-polymer (2.5 mg mL^{-1}) and the solutions were prepared by weight, this can be explained by the P3HT$_{50}$-*b*-PSS$_{16}$ film having a lower relative amount of P3HT compared to the P3HT$_{50}$-*b*-PSS$_9$ film. This trend is also shown by non-deprotected films as it can be seen in figure 70 that the 19 nm P3HT$_{50}$-*b*-PNSS$_{23}$ film has a higher transmittance than the 19 nm P3HT$_{50}$-*b*-PSS$_9$ film.

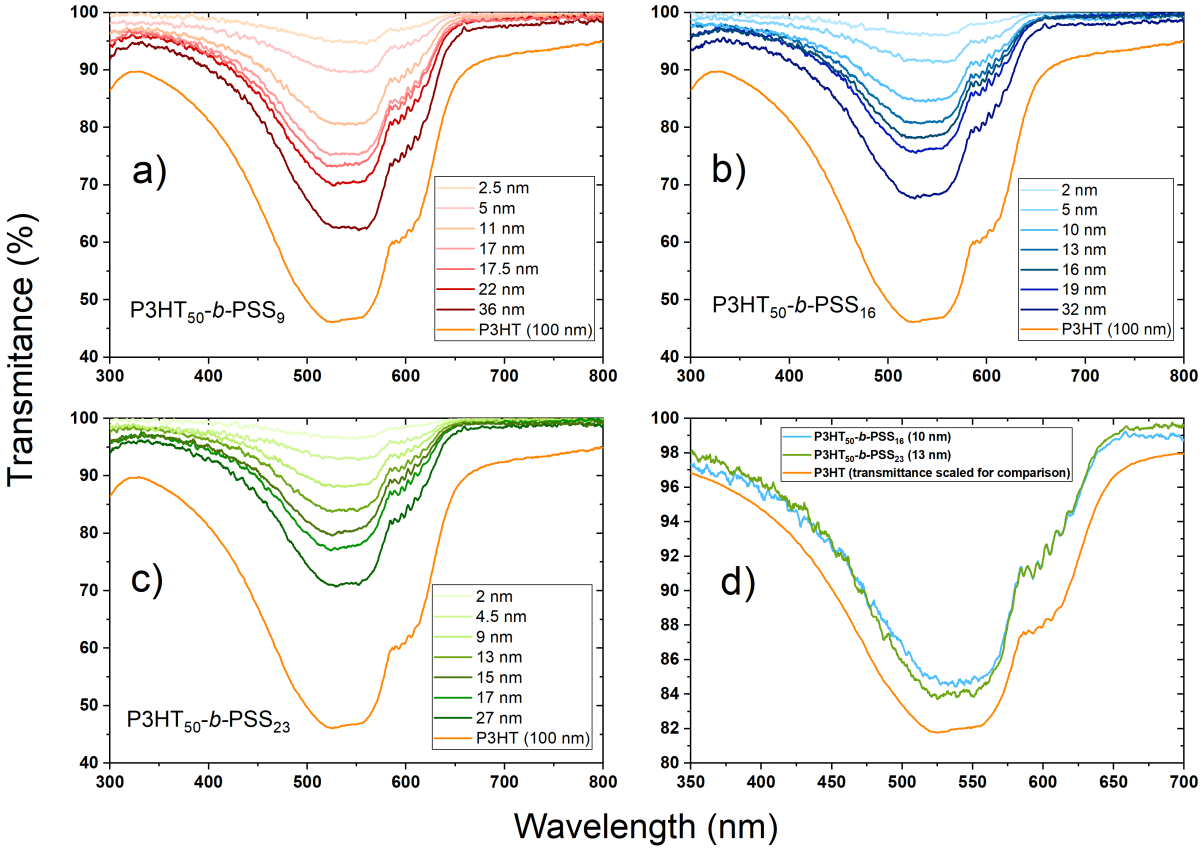

Figure 69: *UV-Vis transmittance of a) P3HT$_{50}$-b-PSS$_9$, b) P3HT$_{50}$-b-PSS$_{16}$, and c) P3HT$_{50}$-b-PSS$_{23}$ deposited as seven different thickness films. The spectra of the 10 nm P3HT$_{50}$-b-PSS$_{16}$ and 13 nm P3HT$_{50}$-b-PSS$_{23}$ films which resulted in the best performing devices when incorporated into OSC is shown separately (d) for comparison*

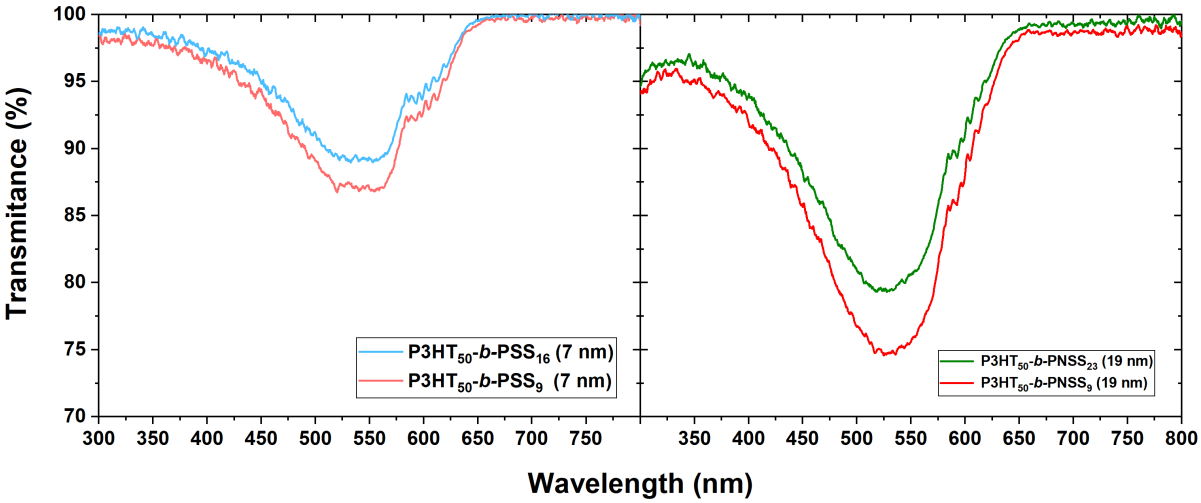

Figure 70: *(Left) UV-vis transmittance of the deprotected 7 nm P3HT$_{50}$-b-PSS$_9$ and P3HT$_{50}$-b-PSS$_{16}$ films. (Right) Uv-vis transmittance of the non-deprotected 19 nm P3HT$_{50}$-b-PNSS$_9$ and the P3HT$_{50}$-b-PNSS$_{23}$ films.*

It is well known that the surface roughness of the different layers that comprise the structure of the device has an impact on its performance[318–322]. Therefore, to investigate the cause of the slightly increased fill factor of the 10 nm P3HT$_{50}$-*b*-PSS$_{16}$ and 13 nm P3HT$_{50}$-*b*-PSS$_{23}$ incorporated devices, the surface of the block co-polymers and PEDOT:PSS films was analysed by atomic force microscopy (AFM). Figures 71a and 71d show the height 2D and 3D images respectively of PEDOT:PSS which has an average root mean square roughness (σ_{RMS}) of 1.49 ± 0.13 nm, a value that is consistent with literature[230;323]. Meanwhile, the 10 nm P3HT$_{50}$-*b*-PSS$_{16}$ (figures 71b and 71e) and 13 nm P3HT$_{50}$-*b*-PSS$_{23}$ (figures 71c and 71f) films have a very similar σ_{RMS} of 0.49 ± 0.05 and 0.51 ± 0.05 respectively which is three times lower than that of PEDOT:PSS. Such smoother surface of the block co-polymers allows the formation of an enhanced contact with the P3HT:PCBM layer improving the fill factor of the device. This could explain why thinner block co-polymer layers (<9 nm) result in a decreased fill factor when incorporated in devices (see figure 66 and table 15). While the 10 nm and 13 nm block co-polymer films are thick enough to overcome the peak to valley average height of the PEDOT:PSS surface (Rz=5.85±0.51 nm), thinner films such as the 2.5 nm and 5 nm, and 2.5nm and 4.5nm of P3HT$_{50}$-*b*-PSS$_{16}$ and P3HT$_{50}$-*b*-PSS$_{23}$ respectively, are sufficiently thin to have their surface roughness significantly affected by the PEDOT:PSS roughness.

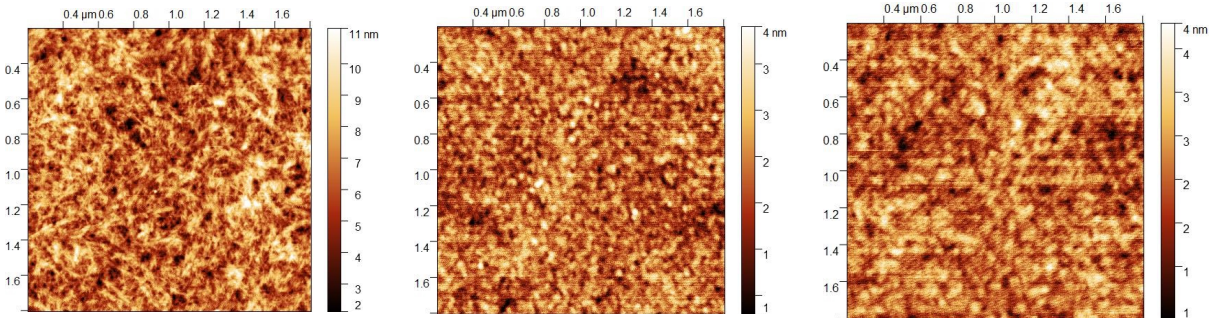

(a) PEDOT:PSS
$\sigma_{RMS} = 1.49 \pm 0.13$ nm
Rz = 5.85±0.51 nm

(b) 10 nm P3HT$_{50}$-*b*-PSS$_{16}$
$\sigma_{RMS} = 0.49 \pm 0.05$
Rz = 2.03±0.17 nm nm

(c) 13 nm P3HT$_{50}$-*b*-PSS$_{23}$
$\sigma_{RMS} = 0.51 \pm 0.05$
Rz = 2.03±0.19 nm

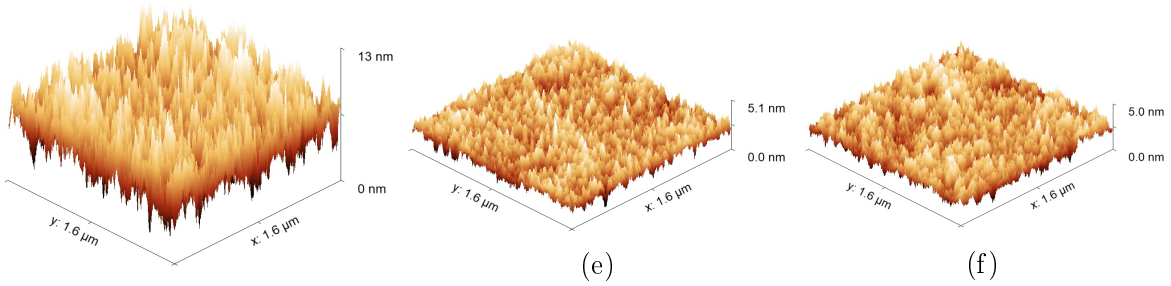

(d) (e) (f)

Figure 71: *AFM height 2D (top) and 3D (bottom) images of pristine PEDOT:PSS (a and d), 10 nm thick P3HT$_{50}$-b-PSS$_{16}$ (b and e), and 13 nm thick P3HT$_{50}$-b-PSS$_{23}$ (c and f). Root mean square roughness (σ_{RMS}) and average peak to valley roughness (Rz) are shown for comparison. The error represent the standard deviation*

To investigate whether the low thickness of the block co-polymers films is responsible for the low fill factor of the devices with a <9 nm block co-polymer film (figure 66), the 2.4 nm P3HT$_{50}$-*b*-PSS$_9$, 2.2 nm P3HT$_{50}$-*b*-PSS$_{16}$, and 2.2 nm P3HT$_{50}$-*b*-PSS$_{23}$ films were analysed with AFM. Figure 72 shows the 2D and 3D height images of such films where some protuberances can be immediately identified. The protuberances shown in the images are likely to be block co-polymer aggregates. The cause of the aggregation of block co-polymer can be attributed to the low amount of block co-polymer spin-coated and consequently the low thickness of the films. Figure 72 seems to indicate that rather than forming a smooth uniform film, the spin-coating of dilute block co-polymer solutions results in unevenly coated films that have several clustering points where the block co-polymer aggregates. These aggregates could cause a poor contact between the block co-polymer layer and the active layer which allows leakage current to flow within the device. This results in the decreased shunt resistance of the device which is evidenced by the decreased fill factor of the devices.

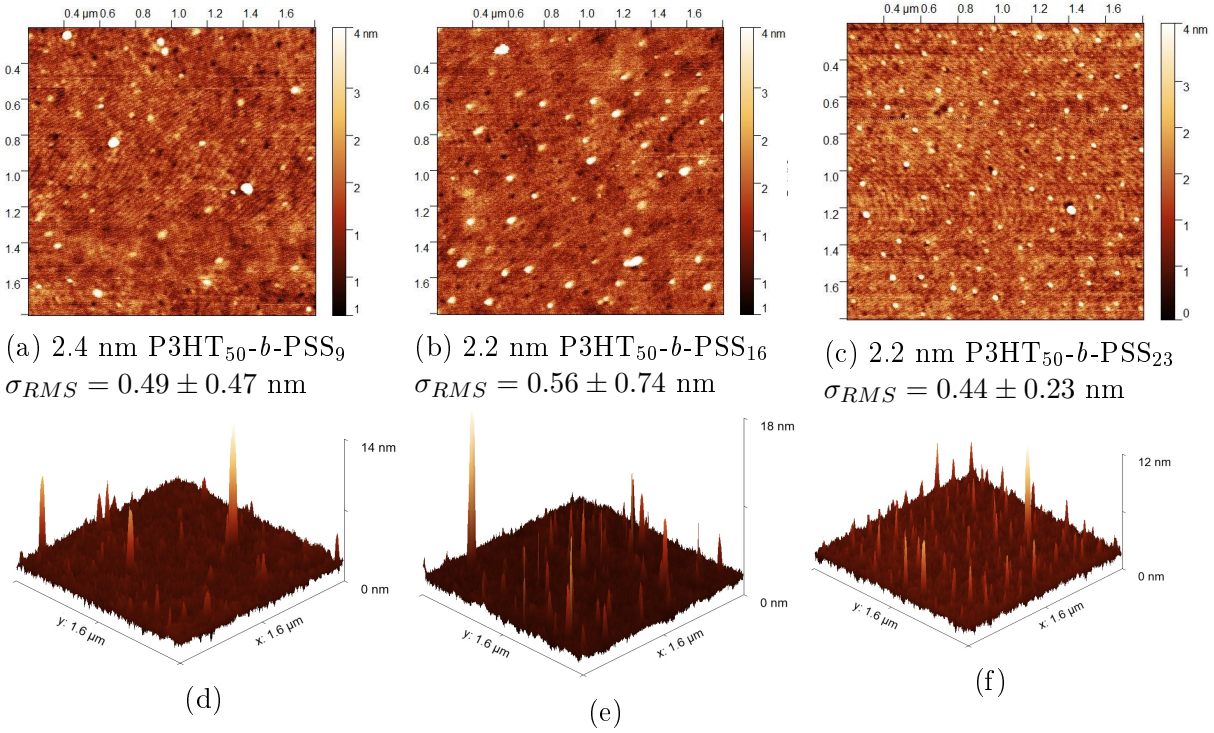

(a) 2.4 nm P3HT$_{50}$-*b*-PSS$_9$ $\sigma_{RMS} = 0.49 \pm 0.47$ nm

(b) 2.2 nm P3HT$_{50}$-*b*-PSS$_{16}$ $\sigma_{RMS} = 0.56 \pm 0.74$ nm

(c) 2.2 nm P3HT$_{50}$-*b*-PSS$_{23}$ $\sigma_{RMS} = 0.44 \pm 0.23$ nm

(d)

(e)

(f)

Figure 72: *AFM height 2D (top) and 3D (bottom) images of 2.4 nm thick P3HT$_{50}$-b-PSS$_9$ (a and d), 2.2 nm thick P3HT$_{50}$-b-PSS$_{16}$ (b and e), and 2.2 nm thick P3HT$_{50}$-b-PSS$_{23}$ (c and f). Root mean square roughness is shown for comparison.*

In figures 66b and 66c it can also be noticed that the fill factor continues to improve in P3HT$_{50}$-*b*-PSS$_{16}$ and P3HT$_{50}$-*b*-PSS$_{23}$ incorporated devices as the thickness is increased further above 10 nm and 13 nm respectively. This is true until the decrease in J_{sc} is significant enough to overcome the benefit of an enhaced contact quality between the PAL and HTL provided by the block co-polymers resulting in an overall decreased fill factor. This corroborates that the fill factor of the block co-polymer incorporated devices benefits from an improved thickness of the block co-polymers. It is worth noting that the smoother surface of the block co-polymers is not the only contributing factor to the enhanced contact. Since the deprotected block co-polymer surface is comprised mostly of P3HT (as demonstrated in section 6.3.3), it is likely that the P3HT chains in the active layer have an enhanced adhesion to the P3HT chains in the block co-polymers than the adhesion they would have to the PEDOT:PSS chains of the HTL. Moreover, since the deprotection process promotes the precipitation of PSS towards the bottom of the film[324] (see section 6.3.3), the PSS chains in the block co-polymer can take part in electrostatic interactions with the PEDOT:PSS enhancing the inter-facial contact

between PEDOT:PSS and the block co-polymers compared to that of PEDOT:PSS and P3HT:PCBM. This also provides an explanation for the reduced photovoltaic performance of the P3HT$_{50}$-*b*-PSS$_9$ incorporated devices regardless of the block co-polymer thickness used. The low performance of P3HT$_{50}$-*b*-PSS$_9$ incorporated devices can be attributed to the insufficient PSS in the block co-polymer film to provide a favourable adhesion to PEDOT:PSS. Since the P3HT block is highly dominant in the block co-polymer, the film behaves functionally as an additional P3HT layer rather than a block co-polymer hindering the inter-facial quality and thus, the fill factor of the device as shown by figure 66a.

6.3.3 Effects of the deprotection process on the block co-polymers

To investigate the effects of the deprotection process on the morphology of the films, UV-Vis was conducted on all the different thickness block co-polymer films. It was found that the vibronic shoulders at λ=520 nm, λ=554 nm, and λ=610 nm increase after the thermal annealing process despite the reduced thickness as shown in figure 64 and table 13. This results in the reduced transmittance of the films at such wavelengths. The increased vibronic peaks can be attributed to the improved crystallinity of P3HT triggered by the thermal annealing step[325]. The three vibronic shoulders of P3HT are caused by the π-$\pi*$ transitions in crystalline π-π stacking[218] and as temperature increases, the P3HT crystals grow and its chains become more ordered improving the stacking and promoting π-π interactions[219;326].

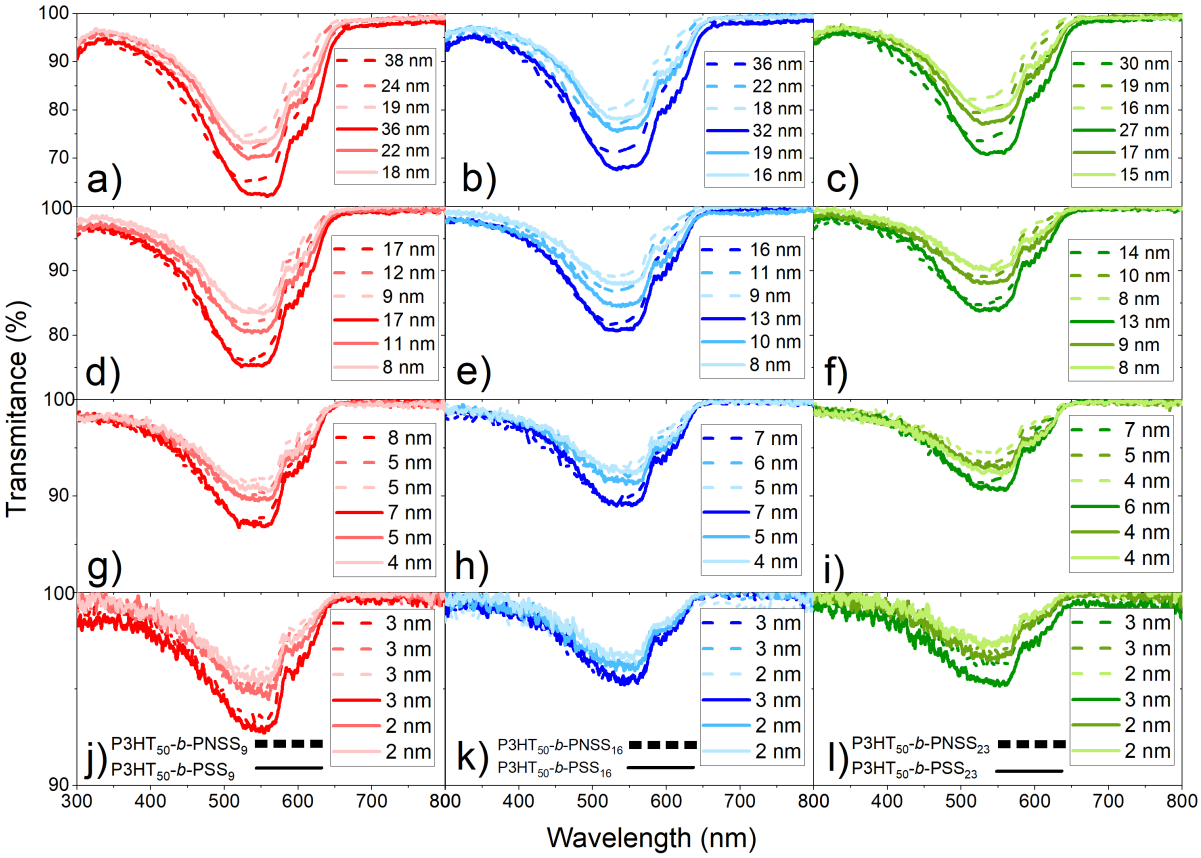

Figure 73: *UV-Vis transmittance of the block co-polymers before and after deprotection at different thicknesses.*

The effect of the deprotection process on the surface of the block co-polymers was also analysed with AFM. Figures 74d, 74e, and 74f show the AFM height images of the 11 nm P3HT$_{50}$-*b*-PSS$_9$, 10 nm P3HT$_{50}$-*b*-PSS$_{16}$, and 13 nm P3HT$_{50}$-*b*-PSS$_{23}$ films respectively before deprotection where plenty of amorphous material can be quickly identified. This indicates that the surface of these films is likely to be dominated by PNSS as it is highly amorphous[301] and it has been shown before that upon solution coating, PSS based polymers tend to have a top rich PSS layer[327]. Upon thermal annealing, such amorphous surface disappears and instead a more crystalline surface emerges as evidenced by figures 74a, 74b, and 74c. This can be attributed to the growth of P3HT crystals and the improved order of its chains enabling P3HT to emerge to the surface, and to the precipitation of PSS due to the 150°C thermal annealing[324]. The AFM height images corroborate that after thermal deprotection the surface of the block co-polymers films is mostly comprised of the P3HT block, which will come into contact with the active layer in device fabrication. Moreover, the improved vertical stratification of PSS means that

there will be more of it at the bottom of the film to come into electrostatic interactions with PEDOT:PSS.

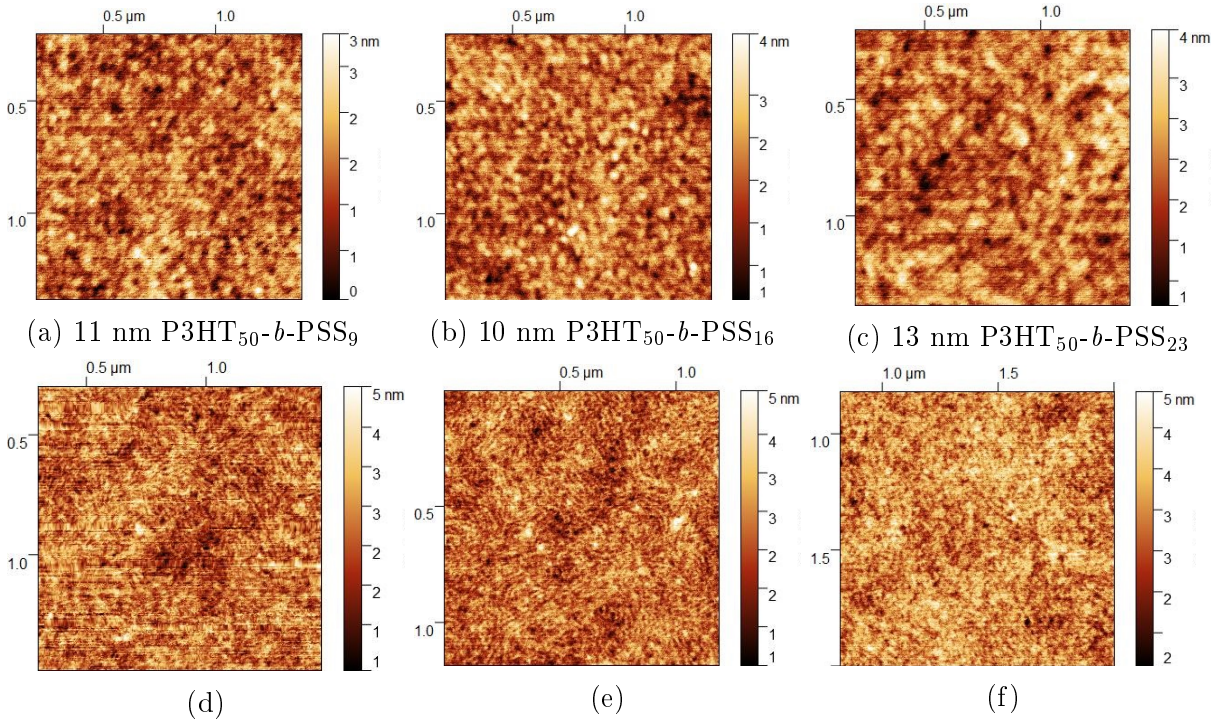

(a) 11 nm P3HT$_{50}$-*b*-PSS$_9$ (b) 10 nm P3HT$_{50}$-*b*-PSS$_{16}$ (c) 13 nm P3HT$_{50}$-*b*-PSS$_{23}$

(d) (e) (f)

Figure 74: *AFM height images of 11 nm thick P3HT$_{50}$-b-PSS$_9$ (a and d), 10 nm thick P3HT$_{50}$-b-PSS$_{16}$ (b and e), and 13 nm thick P3HT$_{50}$-b-PSS$_{23}$ (c and f) before (bottom) and after (top) deprotection*

6.3.4 Lifetime of the block co-polymer incorporated devices

Over time, the physical and chemical interactions between PEDOT:PSS and P3HT:acceptor can degrade the materials and result in detrimental effects for device performance. This interface can experience degradation mechanisms specific to the contact between the adjacent layers such as delamination, intermixing, and chemical reactivity[179;180;286], resulting in the breakdown of device performance over time. The interfacial block co-polymer incorporated between the HTL and the PAL is expected to serve as a barrier to prevent some of these processes to happen given that, as discussed before, the P3HT block in the block co-polymer comes into contact mainly with the P3HT in the PAL, and that the PSS block comes into contact with the PEDOT:PSS. Therefore, lifetime tests were conducted on the devices with the 10 nm P3HT$_{50}$-*b*-PNSS$_{16}$ and the 13 nm P3HT$_{50}$-*b*-PNSS$_{23}$ films to determine if they would degrade at a slower rate than a reference device without any block co-polymer. First, a lifetime test under constant illumination was conducted. As

shown in figure 75, it was found that all the devices degrade at very similar rates having their PCE decreased to <30% of their initial value after 160 hours. Given that all the devices degraded in less than 160 hours at virtually the same rate, it was concluded that the degradation of the devices within this short time was not due to the long term effects described above, but rather due to the quick photochemical degradation of P3HT caused by the reaction of the device with O_2 and H_2O from the atmosphere which is accelerated by constant exposure to light[328–330]. The exposure of P3HT to both UV light and oxygen severely damages the polymer structure resulting in the decreased and blue-shifted UV-vis absorption spectrum of P3HT[331]. Additionally, the exposure of OSCs to constant illumination has been shown to result in an immediate decay of the V_{oc} of the devices which is not exhibited by the similar devices not exposed to constant illumination conditions[332]. The results from the lifetime test under constant illumination, however, show that the stability of the devices with the block co-polymers are not any more susceptible to ambient degradation than the reference devices. This is an interesting finding since the devices with a block co-polymers have an additional layer that could have provided an additional degradation route to the device.

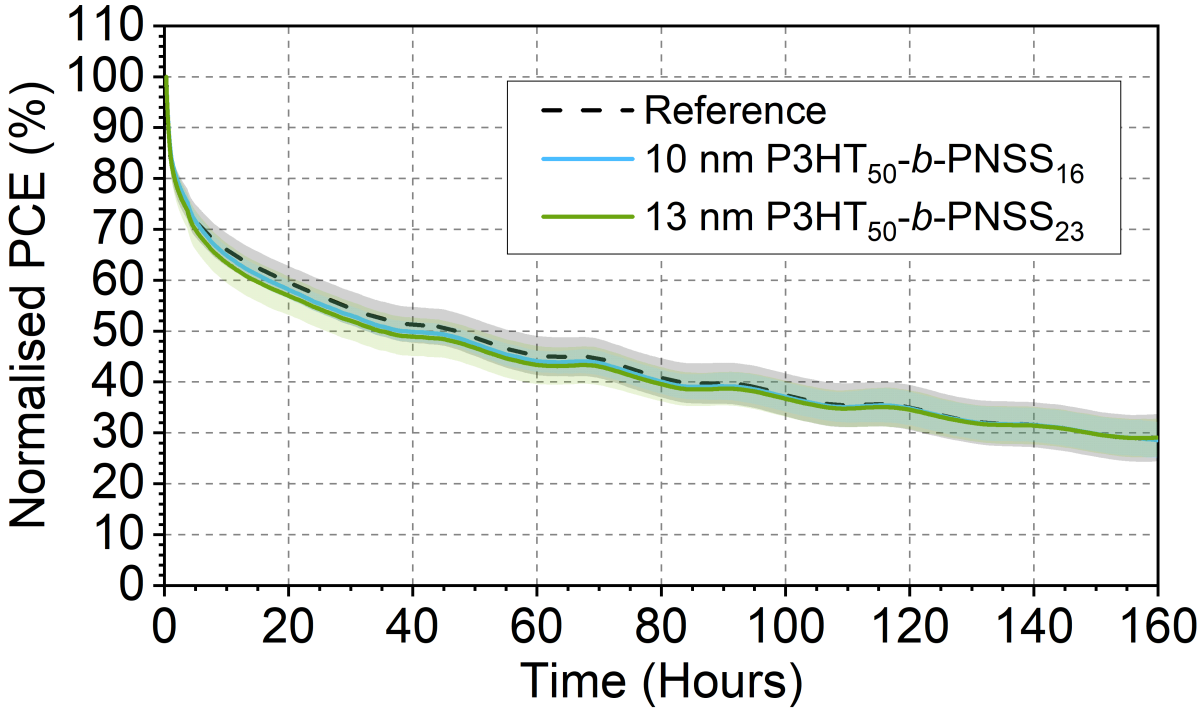

Figure 75: *Normalised power conversion efficiency as a function of time under constant illumination of a reference device, and 10 nm $P3HT_{50}$-b-PSS_{16} and 13 nm $P3HT_{50}$-b-$PNSS_{23}$ incorporated devices. The shade represents the standard deviation*

To determine if the block co-polymers prevent long term degradation mechanisms (e.g. chemical reactivity), a second set of lifetime experiments were conducted on a new batch of devices, this time by storing the devices in the dark under constant temperature and humidity, and exposed to light only when measured occasionally during a period of 2232 hours. This way, the quick photochemical degradation due to the combination of oxygen, water and light that occur during the constant illumination test was minimized. The devices were first measured every 24 hours over 168 hours to obtain multiple data points within the same time period as that used for the constant illumination measurements. As shown in figure 76, none of the devices degraded significantly, and neither did they exhibited different degradation rates during the first 168 hours as evidenced by the widely overlapping error bars. These results confirm that the quick decrease in performance of the devices under constant illumination was due to photochemical degradation, and that such period of time is too short to determine if the block co-polymers prevent any long-term device degradation mechanisms. The devices were then stored for 192 additional hours and then measured again (at 360 hours after fabrication). This time, the reference device showed slightly more degradation (97.40±1.02% normalised PCE), than the device with the block co-polymers (98.87±0.96% and 99.67±0.97% normalised PCE for the device with the 10 nm P3HT$_{50}$-*b*-PNSS$_{16}$, and the 13 nm P3HT$_{50}$-*b*-PNSS$_{23}$ films, respectively). The devices were stored again for 552 additional hours, and within that time, measured 5 more times in which the reference device showed more degradation than the devices with the block co-polymers. After a total of 912 hours since fabrication, the reference device was clearly more degraded (94.33±1.57% normalised PCE) than the ones with the 10 nm P3HT$_{50}$-*b*-PNSS$_{16}$, and the 13 nm P3HT$_{50}$-*b*-PNSS$_{23}$ (97.64±0.58% and 98.09±0.92% normalised PCE, respectively). Finally, all the devices were stored again for 1320 additional hours (a total of 2232 hours since fabrication) and measured twice within that period of time. These two measurements confirmed that the reference device degrades faster than the devices with the block co-polymers. The final normalised PCE of the reference device was 92.33±1.69%, while the final normalised PCE of the devices with the 10 nm P3HT$_{50}$-*b*-PNSS$_{16}$ and the 13 nm P3HT$_{50}$-*b*-PNSS$_{23}$ films were 95.58±1.45%, and 95.12±0.67%, respectively. To corroborate these findings, the experiments were repeated by fabricating another batch of devices and testing them under the same conditions (stored in the dark and exposed to light only when measured) for a

similar period of time. The results of the replicated experiment followed the same trend as figure 76 and thus confirmed that the reference device degrades faster than the devices with the block co-polymers (see figure 87 in the appendixes). From the constant illumination lifetime results, it is concluded that the ambient conditions affect all devices equally. Therefore, it is highly likely that the improved long term stability of the block co-polymer incorporated devices can be attributed to the prevention of degradation mechanisms such as delamination and chemical reactivity resulting from the contact between PEDOT:PSS and P3HT:acceptor that occur in the reference device.

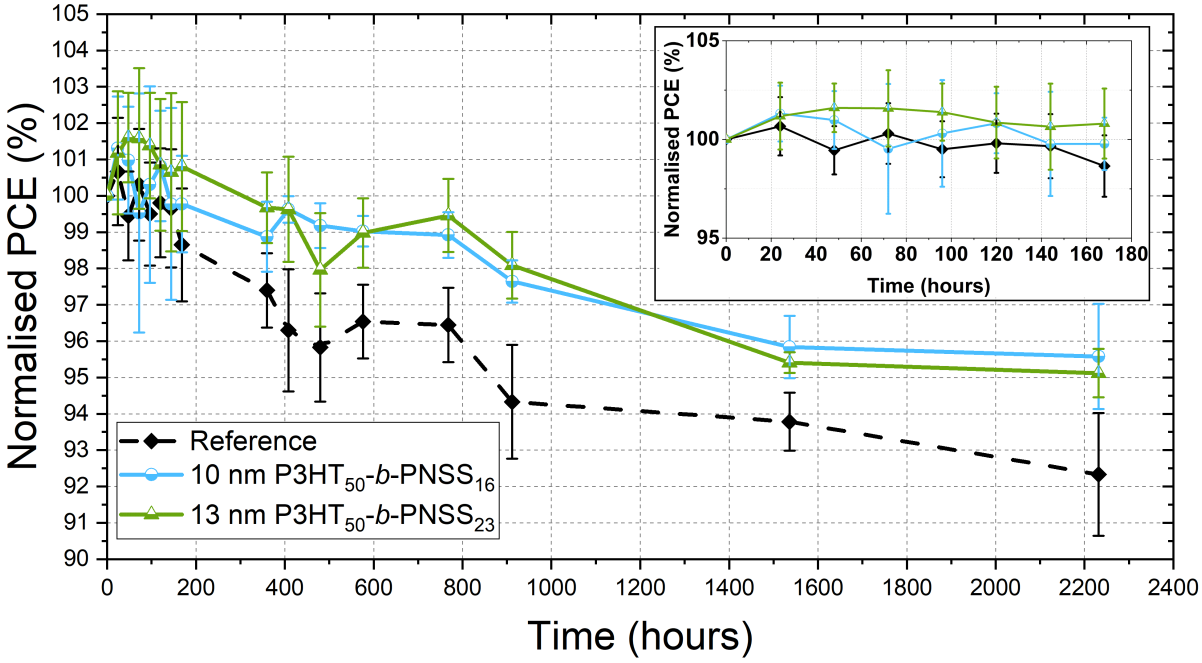

Figure 76: *Normalised power conversion efficiency as a function of time of a reference device, and 10 nm $P3HT_{50}$-b-PSS_{16} and 13 nm $P3HT_{50}$-b-$PNSS_{23}$ incorporated devices. The error bars represent one standard deviation on each side of the average value. Devices were kept stored in the dark except when measured.*

6.4 Conclusions

In summary, three variants of a P3HT-*b*-PSS block co-polymer with different PSS block lengths (9, 16, and 23 units per 50 units of P3HT) were incorporated as an inter-facial layer between the PEDOT:PSS HTL and P3HT:PCBM PAL in OSCs. It was found that the thickness of the block co-polymers depends not only on the concentration of the solution and spin-casting speed, but also on the PSS block length. As the PSS block

length increases, the thickness of the film decreases. When incorporated into devices, $P3HT_{50}$:*b*:PSS_{16} and $P3HT_{50}$:*b*:PSS_{23} improved the efficiency of devices optimally when deposited as a 10 nm and a 13 nm thick film respectively. The improved efficiency is caused mainly by a 9% increase in the V_{oc}, but also by a slight increase of 2.8% and 6.2% in the FF for the $P3HT_{50}$:*b*:PSS_{16} and $P3HT_{50}$:*b*:PSS_{23} respectively. Both the improved V_{oc} and FF compensate for a decrease in J_{sc} caused by the light absorption of the block co-polymers which results in less light reaching the P3HT:PCBM active layer. The improved V_{oc} is a result of the more favourable HOMO levels of the block co-polymer (compared to the HOMO levels of PEDOT) for holes to travel to from the P3HT. The improved FF of the $P3HT_{50}$:*b*:PSS_{16} and $P3HT_{50}$:*b*:PSS_{23} incorporated devices is due to an enhanced contact between the block co-polymer and the P3HT:PCBM layer allowed by the smoother surface of the block co-polymers compared to that of PEDOT:PSS, and to the interactions between the P3HT block with the PAl and the PSS block with the HTL. The FF and PCE of the block co-polymer incorporated devices are only improved if the thickness of the respective block co-polymers is $\leq$ 10 nm due to the presence of small particles contaminating the surface on which the block co-polymers are deposited. The best performing block co-polymer incorporated devices also exhibited a higher normalised efficiency after 2000 hours of storage compared to the reference devices. This was attributed to the block co-polymer acting as a barrier to prevent degradation mechanisms caused by the long-term interactions between PEDOT:PSS and P3HT:PCBM. Finally, it was corroborated that the block co-polymers do not increase the vulnerability of the devices to the combined degradation effects of oxygen, water, and light.

7 Conclusions

The characterisation and optimisation of PEDOT:PSS and $P3HT_{50}$-*b*-PSS_X hole transporting interfacial materials led to the improvement of the photovoltaic performance of devices and the prevention of their long-term degradation meeting the general objectives presented in section 1.1, and the specific objectives presented in section 3.8.

Chapter 4 focused on the first specific objective which was the successful fabrication of OSC devices that performed at a standard compared to those reported in literature. It was found that an electron beam evaporation technique used to deposit the metal electron conducting electrode can be highly detrimental for the performance of the device. This is due to the transition from crystalline to amorphous P3HT which is evidenced by the complete disappearance of two of its three vibronic peaks and the significant decrease and blueshift of the other one. This is highly likely to be caused by the byproduct radiation from the electron beam striking the source material (Al). This byproduct radiation was attributed to the fixed high voltage settings of the electron-beam evaporator used. In contrast, a thermal evaporation technique used to deposit the Al proved to be successful and reliable for producing standard performing P3HT and PCDTBT based devices. Once the methodology to fabricate consistently standard performance OSCs was developed, it was possible to investigate different methodologies to improve the interface between PEDOT:PSS and P3HT:PCBM.

In chapter 5 the second specific objective was addressed. This was done by using four zwitterion species to dope PEDOT:PSS in an attempt to improve its conductivity, and by investigating the mechanisms of morphology modification of PEDOT:PSS (both in dispersion and as a thin film) after being doped with a asymmetrically charged dopant such as an ionic liquid, acids, surfactants, or, in this case, zwitterions. Only one of the zwitterions (DYMAP) successfully decreased the thin film sheet resistance of the PEDOT:PSS without causing the dispersion to gelate. The mechanisms of morphology modification of the PSS backbone chain in the PEDOT:PSS dispersion after DYMAP doping were investigated with small angle neutron scattering and using a deuterated version of PEDOT:PSS (PEDOT:d-PSS). It was found that the interchain spacing between d-PSS backbone chain segments increases as the concentration of DYMAP increases, probably

due to steric hindrance between d-PSS and the formation of worm-like DYMAP micelles which are suspected to grow as a function of the dopant concentration. Eventually, the worm-like micelles grow long enough to form an interconnected network between themselves and with the negatively charged d-PSS backbone chain segments. The worm-like micelles and d-PSS backbone interactions are attributed to coulombic attraction forces between the negatively charged d-PSS and the positively charged quaternary ammonium ion in DYMAP resulting in the gelation of the dispersion. This later interaction results also in the increase of the screening length of the neutralised d-PSS segments that are attached to the PEDOT oligomers due to the neutralisation of the adjacent negatively charged d-PSS segments.

Subsequently, DYMAP doped PEDOT:PSS films were investigated with neutron reflectivity to determine their vertical stratification. It was found that the thickness of the films increases as the DYMAP concentration increases and that the surface roughness of the films decreases as the DYMAP concentration increases. Moreover, it was found that at a low doping concentration, DYMAP segregates at the bottom of the film causing the entire film to separate into a quasi bi-layer film. However, at a higher doping concentration, the PEDOT:PSS:DYMAP film exhibits complete intermixing resulting in a homogeneous film which also exhibits an increase of almost two orders of magnitude compared to an un-doped PEDOT:PSS film. The DYMAP doped PEDOT:PSS films were then incorporated as an HTL in P3HT and PCDTBT devices, and an increase in the photovoltaic performance of the device due to the increased conductivity was expected. However, it was found that the devices with the DYMAP doped PEDOT:PSS HTLs performed worse than the control devices with a pristine PEDOT:PSS HTL. This was attributed to the increased phobicity of the DYMAP doped PEDOT:PSS films towards the organic solvent in which the active layer was dissolved. This resulted in the poor contact quality between the HTL and the active layer which caused a decreased V_{oc} and FF of the devices. Additionally, it is suggested that DYMAP may induce an energy change in PEDOT:PSS that hinders its electron block capabilites resulting in the increase of recombination events happening in the HTL of the devices. At this point it became clear that the quality of the contact and beneficial energy aligment between the PEDOT:PSS HTL and the P3HT:PCBM layer plays a very important role on the

performance of the devices and therefore, the next step was to investigate a method to improve this interface.

The third specific objective was to incorporate three variants of a P3HT-*b*-PSS block co-polymer as an interfacial layer between the PEDOT:PSS HTL and the P3HT:PCBM active layer to improve the interface quality between such layers and prevent long-term degradation mechanisms caused by the reaction between PEDOT:PSS and P3HT. This was done in chapter 6, and it was found that incorporating a 10 nm $P3HT_{50}$-*b*-PSS_{16} or a 13 nm $P3HT_{50}$-*b*-PSS_{16} interfacial into the devices improves their photovoltaic performance. This is mainly attributed to an increase in the V_{oc} of the block co-polymer incorporated devices caused by the beneficial HOMO alignment of the block co-polymers with the HOMO of the P3HT donor for improved charge transport from the active layer to the block co-polymer. Additionally, an enhanced contact between the block co-polymer interfacial layer and the adjacent layers is allowed by the interactions of the PSS block with the PEDOT:PSS and the P3HT block with the P3HT of the active layer, and by the smoother surface of the block co-polymer (compared to the rougher surface of PEDOT:PSS). Such enhanced contact results in an increased FF of the block co-polymer incorporated devices compared to the control devices. Moreover, the block co-polymer serves as a barrier to prevent the long-term degradation mechanisms of the device caused by the reaction between the PEDOT:PSS and P3HT:PCBM layers. This last chapter demonstrated that a specifically designed block co-polymer can be incorporated as an interfacial layer in OSCs for improved photovoltaic performance and lifetime, fulfilling the objective of this thesis of improving the quality of the interface between the HTL and active layer of OSCs.

8 Future work

This thesis presented a systematic and comprehensive study to improve the efficiency and stability of OSCs through the characterisation and optimisation of the hole transport interface. Thus, a typical optimisation process that leads to the improvement of a specific technology was demonstrated. However, due to the specific focus on the objectives set for this thesis, there were some aspects, which will be discussed below, of this research that were not addressed or studied in detail that could potentially provide valuable knowledge to the further improvement of OSCs technology. Moreover, the methodologies presented in chapters 6 and 5.3.2 to optimise hole transporting materials for improved photovoltaic performance and stability of devices, can be used in the future to design interfacial materials that can be incorporated in higher performing active layer blends such as PBDB-T-Cl or PM6. Therefore, some suggestions for further research based on this thesis are presented here for members of the scientific community who could potentially continue the investigation of the improvement of the interface quality between the HTL and active layer in OSCs.

As mentioned in the conclusions section of chapter 4, the high voltage used for the electron-beam evaporation was probably the factor causing the degradation of P3HT in the active layer of the devices. It is recommended that a systematic study of e-beam voltage vs device performance and P3HT damage is done to determine the correct parameters for e-beam evaporation of electrodes for OSCs. Additionally, a gas x-ray detector can be placed next to the device in the evaporation chamber to measure the byproduct radiation produced by the electron beam striking the evaporation source. This experiment can be repeated for other source materials such as Ag, Au, or Pt, which are also commonly used in OSCs.

Chapter 5 provided an in-depth study on the morphological changes that PEDOT:PSS experiences after DYMAP doping, however, there are still some areas of further research that would lead to improve the current knowledge on dual-charge doped PEDOT:PSS. First, an ultra small angle neutron scattering experiment could be conducted to understand the morphology modification of PEDOT:PSS at the micron scale level to understand the interactions between the colloidal PEDOT:PSS structures with each other

in the dispersion. This could provide insight on the charge transfer at the micron scale within DYMAP doped PEDOT:PSS which could further explain the reason for conductivity improvement. In section 5.3.3 it was also shown that the conductivity increased dramatically from the 10 mM to the 20 mM sample, which is indicative of a percolation effect. This can be investigated by simply measuring the sheet resistance and thickness of several DYMAP doped PEDOT:PSS films with several doping concentrations between 10 and 20 mM, and plotting their conductivities against the doping concentration to determine the threshold at which the conductivity is increased dramatically. Regarding the bi-layer separation mentioned in section 5.3.4 the reason behind DYMAP precipitating towards the bottom of the film could be determined by calculating the surface energies of the silicon substrate and a DYMAP film. This can be done by measuring the contact angle of different solvents on the silicon and DYMAP films. Finally, the poor contact between the DYMAP doped PEDOT:PSS films and the active layer due to the phobicity of the doped HTL to the active layer solvent described in section 5.3.6 could be addressed by trying different solvents for the active layer blends, preferably, solvents with a higher polarity such as chloroform, dimethylformamide, and 2-propanol. However, if this method is not successful, a more complicated approach would be needed such as synthesising polar soluble active layer materials. It is also advised that the LUMO levels of DYMAP doped PEDOT:PSS are obtained (low energy inverse photoelectron spectroscopy can be used for this) to determine if the electron blocking capabilities PEDOT:PSS are hindered by DYMAP. Finally, regarding other zwitterions, a correlation between the length of the non-polar hydrocarbon chain of the zwitterion and the decrease in sheet resistance was found. It is recommended that other zwitterions with longer hydrocarbon chains than DYMAP are used to dope PEDOT:PSS to study the effect that the length of the hydrocarbon chain has on the conductivity of PEDOT:PSS.

Chapter 6 provides perhaps the most interesting possibilities for future research. First, even though the P3HT-*b*-PSS block co-polymers improved the photovotlaic performance of P3HT:PCBM based devices and prevented some long-term degradation mechanisms, there are improvements that can be done to the processing of the block co-polymers, specifically, to the deprotection step. An annealing annealing treatment of 3 hours and 150°C for the deprotection of the block co-polymers is costly at the indus-

try scale level and therefore not ideal for the commercialization of devices. Therefore, different and more simple deprotection routes should be investigated such as an electromagnetic radiation treatment. However, given that the principle of using a specifically designed block co-polymer to improve the interface between the HTL and the active layer was proven to be successful, the most exciting opportunity for future research is the synthesis of other block co-polymers that are compatible with higher performing donor materials such as PBDB-T-Cl or PffBT4T-2OD and with PEDOT:PSS or other hole transporting materials such as the ones mentioned in section 3.7. This could result in the improved performance and stability of devices with higher performing blends. Moreover, specifically designed block co-polymers could also be used for improving the interface between the materials used in tandem devices to prevent degradation due to the reaction between the materials of such complex structures.

9 Appendices

9.1 Relative errors for figure 43

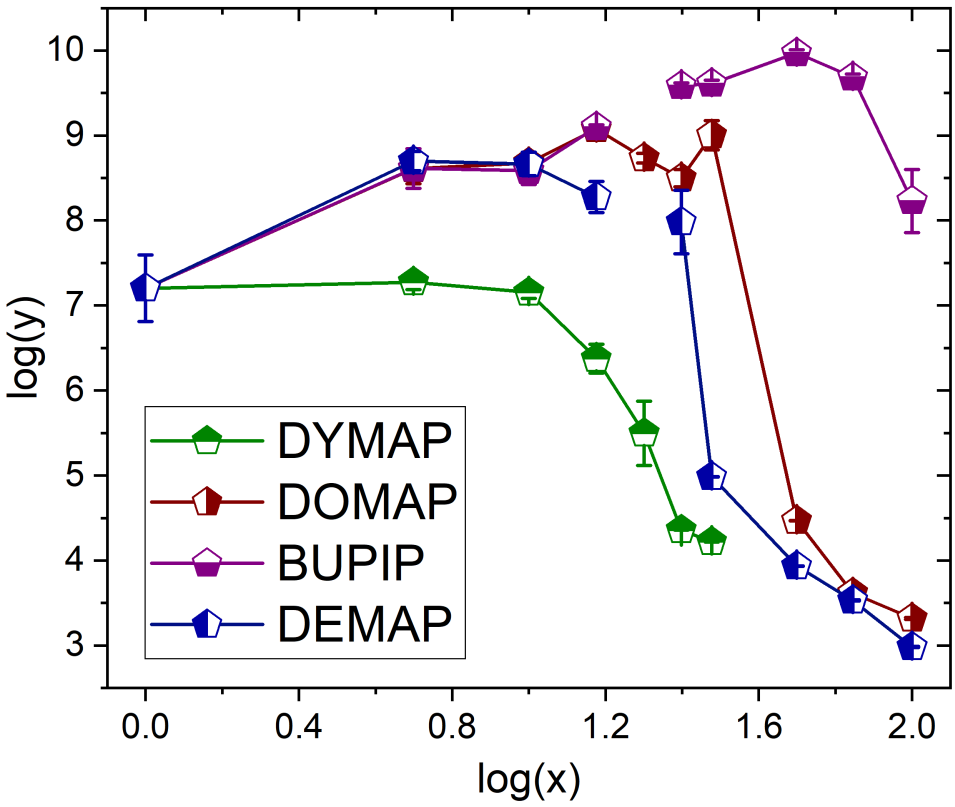

Figure 77: *Sheet resistance measurements of zwitterion doped PEDOT:PSS films as a function of the doping concentration. The relative errors are shown for comparison.*

9.2 Beyond the chi squared analysis of the models

To further confirm our findings, we performed an additional analysis for all the models presented in this work based on the following considerations:

1. Free fitting all the parameters of the system (i.e. SiO_2, PEDOT:PSS and additional layers).

2. Fitting the system with the SiO_2 layer highly constrained to represent consistency across the different wafers.

3. Fitting the systems with n+1 layers of PEDOT:PSS, where n is the number of layers which gives the best fit.

The analysis of the fits were based on the following considerations:

1. The goodness of the fit, which is represented by the probabilistic evidence.
2. The change in SLD and the data's sensitivity to it.
3. Improvement of the fit over a simpler model

All of the fits were contstrained to the Nevot Croce theory[269], so roughness could not be more than half the layer thickness, and no sharp transitions were allowed. Fits were stopped when the models were stable to perturbation, i.e. obtain a fit, then change one of the parameters then refit and the same solution is achieved. The normalisation constant used was a log with error-bar based figure of merit (described in GenX help) as this gave greater sensitivity across the range of Q. The reflectivity curves are all of high enough quality to resolve the differences we are looking at.

9.2.1 Native oxide layer

This was set for all wafers to be around 40 Å thick, with an SLD around 3.5×10^{-6} Å^{-2}.

9.2.2 Pristine PEDOT:PSS

Table 17: *Figure of merit (FOM), scattering length densities (SLD's) and total thickness resulting from 1 layer and 2 layer models for the pristine sample.*

Pristine PEDOT:PSS		
	1 layer	2 layers
FOM	1.65	1.648
SLD 1 (10^{-6}Å^{-2})	1.399	1.4
SLD 2 (10^{-6}Å^{-2})	-	1.399
Total thickness (Å)	481	481

As shown in table 17 , and figures 78 and 79, the data is clearly described as well as it could be using a single PEDOT-PSS layer. The SLD and fit curves both look almost identical for the 1 and 2 layer models.

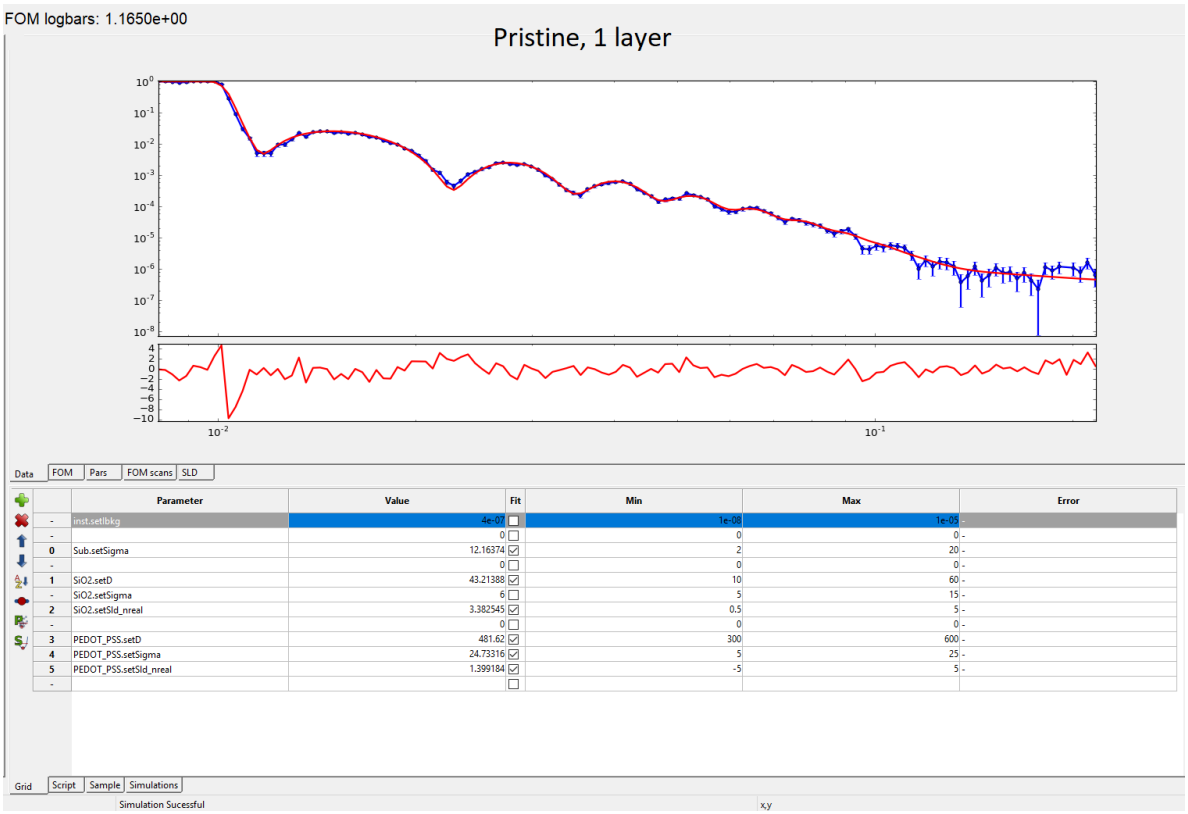

Figure 78: *Neutron reflectivity data, fit, and fitting parameters for the 1 layer model of the pristine sample in GenX.*

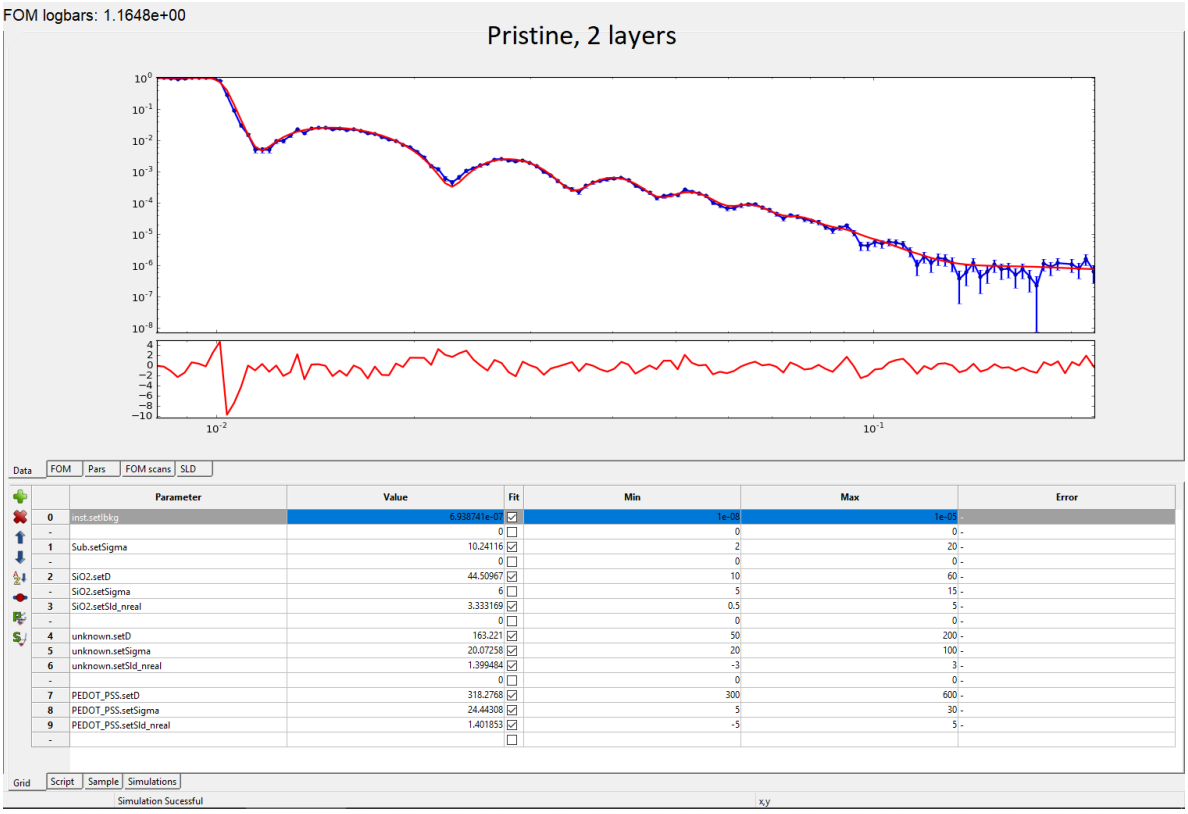

Figure 79: *Neutron reflectivity data, fit, and fitting parameters for the 2 layer model of the pristine sample in GenX.*

9.2.3 10 mM DYMAP doped PEDOT:PSS

Table 18: *Figure of merit (FOM), scattering length densities (SLD's) and total thickness resulting from 1 layer, 2 layers, and 3 layer models for the 10 mM sample.*

10 mM DYMAP doped PEDOT:PSS

	1 layer	2 layers	3 layers
FOM	1.28	1.10	1.10
SLD 1 (10^{-6}Å^{-2})	1.16	1.11	1.11
SLD 2 (10^{-6}Å^{-2})	-	1.24	1.18
SLD 3 (10^{-6}Å^{-2})	-	-	1.24
Total thickness (Å)	554	554	554

As shown in table 18 and figures 80, 81, and 82, the fit here is improved both by the metric of FOM, and visually, by the splitting of the PEDOT:PSS into two distinct layers. Adding a third layer to the system does not improve the FOM, but interestingly it does seem to reproduce the SLD of the 2 layer model, suggesting a stable minima in the fit.

Compared to the pristine film, this film (10 mM) is thicker and has a lower SLD. The preparation of the films was identical in the procedure, but the addition of the DYMAP does increase the viscosity of the solution, thus a thicker film is expected. In addition, since DYMAP causes the films to swell in this system, it is also likely to have changed the SLD of the film. Since the combination of increased viscosity and swelling can both have the same effect, we cannot easily disentangle each's contribution.

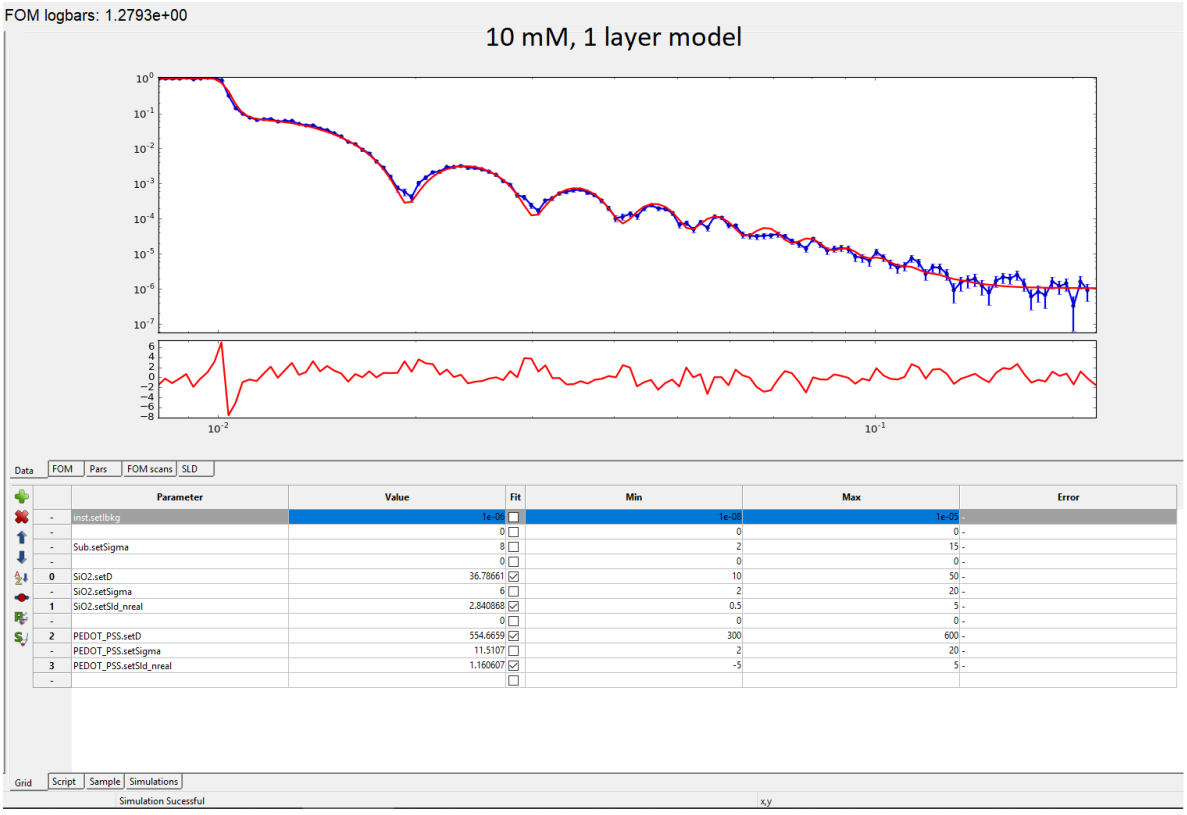

Figure 80: *Neutron reflectivity data, fit, and fitting parameters for the 1 layer model of the 10 mM sample in GenX.*

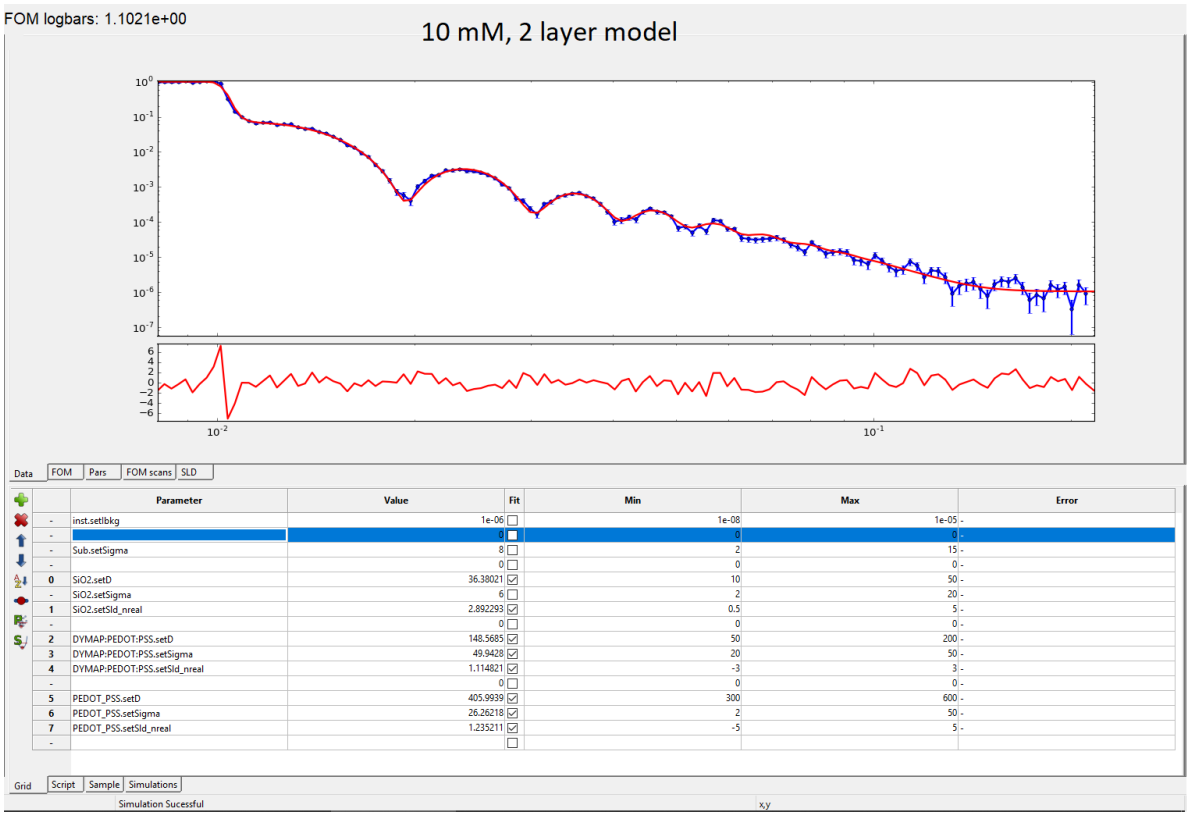

Figure 81: *Neutron reflectivity data, fit, and fitting parameters for the 1 layer and 2 layer models of the 10 mM sample in GenX.*

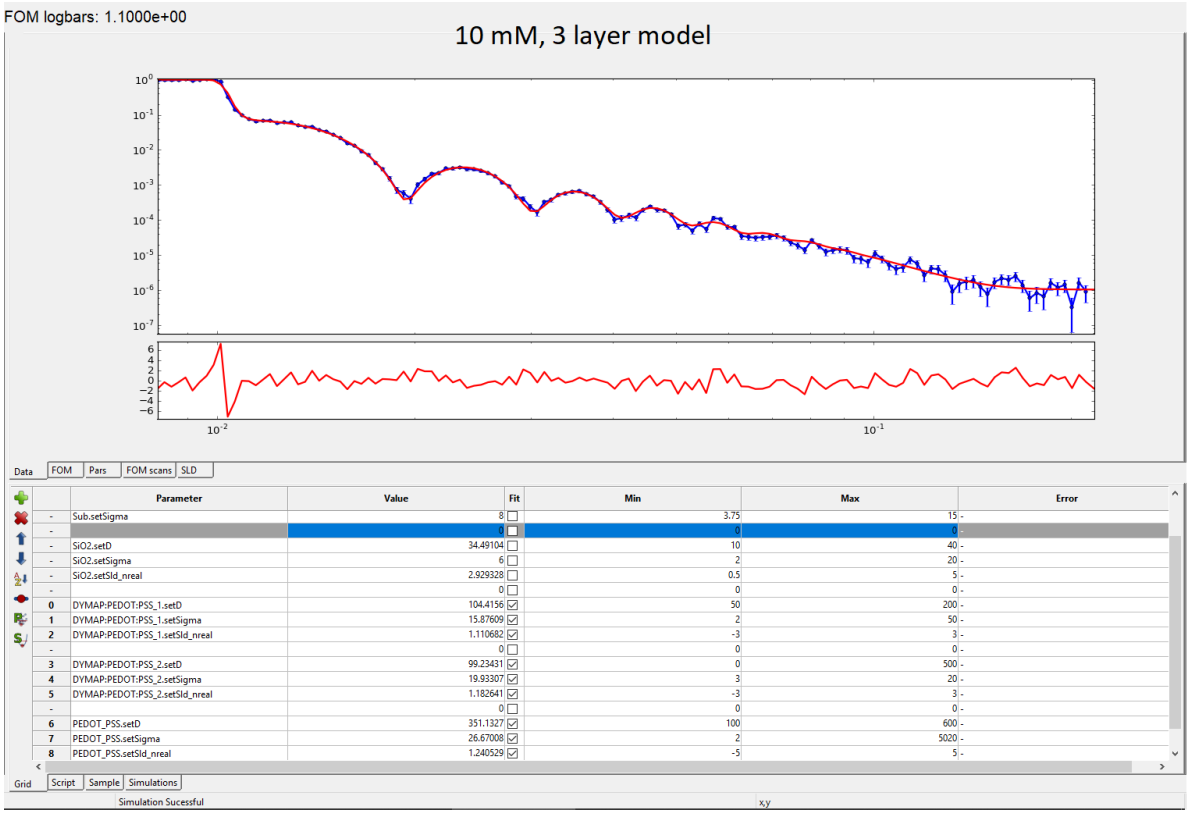

Figure 82: *Neutron reflectivity data, fit, and fitting parameters for the 1 layer, 2 layers, and 3 layer models of the 10 mM sample in GenX.*

9.2.4 20 mM DYMAP doped PEDOT:PSS

Table 19: *Figure of merit (FOM), scattering length densities (SLD's) and total thickness resulting from 1 layer, 2 layers, and 3 layer models for the 10 mM sample.*

20 mM DYMAP doped PEDOT:PSS			
	1 layer	2 layers	3 layers
FOM	1.03	0.99	0.95
SLD 1 (10^{-6}Å^{-2})	0.81	0.69	1.08
SLD 2 (10^{-6}Å^{-2})	-	0.87	0.82
SLD 3 (10^{-6}Å^{-2})	-	-	1.18
Total thickness (Å)	771	791	778

As shown in table 19 and figures 83, 84, and 85 the changes in FOM elicited by the increase in layers are less clear cut in this sample. The SLDs of the films are again reduced with respect to the undoped sample, and the thickness again increased. As discussed for the 10mM sample, this is not unexpected, nor easily anlysed further.

The SLD change for the two layer structure is less than half that of the 10mM sample and possibly pushing the limits of what sort of change would be detectable for an NR experiment. A similar size of SLD change is observed in the three layer model. In the three layer and two layer models we see that for the first time, the total thickness does not agree across the three fits. This is possibly due to the fact that the top layer of the such models is a change to the top interface, making a previously rough looking interface into almost a step function. Since the fits and the FOM's are nearly identical, we can say that we do not have the ability to distinguish between the two models. However, Occam's razor[268] would suggest to take a model with less parameters and a similar goodness of fit. Overall, the 20 mM sample's models with additional layers do not improve the agreement with the data enough to justify their inclusion. If any additional layers might be present, the SLD's would suggest a slightly lower SLD layer nearer the Si surface, in the same manner that we saw with the 10mM film. However, to conclude this would not be reasonable given the experimental data. Therefore we conclude that this film is best described by a single layer model.

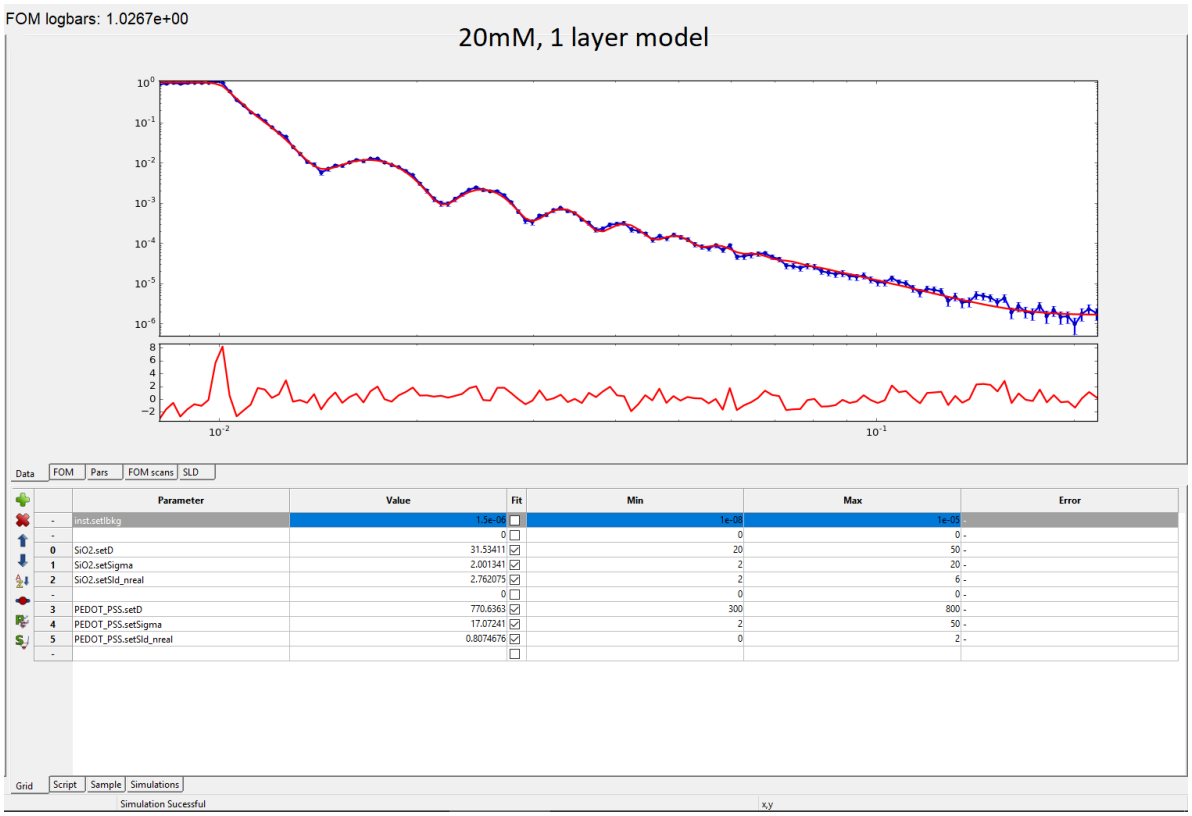

Figure 83: *Neutron reflectivity data, fit, and fitting parameters for the 1 layer model of the 20mM sample in GenX.*

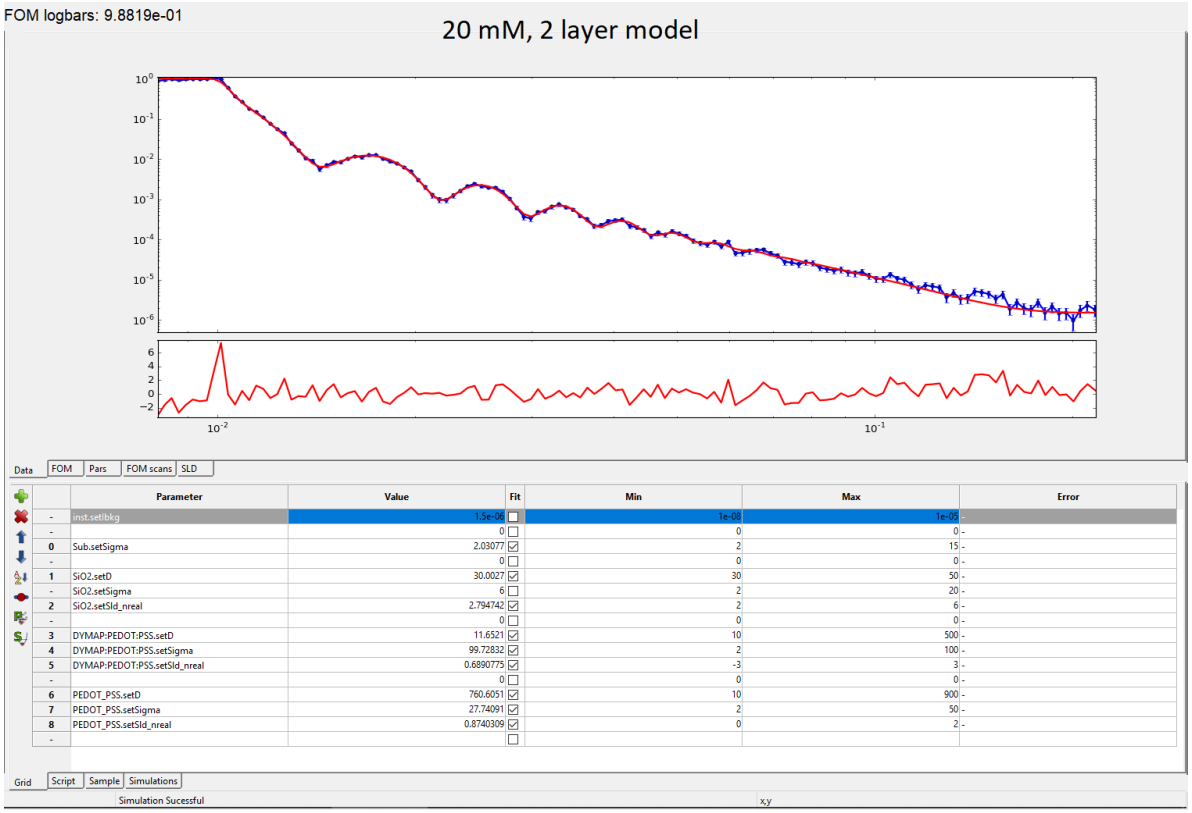

Figure 84: *Neutron reflectivity data, fit, and fitting parameters for the 2 layer model of the 20 mM sample in GenX.*

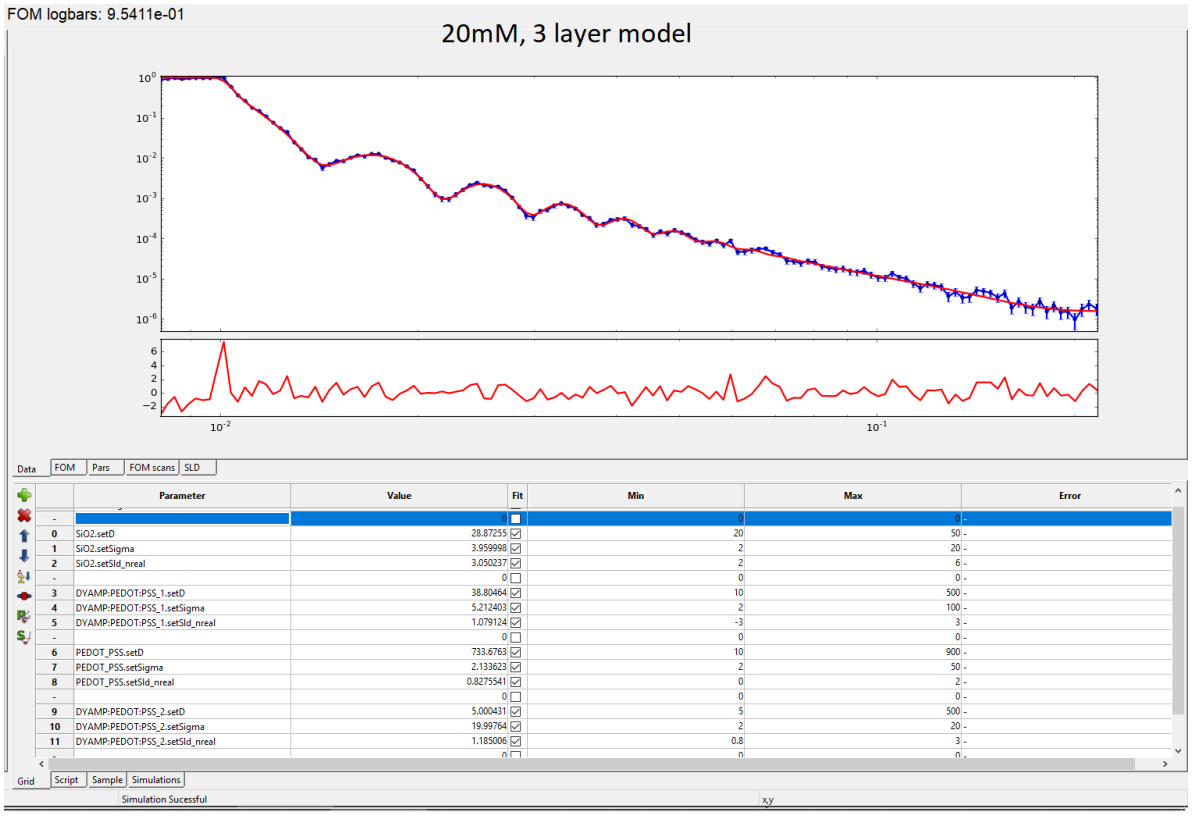

Figure 85: *Neutron reflectivity data, fit, and fitting parameters for the 3 layer model of the 20 mM sample in GenX.*

9.3 Swelling of PEDOT:PSS films

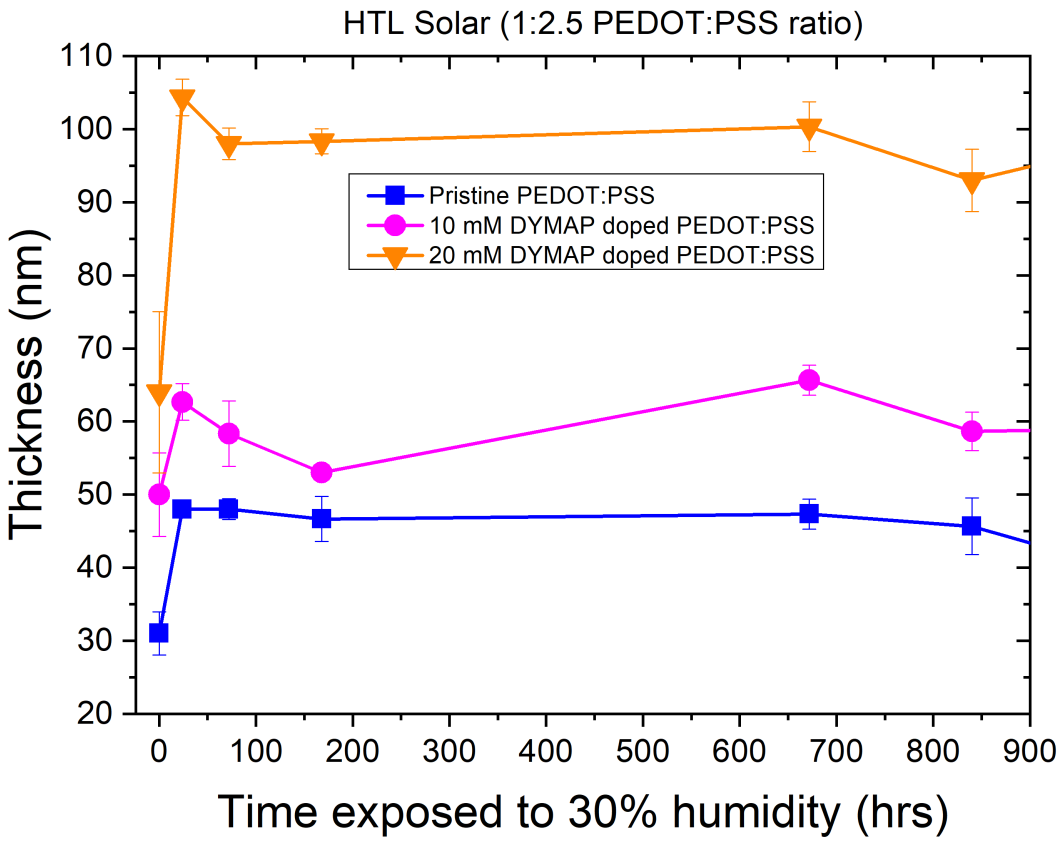

Figure 86: *Thickness of the pristine PEDOT:PSS, and the 10 mM and 20 mM doped PEDOT:PSS films as a function of time while exposed to a 30% ambient humidity. The humidity percentage was controlled by the default conditions of a cleanroom.*

9.4 Corroboration of lifetime measurements

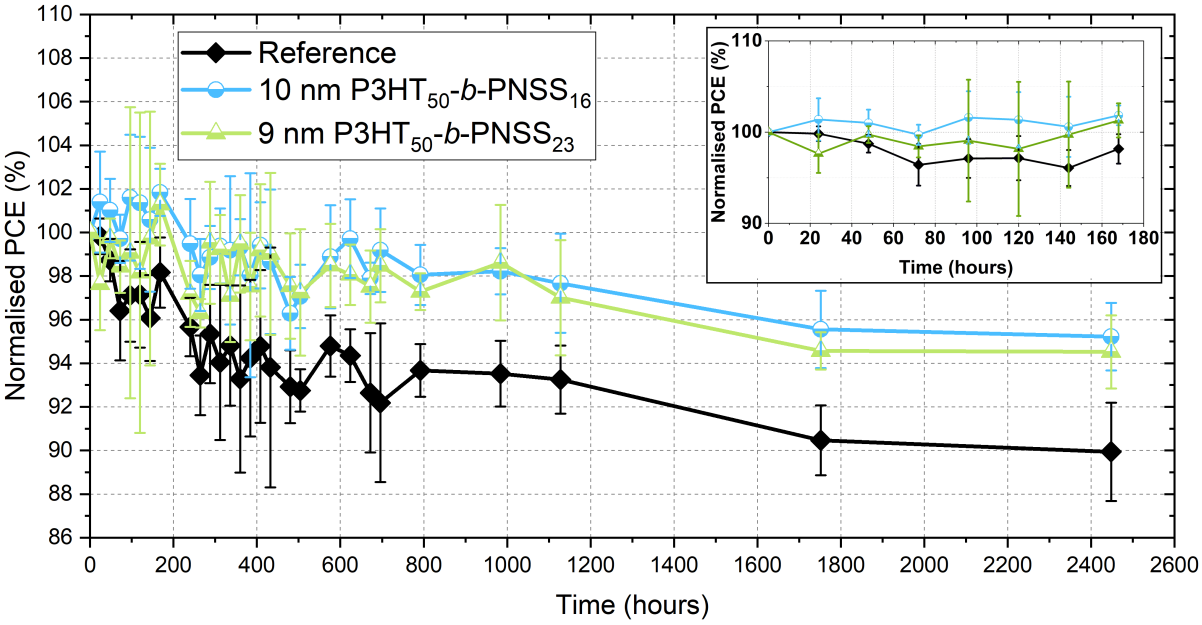

Figure 87: *Normalised power conversion efficiency as a function of time of a reference device, and 10 nm $P3HT_{50}$-b-PSS_{16} and 9 nm $P3HT_{50}$-b-$PNSS_{23}$ incorporated devices. The error bars represent one standard deviation on each side of the average value. Devices were kept stored in the dark except when measured.*

9.5 UPS spectra

Table 20: *Different energy levels obtained by ultraviolet photoelectron spectroscopy. The units of the values are eV and the energy of the ultraviolet beam was 21.2 eV.*

	Binding energy	Kinetic Energy	HOMO to Fermi energy	HOMO
PEDOT:PSS	16.17	5.03	-0.055	4.98
$P3HT_{50}$-b-PSS_9	16.85	4.35	0.145	4.50
$P3HT_{50}$-b-PSS_{16}	16.85	4.35	0.195	4.55
$P3HT_{50}$-b-PSS_{23}	16.68	4.52	0.15	4.68

9.5.1 PEDOT:PSS

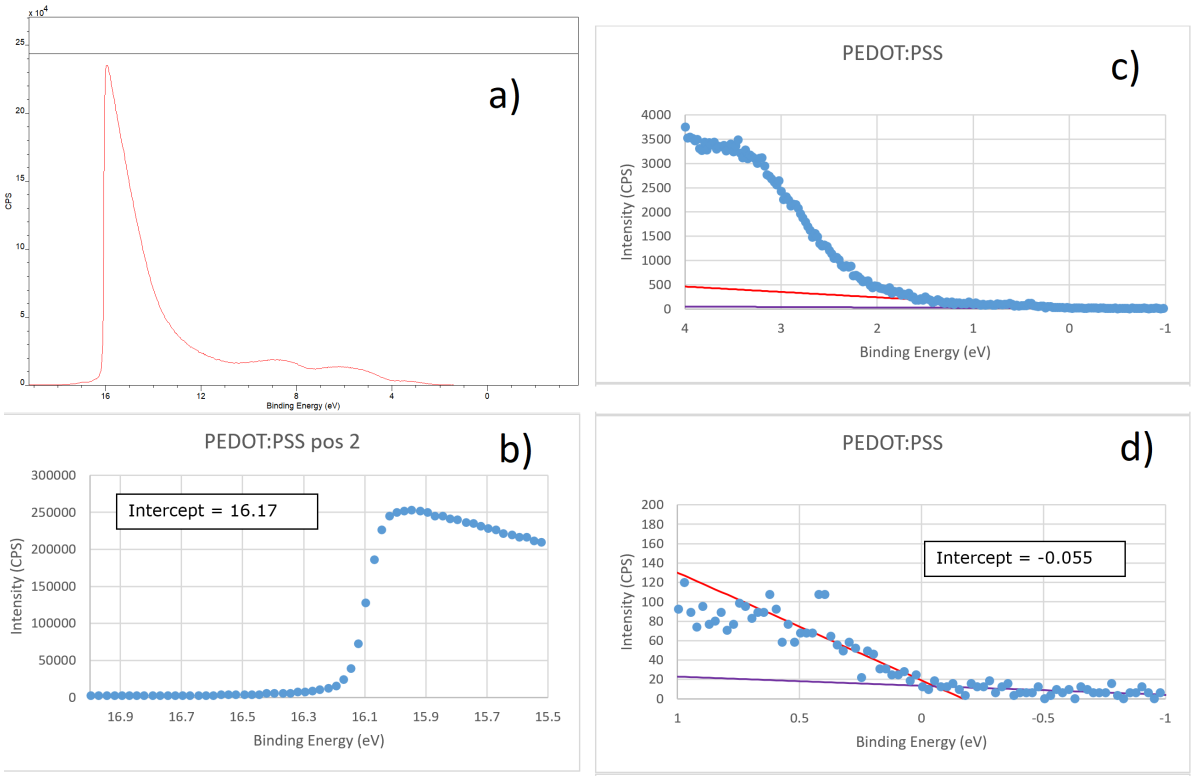

Figure 88: *Photoelectron spectra of PEDOT:PSS (a). A zoom to the high energy cut-off (b) and the low energy cut-off (c) of the spectra is shown. The tangents on the low energy cut-off are shown (d) to demonstrate the intercept value.*

9.5.2 Block co-polymer with 9 PSS units

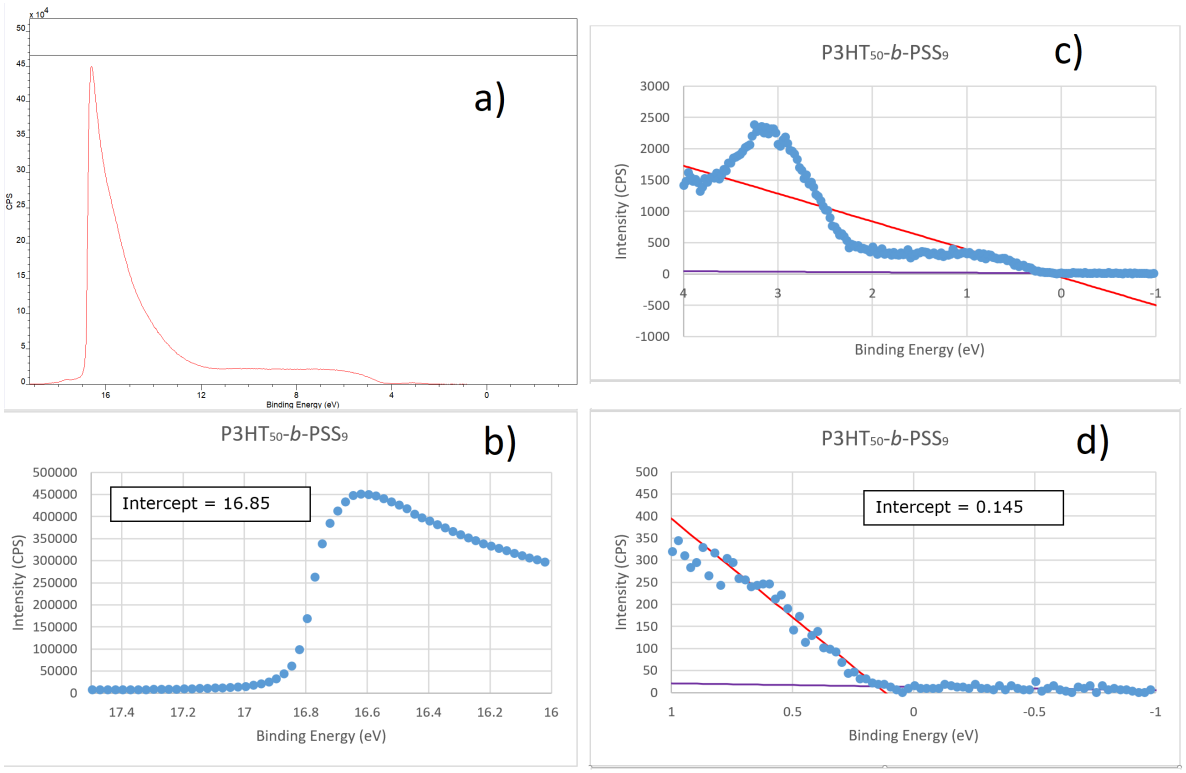

Figure 89: *Photoelectron spectra of P3HT$_{50}$-b-PSS$_9$ (a). A zoom to the high energy cut-off (b) and the low energy cut-off (c) of the spectra is shown. The tangents on the low energy cut-off are shown (d) to demonstrate the intercept value.*

9.5.3 Block co-polymer with 16 PSS units

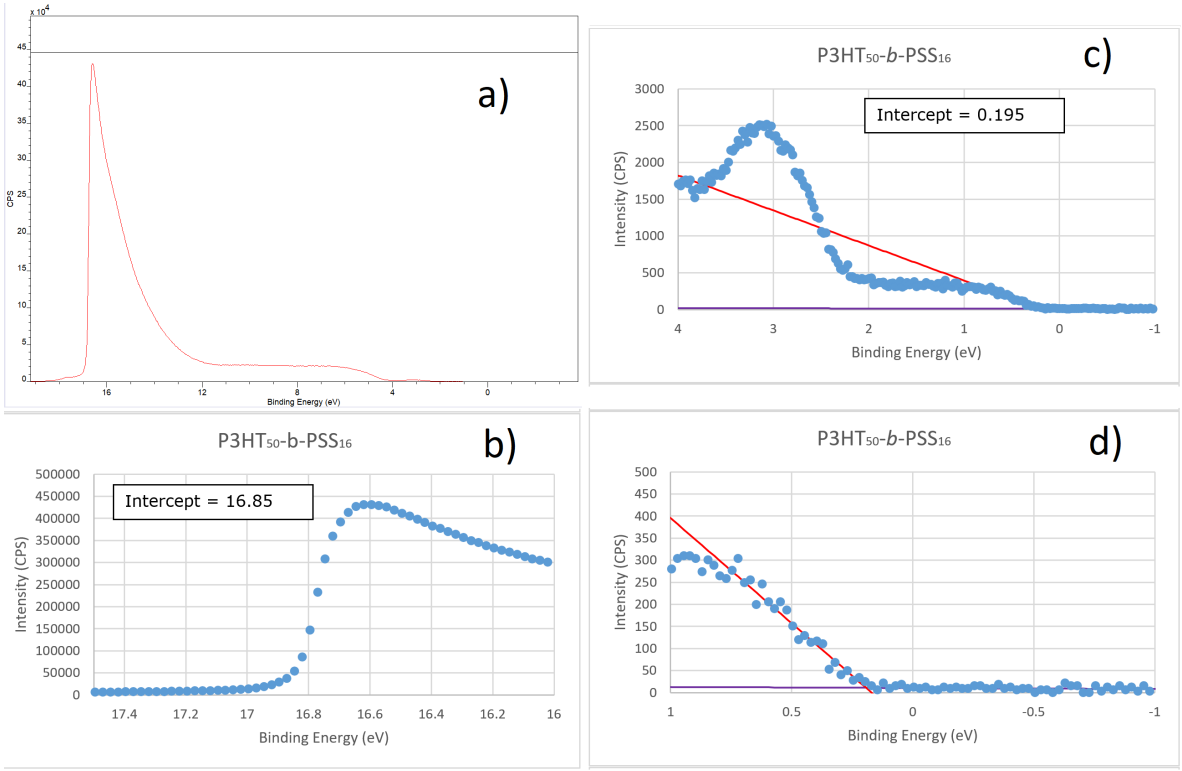

Figure 90: *Photoelectron spectra of P3HT$_{50}$-b-PSS$_{16}$ (a). A zoom to the high energy cut-off (b) and the low energy cut-off (c) of the spectra is shown. The tangents on the low energy cut-off are shown (d) to demonstrate the intercept value.*

9.5.4 Block co-polymer with 23 PSS units

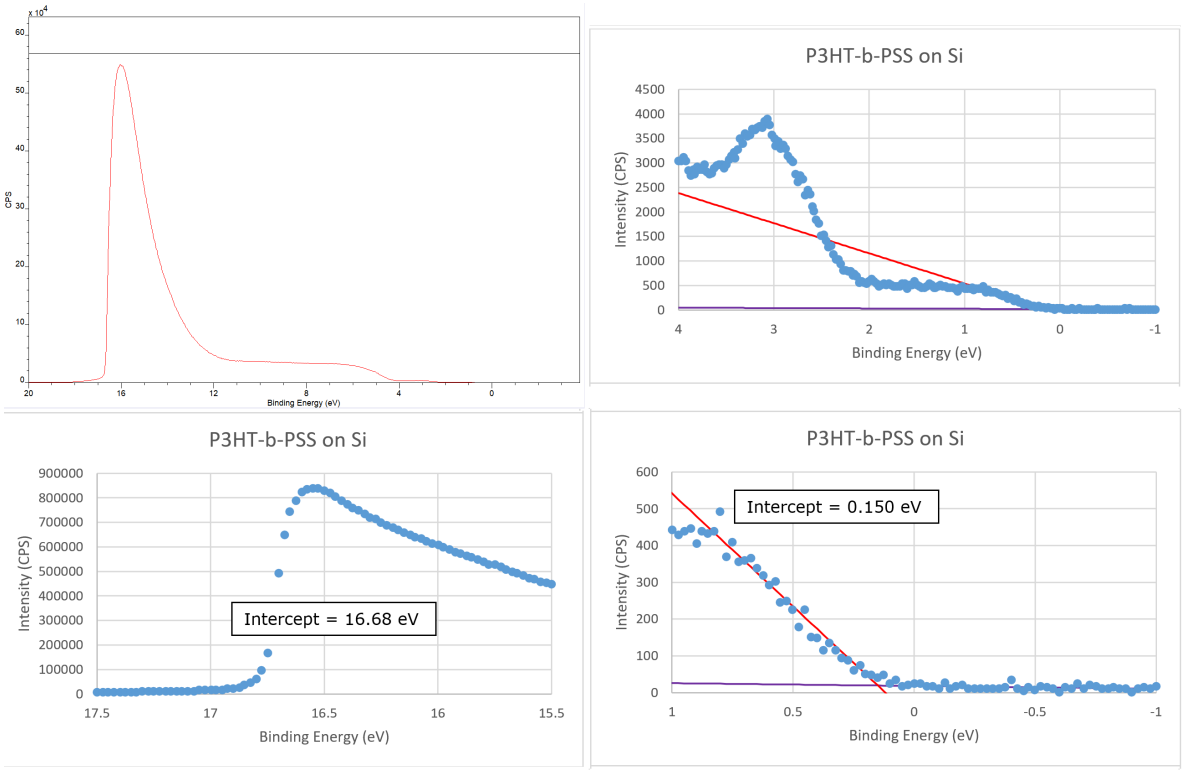

Figure 91: *Photoelectron spectra of $P3HT_{50}$-b-PSS_{23} (a). A zoom to the high energy cut-off (b) and the low energy cut-off (c) of the spectra is shown. The tangents on the low energy cut-off are shown (d) to demonstrate the intercept value.*

References

[1] R. Dudley, "BP statistical review of world energy." Available from www.bp.com: `https://www.bp.com/en/global/corporate/energy-economics/statistical-review-of-world-energy.html`, 2019. Last accesed: 12 September 2019.

[2] P. Forster, V. Ramaswamy, P. Artaxo, T. Berntsen, R. Betts, D. Fahey, J. Haywood, J. Lean, D. Lowe, G. Myhre, J. Nganga, R. Prinn, G. Raga, M. Schulz, and R. van Dorland, "Changes in amospheric constituents and in radiative forcing," in *Climate Change 2007: The Physical Science Basis. Contribution of Working Group I to the Fourth Assessment Report of the Intergovernmental Panel on Climate Change [Solomon, S., D. Quin, M. Manning, Z. Chen, M. Marquis, K.B. Averyt, M.Tignor and H.L. Miller (eds)]*, Cambridge, United Kingdom and New Yourk, NY, USA.: Cambridge University Press, 2007. Cambridge, United Kingdom and New Yourk, NY, USA.

[3] C. Le Quéré, R. M. Andrew, P. Friedlingstein, S. Sitch, J. Hauck, J. Pongratz, P. A. Pickers, J. I. Korsbakken, G. P. Peters, J. G. Canadell, A. Arneth, V. K. Arora, L. Barbero, A. Bastos, L. Bopp, F. Chevallier, L. P. Chini, P. Ciais, S. C. Doney, T. Gkritzalis, D. S. Goll, I. Harris, V. Haverd, F. M. Hoffman, M. Hoppema, R. A. Houghton, G. Hurtt, T. Ilyina, A. K. Jain, T. Johannessen, C. D. Jones, E. Kato, R. F. Keeling, K. K. Goldewijk, P. Landschützer, N. Lefèvre, S. Lienert, Z. Liu, D. Lombardozzi, N. Metzl, D. R. Munro, J. E. M. S. Nabel, S. Nakaoka, C. Neill, A. Olsen, T. Ono, P. Patra, A. Peregon, W. Peters, P. Peylin, B. Pfeil, D. Pierrot, B. Poulter, G. Rehder, L. Resplandy, E. Robertson, M. Rocher, C. Rödenbeck, U. Schuster, J. Schwinger, R. SÃľfÃľrian, I. Skjelvan, T. Steinhoff, A. Sutton, P. P. Tans, H. Tian, B. Tilbrook, F. N. Tubiello, I. T. van der Laan-Luijkx, G. R. van der Werf, N. Viovy, A. P. Walker, and A. J. Wiltshire, "Global carbon budget 2018," *Earth Syst. Sci. Data*, vol. 10, pp. 2141–2194, 2018.

[4] G. Myre, D. Shindell, W. Breon, J. Collins, J. Fuglestvedt, D. Huang, J. Koch, D. Lamarque, D. Lee, T. Mendoza, A. Nakajima, A. Robok, G. Stephens, H. Takemura, and Z. H., "Anthropogenic and natural radiative forcing," in *Climate Change*

2013: The Physical Science Basis. Contribution of Working Group I to the Fifth Assessment Report of the Intergovernmental Panel on Climate Change [Stocker, T.F., D. Qin, G.-K. Plattner, M. Tignor, S.K. Allen, J. Boschung, A. Nauels, Y. Xia, V. Bex and P.M. Midgley (eds.)], Cambridge, United Kingdom and New Yourk, NY, USA.: Cambridge University Press, 2013. Cambridge, United Kingdom and New Yourk, NY, USA.

[5] S. Arrhenius, "On the influence of carbonic acid in the air upon the temperature of the ground," *Philos. Mag.*, vol. 41, pp. 237–276, 1896.

[6] G. S. Callendar, "The artificial production of carbon dioxide and its influence on temperature," *Q. J. Royal Meteorol. Soc.*, vol. 64, pp. 223–240, 1938.

[7] UN, "Report of the united nations conference on the human environment." Retreived from Unted Nations Website: `http://www.un-documents.net/aconf48-14r1.pdf`, 1972. Last accessed: 14 March 2016.

[8] UN, "Kyoto protocol to the united nations framework convention on climate change." Retreived from Unted Nations Framework Convention on Climate Change Website: `http://unfccc.int/resource/docs/convkp/kpeng.pdf`, 1998. Last accessed: 14 March 2016.

[9] E. Jansen, J. Overpeck, K. Briffa, J.-C. Duplessy, F. Joos, V. Masson-Delmotte, D. Olago, B. Otto-Bliesner, W. Peltier, S. Rahmstorf, R. Ramesh, D. Raynaud, D. Rind, O. Solomina, R. Villalba, and D. Zhang, "Paleoclimate," in *Climate Change 2007: The Physical Science Basis. Contribution of Working Group I to the Fourth Assessment Report of the Intergovernmental Panel on Climate Change [Solomon, S., D. Quin, M. Manning, Z. Chen, M. Marquis, K.B. Averyt, M.Tignor and H.L. Miller (eds)]*, Cambridge, United Kingdom and New Yourk, NY, USA.: Cambridge University Press, 2007. Cambridge, United Kingdom and New Yourk, NY, USA.

[10] IEA, "Key world energy statistics." Available from www.iea.org: `https://webstore.iea.org/key-world-energy-statistics-2018`, 2019. Last accesed: 13 September 2019.

[11] I. E. Agency, "Petroleum and other liquds prices." Retreived from U.S. Energy

Information Administration Website: https://www.eia.gov/dnav/pet/hist/LeafHandler.ashx?n=PET&s=RWTC&f=A, 2015. Last accessed: 14 March 2016.

[12] D. Yergin, *The Quest: Energy, Security, and the Remaking of the Modern World.* New York, NY: Penguin Press, 2011.

[13] W. Moomaw, F. Yamba, M. Kamimoto, L. Maurice, J. Nyboer, K. Urama, and T. Weir, "Introduction," in *IPCC Special Report on Renewable Energy Sources and Climate Change Mitigation [O. Edenhofer, R. Pichs-Madruga, Y. Sokona, K. Seyboth, P. Matschoss, S. Kadner, T. Zwickel, P. Eickemeier, G. Hansen, S. Schlömer, C.von Stechow (eds)]*, Cambridge, United Kingdom and New Yourk, NY, USA.: Cambridge University Press, 2011. Cambridge, United Kingdom and New Yourk, NY, USA.

[14] N. Lewis, "Powering the planet." Retreived from the California Institute of Technology Website: nsl.caltech.edu/_media/energy:energy6.pdf, 2007. Last accessed: 15 March 2016.

[15] R. Detz, J. N. Reek, and B. Van Der Zwaan, "The future of solar fuels: When could they become competitive?," *Energy Environ. Sci.*, vol. 11, no. 7, pp. 1653–1669, 2018.

[16] IEA, "CO_2 emissions from fuel combustion overview." Available from www.iea.org: https://webstore.iea.org/co2-emissions-from-fuel-combustion-2018, 2019. Last accesed: 13 September 2019.

[17] D. Mills, "Advances in solar thermal electricity technology," *Sol. Energy*, vol. 76, no. 1-3, pp. 19–31, 2004.

[18] M. Grätzel, "Solar energy conversion by dye-sensitized photovoltaic cells," *Inorg. Chem.*, vol. 44, no. 20, pp. 6841–6851, 2005.

[19] J. Ramanujam, A. Verma, B. González-Díaz, R. Guerrero-Lemus, C. del Canizo, E. Garcia-Tabares, I. Rey-Stolle, F. Granek, L. Korte, M. Tucci, *et al.*, "Inorganic photovoltaics–planar and nanostructured devices," *Prog. Mater. Sci.*, vol. 82, pp. 294–404, 2016.

[20] A. Einstein, "Über einen die erzeugung und verwandlung des lichtes betreffenden heuristischen gesichtspunkt," *Annalen der Physik*, vol. 322, no. 6, pp. 132–148, 1905.

[21] R. E. Bird, R. L. Hulstrom, and L. J. Lewis, "Terrestrial solar spectral data sets," *Sol. Energy*, vol. 30, no. 6, pp. 563–573, 1983.

[22] ASTM, "Astm g159-98." Available from the American Society of Testing Materials Website: `http://compass.astm.org/Standards/WITHDRAWN/G159.htm`, 2005. Accesed: 12 September 2016.

[23] J. Nelson, *The Physics of Solar Cells*. london, UK: Imperial College Press, 2003.

[24] C. Honsberg and S. Bowden, "Photovoltaics education website." Available from www.pveducation.org: `https://www.pveducation.org/`, 2019. Last accesed: 13 September 2016.

[25] W. Shockley, "The theory of p-n junctions in semiconductors and p-n junction transistors," *The Bell System Technical Journal*, vol. 28, pp. 435–489, 1949.

[26] A. Cuevas, "The recombination parameter J_0," *Proceedings of the 4th International Conference on Crystalline Silicon Photovoltaics (Siliconpv 2014)*, vol. 55, pp. 53–62, 2014.

[27] F. Lindholm, J. Fossum, and E. Burgess, "Application of the superposition principle to solar-cell analysis," *IEEE Transactions on Electron Devices*, vol. 26, no. 3, p. 165–171, 1979.

[28] C. Honsberg and S. Bowden, "'IV curve' page." Available from www.pveducation.org: `https://www.pveducation.org/pvcdrom/solar-cell-operation/iv-curve`, 2019. Last accesed: 12 September 2019.

[29] C. Honsberg and S. Bowden, "Series resistance." Available from www.pveducation.org: `https://www.pveducation.org/pvcdrom/solar-cell-operation/series-resistance`, 2016. Accesed: 14 September 2016.

[30] E. Becquerel, "Memoire sur les effets electriques produits sous l'influence des rayons solaires," *Comptes Rendus*, vol. 9, pp. 561–567, 1839.

[31] W. Adams and R. Day, "The action of light on selenium," *Phil. Trans. R. Soc. Lond.*, vol. 167, pp. 313–349, 1877.

[32] D. M. Chapin, C. S. Fuller, and G. L. Pearson, "A new silicon p-n junction photocell for converting solar radiation into electrical power," *J. Appl. Phys.*, vol. 25, no. 5, 1954.

[33] W. Shockley and H. J. Queisser, "Detailed balance limit of efficiency of p-n junction solar cells," *J. Appl. Phys.*, vol. 32, no. 3, pp. 510–519, 1961.

[34] J. Byrne and L. Kurdgelashvili, "The role of policy in pv industry growth: Past, present and future," in *Handbook of Photovoltaic Science and Engineering*, John Wiley & sons., 2011. Chichester, United Kingdom.

[35] J. Ramanujam, A. Verma, B. González-Díaz, R. Guerrero-Lemus, C. del Cañizo, E. García-Tabarés, I. Rey-Stolle, F. Granek, L. Korte, M. Tucci, J. Rath, U. P. Singh, T. Todorov, O. Gunawan, S. Rubio, J. Plaza, E. Diéguez, B. Hoffmann, S. Christiansen, and G. E. Cirlin, "Inorganic photovoltaics - planar and nanostructured devices," *Prog. Mater. Sci.*, vol. 82, pp. 294–404, 2016.

[36] M. Woodhouse, B. Smith, A. Ramdas, and R. Margolis, "Crystalline silicon photovoltaic module manufacturing costs and sustainable pricing: 1h 2018 benchmark and cost reduction roadmap.." Available from www.nrel.gov: `https://www.nrel.gov/docs/fy19osti/72134.pdf`, 2019. Last accesed: 13 September 2019.

[37] G. Masson and I. Kaizuka, "Trends in 2018 in photovoltaic applications." Available from www.eia.org: `http://www.iea-pvps.org/fileadmin/dam/public/report/statistics/2018_iea-pvps_report_2018.pdf`, 2019. Last accesed: 13 September 2019.

[38] K. Yoshikawa, H. Kawasaki, W. Yoshida, T. Irie, K. Konishi, K. Nakano, T. Uto, D. Adachi, M. Kanematsu, H. Uzu, *et al.*, "Silicon heterojunction solar cell with interdigitated back contacts for a photoconversion efficiency over 26%," *Nat. Energy*, vol. 2, no. 5, p. 17032, 2017.

[39] A. F. Sherwani, J. A. Usmani, and Varun, "Life cycle assessment of solar pv based electricity generation systems: A review," *Renew. Sustain. Energy Rev.*, vol. 14, no. 1, pp. 540–544, 2010.

[40] M. Schumann, T. Orellana-Perez, and S. Riepe, "The solar cell wafering process," *Photovoltaics International*, 2009.

[41] MMTA, "Silicon market overview." Available from MMTA at: `http://www.mmta.co.uk/silicon-market-overview`, 2016. Accesed: 28 August 2016.

[42] A. Sayigh, "1.19 - cadmium telluride photovoltaic thin film: CdTe," in *Comprehensive Renewable Energy*, pp. 423 – 438, Oxford: Elsevier, 2012.

[43] ICdA, "Cadmium." Available from ICdA.org at: `http://www.cadmium.org/introduction`, 2016. Accesed: 28 August 2016.

[44] Polinares, "Fact sheet: Indium." Available from EU Policy on Natural Resources at: `http://www.polinares.eu/docs/d2-1/polinares_wp2_annex2_factsheet5.pdf`, 2012. Accesed: 28 August 2016.

[45] REI, "Statistics, international electricity." Available from www.renewable-ei.org: `https://www.renewable-ei.org/en/statistics/international/`, 2019. Last accesed: 13 September 2019.

[46] H. Shirakawa, E. J. Louis, A. G. MacDiarmid, C. K. Chiang, and A. J. Heeger, "Synthesis of electrically conducting organic polymers: Halogen derivatives of polyacetylene, $(CH)^x$," *J. Chem. Soc. Chem. Comm.*, no. 16, pp. 578–580, 1977.

[47] K. Vanderwal, K. Tvingstedt, and O. Inganas, "Charge transfer states in organic donor-acceptor solar cells," in *Quantum efficiency in complex systems, Part II: From molecular aggregates to organic solar cells*, Elsevier Inc., 2011. Amsterdam and London.

[48] U. Zhokhavets, T. Erb, G. Gobsch, M. Al-Ibrahim, and O. Ambacher, "Relation between absorption and crystallinity of poly (3-hexylthiophene)/fullerene films for plastic solar cells," *Chem. Phys. Lett*, vol. 418, no. 4-6, pp. 347–350, 2006.

[49] F. C. Krebs, "All solution roll-to-roll processed polymer solar cells free from indium-tin-oxide and vacuum coating steps," *Org. Electron.*, vol. 10, no. 5, pp. 761–768, 2009.

[50] M. Einzinger, T. Wu, J. F. Kompalla, H. L. Smith, C. F. Perkinson, L. Nienhaus, S. Wieghold, D. N. Congreve, A. Kahn, M. G. Bawendi, *et al.*, "Sensitization of silicon by singlet exciton fission in tetracene," *Nature*, vol. 571, no. 7763, p. 90, 2019.

[51] S. H. Ahn and L. J. Guo, "High-speed roll-to-roll nanoimprint lithography on flexible plastic substrates," *Adv. Mater.*, vol. 20, no. 11, pp. 2044–2049, 2008.

[52] M. Senghor, M. Manceau, F. Ardiaca, R. de Bettignies, S. Berson, L. Dassas, S. Poughon, C. Dossou-Yovo, and R. Noguera, "High-speed inkjet printing for organic photovoltaic devices," in *Organic Photovoltaics XIII*, vol. 8477, p. 84770M, International Society for Optics and Photonics, 2012.

[53] NREL, "Best research-cell efficiency chart." Available from www.nrel.gov: `https://www.nrel.gov/pv/cell-efficiency.html`. Last accessed: 14 September 2019.

[54] A. K. Jena, A. Kulkarni, and T. Miyasaka, "Halide perovskite photovoltaics: Background, status, and future prospects," *Chem. Rev.*, vol. 119, no. 5, pp. 3036–3103, 2019.

[55] A. M. Bagher, "Comparison of organic solar cells and inorganic solar cells," *J Renew. Sustain. Ener.*, vol. 3, no. 3, pp. 53–58, 2014.

[56] Y. Zhang, E. Bovill, J. Kingsley, A. R. Buckley, H. Yi, A. Iraqi, T. Wang, and D. G. Lidzey, "PCDTBT based solar cells: One year of operation under real-world conditions," *Sci. Rep.*, vol. 6, p. 21632, 2016.

[57] J. Yang, N. Clark, M. Long, J. Xiong, D. J. Jones, B. Yang, and C. Zhou, "Solution stability of active materials for organic photovoltaics," *Sol. Energy*, vol. 113, pp. 181–188, 2015.

[58] M. Jørgensen, K. Norrman, and F. C. Krebs, "Stability/degradation of polymer solar cells," *Sol. Energ. Mat. Sol. C.*, vol. 92, no. 7, pp. 686–714, 2008.

[59] W. Ma, C. Yang, X. Gong, K. Lee, and A. J. Heeger, "Thermally stable, efficient polymer solar cells with nanoscale control of the interpenetrating network morphology," *Adv. Funct. Mater.*, vol. 15, no. 10, pp. 1617–1622, 2005.

[60] X. Gao, J. Gao, Z. Xue, H. Wang, J. Wang, Y. Cheng, Z. Li, F. Zhu, S. Huettner, H. Li, *et al.*, "Benzodithiophene-modified terpolymer acceptors with reduced molecular planarity and crystallinity: improved performance and stability for all-polymer solar cells," *J. Mater. Chem. C*, vol. 7, no. 33, pp. 10338–10351, 2019.

[61] V. Singh, S. Arora, M. Arora, V. Sharma, and R. Tandon, "Characterization of doped pedot:pss and its influence on the performance and degradation of organic solar cells," *Semicond. Sci. Tech.*, vol. 29, no. 4, p. 045020, 2014.

[62] W. Zhao, S. Li, H. Yao, S. Zhang, Y. Zhang, B. Yang, and J. Hou, "Molecular optimization enables over 13% efficiency in organic solar cells," *J. Am. Chem. Soc.*, vol. 139, no. 21, pp. 7148–7151, 2017.

[63] J. Yuan, Y. Zhang, L. Zhou, G. Zhang, H.-L. Yip, T.-K. Lau, X. Lu, C. Zhu, H. Peng, P. A. Johnson, *et al.*, "Single-junction organic solar cell with over 15% efficiency using fused-ring acceptor with electron-deficient core," *Joule*, vol. 3, no. 4, pp. 1140–1151, 2019.

[64] C. Yan, S. Barlow, Z. Wang, H. Yan, A. K.-Y. Jen, S. R. Marder, and X. Zhan, "Non-fullerene acceptors for organic solar cells," *Nat. Rev. Mater.*, vol. 3, p. 18003, 2018.

[65] Q. Wu, D. Zhao, A. M. Schneider, W. Chen, and L. Yu, "Covalently bound clusters of alpha-substituted pdi-rival electron acceptors to fullerene for organic solar cells," *J. Am. Chem. Soc.*, vol. 138, no. 23, pp. 7248–7251, 2016.

[66] W. Zhao, D. Qian, S. Zhang, S. Li, O. Inganäs, F. Gao, and J. Hou, "Fullerene-free polymer solar cells with over 11% efficiency and excellent thermal stability," *Adv. Mater.*, vol. 28, no. 23, pp. 4734–4739, 2016.

[67] B. Fan, D. Zhang, M. Li, W. Zhong, Z. Zeng, L. Ying, F. Huang, and Y. Cao, "Achieving over 16% efficiency for single-junction organic solar cells," *Sci. China Chem.*, vol. 62, no. 6, pp. 746–752, 2019.

[68] S. Rogers, "New organic solar cells become the most efficient to date." Available from www.interestingengineering.com: https://interestingengineering.com/new-organic-solar-cells-become-most-efficient-to-date, 2019. Last accesed: 14 September 2019.

[69] EIA, "Average price of electricity to ultimate customers by end-use sector." Available from www.eia.org: https://www.eia.gov/electricity/monthly/epm_table_grapher.php?t=epmt_5_6_a, 2019. Last accesed: 14 September 2019.

[70] P. Atkins and L. Jones, *Chemical principles: the quest for insight*. New York, NY: W.H. Freeman and Company, 2001.

[71] W. P. Su, J. R. Schrieffer, and A. J. Heeger, "Solitons in polyacetylene," *Phys. Rev. Lett.*, vol. 42, pp. 1698–1701, 1979.

[72] C. S. Yannoni and T. C. Clarke, "Molecular geometry of *cis* - and *trans* - polyacetylene by nutation nmr spectroscopy," *Phys. Rev. Lett.*, vol. 51, pp. 1191–1193, 1983.

[73] R. E. Peierls, *Quantum theory of solids*. Clarendon Press, 1996.

[74] G. Macfarlane, T. McLean, J. Quarrington, and V. Roberts, "Exciton and phonon effects in the absorption spectra of germanium and silicon," *J. Phys. Chem. Solids*, vol. 8, pp. 388–392, 1959.

[75] Y. Sudhakar, M. Selvakumar, and D. Krishna Bhat, "Chapter 4 - biopolymer electrolytes for solar cells and electrochemical cells," in *Biopolymer Electrolytes* (Y. Sudhakar, M. Selvakumar, and D. K. Bhat, eds.), pp. 117 – 149, Elsevier, 2018.

[76] P. Peumans, A. Yakimov, and S. R. Forrest, "Small molecular weight organic thin-film photodetectors and solar cells," *J. Appl. Phys.*, vol. 93, no. 7, pp. 3693–3723, 2003.

[77] T. Stübinger and W. Brütting, "Exciton diffusion and optical interference in organic donor–acceptor photovoltaic cells," *J. Appl. Phys.*, vol. 90, no. 7, pp. 3632–3641, 2001.

[78] O. V. Mikhnenko, J. Lin, Y. Shu, J. E. Anthony, P. W. Blom, T.-Q. Nguyen, and M. A. Loi, "Effect of thermal annealing on exciton diffusion in a diketopyrrolopyrrole derivative," *Phys. Chem. Chem. Phys.*, vol. 14, no. 41, pp. 14196–14201, 2012.

[79] C. Deibel and V. Dyakonov, "Polymer-fullerene bulk heterojunction solar cells," *Rep. Prog. Phys*, vol. 73, no. 9, 2010.

[80] M. T. Dang, L. Hirsch, and G. Wantz, "P3HT:PCBM, best seller in polymer photovoltaic research," *Adv. Mater.*, vol. 23, no. 31, pp. 3597–3602, 2011.

[81] S. H. Ahn and L. J. Guo, "High-speed roll-to-roll nanoimprint lithography on flexible plastic substrates," *Adv. Mater.*, vol. 20, no. 11, pp. 2044–2049, 2008.

[82] L. Lu, T. Zheng, Q. Wu, A. M. Schneider, D. Zhao, and L. Yu, "Recent advances in bulk heterojunction polymer solar cells," *Chem. Rev.*, vol. 115, no. 23, pp. 12666–12731, 2015.

[83] Y. Huang, E. J. Kramer, A. J. Heeger, and G. C. Bazan, "Bulk heterojunction solar cells: Morphology and performance relationships," *Chem. Rev.*, vol. 114, no. 14, pp. 7006–7043, 2014.

[84] H. Gaspar, F. Figueira, L. Pereira, A. Mendes, J. Viana, and G. Bernardo, "Recent developments in the optimization of the bulk heterojunction morphology of polymer: Fullerene solar cells," *Materials*, vol. 11, no. 12, p. 2560, 2018.

[85] J.-L. Brédas, J. E. Norton, J. Cornil, and V. Coropceanu, "Molecular understanding of organic solar cells: the challenges," *Acc. Chem. Res*, vol. 42, no. 11, pp. 1691–1699, 2009.

[86] C. M. Proctor, M. Kuik, and T.-Q. Nguyen, "Charge carrier recombination in organic solar cells," *Prog. Polym. Sci.*, vol. 38, no. 12, pp. 1941–1960, 2013.

[87] S. R. Cowan, N. Banerji, W. L. Leong, and A. J. Heeger, "Charge formation, recombination, and sweep-out dynamics in organic solar cells," *Adv. Funct. Mater.*, vol. 22, no. 6, pp. 1116–1128, 2012.

[88] G. Dennler, M. C. Scharber, and C. J. Brabec, "Polymer-fullerene bulk-heterojunction solar cells," *Adv. Mater.*, vol. 21, no. 13, pp. 1323–1338, 2009.

[89] A. Miller and E. Abrahams, "Impurity conduction at low concentrations," *Phys. Rev.*, vol. 120, no. 3, pp. 745–755, 1960.

[90] J. Kettle, H. Waters, M. Horie, and S. Chang, "Effect of hole transporting layers on the performance of pcpdtbt:pcbm organic solar cells," *J. Phys. D*, vol. 45, no. 12, p. 125102, 2012.

[91] K. Yoshida, T. Oku, A. Suzuki, T. Akiyama, and Y. Yamasaki, "Fabrication and characterization of PCBM:P3HT bulk heterojunction solar cells doped with germanium phthalocyanine or germanium naphthalocyanine," *Mater. Sci. Appl.*, vol. 4, no. 04, p. 1, 2013.

[92] B. Weinberger, M. Akhtar, and S. Gau, "Polyacetylene photovoltaic devices," *Synth. Met.*, vol. 4, no. 3, pp. 187–197, 1982.

[93] S. Glenis, G. Horowitz, G. Tourillon, and F. Garnier, "Electrochemically grown polythiophene and poly (3-methylthiophene) organic photovoltaic cells," *Thin Solid Films*, vol. 111, no. 2, pp. 93–103, 1984.

[94] S. Karg, W. Riess, V. Dyakonov, and M. Schwoerer, "Electrical and optical characterization of poly (phenylene-vinylene) light emitting diodes," *Synth. Met.*, vol. 54, no. 1-3, pp. 427–433, 1993.

[95] C. Tang and A. Albrecht, "Transient photovoltaic effects in metal–chlorophyll-a–metal sandwich cells," *J. Chem. Phys.*, vol. 63, no. 2, pp. 953–961, 1975.

[96] H. W. Kroto, J. R. Heath, S. C. O'Brien, R. F. Curl, and R. E. Smalley, "C60: Buckminsterfullerene," *Nature*, vol. 318, no. 6042, p. 162, 1985.

[97] N. Sariciftci, L. Smilowitz, A. Heeger, and F. Wudl, "Semiconducting polymers (as donors) and buckminsterfullerene (as acceptor): Photoinduced electron transfer and heterojunction devices," *Synth. Met.*, vol. 59, no. 3, pp. 333–352, 1993.

[98] G. Yu, J. Gao, J. C. Hummelen, F. Wudl, and A. J. Heeger, "Polymer photovoltaic cells: Enhanced efficiencies via a network of internal donor-acceptor heterojunctions," *Science*, vol. 270, no. 5243, pp. 1789–1791, 1995.

[99] G. Yu, K. Pakbaz, and A. Heeger, "Semiconducting polymer diodes: Large size, low cost photodetectors with excellent visible-ultraviolet sensitivity," *Appl. Phys. Lett.*, vol. 64, no. 25, pp. 3422–3424, 1994.

[100] S. E. Shaheen, C. J. Brabec, N. S. Sariciftci, F. Padinger, T. Fromherz, and J. C. Hummelen, "2.5% efficient organic plastic solar cells," *Appl. Phys. Lett.*, vol. 78, no. 6, pp. 841–843, 2001.

[101] D. Mühlbacher, M. Scharber, M. Morana, Z. Zhu, D. Waller, R. Gaudiana, and C. Brabec, "High photovoltaic performance of a low-bandgap polymer," *Adv. Mater.*, vol. 18, no. 21, pp. 2884–2889, 2006.

[102] Z. Tan, E. Zhou, X. Zhan, X. Wang, Y. Li, S. Barlow, and S. R. Marder, "Efficient all-polymer solar cells based on blend of tris (thienylenevinylene)-substituted polythiophene and poly [perylene diimide-alt-bis (dithienothiophene)]," *Appl. Phys. Lett.*, vol. 93, no. 7, p. 307, 2008.

[103] J. Hou, H.-Y. Chen, S. Zhang, G. Li, and Y. Yang, "Synthesis, characterization, and photovoltaic properties of a low band gap polymer based on silole-containing polythiophenes and 2, 1, 3-benzothiadiazole," *J. Am. Chem. Soc.*, vol. 130, no. 48, pp. 16144–16145, 2008.

[104] C.-P. Chen, S.-H. Chan, T.-C. Chao, C. Ting, and B.-T. Ko, "Low-bandgap poly (thiophene-phenylene-thiophene) derivatives with broaden absorption spectra for use in high-performance bulk-heterojunction polymer solar cells," *J. Am. Chem. Soc.*, vol. 130, no. 38, pp. 12828–12833, 2008.

[105] Z. He, C. Zhong, S. Su, M. Xu, H. Wu, and Y. Cao, "Enhanced power-conversion efficiency in polymer solar cells using an inverted device structure," *Nat. Photonics*, vol. 6, no. 9, p. 591, 2012.

[106] Y. Liu, J. Zhao, Z. Li, C. Mu, W. Ma, H. Hu, K. Jiang, H. Lin, H. Ade, and H. Yan, "Aggregation and morphology control enables multiple cases of high-efficiency polymer solar cells," *Nat. Commun.*, vol. 5, p. 5293, 2014.

[107] S. Zhang, Y. Qin, J. Zhu, and J. Hou, "Over 14% efficiency in polymer solar cells

enabled by a chlorinated polymer donor," *Adv. Mater.*, vol. 30, no. 20, p. 1800868, 2018.

[108] A. Facchetti, "Polymer donor–polymer acceptor (all-polymer) solar cells," *Mater. Today*, vol. 16, no. 4, pp. 123–132, 2013.

[109] R. S. Gurney, D. G. Lidzey, and T. Wang, "A review of non-fullerene polymer solar cells: From device physics to morphology control," *Rep. Prog. Phys.*, vol. 82, no. 3, p. 036601, 2019.

[110] L. Meng, Y. Zhang, X. Wan, C. Li, X. Zhang, Y. Wang, X. Ke, Z. Xiao, L. Ding, R. Xia, H.-L. Yip, Y. Cao, and C. Yongsheng, "Organic and solution-processed tandem solar cells with 17.3% efficiency," *Science*, vol. 361, no. 6407, pp. 1094–1098, 2018.

[111] S.-H. Lee, D.-H. Kim, J.-H. Kim, G.-S. Lee, and J.-G. Park, "Effect of metal-reflection and surface-roughness properties on power-conversion efficiency for polymer photovoltaic cells," *J. Phys. Chem. C*, vol. 113, no. 52, pp. 21915–21920, 2009.

[112] A. J. Moulé and K. Meerholz, "Controlling morphology in polymer–fullerene mixtures," *Adv. Mater.*, vol. 20, no. 2, pp. 240–245, 2008.

[113] G. Li, V. Shrotriya, J. Huang, Y. Yao, T. Moriarty, K. Emery, and Y. Yang, "High-efficiency solution processable polymer photovoltaic cells by self-organization of polymer blends," in *Materials For Sustainable Energy: A Collection of Peer-Reviewed Research and Review Articles from Nature Publishing Group*, pp. 80–84, World Scientific, 2011.

[114] C. Müller, T. A. Ferenczi, M. Campoy-Quiles, J. M. Frost, D. D. Bradley, P. Smith, N. Stingelin-Stutzmann, and J. Nelson, "Binary organic photovoltaic blends: a simple rationale for optimum compositions," *Adv. Mater.*, vol. 20, no. 18, pp. 3510–3515, 2008.

[115] A. J. Parnell, A. D. Dunbar, A. J. Pearson, P. A. Staniec, A. J. Dennison, H. Hamamatsu, M. W. Skoda, D. G. Lidzey, and R. A. Jones, "Depletion of PCBM at the cathode interface in P3HT/PCBM thin films as quantified via neutron reflectivity measurements," *Adv. Mater.*, vol. 22, no. 22, pp. 2444–2447, 2010.

[116] J. Halls, C. Walsh, N. C. Greenham, E. Marseglia, R. H. Friend, S. Moratti, and A. Holmes, "Efficient photodiodes from interpenetrating polymer networks," *Nature*, vol. 376, no. 6540, p. 498, 1995.

[117] C. R. McNeill, S. Westenhoff, C. Groves, R. H. Friend, and N. C. Greenham, "Influence of nanoscale phase separation on the charge generation dynamics and photovoltaic performance of conjugated polymer blends: Balancing charge generation and separation," *J. Phys. Chem. C*, vol. 111, no. 51, pp. 19153–19160, 2007.

[118] E. Zhou, J. Cong, K. Hashimoto, and K. Tajima, "Control of miscibility and aggregation via the material design and coating process for high-performance polymer blend solar cells," *Adv. Mater.*, vol. 25, no. 48, pp. 6991–6996, 2013.

[119] B. Kadem, A. Hassan, and W. Cranton, "Performance optimization of P3HT:PCBM solar cells by controlling active layer thickness," in *Proceedings of the 31st European photovoltaic solar energy conference and exhibition, EUPVSEC (2015, Hamburg, Germany)*, 2015.

[120] S. van Bavel, E. Sourty, G. de With, K. Frolic, and J. Loos, "Relation between photoactive layer thickness, 3d morphology, and device performance in P3HT/PCBM bulk-heterojunction solar cells," *Macromolecules*, vol. 42, no. 19, pp. 7396–7403, 2009.

[121] C. Kapnopoulos, E. D. Mekeridis, L. Tzounis, C. Polyzoidis, A. Zachariadis, S. Tsimikli, C. Gravalidis, A. Laskarakis, N. Vouroutzis, and S. Logothetidis, "Fully gravure printed organic photovoltaic modules: A straightforward process with a high potential for large scale production," *Sol. Energy Mater. Sol. Cells*, vol. 144, pp. 724–731, 2016.

[122] M. Finn III, C. J. Martens, A. V. Zaretski, B. Roth, R. R. Søndergaard, F. C. Krebs, and D. J. Lipomi, "Mechanical stability of roll-to-roll printed solar cells under cyclic bending and torsion," *Sol. Energy Mater. Sol. Cells*, vol. 174, pp. 7–15, 2018.

[123] R. R. Søndergaard, M. Hösel, and F. C. Krebs, "Roll-to-roll fabrication of large area functional organic materials," *J. Polym. Sci. B Polym. Phys.*, vol. 51, no. 1, pp. 16–34, 2013.

[124] R. Po, C. Carbonera, A. Bernardi, and N. Camaioni, "The role of buffer layers in polymer solar cells," *Energy Environ. Sci.*, vol. 4, pp. 285–310, 2011.

[125] H. Ma, H.-L. Yip, F. Huang, and A. K.-Y. Jen, "Interface engineering for organic electronics," *Adv. FUnct. Mater.*, vol. 20, no. 9, pp. 1371–1388, 2010.

[126] Z. He, H. Wu, and Y. Cao, "Recent advances in polymer solar cells: Realization of high device performance by incorporating water/alcohol-soluble conjugated polymers as electrode buffer layer," *Adv. Mater.*, vol. 26, no. 7, pp. 1006–1024, 2014.

[127] M. Fahlman and W. R. Salaneck, "Surfaces and interfaces in polymer-based electronics," *Surf. Sci.*, vol. 500, no. 1-3, pp. 904–922, 2002.

[128] Y. Park, V. Choong, Y. Gao, B. Hsieh, and C. Tang, "Work function of indium tin oxide transparent conductor measured by photoelectron spectroscopy," *Appl. Phys. Lett.*, vol. 68, no. 19, pp. 2699–2701, 1996.

[129] H. Spanggaard and F. C. Krebs, "A brief history of the development of organic and polymeric photovoltaics," *Sol. Energy Mater. Sol. Cells*, vol. 83, no. 2-3, pp. 125–146, 2004.

[130] K. Seki, N. Hayashi, H. Oji, E. Ito, Y. Ouchi, and H. Ishii, "Electronic structure of organic/metal interfaces," *Thin Solid Films*, vol. 393, no. 1-2, pp. 298–303, 2001.

[131] R. Marks, J. Halls, D. Bradley, R. Friend, and A. Holmes, "The photovoltaic response in poly (p-phenylene vinylene) thin-film devices," *J. Phys. Condens. Matter*, vol. 6, no. 7, p. 1379, 1994.

[132] Z. Zhao, W. Zhang, X. Zhao, and S. Yang, "Interfacial materials toward efficiency of polymer solar cells," in *Organic Solar Cells materials, devices, interfaces, and modeling*, Boca Raton: CRC Press, 2015. London.

[133] M. T. Lloyd, D. C. Olson, P. Lu, E. Fang, D. L. Moore, M. S. White, M. O. Reese, D. S. Ginley, and J. W. Hsu, "Impact of contact evolution on the shelf life of organic solar cells," *J. Mater. Chem*, vol. 19, no. 41, pp. 7638–7642, 2009.

[134] L. Groenendaal, F. Jonas, D. Freitag, H. Pielartzik, and J. R. Reynolds, "Poly(3,4-ethylenedioxythiophene) and its derivatives: Past, present, and future," *Adv. Mater.*, vol. 12, no. 7, pp. 481–494, 2000.

[135] C. J. Brabec, A. Cravino, D. Meissner, N. S. Sariciftci, T. Fromherz, M. T. Rispens, L. Sanchez, and J. C. Hummelen, "Origin of the open circuit voltage of plastic solar cells," *Adv. Funct. Mater.*, vol. 11, no. 5, pp. 374–380, 2001.

[136] V. Gupta, A. K. K. Kyaw, D. H. Wang, S. Chand, G. C. Bazan, and A. J. Heeger, "Barium: an efficient cathode layer for bulk-heterojunction solar cells," *Sci. Rep.*, vol. 3, p. 1965, 2013.

[137] S. K. Hau, H.-L. Yip, H. Ma, and A. K.-Y. Jen, "High performance ambient processed inverted polymer solar cells through interfacial modification with a fullerene self-assembled monolayer," *Appl. Phys. Lett.*, vol. 93, no. 23, p. 441, 2008.

[138] J.-C. Wang, W.-T. Weng, M.-Y. Tsai, M.-K. Lee, S.-F. Horng, T.-P. Perng, C.-C. Kei, C.-C. Yu, and H.-F. Meng, "Highly efficient flexible inverted organic solar cells using atomic layer deposited ZnO as electron selective layer," *J. Mater. Chem.*, vol. 20, no. 5, pp. 862–866, 2010.

[139] I. Ullah, S. K. Shah, S. Wali, K. Hayat, S. A. Khattak, and A. Khan, "Enhanced efficiency of organic solar cells by using ZnO as an electron-transport layer," *Mater. Res. Express.*, vol. 4, no. 12, p. 125505, 2017.

[140] A. Sukee, E. Kantarak, and P. Singjai, "Preparation of aluminum doped zinc oxide thin films on glass substrate by sparking process and their optical and electrical properties," *Journal of Physics: Conference Series*, vol. 901, no. 1, p. 012153, 2017.

[141] Z. Lin, C. Jiang, C. Zhu, and J. Zhang, "Development of inverted organic solar cells with TiO_2 interface layer by using low-temperature atomic layer deposition," *ACS Appl. Mater. Interfaces*, vol. 5, no. 3, pp. 713–718, 2013.

[142] C. J. Brabec, S. E. Shaheen, C. Winder, N. S. Sariciftci, and P. Denk, "Effect of LiF/metal electrodes on the performance of plastic solar cells," *Appl. Phys. Lett.*, vol. 80, no. 7, pp. 1288–1290, 2002.

[143] E. Ahlswede, J. Hanisch, and M. Powalla, "Comparative study of the influence of LiF, NaF, and KF on the performance of polymer bulk heterojunction solar cells," *Appl. Phys. Lett.s*, vol. 90, no. 16, p. 163504, 2007.

[144] D. M. Stevens, Y. Qin, M. A. Hillmyer, and C. D. Frisbie, "Enhancement of the morphology and open circuit voltage in bilayer polymer/fullerene solar cells," *J. Phys. Chem. C*, vol. 113, no. 26, pp. 11408–11415, 2009.

[145] F.-C. Chen and S.-C. Chien, "Nanoscale functional interlayers formed through spontaneous vertical phase separation in polymer photovoltaic devices," *J. Mater. Chem.*, vol. 19, no. 37, pp. 6865–6869, 2009.

[146] Z. He, C. Zhong, X. Huang, W.-Y. Wong, H. Wu, L. Chen, S. Su, and Y. Cao, "Simultaneous enhancement of open-circuit voltage, short-circuit current density, and fill factor in polymer solar cells," *Adv. Mater.*, vol. 23, no. 40, pp. 4636–4643, 2011.

[147] Q. Wei, T. Nishizawa, K. Tajima, and K. Hashimoto, "Self-organized buffer layers in organic solar cells," *Adv. Mater.*, vol. 20, no. 11, pp. 2211–2216, 2008.

[148] J. Liu, Y. Xue, Y. Gao, D. Yu, M. Durstock, and L. Dai, "Hole and electron extraction layers based on graphene oxide derivatives for high-performance bulk heterojunction solar cells," *Adv. Mater.*, vol. 24, no. 17, pp. 2228–2233, 2012.

[149] K. Zilberberg, H. Gharbi, A. Behrendt, S. Trost, and T. Riedl, "Low-temperature, solution-processed MoO_x for efficient and stable organic solar cells," *ACS Appl. Mater. Interfaces*, vol. 4, no. 3, pp. 1164–1168, 2012.

[150] J. Meyer, K. Zilberberg, T. Riedl, and A. Kahn, "Electronic structure of vanadium pentoxide: An efficient hole injector for organic electronic materials," *J. Appl. Phys*, vol. 110, no. 3, p. 033710, 2011.

[151] H. Choi, B. Kim, M. J. Ko, D.-K. Lee, H. Kim, S. H. Kim, and K. Kim, "Solution processed WO_3 layer for the replacement of pedot: Pss layer in organic photovoltaic cells," *Org. Electron.*, vol. 13, no. 6, pp. 959–968, 2012.

[152] M. D. Irwin, D. B. Buchholz, A. W. Hains, R. P. Chang, and T. J. Marks, "p-type semiconducting nickel oxide as an efficiency-enhancing anode interfacial layer in

polymer bulk-heterojunction solar cells," *Proceedings of the National Academy of Sciences*, vol. 105, no. 8, pp. 2783–2787, 2008.

[153] A. P. Wanninayake, S. Gunashekar, S. Li, B. C. Church, and N. Abu-Zahra, "Performance enhancement of polymer solar cells using copper oxide nanoparticles," *Semicond. Sci. Tech.*, vol. 30, no. 6, p. 064004, 2015.

[154] C. Girotto, E. Voroshazi, D. Cheyns, P. Heremans, and B. P. Rand, "Solution-processed MoO_3 thin films as a hole-injection layer for organic solar cells," *ACS Appl. Mater. Interfaces*, vol. 3, no. 9, pp. 3244–3247, 2011.

[155] K. Zilberberg, S. Trost, J. Meyer, A. Kahn, A. Behrendt, D. Lützenkirchen-Hecht, R. Frahm, and T. Riedl, "Inverted organic solar cells with sol–gel processed high work-function vanadium oxide hole-extraction layers," *Adv. Funct. Mater.*, vol. 21, no. 24, pp. 4776–4783, 2011.

[156] H. Bejbouji, L. Vignau, J. L. Miane, M.-T. Dang, E. M. Oualim, M. Harmouchi, and A. Mouhsen, "Polyaniline as a hole injection layer on organic photovoltaic cells," *Sol. Energ. Mat. Sol. C.*, vol. 94, no. 2, pp. 176–181, 2010.

[157] J. Fan, J. Michalik, L. Casado, S. Roddaro, M. Ibarra, and J. De Teresa, "Investigation of the influence on graphene by using electron-beam and photo-lithography," *Solid State Commun.*, vol. 151, no. 21, pp. 1574–1578, 2011.

[158] V. Gogte, L. Shah, B. Tilak, K. Gadekar, and M. Sahasrabudhe, "Synthesis of potential anticancer agents-i: Synthesis of substituted thiophenes," *Tetrahedron*, vol. 23, no. 5, pp. 2437–2441, 1967.

[159] A. Bayer, "Polythiophenes, process for their preparation and their use," *European Patent*, vol. 339340, 1988.

[160] W. Holzer, E. Schmid, and C. Slatin, "On the reaction of diethyl 3, 4-dihydroxythiophene-2, 5-dicarboxylate with 1, 2-dibromoethane," *Monatsh. Chem.*, vol. 125, no. 11, pp. 1287–1291, 1994.

[161] G. Heywang and F. Jonas, "Poly (alkylenedioxythiophene) s-new, very stable conducting polymers," *Adv. Mater.*, vol. 4, no. 2, pp. 116–118, 1992.

[162] D. M. De Leeuw, P. Kraakman, P. Bongaerts, C. Mutsaers, and D. Klaassen, "Electroplating of conductive polymers for the metallization of insulators," *Synth. Met.*, vol. 66, no. 3, pp. 263–273, 1994.

[163] M. Dietrich, J. Heinze, G. Heywang, and F. Jonas, "Electrochemical and spectroscopic characterization of polyalkylenedioxythiophenes," *J. Electroanal. Chem.*, vol. 369, pp. 87–92, 1994.

[164] J. Kawahara, P. A. Ersman, I. Engquist, and M. Berggren, "Improving the color switch contrast in PEDOT:PSS-based electrochromic displays," *Org. Electron.*, vol. 13, no. 3, pp. 469–474, 2012.

[165] T.-H. Han, S.-H. Jeong, Y. Lee, H.-K. Seo, S.-J. Kwon, M.-H. Park, and T.-W. Lee, "Flexible transparent electrodes for organic light-emitting diodes," *J. Inf. Disp.*, vol. 16, no. 2, pp. 71–84, 2015.

[166] C. K. Kwak, G. E. Pérez, B. G. Freestone, S. A. Al-Isaee, A. Iraqi, D. G. Lidzey, and A. D. F. Dunbar, "Improved efficiency in organic solar cells via conjugated polyelectrolyte additive in the hole transporting layer," *J. Mater. Chem. C*, vol. 4, pp. 10722–10730, 2016.

[167] S. Khan, M. Ul-Islam, M. W. Ullah, Y. Kim, and J. K. Park, "Synthesis and characterization of a novel bacterial cellulose–poly (3, 4-ethylenedioxythiophene)–poly (styrene sulfonate) composite for use in biomedical applications," *Cellulose*, vol. 22, no. 4, pp. 2141–2148, 2015.

[168] S.-C. Luo, E. Mohamed Ali, N. C. Tansil, H.-h. Yu, S. Gao, E. A. Kantchev, and J. Y. Ying, "Poly (3, 4-ethylenedioxythiophene)(pedot) nanobiointerfaces: Thin, ultrasmooth, and functionalized pedot films with in vitro and in vivo biocompatibility," *Langmuir*, vol. 24, no. 15, pp. 8071–8077, 2008.

[169] S. M. Richardson-Burns, J. L. Hendricks, and D. C. Martin, "Electrochemical polymerization of conducting polymers in living neural tissue," *J. Neural. Eng.*, vol. 4, no. 2, p. L6, 2007.

[170] J. Yang, D. H. Kim, J. L. Hendricks, M. Leach, R. Northey, and D. C. Martin, "Ordered surfactant-templated poly (3, 4-ethylenedioxythiophene)(PEDOT) con-

ducting polymer on microfabricated neural probes," *Acta Biomater.*, vol. 1, no. 1, pp. 125–136, 2005.

[171] Y. Xiao, D. C. Martin, X. Cui, and M. Shenai, "Surface modification of neural probes with conducting polymer poly (hydroxymethylated-3, 4-ethylenedioxythiophene) and its biocompatibility," *Biotechnol. Appl. Biochem.*, vol. 128, no. 2, pp. 117–129, 2006.

[172] M. Hokazono, H. Anno, and N. Toshima, "Thermoelectric properties and thermal stability of PEDOT:PSS films on a polyimide substrate and application in flexible energy conversion devices," *J. Electron. Mater.*, vol. 43, no. 6, pp. 2196–2201, 2014.

[173] C.-K. Cho, W.-J. Hwang, K. Eun, S.-H. Choa, S.-I. Na, and H.-K. Kim, "Mechanical flexibility of transparent PEDOT:PSS electrodes prepared by gravure printing for flexible organic solar cells," *Sol. Energ. Mat. Sol. C.*, vol. 95, no. 12, pp. 3269 – 3275, 2011.

[174] E. Vitoratos, S. Sakkopoulos, E. Dalas, N. Paliatsas, D. Karageorgopoulos, F. Petraki, S. Kennou, and S. Choulis, "Thermal degradation mechanisms of PEDOT:PSS," *Org. Electron.*, vol. 10, no. 1, pp. 61–66, 2009.

[175] M. D. Irwin, D. B. Buchholz, A. W. Hains, R. P. H. Chang, and T. J. Marks, "p-type semiconducting nickel oxide as an efficiency-enhancing anode interfacial layer in polymer bulk-heterojunction solar cells," *Proc. Natl. Acad. Sci. U.S.A.*, vol. 105, no. 8, pp. 2783–2787, 2008.

[176] G. Li, C.-W. Chu, V. Shrotriya, J. Huang, and Y. Yang, "Efficient inverted polymer solar cells," *Appl. Phys. Lett.*, vol. 88, no. 25, 2006.

[177] R. Søndergaard, M. Hösel, D. Angmo, T. T. Larsen-Olsen, and F. C. Krebs, "Roll-to-roll fabrication of polymer solar cells," *Mater. today*, vol. 15, no. 1-2, pp. 36–49, 2012.

[178] A. M. Nardes, M. Kemerink, M. De Kok, E. Vinken, K. Maturova, and R. Janssen, "Conductivity, work function, and environmental stability of PEDOT:PSS thin films treated with sorbitol," *Org. Electron.*, vol. 9, no. 5, pp. 727–734, 2008.

[179] D. M. Huang, S. A. Mauger, S. Friedrich, S. J. George, D. Dumitriu-LaGrange, S. Yoon, and A. J. Moulé, "The consequences of interface mixing on organic photovoltaic device characteristics," *Adv. Funct. Mater.*, vol. 21, no. 9, pp. 1657–1665, 2011.

[180] S. R. Dupont, E. Voroshazi, P. Heremans, and R. H. Dauskardt, "Adhesion properties of inverted polymer solar cells: Processing and film structure parameters," *Org. Electron.*, vol. 14, no. 5, pp. 1262–1270, 2013.

[181] S. R. Dupont, M. Oliver, F. C. Krebs, and R. H. Dauskardt, "Interlayer adhesion in roll-to-roll processed flexible inverted polymer solar cells," *Sol. Energ. Mat. Sol. C.*, vol. 97, pp. 171–175, 2012.

[182] A. M. Higgins, S. J. Martin, P. C. Jukes, M. Geoghegan, R. A. Jones, S. Langridge, R. Cubitt, S. Kirchmeyer, A. Wehrum, and I. Grizzi, "Interfacial structure in semiconducting polymer devices," *J. Mater. Chem.*, vol. 13, no. 11, pp. 2814–2818, 2003.

[183] Y. H. Kim, C. Sachse, M. L. Machala, C. May, L. Müller-Meskamp, and K. Leo, "Highly conductive PEDOT:PSS electrode with optimized solvent and thermal post-treatment for ITO-free organic solar cells," *Adv. Funct. Mater.*, vol. 21, no. 6, pp. 1076–1081, 2011.

[184] H. K. Lee, J.-K. Kim, and O. O. Park, "Effects of UV light-irradiated buffer layer on the performance of polymer solar cells," *Org. Electron.*, vol. 10, no. 8, pp. 1641–1644, 2009.

[185] J. S. Yang, S. H. Oh, D. L. Kim, S. J. Kim, and H. J. Kim, "Hole transport enhancing effects of polar solvents on poly (3, 4-ethylenedioxythiophene): Poly (styrene sulfonic acid) for organic solar cells," *ACS Appl. Mater. Interfaces*, vol. 4, no. 10, pp. 5394–5398, 2012.

[186] Y. Xia, H. Zhang, and J. Ouyang, "Highly conductive PEDOT:PSS films prepared through a treatment with zwitterions and their application in polymer photovoltaic cells," *J. Mater. Chem.*, vol. 20, no. 43, pp. 9740–9747, 2010.

[187] E. G. Langford, K. D. Shaughnessy, T. C. Devore, D. Lawrence, and C. Constantin, "Analysis of PEDOT:PSS films after sulfuric acid treatment on silicon and fused silica using FT-IR and UV-VIS," *MRS Advances*, vol. 1, no. 7, pp. 465–469, 2016.

[188] J. Yang, S. Oh, D. Kim, S. Kim, and H. Kim, "Hole transport enhancing effects of polar solvents on poly(3,4- ethylenedioxythiophene):poly(styrene sulfonic acid) for organic solar cells," *ACS Appl. Mater. Interfaces*, vol. 4, no. 10, pp. 5394–5398, 2012.

[189] Z. Hu, J. Zhang, Z. Hao, and Y. Zhao, "Influence of doped PEDOT:PSS on the performance of polymer solar cells," *Sol. Energ. Mat. Sol. C.*, vol. 95, no. 10, pp. 2763 – 2767, 2011.

[190] D. Alemu, H.-Y. Wei, K.-C. Ho, and C.-W. Chu, "Highly conductive PEDOT:PSS electrode by simple film treatment with methanol for ITO-free polymer solar cells," *Energy Environ. Sci.*, vol. 5, no. 11, pp. 9662–9671, 2012.

[191] C. Girotto, D. Moia, B. Rand, and P. Heremans, "High-performance organic solar cells with spray-coated hole-transport and active layers," *Adv. Funct. Mater.*, vol. 21, no. 1, pp. 64–72, 2011.

[192] M. Dobbelin, R. Marcilla, M. Salsamendi, C. Pozo-Gonzalo, P. Carrasco, J. Pomposo, and D. Mecerreyes, "Influence of ionic liquids on the electrical conductivity and morphology of PEDOT:PSS films," *Chem. Mater.*, vol. 19, no. 9, pp. 2147–2149, 2007.

[193] Y. Xia and J. Ouyang, "Significant conductivity enhancement of conductive poly(3,4- ethylenedioxythiophene):poly(styrenesulfonate) films through a treatment with organic carboxylic acids and inorganic acids," *ACS Appl. Mater. Interfaces*, vol. 2, no. 2, pp. 474–483, 2010.

[194] C.-C. Lin, C.-K. Huang, Y.-C. Hung, and M.-Y. Chang, "Enhanced conductivity of poly(3,4-ethylenedioxythiophene):poly(styrene sulfonate) film by acid treatment for indium tin oxide-free organic solar cells," *Jpn. J. Appl. Phys.*, vol. 55, no. 8, p. 081602, 2016.

[195] G. Fang, S. Wu, Z. Xie, Y. Geng, and L. Wang, "Enhanced performance for polymer solar cells by using surfactant-modified PEDOT:PSS as the anode buffer layer," *Macromol. Chem. Phys.*, vol. 212, no. 17, pp. 1846–1851, 2011.

[196] Z. Zhao, Q. Wu, F. Xia, X. Chen, Y. Liu, W. Zhang, J. Zhu, S. Dai, and S. Yang, "Improving the conductivity of PEDOT:PSS hole transport layer in polymer solar cells via copper(ii) bromide salt doping," *ACS Appl. Mater. Interfaces*, vol. 7, no. 3, pp. 1439–1448, 2015.

[197] Y. Xia and J. Ouyang, "Anion effect on salt-induced conductivity enhancement of poly(3,4-ethylenedioxythiophene):poly(styrenesulfonate) films," *Org. Electron.*, vol. 11, no. 6, pp. 1129–1135, 2010.

[198] Y. Xia and J. Ouyang, "Salt-induced charge screening and significant conductivity enhancement of conducting poly(3,4-ethylenedioxythiophene):poly(styrenesulfonate)," *Macromolecules*, vol. 42, no. 12, pp. 4141–4147, 2009.

[199] Z. Fan, D. Du, Z. Yu, P. Li, Y. Xia, and J. Ouyang, "Significant enhancement in the thermoelectric properties of PEDOT:PSS films through a treatment with organic solutions of inorganic salts," *ACS Appl. Mater. Interfaces*, vol. 8, no. 35, pp. 23204–23211, 2016.

[200] Z. Zhao, X. Chen, Q. Liu, Q. Wu, J. Zhu, S. Dai, and S. Yang, "Efficiency enhancement of polymer solar cells via zwitterion doping in PEDOT:PSS hole transport layer," *Org. Electron.*, vol. 27, pp. 232–239, 2015.

[201] J. Ouyang, ""Secondary doping" methods to significantly enhance the conductivity of PEDOT:PSS for its application as transparent electrode of optoelectronic devices," *Displays*, vol. 34, no. 5, pp. 423–436, 2013.

[202] J. Kim, J. Jung, D. Lee, and J. Joo, "Enhancement of electrical conductivity of poly(3,4-ethylenedioxythiophene)/poly(4-styrenesulfonate) by a change of solvents," *Synth. Met.*, vol. 126, no. 2-3, pp. 311–316, 2002.

[203] Y. Xia and J. Ouyang, "PEDOT:PSS films with significantly enhanced conduc-

tivities induced by preferential solvation with cosolvents and their application in polymer photovoltaic cells," *J. Mater. Chem.*, vol. 21, no. 13, pp. 4927–4936, 2011.

[204] X. Crispin, F. Jakobsson, A. Crispin, P. Grim, P. Andersson, A. Volodin, C. Van Haesendonck, M. Van Der Auweraer, W. Salaneck, and M. Berggren, "The origin of the high conductivity of poly(3,4-ethylenedioxythiophene)-poly(styrenesulfonate) (PEDOT-PSS) plastic electrodes," *Chem. Mater.*, vol. 18, no. 18, pp. 4354–4360, 2006.

[205] J. Kim, J.-S. Kim, S.-W. Kwak, J.-S. Yu, Y. Jang, J. Jo, T.-M. Lee, and I. Kim, "Effects of the al cathode evaporation rate on the performance of organic solar cells," *Appl. Phys. Lett.*, vol. 101, no. 21, p. 213304, 2012.

[206] C. Zhang, S. Tong, C. Zhu, C. Jiang, E. Kang, and D. Chan, "Enhancement in open circuit voltage induced by deep interface hole traps in polymer-fullerene bulk heterojunction solar cells," *Appl. Phys. Lett.*, vol. 94, no. 10, p. 79, 2009.

[207] E. Yengel and M. S. Islam, "Effect of cathode metal evaporation rate on the deep trapped hole formation in bulk heterojunction organic solar cells," *Mater. Res. Soc. Symp. Proc.*, vol. 1390, 2012.

[208] M. H. Yun, G.-H. Kim, C. Yang, and J. Y. Kim, "Towards optimization of P3HT:bisPCBM composites for highly efficient polymer solar cells," *J. Mater. Chem.*, vol. 20, no. 36, pp. 7710–7714, 2010.

[209] N. Chaudhary, R. Chaudhary, J. Kesari, and A. Patra, "Effect of composition ratio of P3HT:$PC_{61}BM$ in organic solar cells: Optical and morphological properties," *Mater. Res. Innov.*, vol. 22, no. 5, pp. 282–286, 2018.

[210] S. Wakim, S. Beaupré, N. Blouin, B.-R. Aich, S. Rodman, R. Gaudiana, Y. Tao, and M. Leclerc, "Highly efficient organic solar cells based on a poly (2,7-carbazole) derivative," *J. Mater. Chem.*, vol. 19, no. 30, pp. 5351–5358, 2009.

[211] K. Kutlu, P. Kavak, E. A. Parlak, A. E. Saatci, F. P. Gökdemir, U. D. Menda, and O. Özdemir, "Energy-band diagram of PCDTBT, PCBM and blend by cyclic voltammetry and Uv-Visible measurements," *AIP Conf. Proc.*, vol. 1569, no. 1, pp. 283–287, 2013.

[212] A. G. Emslie, F. T. Bonner, and L. G. Peck, "Flow of a viscous liquid on a rotating disk," *J. Appl. Phys.*, vol. 29, no. 5, pp. 858–862, 1958.

[213] C. Lawrence and W. Zhou, "Spin coating of non-newtonian fluids," *J. Nonnewton. Fluid Mech.*, vol. 39, no. 2, pp. 137–187, 1991.

[214] D. C. Watters, *Characterisation and Optimisation of Donor-Acceptor Conjugated Copolymers for Applications in Bulk Heterojunction Organic Solar Cells.* PhD thesis, University of Sheffield, 2014.

[215] P. S. Ho, P. Hahn, J. Bartha, G. Rubloff, F. LeGoues, Silverman, and BD, "Chemical bonding and reaction at metal/polymer interfaces," *J. Vac. Sci. Technol. A*, vol. 3, no. 3, pp. 739–745, 1985.

[216] N. K. Elumalai and A. Uddin, "Open circuit voltage of organic solar cells: An in-depth review," *Energy Environ. Sci.*, vol. 9, no. 2, pp. 391–410, 2016.

[217] P. Nguyen, S. Scheinert, S. Berleb, W. Brütting, and G. Paasch, "The influence of deep traps on transient current–voltage characteristics of organic light-emitting diodes," *Org. Electron.*, vol. 2, no. 3-4, pp. 105–120, 2001.

[218] A. A. Hussein, A. A. Sultan, M. T. Obeid, A. T. Abdulnabi, and M. T. Ali, "Synthesis and characterization of poly(3-hexylthiophene)," *Int. J. Sci. Eng. Appl. Sci.*, vol. 1, no. 1-3, pp. 2395–3470, 2015.

[219] V. Shrotriya, J. Ouyang, R. J. Tseng, G. Li, and Y. Yang, "Absorption spectra modification in poly (3-hexylthiophene): Methanofullerene blend thin films," *Chem. Phys. Lett.*, vol. 411, no. 1-3, pp. 138–143, 2005.

[220] K. Zhao, L. Xue, J. Liu, X. Gao, S. Wu, Y. Han, , and Y. Geng, "A new method to improve poly(3-hexyl thiophene) (P3HT) crystalline behavior: Decreasing chains entanglement to promote order-disorder transformation in solution," *Langmuir*, vol. 26, no. 1, pp. 471–477, 2010.

[221] Y. A. Ismail, T. Soga, and T. Jimbo, "Effect of composition on conjugation structure and energy gap of P3HT:PCBM organic solar cell," *Int. J. New. Hor. Phys*, vol. 2, no. 2, pp. 87–93, 2015.

[222] D. Chirvase, J. Parisi, J. C. Hummelen, and V. Dyakonov, "Influence of nanomorphology on the photovoltaic action of polymer–fullerene composites," *Nanotechnology*, vol. 15, no. 9, p. 1317, 2004.

[223] Y. Kim, S. A. Choulis, J. Nelson, D. D. Bradley, S. Cook, and J. R. Durrant, "Composition and annealing effects in polythiophene/fullerene solar cells," *J. Mater. Sci.*, vol. 40, no. 6, pp. 1371–1376, 2005.

[224] S. Rafique, S. M. Abdullah, M. M. Shahid, M. O. Ansari, and K. Sulaiman, "Significantly improved photovoltaic performance in polymer bulk heterojunction solar cells with graphene oxide/PEDOT:PSS double decked hole transport layer," *Sci Rep.*, vol. 7, p. 39555, 2017.

[225] S. M. Abdullah, S. Rafique, K. S. Hamdan, K. Sulaiman, D. Taguchi, and M. Iwamoto, "Mathematical modelling of degradation phenomena in organic solar cells under various fabrication conditions," *Org. Electron.*, vol. 58, pp. 46–52, 2018.

[226] K. Sun, B. Zhao, V. Murugesan, A. Kumar, K. Zeng, J. Subbiah, W. W. Wong, D. J. Jones, and J. Ouyang, "High-performance polymer solar cells with a conjugated zwitterion by solution processing or thermal deposition as the electron-collection interlayer," *J. Mater. Chem.*, vol. 22, no. 45, pp. 24155–24165, 2012.

[227] Y. Shao-Peng, K. Wei-Guang, L. Bo-Ya, Z. Wen-Yao, L. Bao-Min, L. Xian-Hao, and F. Guang-Sheng, "Highly efficient PCDTBT:$PC_{71}BM$ based photovoltaic devices without thermal annealing treatment," *Chin. Phys. Lett.*, vol. 28, no. 12, p. 128401, 2011.

[228] G. Sivakumar, T. Pratyusha, D. Gupta, and W. Shen, "Doping of hole transport layer PEDOT:PSS with pentacene for PCDTBT:PCBM based organic solar cells," *Mater. Today*, vol. 4, no. 7, pp. 6814–6819, 2017.

[229] J. W. Kingsley, P. P. Marchisio, H. Yi, A. Iraqi, C. J. Kinane, S. Langridge, R. L. Thompson, A. J. Cadby, A. J. Pearson, D. G. Lidzey, A. L. J. Jones, and A. J. Parnell, "Molecular weight dependent vertical composition profiles of PCDTBT:$PC_{71}BM$ blends for organic photovoltaics," *Sci. Rep.*, vol. 4, p. 5286, 2014.

[230] G. E. Pérez, G. Bernardo, H. Gaspar, J. F. K. Cooper, F. Bastianini, A. J. Parnell, and A. D. F. Dunbar, "Determination of the thin-film structure of zwitterion-doped poly(3,4-ethylenedioxythiophene):poly(styrenesulfonate): A neutron reflectivity study," *ACS Appl. Mater. Interfaces*, vol. 11, no. 14, pp. 13803–13811, 2019.

[231] M. N. Gueye, A. Carella, N. Massonnet, E. Yvenou, S. Brenet, J. Faure-Vincent, S. Pouget, F. Rieutord, H. Okuno, A. Benayad, R. Demadrille, and J.-P. Simonato, "Structure and dopant engineering in PEDOT thin films: Practical tools for a dramatic conductivity enhancement," *Chem. Mater.*, vol. 28, no. 10, pp. 3462–3468, 2016.

[232] T. Etampawala, M. Tehrani, A. Nematollahi, L. He, and M. Dadmun, "The impact of solvent doping on the morphology and performance of spray-coated PEDOT:DPSS: A USANS and SANS study," *Org. Electron.*, vol. 51, pp. 86–93, 2017.

[233] M. Lefebvre, Z. Qi, D. Rana, and P. G. Pickup, "Chemical synthesis, characterization, and electrochemical studies of poly (3, 4-ethylenedioxythiophene)/poly (styrene-4-sulfonate) composites," *Chem. Mater.*, vol. 11, no. 2, pp. 262–268, 1999.

[234] F. Jonas and G. Heywang, "Technical applications for conductive polymers," *Electrochim. Acta*, vol. 39, no. 8-9, pp. 1345–1347, 1994.

[235] M. T. Hutchings, P. J. Withers, T. M. Holden, and T. Lorentzen, *Introduction to the Characterization of Residual Stress by Neutron Diffraction*. CRC press, 2005.

[236] ISIS, "LOQ specifications." Available from www.isis.stfc.ac.uk: `https://www.isis.stfc.ac.uk/Pages/Loq-technical-information.aspx`, 2019. Last accessed: 07 May 2019.

[237] O. Arnold, J. Bilheux, J. Borreguero, A. Buts, S. Campbell, L. Chapon, M. Doucet, N. Draper, R. F. Leal, M. Gigg, V. Lynch, A. Markvardsen, D. Mikkelson, R. Mikkelson, R. Miller, K. Palmen, P. Parker, G. Passos, T. Perring, P. Peterson, S. Ren, M. Reuter, A. Savici, J. Taylor, R. Taylor, R. Tolchenov, W. Zhou, and J. Zikovsky, "Mantid-data analysis and visualization package for neutron scattering and μ sr experiments," *Nucl. Instrum. Methods Phys. Res. A*, vol. 764, pp. 156–166, 2014.

[238] SasView, "Broad peak model." Available from www.sasview.org: http://marketplace.sasview.org/models/37/, 2019. Last accessed: 07-05-2019.

[239] SasView, "Sasview software." Available from www.sasview.org: http://www.sasview.org/, 2019. Last accessed: 07 May 2019.

[240] NIST, "NIST centre for neutron research neutron activation and scattering calculator." Available from www.ncnr.nist.gov: https://www.ncnr.nist.gov/resources/activation/. Last accessed: 05 May 2019.

[241] T. Crowley, E. Lee, E. Simister, and R. Thomas, "The use of contrast variation in the specular reflection of neutrons from interfaces," *Physica B*, vol. 173, no. 1-2, pp. 143–156, 1991.

[242] A. J. Jackson, "Introduction to small-angle neutron scattering and neutron reflectometry," *NIST Center for Neutron Research*, pp. 1–24, 2008.

[243] W. Voegeli, C. Kamezawa, E. Arakawa, Y. F. Yano, T. Shirasawa, T. Takahashi, and T. Matsushita, "A quick convergent-beam laboratory x-ray reflectometer using a simultaneous multiple-angle dispersive geometry," *J. Appl. Crystallogr.*, vol. 50, no. 2, pp. 570–575, 2017.

[244] D. Bagchi and R. Menon, "Conformational modification of conducting polymer chains by solvents: Small-angle x-ray scattering study," *Chem. Phys. Lett.*, vol. 425, no. 1-3, pp. 114–117, 2006.

[245] T. Takano, H. Masunaga, A. Fujiwara, H. Okuzaki, and T. Sasaki, "PEDOT nanocrystal in highly conductive PEDOT:PSS polymer films," *Macromolecules*, vol. 45, no. 9, pp. 3859–3865, 2012.

[246] R. J. Murphy, K. M. Weigandt, D. Uhrig, A. Alsayed, C. Badre, L. Hough, and M. Muthukumar, "Scattering studies on poly (3, 4-ethylenedioxythiophene)–polystyrenesulfonate in the presence of ionic liquids," *Macromolecules*, vol. 48, no. 24, pp. 8989–8997, 2015.

[247] S. T. Lee, Z. Q. Gao, and L. S. Hung, "Metal diffusion from electrodes in organic light-emitting diodes," *Appl. Phys. Lett.*, vol. 75, no. 10, pp. 1404–1406, 1999.

[248] F. Horkay and B. Hammouda, "Small-angle neutron scattering from typical synthetic and biopolymer solutions," *Colloid Polym. Sci.*, vol. 286, no. 6-7, pp. 611–620, 2008.

[249] N. Ise and T. Okubo, ""Ordered" distribution of electrically charged solutes in dilute solutions," *Acc. Chem. Res.*, vol. 13, no. 9, pp. 303–309, 1980.

[250] M. Nierlich, C. Williams, F. Boue, J. Cotton, M. Daoud, B. Famoux, G. Jannink, C. Picot, M. Moan, C. Wolff, M. Rinaudo, and P. G. de Gennes, "Small angle neutron scattering by semi-dilute solutions of polyelectrolyte," *J. Phys.*, vol. 40, no. 7, pp. 701–704, 1979.

[251] M. Nierlich, F. Boue, A. Lapp, and R. Oberthür, "Characteristic lengths and the structure of salt free polyelectrolyte solutions. a small angle neutron scattering study," *Colloid Polym. Sci.*, vol. 263, no. 12, pp. 955–964, 1985.

[252] M. Drifford and J. P. Dalbiez, "Light scattering by dilute solutions of salt-free polyelectrolytes," *J. Phys. Chem.*, vol. 88, no. 22, pp. 5368–5375, 1984.

[253] P.-G. De Gennes, P. Pincus, R. Velasco, and F. Brochard, "Remarks on polyelectrolyte conformation," *J. Phys.*, vol. 37, no. 12, pp. 1461–1473, 1976.

[254] SasView, "Sphere model." Available from www.sasview.org: `http://www.sasview.org/docs/user/models/sphere.html`, 2019. Last accessed: 30 May 2019.

[255] A. Guiner, G. Fournet, C. Walker, and K. L. Yudowitch, "Small angle scattering of x-rays," *Jahn Willey-Champan, New-York*, 1955.

[256] S. R. Raghavan, "Distinct character of surfactant gels: a smooth progression from micelles to fibrillar networks," *Langmuir*, vol. 25, no. 15, pp. 8382–8385, 2009.

[257] P.-G. De Gennes, *Scaling Concepts in Polymer Physics*. Cornell University Press, 1979.

[258] J. Kim, J. Jung, D. Lee, and J. Joo, "Enhancement of electrical conductivity of poly(3,4-ethylenedioxythiophene)/poly(4-styrenesulfonate) by a change of solvents," *Synth. Met.*, vol. 126, no. 2, pp. 311 – 316, 2002.

[259] C. Lee, J. Kim, D. Lee, Y. Koo, J. Joo, S. Han, Y. Beag, and S. Koh, "Organic based flexible speaker through enhanced conductivity of PEDOT/PSS with various solvents," *Synth. Met.*, vol. 135-136, pp. 13–14, 2003.

[260] A. Parnell, A. Dunbar, A. Pearson, P. Staniec, A. Dennison, H. Hamamatsu, M. Skoda, D. Lidzey, and R. Jones, "Depletion of PCBM at the cathode interface in P3HT/PCBM thin films as quantified via neutron reflectivity measurements," *Adv. Mater*, vol. 22, pp. 2444–2447, 2010.

[261] W. Ma, C. Yang, X. Gong, K. Lee, and A. J. Heeger, "Thermally stable, efficient polymer solar cells with nanoscale control of the interpenetrating network morphology," *Adv. Funct. Mater.*, vol. 15, no. 10, pp. 1617–1622, 2005.

[262] C. Kwak, *New Challenges in Environmentally Friendly Materials for Organic and Perovskite Photovoltaic Cells*. PhD thesis, The Univesrity of Sheffield, 2016.

[263] E. Pavlopoulou, G. Fleury, D. Deribew, F. Cousin, M. Geoghegan, and G. Hadziioannou, "Phase separation-driven stratification in conventional and inverted P3HT:PCBM organic solar cells," *Org. Electron.*, vol. 14, no. 5, pp. 1249–1254, 2013.

[264] D. Sivia and J. Webster, "The bayesian approach to reflectivity data," *Physica B: Condens. Matter*, vol. 248, no. 1-4, pp. 327–337, 1998.

[265] W. Wang, E. Metwalli, J. Perlich, C. Papadakis, R. Cubitt, and P. Müller-Buschbaum, "Cyclic switching of water storage in thin block copolymer films containing poly (n-isopropylacrylamide)," *Macromolecules*, vol. 42, no. 22, pp. 9041–9051, 2009.

[266] Q. Zhong, E. Metwalli, M. Rawolle, G. Kaune, A. M. Bivigou-Koumba, A. Laschewsky, C. M. Papadakis, R. Cubitt, and P. Müller-Buschbaum, "Rehydration of thermoresponsive poly (monomethoxydiethylene glycol acrylate) films probed in situ by real-time neutron reflectivity," *Macromolecules*, vol. 48, no. 11, pp. 3604–3612, 2015.

[267] Q. Zhong, E. Metwalli, M. Rawolle, G. Kaune, A. M. Bivigou-Koumba, A. Laschewsky, C. M. Papadakis, R. Cubitt, J. Wang, and P. Müller-Buschbaum,

"Influence of hydrophobic polystyrene blocks on the rehydration of polystyrene-block-poly (methoxy diethylene glycol acrylate)-block-polystyrene films investigated by in situ neutron reflectivity," *Macromolecules*, vol. 49, no. 1, pp. 317–326, 2015.

[268] D. Walsh, "Occam's razor: A principle of intellectual elegance," *Am. Philos. Q.*, vol. 16, no. 3, pp. 241–244, 1979.

[269] L. Nevot and P. Croce, "Caractérisation des surfaces par réflexion rasante de rayons x. application à l'étude du polissage de quelques verres silicates," *Rev. Phys. Appl.*, vol. 15, no. 3, pp. 761–779, 1980.

[270] Y. Kim, A. M. Ballantyne, J. Nelson, and D. D. Bradley, "Effects of thickness and thermal annealing of the PEDOT:PSS layer on the performance of polymer solar cells," *Org. Electron.*, vol. 10, no. 1, pp. 205 – 209, 2009.

[271] B. Friedel, P. Keivanidis, T. Brenner, A. Abrusci, C. McNeill, R. Friend, and N. Greenham, "Effects of layer thickness and annealing of PEDOT:PSS layers in organic photodetectors," *Macromolecules*, vol. 42, no. 17, pp. 6741–6747, 2009.

[272] Y. Wang, Q. Luo, N. Wu, Q. Wang, H. Zhu, L. Chen, Y.-Q. Li, L. Luo, and C.-Q. Ma, "Solution-processed MoO_3:PEDOT:PSS hybrid hole transporting layer for inverted polymer solar cells," *ACS Appl. Mater. Interfaces*, vol. 7, no. 13, pp. 7170–7179, 2015.

[273] Y. Liang, Z. Xu, J. Xia, S.-T. Tsai, Y. Wu, G. Li, C. Ray, and L. Yu, "For the bright future-bulk heterojunction polymer solar cells with power conversion efficiency of 7.4%," *Adv. Mater.*, vol. 22, no. 20, pp. E135–E138, 2010.

[274] S. Zhang, L. Ye, W. Zhao, D. Liu, H. Yao, and J. Hou, "Side chain selection for designing highly efficient photovoltaic polymers with 2D-conjugated structure," *Macromolecules*, vol. 47, no. 14, pp. 4653–4659, 2014.

[275] J. Zhang, H. Tan, X. Guo, A. Facchetti, and H. Yan, "Material insights and challenges for non-fullerene organic solar cells based on small molecular acceptors," *Nat. Energy*, vol. 3, no. 9, pp. 720–731, 2018.

[276] S. B. Dkhil, M. Pfannmöller, S. Bals, T. Koganezawa, N. Yoshimoto, D. Hannani, M. Gaceur, C. Videlot-Ackermann, O. Margeat, and J. Ackermann, "Square-centimeter-sized high-efficiency polymer solar cells: How the processing atmosphere and film quality influence performance at large scale," *Adv. Energy Mater.*, vol. 6, no. 13, p. 1600290, 2016.

[277] N. Li, J. D. Perea, T. Kassar, M. Richter, T. Heumueller, G. J. Matt, Y. Hou, N. S. Güldal, H. Chen, S. Chen, S. Langner, M. Berlinghof, T. Unruh, and C. J. Brabec, "Abnormal strong burn-in degradation of highly efficient polymer solar cells caused by spinodal donor-acceptor demixing," *Nat. Commun.*, vol. 8, p. 14541, 2017.

[278] R. Xue, J. Zhang, Y. Li, and Y. Li, "Organic solar cell materials toward commercialization," *Small*, vol. 14, no. 41, p. 1801793, 2018.

[279] A. T. Kleinschmidt, S. E. Root, and D. J. Lipomi, "Poly (3-hexylthiophene)(P3HT): Fruit fly or outlier in organic solar cell research?," *J. Mater. Chem. A*, vol. 5, no. 23, pp. 11396–11400, 2017.

[280] J. Wu, Y. Xu, Z. Yang, Y. Chen, X. Sui, L. Yang, P. Ye, T. Zhu, X. Wu, X. Liu, H. Cao, A. Peng, and H. Huang, "Simultaneous enhancement of three parameters of P3HT-based organic solar cells with one oxygen atom," *Adv. Energy Mater.*, vol. 9, no. 6, p. 1803012, 2019.

[281] T. Soga, S. Kato, S. Kato, and N. Kishi, "Role of polyethylene glycol addition on the improvement of P3HT:PCBM organic solar cells," *J. Mater. Sci. Mater. Electron.*, vol. 30, no. 4, pp. 3332–3337, 2019.

[282] S. Molamohammadi, S. A. Nia, and Y. S. Jalili, "Improvement of inverted structure organic solar cells by ar plasma treatment on P3HT:$PC_{61}BM$ active layer," *Sustain. Energy Techn.*, vol. 34, pp. 43–48, 2019.

[283] A. M. Velazquez, D. Canto-Reyes, J. Mendez-Gamboa, and M. Acosta, "Optical absorption enhancement of P3HT:PCBM films through nanocavities using polystyrene as a template," *Mater. Lett.*, vol. 245, pp. 65–67, 2019.

[284] C. Kong, B. Song, E. A. Mueller, J. Kim, and A. J. McNeil, "Random copolymers

outperform gradient and block copolymers in stabilizing organic photovoltaics," *Adv. Funct. Mater.*, p. 1900467, 2019.

[285] K. Xing, M. Fahlman, X. Chen, O. Inganäs, and W. Salaneck, "The electronic structure of poly (3, 4-ethylene-dioxythiophene): Studied by xps and ups," *Synth. Met.*, vol. 89, no. 3, pp. 161–165, 1997.

[286] B. Y. Kadem, M. Al-Hashimi, A. S. Hasan, R. G. Kadhim, Y. Rahaq, and A. K. Hassan, "The effects of the PEDOT:PSS acidity on the performance and stability of P3HT:PCBM-based oscs," *J. Mater. Sci. Mater. Electron.*, vol. 29, no. 22, pp. 19287–19295, 2018.

[287] X. Hou, Q. Li, T. Cheng, L. Yu, F. Wang, J. Lin, S. Dai, Y. Li, and Z. Tan, "Improvement of the power conversion efficiency and long term stability of polymer solar cells by incorporation of amphiphilic nafion doped PEDOT-PSS as a hole extraction layer," *J. Mater. Chem. A*, vol. 3, no. 36, pp. 18727–18734, 2015.

[288] Y. Shi, F. Li, and Y. Chen, "Controlling morphology and improving the photovoltaic performances of P3HT/ZnO hybrid solar cells via P3HT-b-PEO as an interfacial compatibilizer," *New J. Chem.*, vol. 37, pp. 236–244, 2013.

[289] C. Yang, J. K. Lee, A. J. Heeger, and F. Wudl, "Well-defined donor-acceptor rodâĂŞcoil diblock copolymers based on P3HT containing C60: the morphology and role as a surfactant in bulk-heterojunction solar cells," *J. Mater. Chem.*, vol. 19, pp. 5416–5423, 2009.

[290] I. Botiz and S. B. Darling, "Self-assembly of poly (3-hexylthiophene)-block-polylactide block copolymer and subsequent incorporation of electron acceptor material," *Macromolecules*, vol. 42, no. 21, pp. 8211–8217, 2009.

[291] B. W. Boudouris, C. D. Frisbie, and M. A. Hillmyer, "Nanoporous poly(3-alkylthiophene) thin films generated from block copolymer templates," *Macromolecules*, vol. 41, no. 1, pp. 67–75, 2008.

[292] B. de Boer, U. Stalmach, P. F. van Hutten, C. Melzer, V. V. Krasnikov, and G. Hadziioannou, "Supramolecular self-assembly and opto-electronic properties of semiconducting block copolymers," *Polymer*, vol. 42, no. 21, pp. 9097–9109, 2001.

[293] B. Gholamkhass and S. Holdcroft, "Toward stabilization of domains in polymer bulk heterojunction films," *Chem. Mater.*, vol. 22, no. 18, pp. 5371–5376, 2010.

[294] D. Zhou, X. Cheng, H. Xu, H. Yang, H. Liu, F. Wu, L. Chen, and Y. Chen, "Interface-induced face-on orientation of the active layer by self-assembled diblock conjugated polyelectrolytes for efficient organic photovoltaic cells," *J. Mater. Chem. A*, vol. 4, pp. 18478–18489, 2016.

[295] G. Pirotte, J. Kesters, P. Verstappen, S. Govaerts, J. Manca, L. Lutsen, D. Vanderzande, and W. Maes, "Continuous flow polymer synthesis toward reproducible large-scale production for efficient bulk heterojunction organic solar cells," *ChemSusChem*, vol. 8, no. 19, pp. 3228–3233, 2015.

[296] M. W. Matsen and F. S. Bates, "Unifying weak- and strong-segregation block copolymer theories," *Macromolecules*, vol. 29, no. 4, pp. 1091–1098, 1996.

[297] L. Leibler, "Theory of microphase separation in block copolymers," *Macromolecules*, vol. 13, no. 6, pp. 1602–1617, 1980.

[298] P. Topham, A. Parnell, and R. Hiorns, "Block copolymer strategies for solar cell technology," *J. Polym. Sci. B*, vol. 49, no. 16, pp. 1131–1156, 2011.

[299] V. Mitchell and D. Jones, "Advances toward the effective use of block copolymers as organic photovoltaic active layers," *Polym. Chem.*, vol. 9, no. 7, pp. 795–814, 2018.

[300] J. Houston, S. Richeter, S. Clément, and R. Evans, "Molecular design of interfacial layers based on conjugated polythiophenes for polymer and hybrid solar cells," *Polym. Int.*, vol. 66, no. 10, pp. 1333–1348, 2017.

[301] H. Erothu, J. Kolomanska, P. Johnston, S. Schumann, D. Deribew, D. T. Toolan, A. Gregori, C. Dagron-Lartigau, G. Portale, W. Bras, T. Arnold, A. Distler, R. C. Hiorns, P. Mokarian-Tabari, T. W. Collins, J. R. Howse, and P. D. Topham, "Synthesis, thermal processing, and thin film morphology of poly (3-hexylthiophene)–poly (styrenesulfonate) block copolymers," *Macromolecules*, vol. 48, no. 7, pp. 2107–2117, 2015.

[302] M. Wong-Stringer, O. S. Game, J. A. Smith, T. J. Routledge, B. A. Alqurashy, B. G. Freestone, A. J. Parnell, N. Vaenas, V. Kumar, M. O. Alawad, A. Iraqi, C. Rodenburg, and D. G. Lidzey, "High-performance multilayer encapsulation for perovskite photovoltaics," *Adv. Energy Mater.*, vol. 8, no. 24, p. 1801234, 2018.

[303] C. Bracher, B. G. Freestone, D. K. Mohamad, J. A. Smith, and D. G. Lidzey, "Degradation of inverted architecture $CH_3NH_3PbI_{3-x}Cl_x$ perovskite solar cells due to trapped moisture," *Energy Sci. Eng.*, vol. 6, no. 1, pp. 35–46, 2018.

[304] SasView, "Poly gauss coil model." Available from www.sasview.org: `http://marketplace.sasview.org/models/37/`, 2019. Last accessed: 07 May 2019.

[305] O. Glatter and O. Kratky, *Small angle X-ray scattering*. Academic press, 1982.

[306] J. S. Higgins and H. C. Benoit, *Polymers and neutron scattering*. Clarendon Press, 1994.

[307] S. King, *Small Angle Neutron Scattering in Modern Techniques for Polymer Characterisation*. Wiley, 1999.

[308] B. Morgan and M. D. Dadmun, "Illumination of conjugated polymer in solution alters its conformation and thermodynamics," *Macromolecules*, vol. 49, no. 9, pp. 3490–3496, 2016.

[309] O. Werzer, K. Matoy, P. Strohriegl, and R. Resel, "Temperature treatment of semiconducting polymers: An x-ray reflectivity study," *Thin Solid Films*, vol. 515, no. 14, pp. 5601–5605, 2007.

[310] E. Verploegen, R. Mondal, C. J. Bettinger, S. Sok, M. F. Toney, and Z. Bao, "Effects of thermal annealing upon the morphology of polymer–fullerene blends," *Adv. Funct. Mater.*, vol. 20, no. 20, pp. 3519–3529, 2010.

[311] S. Grigorian, S. Joshi, and U. Pietsch, "Temperature-dependent structural properties of P3HT FILMS," *IOP Conf. Ser. Mater. Sci. Eng.*, vol. 14, no. 1, p. 012007, 2010.

[312] B. Kitchen, O. Awartani, R. J. Kline, T. McAfee, H. Ade, and B. T. O'Connor, "Tuning open-circuit voltage in organic solar cells with molecular orientation," *ACS Appl. Mater. Interfaces*, vol. 7, no. 24, pp. 13208–13216, 2015.

[313] I. Lange, J. Kniepert, P. Pingel, I. Dumsch, S. Allard, S. Janietz, U. Scherf, and D. Neher, "Correlation between the open circuit voltage and the energetics of organic bulk heterojunction solar cells," *J. Phys. Chem. Lett*, vol. 4, no. 22, pp. 3865–3871, 2013.

[314] A. Ergete, F. K. Sabir, Y. Li, and T. Yohannes, "Effect of solvent additives and P3HT on PDTSTTz/PCBM-based bulk heterojunction solar cells," *J. Photon. Energy*, vol. 5, no. 1, p. 057209, 2015.

[315] Y. Wang, J. Chen, H. D. Kim, B. Wang, R. Iriguchi, and H. Ohkita, "Ternary blend solar cells based on a conjugated polymer with diketopyrrolopyrrole and carbazole units," *Front. Energy Res.*, vol. 6, p. 113, 2018.

[316] O. LTD, "PEDOT:PSS specifications." Available from www.ossila.com: `https://www.ossila.com/products/pedot-pss?variant=22831509825`, 2019. Last accesed: 17 September 2016.

[317] D. Alemu, H.-Y. Wei, K.-C. Ho, and C.-W. Chu, "Highly conductive PEDOT:PSS electrode by simple film treatment with methanol for ITO-free polymer solar cells," *Energy Environ. Sci.*, vol. 5, no. 11, pp. 9662–9671, 2012.

[318] M.-H. Jao, H.-C. Liao, and W.-F. Su, "Achieving a high fill factor for organic solar cells," *J. Mater. Chem. A*, vol. 4, no. 16, pp. 5784–5801, 2016.

[319] Z. Ma, Z. Tang, E. Wang, M. R. Andersson, O. InganäÌĹs, and F. Zhang, "Influences of surface roughness of ZnO electron transport layer on the photovoltaic performance of organic inverted solar cells," *J. Phys. Chem. C*, vol. 116, no. 46, pp. 24462–24468, 2012.

[320] K.-B. Kim, Y.-H. Tak, Y.-S. Han, K.-H. Baik, M.-H. Yoon, and M.-H. Lee, "Relationship between surface roughness of indium tin oxide and leakage current of organic light-emitting diode," *Jpn. J. Appl. Phys*, vol. 42, no. 4B, p. L438, 2003.

[321] B. Friedel, P. E. Keivanidis, T. J. Brenner, A. Abrusci, C. R. McNeill, R. H. Friend, and N. C. Greenham, "Effects of layer thickness and annealing of pedot:pss layers in organic photodetectors," *Macromolecules*, vol. 42, no. 17, pp. 6741–6747, 2009.

[322] C.-C. Chen, S. H. Chang, L.-C. Chen, F.-S. Kao, H.-M. Cheng, S.-C. Yeh, C.-T. Chen, W.-T. Wu, Z.-L. Tseng, C. L. Chuang, and C.-G. Wu, "Improving the efficiency of inverted mixed-organic-cation perovskite absorber based photovoltaics by tailing the surface roughness of PEDOT:PSS thin film," *Solar Energy*, vol. 134, pp. 445–451, 2016.

[323] J. Gasiorowski, R. Menon, K. Hingerl, M. Dachev, and N. S. Sariciftci, "Surface morphology, optical properties and conductivity changes of poly (3, 4-ethylenedioxythiophene): Poly (styrenesulfonate) by using additives," *Thin Solid Films*, vol. 536, pp. 211–215, 2013.

[324] A. J. Moulé, M.-C. Jung, C. W. Rochester, W. Tress, D. LaGrange, I. E. Jacobs, J. Li, S. A. Mauger, M. D. Rail, O. Lin, D. J. Bilsky, Y. Qi, P. Stroeve, L. A. Berben, and R. Moriz, "Mixed interlayers at the interface between PEDOT:PSS and conjugated polymers provide charge transport control," *Journal of Materials Chemistry C*, vol. 3, no. 11, pp. 2664–2676, 2015.

[325] F. Bastianini, G. E. Pérez, A. R. Hobson, S. E. Rogers, A. J. Parnell, M. Grell, A. F. Gutiérrez, and A. D. Dunbar, "In-situ monitoring poly (3-hexylthiophene) nanowire formation and shape evolution in solution via small angle neutron scattering," *Sol. Energ. Mat. Sol. C.*, vol. 202, p. 110128, 2019.

[326] K. Zhao, L. Xue, J. Liu, X. Gao, S. Wu, Y. Han, and Y. Geng, "A new method to improve poly (3-hexyl thiophene)(P3HT) crystalline behavior: Decreasing chains entanglement to promote order- disorder transformation in solution," *Langmuir*, vol. 26, no. 1, pp. 471–477, 2009.

[327] S. A. Mauger, L. Chang, C. W. Rochester, and A. J. Moulé, "Directional dependence of electron blocking in PEDOT:PSS," *Org. Electron.*, vol. 13, no. 11, pp. 2747–2756, 2012.

[328] N. Grossiord, J. M. Kroon, R. Andriessen, and P. W. Blom, "Degradation mechanisms in organic photovoltaic devices," *Org. Electron.*, vol. 13, no. 3, pp. 432–456, 2012.

[329] J. A. Hauch, P. Schilinsky, S. A. Choulis, R. Childers, M. Biele, and C. J. Brabec, "Flexible organic P3HT:PCBM bulk-heterojunction modules with more than 1 year outdoor lifetime," *Sol. Energ. Mat. Sol. C.*, vol. 92, no. 7, pp. 727–731, 2008.

[330] V. I. Madogni, B. Kounouhéwa, A. Akpo, M. Agbomahéna, S. A. Hounkpatin, and C. N. Awanou, "Comparison of degradation mechanisms in organic photovoltaic devices upon exposure to a temperate and a subequatorial climate," *Chem. Phys. Lett.*, vol. 640, pp. 201–214, 2015.

[331] H. Hintz, H.-J. Egelhaaf, L. Lüer, J. Hauch, H. Peisert, and T. Chassé, "Photodegradation of P3HT- a systematic study of environmental factors," *Chem. Mater.*, vol. 23, no. 2, pp. 145–154, 2010.

[332] C. H. Peters, I. Sachs-Quintana, W. R. Mateker, T. Heumueller, J. Rivnay, R. Noriega, Z. M. Beiley, E. T. Hoke, A. Salleo, and M. D. McGehee, "The mechanism of burn-in loss in a high efficiency polymer solar cell," *Adv. Mater.*, vol. 24, no. 5, pp. 663–668, 2012.